Dissertation

zur

Erlangung der Doktorwürde (Dr. rer. nat.)

der

Naturwissenschaftlich-Mathematischen Gesamtfakultät

der

Ruprecht-Karls-Universität Heidelberg

vorgelegt von

Severin Sylvester Schneider

aus Augsburg

Tag der mündlichen Prüfung
29. Oktober 2021

Processing and N-Doping of Polymer and Carbon Nanotube Field-Effect Transistors

Gutachter

Prof. Dr. Jana Zaumseil

Prof. Dr. Dr. Hans-Jörg Himmel

"Malum est consilium, quod mutari non potest." – Publilius Syrus

ACKNOWLEDGEMENTS

This thesis would hardly have been managable without the help and support of numerous people, whom I would like to thank here.

First and foremost, I would like to express my gratitude to *Prof. Jana Zaumseil* for providing me with the opportunity to conduct the research in her group that ultimately resulted in the completion of this thesis. Thank you for the project-related scientific guidance, the support for a horizon-broadening research stay in Canada and the possibility to present my exciting results at various conferences from the very start of my term.

Thank you, *Prof. Hans-Jörg Himmel*, for agreeing to review this dissertation.

Furthermore, I would like to thank my former colleagues in the *Nanomaterials for Opto-electronics (NMOE)* and PhysChem2D groups. My special thanks belong to *Maximilian Brohmann*, mostly for fruitful discussions - both work-related and off-topic, *Felix Berger*, mostly for sharing the sometimes pleasant and sometimes less pleasant experiences in joint projects, as well as *Jan Gotthardt*, primarily for helpful discussions on (not) doping carbon nanotubes and the importance of learning how to deal with bumpy communication.

Moreover, a big 'thank you' goes out to Team SFB1249: *Katelyn Goetz* for providing scientific guidance in a refreshingly laid-back style, *Vaishnavi Rao* for being a great office mate, *Maik Matthiesen* for the huge amount of equipment support that benefited not only me but rather all NMOEans and all of you for the great dinner experiences.

Further thanks belong to *Max, Jan, Felix, Sonja Wieland* and *Martin Held* for their proofreading services and to *Stefan Schießl* for support during the very early and very late stages of this thesis.

Sincere thanks are also due to Team Canada: *Jacques Lefebvre, Patrick Malenfant, François Lapointe, Paul Finnie, Jianfu Ding, Alexandria Snyder* and *Ashish Sapkota* as well as *Kelsey Johnson* for the warm welcome and hospitality.

I am also grateful to the collaboration partners without whose help the projects enclosed in this thesis would not have been possible: *Prof. Michael Zharnikov, Prof. Yana Vaynzof, Prof. Hans-Jörg Himmel, Eric Sauter, David Becker-Koch, Roxana Lorentz* and *Lena Steuer*.

Besides, I would like to thank the students I had the opportunity to supervise for their contributions: *Jan, Jonas Stracke, Nicolas Diercks* and *Juliette Schleicher*.

In addition, I would like to thank the technical staff at the institute of applied physical

ABSTRACT

Semiconducting, single-walled carbon nanotubes (SWCNTs) have mechanical and electronic properties that render them a promising material for solution-processable, stretchable and flexible electronics. However, their strong tendency to form aggregates in dispersion constitutes a large obstacle to realize the film uniformity necessary for the transition of devices from laboratory to commercial scale. The resulting inhomogeneities in film morphology lead to an undesired spread in device performance.

Based on the tailored formulation of colloidal inks *via* suitable solvents and additives the first part of this thesis presents a simple yet effective method to slow down aggregation of polymer-wrapped SWCNTs in organic solvents. This effect on aggregation by 1,10-phenanthroline as a stabilizing additive can be monitored with time-dependent absorption spectroscopy. The improved homogeneity of the SWCNT networks deposited from stabilized dispersions after several days of ink storage lead to higher charge carrier mobilities with strongly reduced device-to-device variations compared to inks without additive.

The intrinsic ambipolarity of SWCNTs is a great disadvantage for their use in electronic circuits as it leads to large power dissipation. While pure hole conduction can be achieved relatively easily by doping with, for example, ambient oxygen, facilitating exclusive electron conduction represents a large challenge. A solution-processable n-dopant from the family of guanidino-functionalized aromatics (GFAs) is introduced to overcome this limitation. The resulting SWCNT network field-effect transistors (FETs) exhibit pure electron transport with high mobility while hole transport is fully suppressed, excellent switching behavior and good operational stability. Their application potential (combined with a doped p-type FET) is highlighted by complementary inverters with very low power dissipation.

This modification of the charge transport behavior is applied to another promising solution-processable semiconductor, *i.e.*, donor-acceptor-polymers. Doping of these polymers with two GFA compounds under various processing conditions improves electron injection and transport while hole transport is suppressed. Again, these transistors display good environmental stability under operating conditions. The extended applicability of the newly introduced GFA dopants to different semiconductors emphasizes their potential for transistors based on solution-processable semiconductors.

KURZFASSUNG

Halbleitende, einwandige Kohlenstoffnanoröhren (engl. *single-walled carbon nanotubes*, SWCNTs) zeichnen sich durch ihre außergewöhnlichen mechanischen und elektronischen Eigenschaften aus, was sie zu einem aussichtsreichen Material für lösungsprozessierte, dehnbare und flexible Elektronik macht. Für den Transfer vom Labor in die kommerzielle Nutzung von SWCNTs stellt deren Neigung zur Aggregation in Dispersion jedoch ein großes Hindernis für die notwendige Gleichmäßigkeit der benötigten Filme dar. Die resultierenden Inhomogenitäten in den Filmen führen dabei zu ungewollten Variationen der Bauteileigenschaften.

Basierend auf der maßgeschneiderten Formulierung kolloidaler Tinten durch geeignete Lösungsmittel und Additive wird eine einfache und effiziente Methode eingeführt, die Aggregation von polymerselektierten SWCNTs in organischen Lösungsmitteln signifikant zu verlangsamen. Dies wird durch die Verwendung von 1,10-Phenanthrolin als Stabilisatorzusatz erreicht, was mittels zeitabhängier Absorptionsspektroskopie bestätigt werden kann. Die deutlich verbesserte Netzwerkhomogenität, auch nach mehrtägiger Lagerung der Tinten, führt zu reproduzierbar höheren Ladungsträgermobilitäten bei stark verringerter Bauteil-zu-Bauteil-Variation im Vergleich zu Filmen aus Tinten ohne Stabilisatorzusatz.

Die intrinsische Ambipolarität der SWCNTs ist ein schwerwiegender Nachteil bei der Verwendung in elektronischen Schaltkreisen, da sie mit hohen Verlustleistungen einhergeht. Während die Überführung des Materials zum reinen Lochleiter relativ einfach durch Dotieren z.B. mittels Luftsauerstoff erfolgen kann, stellt die Umwandlung zum reinen Elektronenleiter eine große Herausforderung dar. Die Substanzklasse der Guanidino-funktionalisierten Aromaten (GFA) wird als neuartiges, lösungsprozessierbares n-Dotandenmaterial eingeführt. Die resultierenden SWCNT-Netzwerk-Feldeffekttransistoren (FETs) weisen reinen Elektronentransport mit hoher Ladungsträgerbeweglichkeit, ausgezeichnetes Schaltverhalten und exzellente Stabilität im Betriebszustand auf, wobei der Lochtransport vollständig unterdrückt wird. Das Anwendungspotenzial (durch Kombination mit einem entsprechend dotierten p-Typ FET) wird in komplementäeren Inverterschaltkreisen mit sehr niedrigen Verlustleistungen verdeutlicht.

Diese Modifizierung der Ladungstransporteigenschaften wird noch auf eine weitere vielversprechende lösungsprozessierbare Halbleitermaterialklasse, die Donor-Akzeptor-Polymere, übertragen. Durch Dotieren mit zwei unterschiedlichen GFA unter verschiedenen Be-

dingungen kann für zwei halbleitendende Polymere die Injektion von Elektronen sowie deren Transport verbessert werden, während der Transport von Löchern unterdrückt wird. Auch hier zeichnen sich die Transistoren durch gute Stabilität im Betriebszustand unter Umgebungsbedingungen aus. Diese Erweiterung der Anwendbarkeit des neu vorgestellten Dotandensystems auf unterschiedliche Halbleiter unterstreicht deren Potenzial für die organische Elektronik.

ABBREVIATIONS

0D	zero-dimensional
1,10-phen	1,10-phenanthroline
1D	one-dimensional
2D	two-dimensional
$^\mathrm{n}$Bu	n-butyl
$^\mathrm{n}$Dec	n-decyl
$^\mathrm{n}$Oct	n-octyl
AFM	atomic force microscopy
Bn	benzyl
DMBI	dimethyldihydrobenzimidazole
DOS	density of states
DPPT-BT	poly[(2,5-bis(2-octyldodecyl)-(5–(benzo[2,1,3]thiadiazole-4,7-diyl)-2,5-diyl)-thiophene-2,5-diyl)–6-(thiophene-2,5-yl)pyrrolo[3,4-c]pyrrole-1,4(2H, 5H)-dione)]
FET	field-effect transistor
GCA	gradual channel approximation
GFA	guanidino-functionalized aromatic
gFPP	gated four point-probe
HOMO	highest occupied molecular orbital
LUMO	lowest unoccupied molecular orbital
Mo(tfd-COCF$_3$)$_3$	molybdenum tris(1-(trifluoroacetyl)-2-(trifluoromethyl)ethane-1,2-dithiolene)
NIR	near infrared
NMP	N-methyl-2-pyrrolidone
OFET	organic field-effect transistor

OLED	organic light-emitting diode
P(NDI2OD-T2)	poly[N,N'-bis(2-octyldodecyl)-naphthalene-1,4,5,8-bis(dicarboximide)-2,6-diyl]-*alt*-5,5'-(2,2'-bithiophene)
P3HT	poly(3-hexylthiophene)
PBTTT	poly(2,5-bis(3-tetradecylthiophene-2-yl)thieno[3,2-*b*]thiophene)
PFO-BPy	poly[(9,9-dioctylfluorenyl-2,7-diyl)-*alt*-(6,6'-2,2'-bipyridine)]
PMMA	poly(methyl methacrylate)
RBM	radial breathing mode
SWCNT	single-walled carbon nanotube
tdmegb	1,2,4,5-tetrakis(N,N'-dimethyl-N,N'-ethylene-guanidino)benzene
ttmg-phen	2,3,7,8-tetrakis(tetramethylguanidino)phenazine
ttmgb	1,2,4,5-tetrakis(tetramethylguanidino)benzene
UV	ultraviolet
vis	visible
WF	work function

Contents

Chapter 1

INTRODUCTION

Single-crystalline silicon has served as the established semiconductor in electronics for decades, however, novel applications such as flexible, foldable or transparent electronics require alternative semiconductors that can be processed from solution at low temperatures. Examples of such materials include metal oxides,[1] small molecules,[2] polymers[3] and nanomaterials like carbon nanotubes.[4] While some of these materials have been successfully introduced to the market in organic light-emitting diodes (OLEDs) for smart phone displays or organic solar cells, the market value of organic field-effect transistors (OFETs) remains restricted to niche products such as electronic papers.

One of these materials that are promising for application in solution-processed electronics are single-walled carbon nanotubes (SWCNTs). SWCNTs are a carbon allotrope in the shape of hollow cylinders with large aspect ratios (length/diameter > 1000). They excel by virtue of their exceptional mechanical properties such as high tensile strength, their chemical stability and their electronic properties such as an intrinsic mobility of several tens of thousands of $cm^2 V^{-1} s^{-1}$. The long-standing limitation preventing the full exploitation of nanotubes, *i.e.*, the mix of metallic and semiconducting species in as-grown nanotube bulk samples, has been resolved in recent years by the development of effective and scalable purification protocols.[5]

Networks of SWCNTs that reach somewhat lower mobilities in field-effect transistors (FETs, up to 100 $cm^2 V^{-1} s^{-1}$)[6] can be deposited with processing techniques compatible with large-area fabrication such as roll-to-roll printing. Such networks have even been used to build a 16-bit microprocessor, highlighting their potential.[7]

An issue that has contributed to the slow transfer from the scientific laboratory to successful commercialization is the tendency of SWCNTs to form aggregates in dispersion. This complicates device processing, leads to film inhomogeneities detrimental to charge transport and, ultimately, device performance variations incompatible with commercial use.

Another drawback of solution-processable semiconductors that also applies to, *e.g.*, semiconducting polymers is their generally inferior performance in n-type compared to p-type transistors. This is due to higher electron injection barriers with common electrode materials, a higher susceptibility of electrons to trapping by polar adsorbates[8] commonly present at relevant interfaces and poor operational stability of the devices in ambient conditions.[9] However, for the realization of energy-efficient complementary circuits, that serve as the basic building block of large-scale integration, equal performance of both p- and n-type transistors is mandatory.

An approach to remedy these drawbacks is the targeted introduction of impurities referred to as doping. While this concept has been widely applied to inorganic semiconductors to create integrated circuits and modern OLED technology heavily relies on it,[10] doping

of carbon-based semiconductors for transistor applications has thus far only been implemented relatively scarcely, particularly for n-type transistors. Ideally, doping improves charge carrier injection and transport as well as device stability.[11,12] However, degenerate doping, *i.e.*, the introduction of excess charge carriers must be avoided as the resulting elevated off-currents limit the degree of switching in the transistor. The ideally localized deposition of dopants, undesired diffusion of dopant species and compatibility to the processing of the semiconductor impose limitations on available materials and processing techniques. Unfortunately, the intrinsically poor environmental stability of n-dopants as well as the formed reaction products, *i.e.*, the doped semiconductor and oxidized dopant species, represent additional complications.

This thesis addresses both of the issues outlined above. Aggregation in SWCNT dispersions is slowed down for more reliable and reproducible device fabrication and a novel class of n-dopants is introduced to alleviate the disparity of p- and n-type transistor performance in solution-processable semiconductors.

This dissertation is structured in the following way: Chapter 2 outlines the theoretical basis and the state of the art in relation to this thesis. The structural, electronic and charge transport properties of the employed semiconductors, *i.e.*, SWCNTs and semiconducting polymers, are described. The general working principles of uni- and ambipolar FETs are explained and linked to the current state of research for transistors using these materials. Finally, the topic of controlling charge injection, which is crucial to improving device performance, is introduced with a strong emphasis on molecular doping.

Chapter 3 summarizes the experimental techniques employed in this work, specifically ink preparation as well as device fabrication and characterization.

Chapter 4 focuses on an investigation of aggregation in polymer-wrapped SWCNT dispersions commonly employed for film deposition. Time-dependent UV-vis-NIR spectroscopy is established as a simple yet effective method to monitor aggregation. The impact of the small-molecule additive 1,10-phenanthroline on the stability of these dispersions is correlated with improved SWCNT thin-film homogeneity, particularly for networks deposited from aged dispersions (up to on week). These SWCNT networks are then incorporated into FETs, which are electrically characterized with a focus on their performance homogeneity.

Chapter 5 introduces guanidino-functionalized aromatic (GFA) compounds as n-dopants to transform SWCNT networks with originally ambipolar to purely n-type charge transport and the possible mechanisms of this conversion are investigated and discussed. Furthermore, the application potential of these n-type devices is demonstrated in complementary inverters and their environmental stability under operating conditions is tested.

In Chapter 6, two representatives of GFA dopants are applied to different polymer transistors. A variety of processing conditions is compared to maximize the dopants' impact on

improving device performance. A discussion of their effect on the efficiency of charge carrier injection is supported by contact resistance measurements. Furthermore, the operational stability of the devices is compared to the findings for the SWCNT network transistors. In Chapter 7, the key insights gathered in this work are summarized and a perspective on potential further research is offered.

Chapter 2

BACKGROUND

This chapter provides an overview on relevant fundamental properties of the carbon-based semiconductors employed in this study. It further describes the working principles of field-effect transistors and how to control charge injection from electrode to semiconductor.

2.1 Carbon Nanotubes

The low-dimensional carbon allotropes discovered over the last four decades, *i.e.*, the zero-dimensional (0D) fullerenes,[13] one-dimensional (1D) carbon nanotubes[14] and two-dimensional (2D) graphene,[15] attracted continuous research interest. All of these nano-materials consist of exclusively sp²-hybridized carbon atoms although in different spatial arrangements. Single-walled carbon nanotubes (SWCNTs) have the shape of hollow cylinders – as opposed to multiwalled carbon nanotubes with at least two shells of carbon nested into one another. SWCNTs exhibit well-defined optical and electronic properties, which render them suitable for a variety of (opto-)electronic applications. The subsequent section describes the structural, electronic and optical properties of SWCNTs and the selective dispersion of semiconducting SWCNTs by polymer wrapping in organic solvents as the method of choice to obtain a single species of SWCNTs.

2.1.1 Structural Properties

The electronic and optical properties of SWCNTs are governed by the precise arrangement of the sp²-hybridized carbon atoms. As illustrated in Figure 2.1, SWCNTs can be considered as rolled-up sheets of graphene along the circumferential roll-up vector $\vec{C_h}$, which leads to coinciding edge carbon atoms. This vector is defined as

$$\vec{C_h} = n\vec{a_1} + m\vec{a_2} \tag{2.1}$$

with $\vec{a_1}$, $\vec{a_2}$ being the two basic unit vectors with a length of $a = \sqrt{3}b_{CC} = 246$ pm in relation to the length of the carbon-carbon bond $b_{CC} = 142$ pm and n, m being integers ($0 \leq m \leq n$) termed chiral indices. SWCNTs are unequivocally defined by this pair of integers (n,m) commonly denoted as *chirality*. If $m = 0$, they are called *zigzag* (*e.g.* (8,0) SWCNT, see Figure 2.1b). If $m = n$, they are called *armchair* SWCNTs (*e.g.* (7,7) SWCNT, see Figure 2.1b). Both species are achiral as opposed to all other SWCNTs, *e.g.*, the (6,5) SWCNT predominantly used in this thesis, which are chiral (see Figure 2.1b).
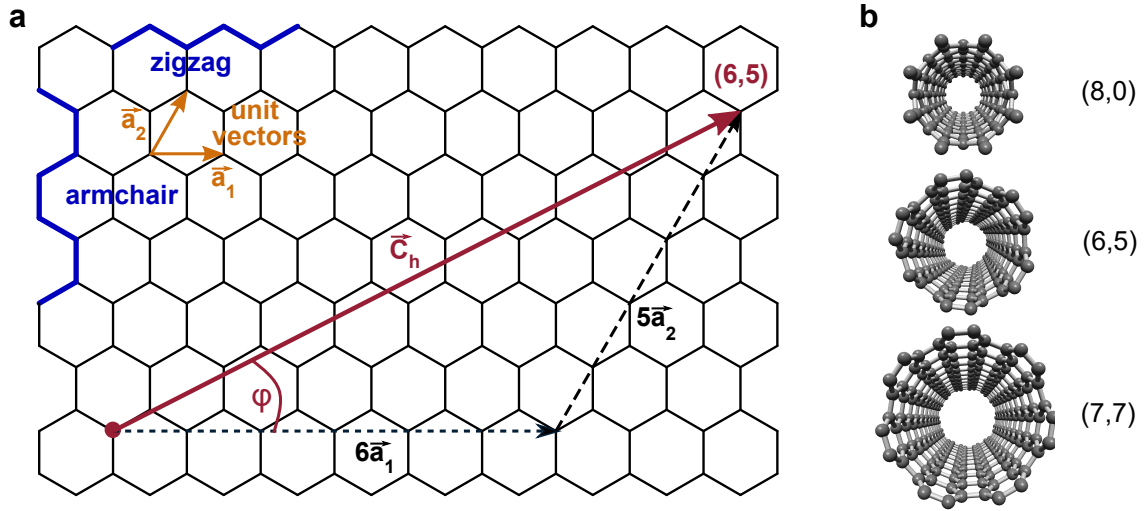
Figure 2.1: (a) SWCNT structure definition referenced to the honeycomb of a graphene sheet. (b) Structural examples of a zigzag (8,0), a chiral (6,5) and an armchair (7,7) SWCNT.

The chiral indices (n,m) directly enable the assessment of the electronic character of a given nanotube. For $(m-n)mod(3) = 0$, the SWCNT is metallic, for $(m-n)mod(3) = \{1,2\}$ the SWCNT is semiconducting with a typical bandgap of $0.5 - 1.5$ eV, which is inversely proportional to their diameter.[16] Based on Equ. 2.1, the diameter d_t as well as the chiral angle φ of any SWCNT species can be calculated according to

$$d_t = \frac{|\vec{C_h}|}{\pi} = \frac{a}{\pi}\sqrt{n^2 + nm + m^2} \tag{2.2}$$

and

$$\cos(\varphi) = \frac{2n + m}{2\sqrt{n^2 + nm + m^2}}. \tag{2.3}$$

Only chiral angles of $0 \leq \varphi \leq 30°$ lead to non-duplicate nanotube species due to the hexagonal symmetry of the graphene lattice.

Given their much larger length (typically hundreds of nm to several microns) than diameter (≈ 1 nm), nanotubes are assumed to be of infinite length and their ends are disregarded for the calculation of their electronic properties.

2.1.2 Electronic and Optical Properties

Analogous to the structure of SWCNTs, their electronic properties can also be understood by deriving them from those of graphene. By rolling up the 2D sheet of graphene along $\vec{C_h}$ (see above), the graphene wavefunction is subject to new periodic boundary conditions (zone-folding model).[16–18] This determines the 1D band structure of each individual SWCNT and consequently leads to characteristic sharp peaks in its density of states (DOS) called van Hove singularities (see Figure 2.2). In contrast to the bandgap in the

semiconducting (6,5) SWCNT, *i.e.*, the DOS is zero at the Fermi level, there is a small yet continuous DOS between the highest occupied and lowest unoccupied van Hove singularity of metallic nanotubes. This band structure defines both the optical and the electronic properties of SWCNTs.
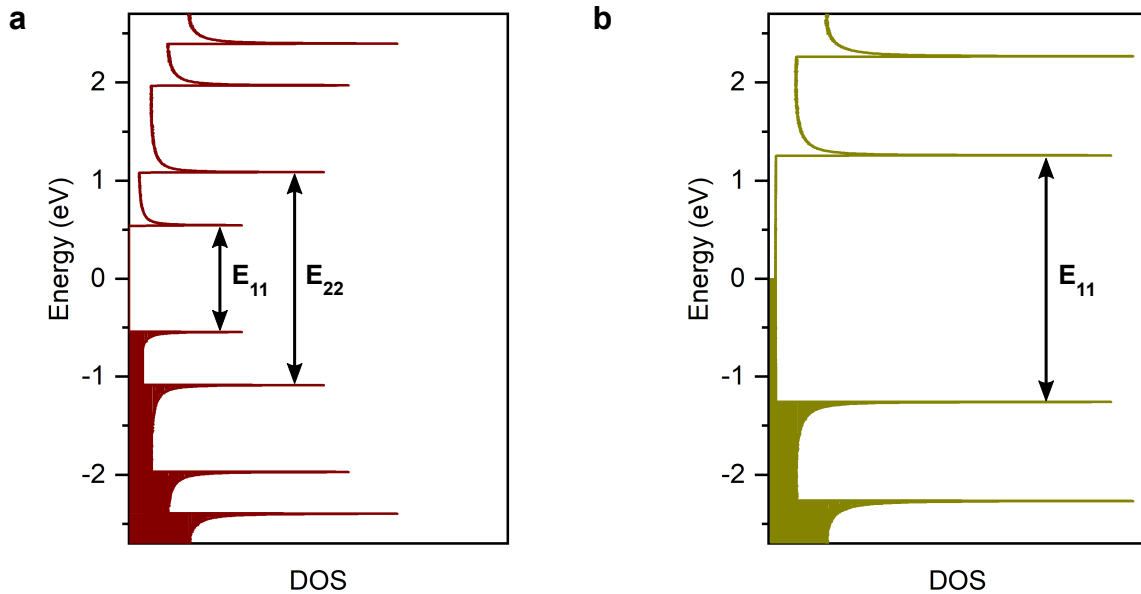
Figure 2.2: Electronic DOS of (a) a semiconducting (6,5) SWCNT and (b) a metallic (7,7) SWCNT with sharp van Hove singularities. Allowed optical transitions are labeled E_{11} and E_{22}. DOS calculated according to reference.[19]

Nanotubes typically absorb light corresponding to different E_{ii} transitions while emission occurs upon relaxation to their lowest excitonic state E_{11}. They exhibit a strong polarization anisotropy, *i.e.*, polarizability in parallel (longitudinal) direction is much larger than that perpendicular (transversal) to the tube axis.[20] Absorption of the latter would result in absorption of light at energy E_{12} but is hardly detectable under standard conditions. For diameters up to 2 nm, the absorption features span the range from ultraviolet (UV), visible (vis) to near infrared (NIR), which is equivalent to wavelengths of 300 – 3000 nm. A UV-vis-NIR spectrum of (6,5) SWCNTs that exhibits the characteristically narrow absorption peaks (full width at half maximum $\approx 40 – 50$ meV) corresponding to the E_{11} and E_{22} transitions serves as an example (see Figure 2.3).

The well known Kataura plot[21,22] summarizes the various possible transition energies as a function of SWCNT diameter (inverse proportionality). It thus provides a general basis to distinguish between metallic and semiconducting nanotube species if their diameter range is established.
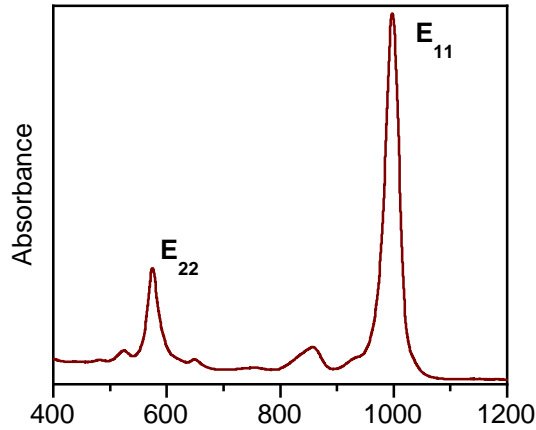
Figure 2.3: Characteristic UV-vis-NIR absorption spectrum of (6,5) SWCNTs dispersed by polymer wrapping in toluene with narrow peaks corresponding to the E_{11} and E_{22} transitions.

A more sensitive assessment of potential metallic impurities in a SWCNT sample is enabled *via* resonant Raman spectroscopy based on the excitation of vibrational modes. If the excitation energy matches one of the E_{ii} transitions, signal intensities are enhanced by several orders of magnitude compared to non-resonant excitation, which makes even single-nanotube detection possible.[23] The diameter-dependent radial breathing modes (RBM) ($100 - 350$ cm^{-1}) are related to radially directed in-phase vibrations. The D-mode ($1250 - 1450$ cm^{-1}) is related to defects in the π-conjugated walls of the nanotube while the G-modes G^+, G^- and E_2 correspond to tangential vibrations in the range of $1500 - 1600$ cm^{-1}.[24] It is important to point out that Raman spectroscopy is a very powerful method for the assessment of SWCNT properties beyond simple composition analysis including the degree of doping[24,25] or alignment[26] in a nanotube sample.

Aside from their spectroscopic properties, the electronic structure (see above) of SWCNTs are the foundation of their extraordinary charge transport properties.
Carrier mobilities of individual nanotubes scale inversely with temperature indicating that they display band transport and they are proportional to the square of the SWCNT diameter.[27,28] Their charge carrier mobilities SWCNTs extend to the order of several thousand cm^2 V^{-1} s^{-1} at room temperature for both holes and electrons. As the valence and conduction bands are nearly symmetric, the effective mass of both carriers are also nearly equal. Given that the bandgaps of SWCNTs are small (typically $0.5 - 1.5$ eV), injection barriers for both carriers with common electrode metals such as gold are low. SWCNTs hence exhibit ambipolar transport (see section 2.3.2), which is important for applications such as the light-emitting field-effect transistor.[29,30] For applications in circuits, this ambipolarity can be modified to obtain unipolar transport and meet low power consumption demands, *e.g.*, by doping (see sections 2.3.1 and 2.4.3 – 2.4.6).

The carrier mobility in semiconducting SWCNTs is strongly dependent on carrier density, which is a result of the shape of their DOS. With increasing gate voltage in a field-effect transistor the carrier mobility increases until the first subband is fully occupied. It then decreases until the states in the next subband can be filled.[28]

Furthermore, the 1D structure of nanotubes necessitates that the coupling of an individual SWCNT to the planar biased gate electrode as well as their quantum capacitance have to be taken into account.[31] In contrast to 3D semiconductors, this quantum capacitance ($\approx 4 \cdot 10^{-10}$ F m^{-1}) has to be considered for the correct determination of carrier density at a given gate voltage as it can be smaller than or similar to the dielectric capacitance.[6]

For networks rather than individual tubes, inter-nanotube electrostatic coupling has to be considered as well. Particularly for sparse networks assumptions based on the plate-plate capacitor model significantly overestimate the correct capacitance.[32,33] While calculations considering the network density can reduce this discrepancy,[34] a direct capacitance measurement on the device is often most reliable.[35]

In comparison to the detailed understanding of charge transport in individual nanotubes, which is well-established,[16] charge transport in random SWCNT networks is still relatively poorly understood. Historically, modeling approaches focused on percolation theory.[36] As networks free of metallic impurities were unavailable,[37] the off-current was governed by the presence of metallic SWCNTs, dense networks exhibited high mobilities with high off-currents while sparser networks suffered from low on-currents. Given the much improved purity of state-of-the-art semiconducting nanotube networks this once considered inevitable trade-off was successfully overcome.[6,38–40]

Typical carrier mobilities in SWCNT network transistors are orders of magnitude lower than in individual nanotubes ($0.1 - 100$ cm^2 V^{-1} s^{-1}, examples are presented in section 2.3.3).[6] Inter-nanotube junctions are considered to be the key limiting factor for charge transport in these networks due to their high junction resistances.[41,42] These junction resistances depend on the diameter (and chirality) of the two involved SWCNTs[43,44] and their angular overlap.[41] The effect of the presence of wrapping polymer[45,46] or surfactant[47] on the junction resistance is still subject to scientific discussion. The electrostatic coupling between nanotubes is negatively affected by the presence of even small SWCNT bundles, which leads to carrier scattering and ultimately limits charge transport and device performance.[42,48] It is hence of great importance to minimize the bundle content in SWCNT networks (see also next two sections).

Overall, the higher the number of junctions a charge has to hop across, the lower is the effective carrier mobility in the network. Hence, longer nanotubes lead to more efficient transport as the number of hopping steps decreases. This aspect of the charge transport mechanism in nanotube networks resembles charge transport in disordered semiconducting

polymers (see section 2.2.2). In addition, dipolar disorder in nanotube networks may be caused due to its high porosity that provides adsorbation sites, *e.g.*, for water molecules, as well as at the dielectric or the substrate interface.[8] Such adsorbates act as electron traps due to the unfavorable energetic alignment of the oxygen/water redox couple in relation to the electron affinity of organic semiconductors.[8,9] A common strategy to partially remove adsorbed water is annealing the networks at high temperatures in vacuum, which has only a temporary (and reversible) effect on SWCNT networks that are exposed to air. Trapping of electrons represents one of the reasons for the overall inferior performance of solution-processed semiconductors in n-type FETs (see section 2.4).

Experimental studies have further revealed the influence of the network density on charge transport. Increasing the network density leads to higher mobilities for low densities.[49] In addition to a larger number of possible current pathways from source to drain, less exposure to polar on-substrate adsorbates (see above) results in more efficient transport in top-gate transistors. At higher densities this effect saturates as only the top layer of a 3D nanotube network is gated due to screening of the electric field.

Temperature-dependent mobility measurements on networks of different nanotube compositions were conducted by several research groups.[50–52] The universally found drop in mobility with decreasing temperature confirmed thermally activated hopping. However, the conventional transport model (*e.g.* variable-range hopping) for disordered semiconductors did not give a satisfactory fit over a wide temperature range. In contrast to that, the fluctuation-induced tunneling model, which was originally developed for large conducting segments separated by insulating barriers,[53] does provide a good fit even though this model does not take into account nanotube-specific parameters (different diameters, DOS, energy levels etc.). This leads to unreliable fit parameter extraction and complicates comparisons between networks of different nanotube compositions.[50]

A relatively recent approach to model the charge transport behavior in semiconducting SWCNT networks was brought forward by Schießl *et al.*[49] The transport across nanotube junctions was modeled by solving the master equation for a network of random resistors.[54,55] This approach was adapted specifically for SWCNTs by taking into account their DOS distribution as a function of network composition from previous models used for simulations of charge transport in typical disordered systems such as organic semiconductors.[49] Unfortunately, this model does not accurately describe certain aspects of charge transport in these networks such as the temperature dependence of charge carrier mobility. Consideration of the intrinsic mobility of specific nanotube chiralities[51] as well as the variations in contact resistance at inter-tube junctions might help improve the fit to experimental data. In summary, while there has been significant progress in understanding some of the aspects that govern charge transport in random networks of semiconducting SWCNT, a holistic

model remains to be found.

2.1.3 Dispersion of Single-Walled Carbon Nanotube by Polymer Wrapping

Large-diameter (1 – 3 nm) carbon nanotubes can be synthesized by carbon vaporization techniques at temperatures above 1,000 °C using laser ablation,[56] arc discharge,[14,57] or plasma-based processes.[58,59] Smaller diameters are commonly achieved by methods based on chemical vapor deposition using gaseous carbon precursors. An example is the CoMoCAT® process that uses a cobalt-molybdenum catalyst and carbon monoxide as precursor. It produces SWCNTs with a diameter distribution of 0.7 – 1.0 nm.[60]

Despite extensive research for selective growth of carbon nanotubes[61–63] all synthesis approaches of commercial relevance produce mixtures of metallic and semiconducting species. Additional impurities that have to be removed include catalyst particles, amorphous carbon and other carbon allotropes. To ensure full access to their exciting properties, for most applications (*e.g.*, metallic SWCNTs for electrodes, semiconducting SWCNTs as material for transistors) sorting of metallic and semiconducting nanotubes is mandatory.

In general, this separation process is conducted in liquid medium, *i.e.*, organic solvent or water. Strong inter-tube van der Waals forces due to the π-π-interactions of the nanotube sidewalls result in a high tendency to form aggregates and bundles, which can be broken up using ultrasonication[64] or shear forces.[65] To prevent re-aggregation, colloidal stabilization is required. Note that only a very small number of solvents (*e.g.*, *N*-cyclohexyl-2-pyrrolidone) disperse any appreciable amount of SWCNTs.[66]

Large quantities of individualized SWCNTs were first demonstrated in aqueous dispersions prepared by sonication with stabilizers such as sodium dodecyl sulfate or sodium cholate. Subsequent centrifugation of the mixture allows for a separation of SWCNTs in the supernatant from unwanted impurities that are sedimented. These dispersions generally contain mixtures of metallic and semiconducting SWCNTs and require further sorting protocols. Those include density gradient ultracentrifugation,[67] gel permeation chromatography,[68,69] dielectrophoresis[70] and aqueous two-phase extraction.[71,72]

In contrast to these methods, the chosen approach in this thesis, *i.e.*, selective dispersion by polymer wrapping first employed by Nish *et al.*,[73] is carried out in organic solvents such as toluene or xylenes.[73,74] Here, the selectivity is achieved during the preparation of the dispersion (sonication or shear-force mixing and centrifugation) by colloidal stabilization of specific nanotube species rather than by an elaborate post-processing protocol. This leads to better scalability and, most importantly, semiconducting SWCNT samples with purity levels suitable for, *e.g.*, transistor fabrication.[39]

The synthesis method of the SWCNTs (see above) defines the range of diameters and specific SWCNT chiralities that can be dispersed, *e.g.*, diameters ≤ 1 nm for samples grown by chemical vapor deposition. However, the key component that affects the selectivity and yield of the purification process is the polymer. A large choice of conjugated polymers that include polyfluorenes[75] such as PFO and a variety of copolymers such as PFO-BPy (bipyridine unit),[76] PFO-BT[74] (benzothiadiazole unit) or PFO-PBAB (phenylamino-bridged phenyl units),[77] polycarbazoles (*e.g.*, poly-*N*-decylcarbazole)[78] and polyalkylthiophenes (*e.g.*, poly-3-dodecylthiophene).[79] Their molecular structures are shown in Figure 2.4.
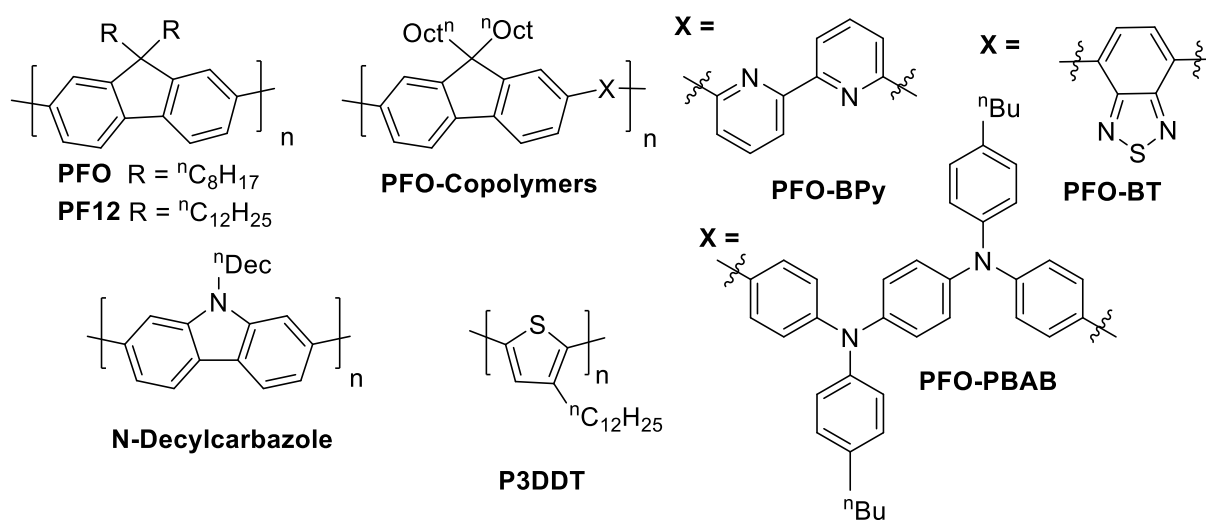
Figure 2.4: Molecular structures of polymers that have been used for the selective dispersion of SWCNTs in organic solvents.

The structure of the polymer backbone governs the wrapping process around specific (semiconducting) SWCNT chiralities enabled by π-π-interactions that compete with inter-nanotube attractive forces.[80] The solubility of the polymer-wrapped SWCNTs are facilitated by the alkyl side chains as they provide colloidal stabilization by steric contributions. Molecular dynamics simulations and transmission electron microscopy have been used to investigate potential wrapping geometries, *i.e.*, linear or helical alignment of the polymer backbone with the SWCNT sidewalls.[75,81,82] Both the nanotube species and the polymer structure have an impact on the wrapping configuration. Polyfluorenes preferentially form a helical structure when wrapped around near-armchair SWCNTs while SWCNTs with a smaller chiral angle lead to a linear alignment of polymer alkyl side chains and nanotube axis.[75,81]

A multitude of factors that affect the selectivity and yield have been investigated in numerous studies. For example, longer alkyl side chains tend to favor the dispersion of SWCNTs with larger diameters compared to analogs with shorter solubilizing side chains for both polythiophenes[79] and polyfluorenes.[75] Relatively small changes in the polymer

backbone structure have a drastic impact on selectivity. For example, PFO-BPy displays a high selectivity towards (6,5) SWCNTs while PFO preferentially disperses (7,5) SWCNTs using the same CoMoCAT® starting material. Still, in either case, the selectivity toward semiconducting SWCNTs is very high.

Other aspects include the temperature during sonication[83] and the viscosity of the dispersion, which is affected by choice of solvent and the molecular weight of the polymer. In general, higher viscosity has been shown to lead to better yields but lower selectivity.[74] Further, the potential impact of ambient p-doping during the selection process rather than differences in affinity of the polymer to specific chiralities were discussed by the Malenfant group.[84,85] Despite these efforts a comprehensive understanding of the origin of the selectivity still appears to be out of immediate reach.

In any case, the dispersions of purely semiconducting SWCNTs obtained after centrifugation still contain a substantial amount of excess polymer (not wrapped around nanotubes). The notion that the polymer needs to be removed in order to ensure uninhibited access to the charge transport properties of the SWCNTs was recently challenged by Mirka *et al.*[86] Using highly soluble fluorene copolymers as wrapping polymers, rinsing off the excess polymer after film deposition was demonstrated to result in similar performance metrics of SWCNT network transistors regardless of polymer content up to a certain threshold polymer concentration.[86] In most other cases, removal of the conjugated polymers used for selective dispersion was thus far considered mandatory as they typically exhibit charge carrier mobilities orders of magnitude lower than the SWCNTs.[87,88] However, a certain amount of polymer must remain in place to provide sufficient solubilization of the SWCNTs to prevent re-aggregation of nanotubes that can severely limit processability and negatively affects device performance (see Chapter 4). The essentials of the well-documented characteristic of nanotube dispersions to aggregate are briefly summarized in the next section. In practice, a number of approaches have been developed for the polymer removal process, including vacuum filtration combined with rinsing and re-dispersion (see section 3.2) or elaborate post-deposition protocols.[7,89]

Regardless of the outlined mechanistic discussions, the wrapping polymer PFO-BPy can be combined with CoMoCAT® nanotube raw material to yield near-monochiral dispersions of (6,5) SWCNTs[76] and with plasma-torch nanotubes to yield a wide range of purely semiconducting, large-diameter SWCNTs (1.17 – 1.55 nm).[51] The former was used as the key material for all SWCNT network transistors and spectroscopic studies applied in this thesis (Chapters 4 and 5). The latter served as an additional reference to demonstrate the versatility of the additives used to improve dispersion stability (Chapter 4).

2.1.4 Aggregation in Single-Walled Carbon Nanotube Dispersions

This section provides a brief and simple overview on the processes that govern aggregation in SWCNT dispersions as well as some methods that have been used to analyze this behavior. It has to be noted that almost all studies on the aggregation of SWCNTs have been conducted using aqueous dispersions. The acquired insights can not necessarily be transferred directly to the dispersions prepared by polymer wrapping in organic solvents used in this thesis. Nevertheless, they provide a relevant foundation for the discussion of the results presented in Chapter 4.

In general, colloidal dispersions are stabilized by steric repulsion, *i.e.*, facilitated by side chains of a polymer or due to entropic considerations, and electrostatic repulsion of charged particles based on the electric double layer present at the interface of colloid and liquid environment (and in some cases repulsive solvation forces).[90] A simplified image of the aggregation of spherical colloids in a liquid medium is provided by the DLVO model named after the researchers Derjaguin, Landau, Verwey and Overbeek. Here, attractive van der Waals forces compete with the aforementioned repulsive electrostatic interactions. Aggregation of a stable colloidal dispersion can be induced by addition of an electrolyte, when it reduces the so called *Debye length* (radius of the ionic cloud) below a critical threshold as it is proportional to the square root of the ionic strength of the dispersion ($\propto 1/\sqrt{I}$).[91,92]

Upon geometrical adaption of the involved relations (nanotubes as cylindrical rods), nanotube aggregation in surfactant-stabilized aqueous dispersions has been found to agree well with the DLVO model.[93,94] For SWCNT dispersions prepared by polymer wrapping in apolar solvents, similar effects on dispersion stability have been found by addition of polar solvents or altering the surface electrochemistry of the SWCNTs *via* a change in pH-value.[84]

Aggregation can also be interpreted as a bimolecular reaction between two particles that requires no activation energy once the particles are in physical contact. This process is determined by the number of collisions and thus is diffusion-limited. The equation that describes the translational diffusion coefficient D_{trans} adapted for rod-shaped particles was described by Broersma:[95]

$$D_{trans} = \frac{k_B T}{6\pi\eta} \frac{2\ln\left(L_r/d_r\right) - \gamma}{L_r},$$ (2.4)

where k_B denotes the Boltzmann constant, T the temperature, η the dispersion viscosity, L_r the rod length and d_r the rod diameter and γ is a correction parameter. Translational diffusion constants in aqueous SWCNT dispersions were determined by Tsyboulski *et al.* with a combination of videomicroscopy and spectroscopy using this relation.[96] As lower diffusion rates lead to slower aggregation, solvents with higher viscosities (*o*-xylene

compared to toluene) have been demonstrated to enable kinetic stabilization of polymer-wrapped SWCNT dispersions.[74,97] Another method to determine diffusion coefficients is dynamic light scattering.[93,94] This experimental tool was also employed to demonstrate that aggregation of SWCNT dispersion can be induced by the addition of electrolytes or slowed down by the addition of, *e.g.*, humic acid, which is relevant for biocompatibility in medical applications.[94] In addition, static light scattering is a characterization technique that enables the measurement of particle parameters such as size and shape.[98,99] For example, static light scattering was used for the measurement of fractal patterns observed on nanotube aggregates induced by exposure to, *e.g.*, biological growth media.[100] Further methods to detect nanotube aggregates include analytical ultracentrifugation[101] and ζ-potential measurements.[102]

Furthermore, resonant Raman spectroscopy has been employed to compare the degree of aggregation in a SWCNT sample.[103] Here, the broadening and red-shift of SWCNT absorption upon aggregation[104] is exploited as it changes the relative intensity of RBM peaks corresponding to different SWCNT species. This method, however, lacks sensitivity and is only able to identify strongly aggregated dispersions with a broad diameter distribution. In contrast to that, variance spectroscopy is a very sensitive approach that can even detect loosely clustered nanotubes.[105,106] This method involves the statistical analysis of many photoluminescence spectra exploiting small differences in the mean and variance data of these spectra of dispersions with different degrees of aggregation. It is able to distinguish between aggregates of different (hetero-) and identical SWCNT species (homoaggregates).[106] Unfortunately, the method based on a custom-built apparatus has thus far only been applied to aqueous dispersions.

In summary, aggregation behavior in aqueous SWCNTs dispersions has been studied to some extent and delivered results that can be correlated with established models for colloidal stabilization. Accordingly, aggregation can be induced, *e.g.*, by addition of electrolytes or slowed down, *e.g.*, by the addition of biomolecules. Characterization of the diffusive behavior of dispersed nanotubes have allowed for rational guidelines, *e.g.*, with regard to the impact of solvent viscosity in dispersions using organic solvents. However, the fact that instead of monodisperse spherical particles, nanotube dispersions contain nanotube-surfactant complexes, whose exact geometry is unknown and size distribution is not uniform, predictions for the aggregation behavior of specific nanotube dispersions based on these findings remain unreliable.

Overall, for the polymer-wrapped dispersions used in this thesis, research studies remain very scarce. Unfortunately, ζ-potential measurements, that enable a quantification of the electrostatic repulsion of the particles and thus provide a suitable metric for the comparison of the stability of different dispersions, require a polar medium and cannot be used for the dispersions in toluene used throughout this thesis.

2.2 Semiconducting Polymers

Semiconducting polymers are another solution-processable semiconductor of high interest for numerous device applications. This section introduces these macromolecules in regard to their structural, morphological and electronic properties with an emphasis on charge transport.

2.2.1 From Polythiophenes to Donor-Acceptor-Polymers

Polymers consist of repeating units based on small-molecule monomers. In semiconducting polymers, these repetitive units form a linear backbone that contains sp^2-hybridized carbon atoms and often heteroatoms such as sulfur or nitrogen. (Partial) delocalization of π-electrons along this backbone is enabled by electrons occupying the p_z orbitals of the contributing atoms. This delocalization of electrons, and thus the conjugation length of the polymer chain, is invariably restricted to a small number of monomer units. This is caused by torsion, defects, twists or kinks in the polymer backbone between repetitive units and results in the characteristic energetic disorder.[107] Hence, conjugated polymers have been interpreted as sequences of variable-length π-conjugated oligomers called chromophores.[108,109] This spread in conjugation lengths of the chromophores leads to a characteristic broadening of the relatively sharp highest occupied molecular orbital (HOMO) and lowest unoccupied molecular orbital (LUMO) energy of a single chromophore to a Gaussian distribution of states (for details, see next section).

A vast number of options in chemical design of monomers enables the fine-tuning of the properties of the conjugated polymer. Synthetic engineering of the polymer side chains is used to optimize their solubility and has been shown to positively affect the crystallinity of the polymer in some cases.[110] Chemical modifications, *e.g.*, by the introduction of electron donating or withdrawing substituents, can be used to adapt their HOMO and LUMO energies as well as their ionization potential and electron affinity in the bulk. Commonly, these options are exploited to optimize the electronic properties for a certain application, such as OLEDs,[111,112] photovoltaic[113,114] and electrochromic[115,116] cells as well as FETs.[117,118] Some examples of semiconducting conjugated polymers are shown in Figure 2.5. For more than a decade regio-regular poly(3-hexylthiophene) (P3HT) was the center of research with its rigid backbone that enables the formation of crystalline domains. Improved π-π-stacking and long-range order were created by extensive efforts to control film morphology, which led to charge carrier mobilities above $0.1 \text{ cm}^2 \text{ V}^{-1} \text{ s}^{-1}$.[119] Later, the rigid-rod polymer, poly(2,5-bis(3-tetradecylthiophene-2-yl)thieno[3,2-*b*]thiophene) (PBTTT) was developed to yield hole mobilities in the range of $0.2 - 0.6 \text{ cm}^2 \text{ V}^{-1} \text{ s}^{-1}$ (see also section 2.3.4).[120]
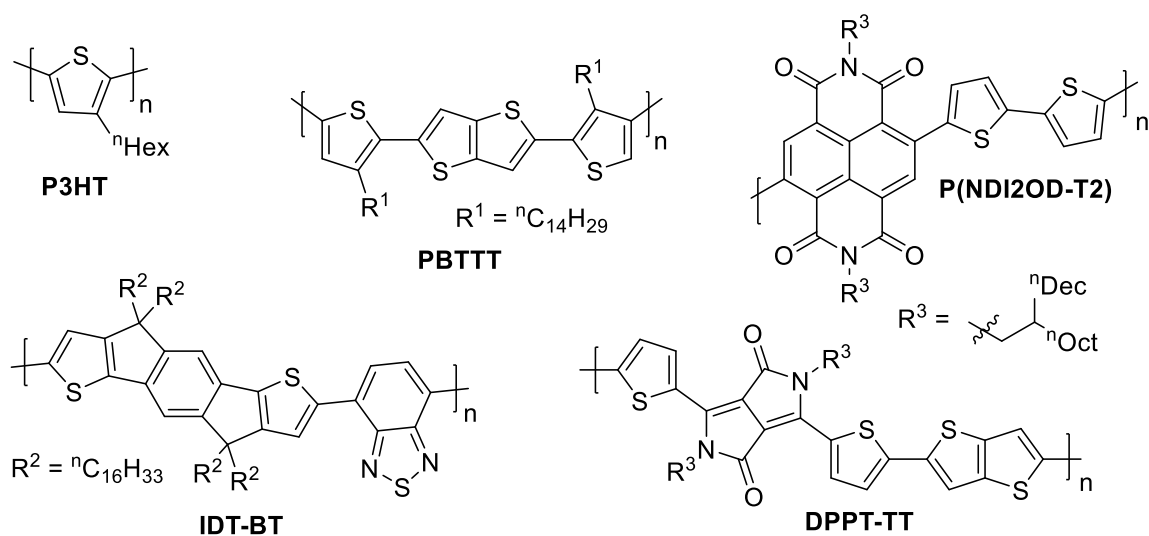
Figure 2.5: Molecular structures of semiconducting polymers that exhibit mainly p-type (P3HT, PBTTT, IDT-BT), ambipolar (DPPT-TT) and n-type (P(NDI2OD-T2)) charge transport chararcteristics.

Subsequently, the focus shifted to donor-acceptor (D-A) polymers, in which the backbone consists of alternating electron-rich and electron-poor motifs with a bandgap of typically below 1.5 eV. Examples include indacenodithiophene–benzothiadiazole copolymer IDT-BT (p-type), the diketopyrrolopyrrole-based DPPT-TT (ambipolar) and the naphthalenediimide-based polymer P(NDI2OD-T2) (n-type charge transport).

Thin films of these polymers necessary for, *e.g.*, electronic devices, can be cast from solution using various deposition techniques such as spin-[121,122] or blade[123] coating as well as ink-jet printing.[124] Note that in some cases, *e.g.*, for P3HT in anisole[125] or P(NDI2OD-T2) in toluene,[126] there is a significant amount of aggregation in solution. In contrast to SWCNTs (see section 2.1.4), these aggregates can lead to the desired morphology improvements of the final film.[126] The molecular structure of the polymer, its molecular weight, the method of deposition, the solvent properties and annealing protocol all affect the morphology of the film, which can have amorphous or semicrystalline with variable grain sizes.[6,117] For example, a higher degree of crystallinity can be achieved by controlled evaporation of solvents with high boiling points[127] while alignment of the backbone chain can be induced with shear forces applied during deposition.[128] In contrast to what one might expect, a maximized degree of crystallinity is not necessarily desired for ideal transport properties due to large barriers between crystalline domains (see discussion in next section).

2.2.2 Electronic Properties

As briefly outlined above, the distribution of conjugation lengths of different chromophores as part of a long polymer chain leads to energetic disorder. This is reflected by a broad

Gaussian distribution of states (see Figure 2.6a). The extent of this broadening is of great importance for understanding the factors that govern charge transport in different semiconducting polymers. In addition to the electronic properties, this energetic structure has a large influence on the optical properties of conjugated polymers, *i.e.*, absorption and emission, as well as exciton transfer and diffusion. A concise description is given in literature.[6]
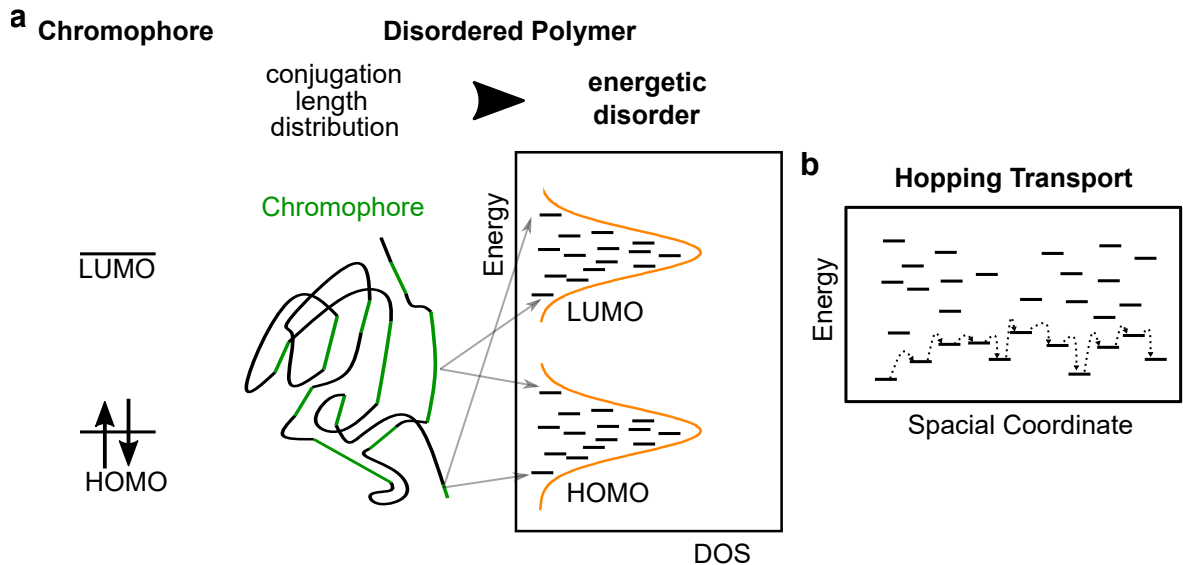
Figure 2.6: (a) Schematic illustration of the broadening of the frontier orbitals in a single chromophore to a Gaussian-shaped DOS in a disordered polymer caused by conjugation length distribution of chromophores with different size. (b) Visualization of electron hopping in a disordered polymer between non-equidistantly localized states with different energies.

Charge transport in materials with large disorder can be described with the variable-range hopping model (see schematic in Figure 2.6b).[129] In this paradigm, the charge carrier hops from one chromophore to another (along the backbone or to an adjacent chain) overcoming an inter-site energy barrier. The non-equidistantly localized electronic states, that overall follow a Gaussian distribution, each have a different energy. Intra-chain transport of carriers is generally assumed to be faster than inter-chain hopping.[6] This is in agreement with the anisotropic carrier mobilities observed for aligned films of semiconducting polymers[128,130,131] as well as the omnipresent higher mobilities with increasing molecular weight.[132] Vissenberg and Matters proposed a model for disordered semiconductors, which suitably describes the temperature dependence ($\mu \propto exp(-E_a/T)$ with E_a being the activation energy associated with the hopping process) of charge carrier mobility in many semiconducting polymers.[133] The larger the energetic disorder in the film, the more the DOS is broadened. In a FET, dipolar disorder present at the interface of dielectric and semiconductor (see also section 2.1.2) can further increase the width

of the DOS. This is associated with an increase in activation energy between hopping sites and thus decrease in charge carrier mobility. This detrimental effect can be limited by the use of low-k dielectrics, *e.g.*, the fluorinated polymer CYTOP[TM].[134] In the early stages of the development of high-mobility semiconducting polymers, the processing of P3HT was optimized to yield highly ordered and crystalline thin films. Later, research was driven by the synthesis of novel rigid-rod conjugated polymers such as PBTTT (molecular structure, see Figure 2.5), which could be deposited as films with long-range order and large crystalline domains.[135] Although tie-molecules were introduced to provide pathways for carriers from one crystalline segment to another,[132] performance could not be improved further. The intrinsic energetic disorder in semiconducting polymers was revealed to be a major barrier that had to be overcome for the realization of the desired higher charge carrier mobilities.[136]

Experimentally, this energetic disorder can be quantified as activation energy from charge carrier mobilities extracted at different temperatures by means of a linear fit to the mobility on a logarithmic scale as a function of inverse temperature.[134] Another approach is photothermal deflection spectroscopy, which enables direct observation of the energetic disorder as the so-called Urbach tail – an exponential sub-bandgap absorption tail – with the corresponding Urbach energy providing a quantitative measure.[137]

A common strategy to minimize energetic disorder in semiconducting polymers is to enhance π-conjugation by implementation of more rigid monomers (*e.g.*, with larger aromatic systems) and limiting the rotational freedom of bonds between donor and acceptor units in donor-acceptor-polymers. While this higher rigidity and less torsion in the polymer backbone led to an increase in conjugation lengths, films of these polymers no longer necessarily exhibit long-range order or large crystalline domains.[138] Examples of these molecules include IDT-BT and DPPT-TT (see Figure 2.5) whereas films of P(NDI2OD-T2) benefit from both a narrow torsion angle distribution in its backbone[139,140] and substantial (semi)crystalline order.[141,142] This paradigm shift from rigid-rod polymers that form largely crystalline films to the donor-acceptor polymers that exhibit the highest mobilities today has revived the attention to semiconducting polymers as a competitor for FET applications, *e.g.*, in circuits.[143,144] The state of the art of high-performance polymer transistors is given in section 2.3.4.

Overall, the development of polymers that are as rigid and planar as possible with extended π-conjugation for minimum energetic disorder, *e.g.*, ladder-type materials,[145], could be interpreted as already completed - with SWCNTs being the ultimate target structure.[6] As described above (see section 2.1.2), the 1D character of individual nanotubes is reflected in their band structure, which governs their electronic and charge transport behavior. Yet, in a random nanotube network, there is a striking similarity in the description of charge transport in both presented semiconducting materials: fast carrier movement (polymer

intra-chain *vs.* intra-tube) alternates with slow hopping over barriers across different localized states (polymer inter-chain *vs.* nanotube junctions).

2.3 Field-Effect Transistors

Field-effect transistors (FETs) serve as amplifiers and digital switches. They are a basic component of electronic circuits, *e.g.*, inverters, NAND gates etc. Solution-processed semiconductors are envisioned to supplement the existing inorganic materials for a variety of interesting applications that require low-temperature processing and flexible substrates such as plastic, paper or textiles.[146] They also act as a platform for fundamental research on charge injection into and charge transport through organic semiconductors. This section describes the fundamentals of uni- and ambipolar FETs, the working principle of the most basic logic element, the inverter, as well as the state of the art of FETs using the two semiconductors used in this thesis, *i.e.*, SWCNTs and polymers.

2.3.1 Unipolar Field-Effect Transistors

Generally, FETs are considered as three-terminal devices, in which the third electrode regulates the current flow between the other two. Figure 2.7a displays a schematic of the required components. The source (S) and drain (D) electrodes are in contact with a semiconducting layer. Their width (W) and the distance between these electrodes (channel length L) describe the channel geometry (see Figure 2.7b).
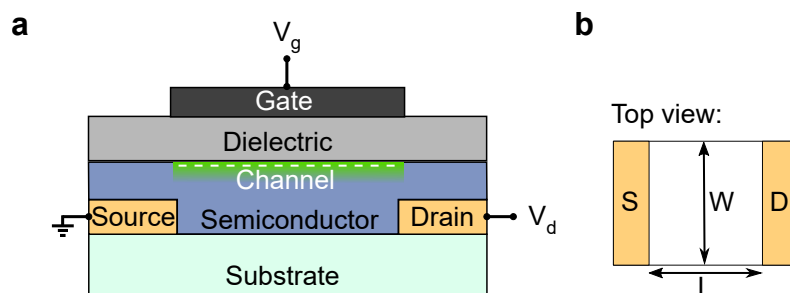
Figure 2.7: (a) Device stack of a bottom-contact/top-gate n-type FET with source, drain and gate electrode. (b) Top view of the bottom electrodes to illustrate channel dimensions.

The third electrode, which is separated from the semiconductor by a dielectric, is called gate electrode (G). In this thesis a bottom-contact/top gate layout is used throughout. Other configurations, *e.g.*, top-contact/top-gate, top-contact/bottom-gate or bottom-contact/bottom-gate configuration, are possible depending on processing and application considerations. For all architectures, a voltage is applied to the drain (V_d) and gate electrode (V_g) whereas the source is usually grounded. In the following, the working

principle of an n-type FET will be explained (electron transport; $V_d, V_g > 0$). In p-type FETs, holes are accumulated and they are operated at negative voltages ($V_d, V_g < 0$). Without any gate voltage applied, the transistor is in its *off*-state if no unintentional doping is present. Upon application of a sufficiently high gate potential mobile carriers are accumulated at the semiconductor/dielectric interface and a conductive channel is formed. When a bias between source and drain is applied, the accumulated charges move from source to drain leading to the drain current (I_d): the FET is switched *on*. However, before charges become mobile, trap states commonly originating from impurities, dopants, surface imperfections and defects in the semiconductor bulk need to be filled. The associated minimum voltage to create mobile charges is referred to as threshold voltage (V_{th}).[146] The unwanted leakage current that flows between gate and source is called gate current (I_g) – it is determined by the quality of the dielectric.

The analytical description of a FET is based on the gradual channel approximation (GCA):[147] the vertical electric field caused by the gate voltage by far exceeds the lateral field between source and drain electrode. In practice, this is realized by restricting the thickness of the gate dielectric to no more than a tenth of the channel length ($d_{dielectric} \leq 0.1$ L).[148]

In the above described transistor, the density of mobile charge carriers is expressed as

$$Q_{mob}(x) = C(V_g - V_{th} - V(x)). \tag{2.5}$$

with the channel position $x \in [0, L]$, the areal capacitance of the dielectric C and the channel potential $V(x) \in [V(0) = 0, V(L) = V_d]$ at channel position x. Using the GCA, neglecting diffusive currents, *i.e.*, taking into account only drift currents,[149] and substituting the electric field at position x ($E_x = \frac{dV}{dx}$), the source-drain current across the channel is given by Equ. 2.6

$$I_d = W \mu Q_{mob}(x) \frac{dV}{dx}. \tag{2.6}$$

Here, μ denotes the charge carrier mobility (unit: $\mathrm{cm^2\,V^{-1}\,s^{-1}}$), which characterizes the drift velocity of a charge carrier in an electric field and governs the drain current per applied voltage and the maximum switching frequency of a transistor.[150,151] Substitution of $Q_{mob}(x)$ according to Equ. 2.5 and integration after variable separation results in

$$I_d = \frac{W}{L} \mu C \left[(V_g - V_{th}) V_d - \frac{1}{2} V_d^2 \right]. \tag{2.7}$$

This is based on the assumption that the charge carrier mobility is not a function of carrier density (and thus gate voltage).

For drain voltages smaller than the effective gate voltage ($V_d < V_g - V_{th}$), electron density across the channel from source to drain decreases linearly due to the linear increase of the

channel potential. The charge carrier distribution in this hence termed linear regime is illustrated in Figure 2.8a. Equ. 2.7 can be simplified to

$$I_{d,lin} = \frac{W}{L}\mu_{lin}C\left(V_g - V_{th}\right)V_d \tag{2.8}$$

as the term $V_d{}^2$ is neglected.[149]
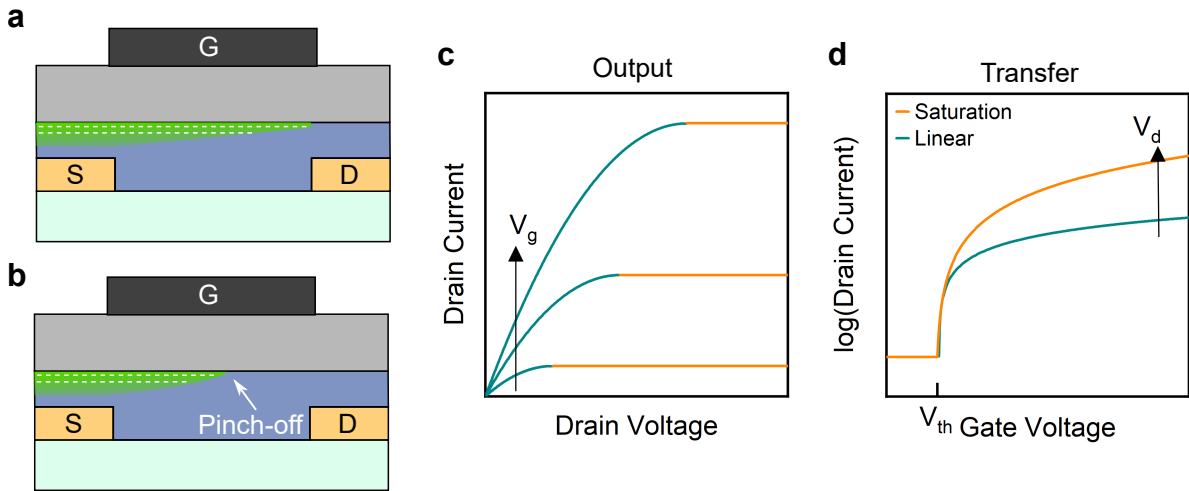
Figure 2.8: Charge carrier distribution (green) in an n-type FET in (a) the linear ($V_d < V_g - V_{th}$) and (b) the saturation regime ($V_d \geq V_g - V_{th}$). (c) Output characteristics for three constant gate voltages. Line color (linear: turquoise, saturation: orange) corresponds to the two transport regimes. Exclusively for $V_d << V_g - V_{th}$, the increase in drain current with increasing drain and gate voltage is effectively linear. (d) Transfer characteristics for two constant drain voltages corresponding to both transport regimes. In the subthreshold region ($V_g < V_{th}$), the transistor is in the off-state. The displayed current-voltage characteristics represent ideal FET behavior, in-practice device behavior may deviate.

At larger V_d the carrier density next to the drain electrode is further reduced until at $V_d = V_g - V_{th}$ the channel is pinched off. Here, the channel potential falls below the effective gate voltage $V(x) < V_g - V_{th}$ and a depletion zone is formed (see Figure 2.8b). Upon further increasing the drain voltage, the channel pinch-off point is moved closer to the source electrode and the drain current saturates as the current flow across the depletion zone is space-charge-limited. By substituting V_d with $V_g - V_{th}$ in Equ. 2.7, the current in the saturation regime is obtained

$$I_{d,sat} = \frac{W}{2L}\mu_{sat}C\left(V_g - V_{th}\right)^2. \tag{2.9}$$

Output characteristics are commonly used to describe transistor behavior (see Figure 2.8c), which displays the drain current at various constant gate voltages as a function of drain voltage. They allow for a concise assessment of both transport regimes outlined above. A typical deviation from the ideal curves displayed here is a non-linear increase at low

drain voltages, which is typically associated with poor carrier injection (see section 2.4). In the other standard current-voltage curves, the transfer characteristics, the drain current is plotted on a log-scale as a function of gate voltage at constant drain voltage. These characteristics also serve as the basis for the extraction of critical device parameters to provide the relevant figures of merit for the evaluation of device performance.

The charge carrier mobility can be extracted using Equ. 2.10 in the linear

$$\mu_{lin} = \frac{L}{WCV_d} \frac{\partial I_{d,lin}}{\partial V_g} \tag{2.10}$$

and Equ. 2.11

$$\mu_{sat} = \frac{L}{WC} \frac{\partial^2 I_{d,sat}}{\partial V_g^2} \tag{2.11}$$

in the saturation regime.

In an ideal FET, the linear and saturation mobilities are equal to one another. In practice, contact resistance often reduces the apparent linear mobility[152] (see section 2.4.2).

The threshold voltage can be determined in the saturation regime by extrapolating the linear increase of the square root of the drain current to zero current when plotted as a function of gate voltage. Precise control of the threshold voltage is critical for efficient device operation. For electrons, a high threshold voltage corresponds to a high operating voltage whereas a negative threshold voltage converts the FET from an accumulation to a depletion mode transistor, which is unfavorable for, *e.g.*, circuit operation.[153] The threshold voltage can be adapted, for example, by doping (see section 2.4.4). A related parameter is the onset voltage (V_{on}), which is the lowest voltage at which the drain current exceeds the gate leakage. Depending on the degree of ideality of the turn-on behavior, the onset voltage can be extracted more reliably compared to V_{th} and can enable more robust comparison of different devices.

Another parameter that allows for an assessment of the switching behavior of a transistor is the subthreshold slope, which reflects the increase in current as a function of gate voltage when the gate voltage surpasses the threshold voltage. Its inverse, the subthreshold swing can also be used to calculate the trap density at the semiconductor/dielectric interface. It is extracted at the transition from the subthreshold region (below V_{th}) to the voltage corresponding to a ten-fold increase in current using the unit $V \, dec^{-1}$:

$$SS = \frac{\partial V_g}{\partial ln(I_d)}. \tag{2.12}$$

Furthermore, the on/off-current ratio is used to evaluate the degree of switching in a transistor. It can be directly extracted from the transfer characteristics. Values of at least 10^6 for FETs in active matrix displays are necessary to achieve the desired brightness

contrast.[154]

For applications in electronic circuits, logic elements are necessary that contain multiple transistors. A simple NOT-gate, also called inverter, is the most basic element of this type. It transforms a small input signal (digital 0) to a large output signal (digital 1) and *vice versa*. While inverters can be realized using two of the same type of unipolar transistor or two ambipolar transistors, a complementary inverter uses a p- and an n-type transistor interconnected according to the circuit diagram in Figure 2.9a. The gates of these two FETs are in contact with another and act as an input node (input voltage V_{in}).
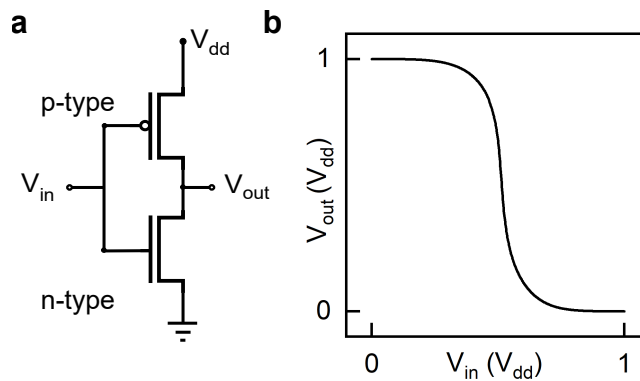
Figure 2.9: (a) Circuit diagram of a complementary inverter using a p- and n-type transistor. (b) Transfer characteristics of a complementary inverter. Both axes are scaled in units of V_{dd} to illustrate the conversion of the input signal from a logical 1 to logical 0 and *vice versa*.

The drains of both transistors are connected as well to form an output node with output signal V_{out}, the source of the n-type FET grounded and the source of the p-type FET is connected to a supply voltage (V_{dd}). Typical transfer characteristics of such a complementary inverter are illustrated in Figure 2.9b. Complementary inverters are considered superior to other inverters due to their much lower power consumption. Except for a very short period during switching one of the two transistors is always off. Hence, its static power consumption is determined by the leakage current. Furthermore, complementary circuits exhibit more reliable operation, allow for better noise margins and can be designed more easily.[149,155]

2.3.2 Ambipolar Field-Effect Transistors

As both semiconducting materials employed in this thesis (see previous sections) are able to accumulate both holes and electrons in the device with fabrication using the chosen processing conditions, the working principle of an ambipolar FET is outlined here. Conceptually, an ambipolar transistor can be seen as a superposition of a p- and an n-type

FET. The accumulated carrier type depends on the applied voltages. While only one carrier is accumulated in the unipolar linear and saturation regimes, simultaneous injection of electrons at the source and holes at the drain electrode takes place in the ambipolar regime. The different transport regimes are visualized in Figure 2.10.
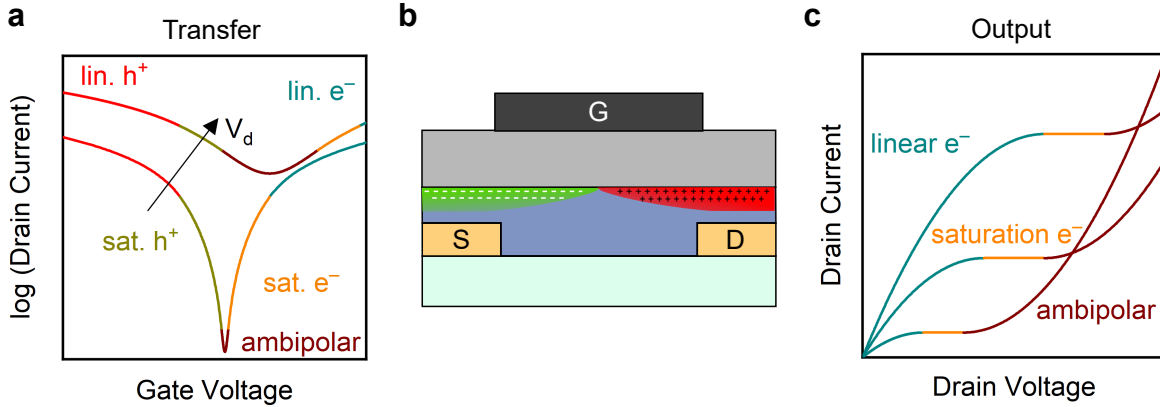
Figure 2.10: (a) Transfer characteristics displaying linear (red) and saturation (sand-yellow) regimes of hole transport, ambipolar transport (brown), saturation (orange) and linear (turquoise) regimes of electron transport. (b) Charge carrier distribution in ambipolar regime: simultaneous accumulation of electrons (mint green) and holes (red). (c) Output characteristics for positive V_g with superlinear drain current increase at high drain voltages typical for ambipolar FETs.

Figure 2.10a displays the transfer characteristics for an ambipolar transistor at positive drain voltages. At $V_g - V_d < V_{th,h}$ and $V_g < V_{th,e}$, holes are injected from the drain electrode (the source electrode acts as a hole drain) and accumulated in the channel corresponding to hole transport in the linear regime (red line). Increasing the gate voltage to ($V_{th,h} < V_g < V_{th,e}$) leads to a saturation of the hole current (sand-yellow line). Continuing the sweep of the gate voltage to $V_g > V_{th,e}$ while $V_g - V_d < V_{th,h}$, the transistor approaches the ambipolar regime (brown line). Now, in addition to the holes injected from the drain electrode, electrons are injected from the source electrode and the pinch-off points of the two accumulation layers (see Figure 2.10b) meet inside the channel area. This junction point, at which charges recombine, can be controlled by the applied voltages and also depends on threshold voltages as well as the charge carrier mobilities of both holes and electrons. The total drain current of an ambipolar transistor (as shown in the tranfer curves) can be calculated according to the Equ. 2.13:[146]

$$I_d = \frac{W}{2L} C \left(\mu_e \left(V_g - V_{th,e} \right)^2 + \mu_h \left(V_g - V_d - V_{th,h} \right)^2 \right). \tag{2.13}$$

An increase of the gate voltage to $V_{th,e} > V_g - V_d > V_{th,h}$ results in pure electron accumulation in the saturation (orange line) and further to $V_g - V_d > V_{th,e}$ in the linear regime

(turquoise line), respectively.

Assuming equal mobilities for holes and electrons and $V_{th,e} = -V_{th,h}$, the transfer characteristics are symmetrical to the voltage corresponding to minimum drain current. At a higher drain voltage, the FET does no longer reach a complete off-state due to the overlapping branches of hole and electron transport (see Figure 2.10a). In the output characteristics of an ambipolar transistor, the injection of the opposite charge carrier leads to a superlinear increase of the drain current at high drain voltages (example for electron accumulation, see Figure 2.10c).

Prerequisites for ambipolar transport include similar effective carrier masses for both holes and electrons and a bandgap that is sufficiently small to result in small injection barriers for both carriers from common electrode metals such as gold. SWCNTs and semiconducting polymers such as DPPT-TT meet these criteria (see sections 2.1.2 and 2.2.2). Ambipolar transport is of high interest for light-emitting field-effect transistors due to the possible radiative recombination of holes and electrons.[29,30,149,156,157] It can also serve as a platform for the scientific investigation of fundamentals of charge transport[50,158,159] as well as the physics of emissive particles such as excitons and trions.[160,161] However, for the realization of low-power complex logic, ambipolar transport is considered disadvantageous and the injection of the opposite carrier should be suppressed and ideally fully avoided. Strategies to accomplish this transformation with an emphasis on achieving solely n-type transport are outlined in section 2.4.

2.3.3 Single-Walled Carbon Nanotube Transistors

Semiconducting SWCNTs are of high interest as active material in (opto-)electronic devices, *e.g.*, FETs[158,162–164] and integrated circuits[165–167] due to their favorable chemical, mechanical and electronic properties (see section 2.1). In the past two decades, a large variety of device architectures using different nanotube species have been employed to develop high-performance transistors. These transistors can generally be organized into three main categories: FETs whose channel is bridged by single SWCNTs, FETs using arrays of SWCNTs and network SWCNT FETs. This section briefly summarizes the substantial progress in recent years as well as the remaining challenges in the field.

Ultra-short channel devices using single SWCNTs with channel lengths below 10 nm have been demonstrated to beat silicon transistors with regard to energy efficiency and current density.[168] Unfortunately, the required processing steps, including individual nanotube selection and electron beam lithography, are time-consuming and expensive. Another issue is the poor performance reproducibility which complicates scalability.

High-density, aligned arrays of SWCNTs can be grown directly on the substrate,[169–171] which allows for a significantly more cost-effective device fabrication compared to FETs based on single nanotube species. In this case, however, elaborate treatments to erase

metallic nanotube species after growth, *e.g.* by selective etching,[172] are required as growth processes with sufficient selectivity towards semiconducting SWCNTs have not yet been demonstrated. Otherwise, these metallic nanotubes severely restrict current modulation. Devices using such nanotube arrays as semiconductor have reached charge carrier mobilities of thousands of $\mathrm{cm^2\,V^{-1}\,s^{-1}}$ with on/off current ratios on the order of 10^5.[172]

Another strategy to deposit aligned nanotube arrays is realized by the deposition from high-purity SWCNT dispersions (see section 2.1.3) using techniques such as self-assembly driven by the evaporation of solvent[173] or *via* vacuum filtration.[26] Again, these methods yield transistors with excellent performance metrics and in a recent report have even successfully been fabricated on a wafer scale but need to be improved further for a transition to commercially viable products, particularly with regard to tube-to-tube pitch uniformity and post-deposition removal of residual polymer.[174]

The third type of SWCNT FET, *i.e.*, that based on nanotube networks, typically exhibits somewhat lower charge carrier mobilities (1-100 $\mathrm{cm^2\,V^{-1}\,s^{-1}}$, comparable to polycrystalline silicon) suitable for, *e.g.*, active-matrix OLED backplanes. This renders SWCNT network FETs a competitor to those based on solution-processable metal oxide semiconductors.[1] Deposition of such networks as thin films in either random or semi-aligned orientation is achieved by a large variety of experimental approaches. Some examples include dropcasting,[175] spin-[164] or dip-coating[174,176] and immersion of the substrate[177] with subsequent photolithographic patterning or direct in-place printing, *e.g.*, *via* aerosol-jet,[178] ink-jet[179] or gravure printing.[180] The latter method enables roll-to-roll processes suitable for large-scale, commercial applications.[180]

In SWCNT networks aligned by a fringing field dielectrophoretic assembly method, on/off current ratios of up to 10^4 were achieved for short-channel FETs ($L = 1$ µm).[181] Given that charge transport in such nanotube networks is typically governed by percolation,[182] purity demands with regard to metallicity of the nanotubes are less strict for longer than shorter transistor channels and better on/off current ratios (up to 10^7) can be achieved.[178] SWCNT networks have also been used in low-voltage devices that operate at high switching speeds even on flexible substrates.[183–185] Various methods (see section 2.4.4) can be employed to adapt their intrinsically equal hole and electron mobilities to enable purely p- or n-type transistors for complementary circuits with minimum power dissipation.[186,187] These complementary nanotube network transistors have even served as the basis for 16-bit microprocessors,[7,188] highlighting their potential for meaningful commercial applications. Despite these advances, particularly exclusive n-type transport in these networks remains a significant challenge as the resulting devices suffer from a number of drawbacks, most importantly, poor operational stability. A description of n-dopants that have been used for SWCNTs is given in section 2.4.5. An approach to address this issue is presented in Chapter 5.

Another general issue that currently hinders the transition of SWCNT FETs based on either SWNCT arrays (see above) or SWCNT networks from the laboratory to commercial applications is their insufficient device performance homogeneity, *e.g.*, caused by impurities originating from dispersants or the presence of nanotube aggregates (see section 2.1.4) negatively affecting charge transport, a challenge tackled in Chapter 4.

2.3.4 Polymer Transistors

Semiconducting polymers are of high interest as active material in FETs as they their chemical structure can be designed to match the desired main carrier type for charge transport, *i.e.*, p-type, n-type or ambipolar. (see section 2.2) Their solution-processability at low temperatures enables compatibility with flexible substrates facilitating a large number of potential applications. As polymers have started to outperform the FETs using amorphous silicon, one of the most commercially interesting of these is the use polymer FETs as drive transistors in display backplanes.[189] However, further performance improvements (*i.e.* higher charge carrier mobilities) are necessary, in particular with regard to operational stability. It has to be noted that widespread erroneous extraction of charge carrier mobilities over the course of several years has cluttered literature with inflated values. Detailed instructions on how to reliably extract mobilities were brought forward in numerous articles.[190–192] This section only mentions explicit values when the extraction of the carrier mobility was reliably documented.

A number of synthetic approaches have been employed to improve the charge transport in semiconducting polymers. Side chain engineering, *e.g.*, by adapting the degree of side chain interdigitation[193] or their regiochemistry[194] in PBTTT or IDT-BT[195] have been demonstrated to improve the hole mobility on the order of $1 - 5$ cm^2 V^{-1} s^{-1}. A similar approach with partial fluorination of the side chain in P(NDI2OD-T2) improved electron transport in FETs by increasing the long-range order in the film.[110] Changes of the polymer backbone were designed to improve planarization of the polymer backbone for extended conjugation lengths. For example, replacement of thiophene with selenophene units in IDT-BT[196] were shown to enhance hole transport while a vinylene linker in employed in P(NDI2OD-T2) lead to an improved electron mobility of 1.8 cm^2 V^{-1} s^{-1}.[197] The bis-lactom core of diketopyrrolopyrrole-based polymers serves as a noncovalent conformational lock, thus enhancing backbone planarization and conjugation, leading to mobilities on the order of 1 cm^2 V^{-1} s^{-1} for both holes and electrons.[138] Further examples are given in literature.[117]

In addition to the outlined synthetic approaches, morphology control for improved crystallization is another strategy to improve charge transport. This has been facilitated by processing from solvents with high boiling points, in swelling/deswelling protocols for, *e.g.*, P3HT[198] or P(NDI2OD-T2)[199] or by deposition from pre-aggregated polymer solutions. In

the latter case, the aggregates have been interpreted as precursors for ordered domains in the deposited films.[141] For P(NDI2OD-T2), electron transport is still efficient even when deposited in a matrix of insulating polystyrene due to the high degree of short-range order present in the typical fibrils.[200] Nikolka *et al.* demonstrated that voids typically present in amorphous polymer film phases can be filled by small molecules to prevent the absorption of species that commonly act as trapping sites for charge carriers. This void-filling also greatly enhanced the environmental stability of the IDT-BT FETs.[201]

Furthermore, a vast number of processing techniques have been explored for unidirectional alignment aimed to exploit the inherent anisotropy of charge transport in semiconducting polymers.[141] Examples to achieve this alignment include mechanical stretching for a hole mobility of 1.7 $cm^2 V^{-1} s^{-1}$ in PBTTT[202] transistors, rubbing[130], directional drying of P3HT films *via* a temperature gradient[203] and off-center spin-coating for P(NDI2OD-T2) FETs with a mobility of 2.6 $cm^2 V^{-1} s^{-1}$.[131] A scalable method compatible with large-area processing is bar coating, which has yielded P(NDI2OD-T2) devices with average mobilities of 4.1 $cm^2 V^{-1} s^{-1}$,[128] which is among the highest reported electron mobilities with a reliable extraction protocol.

Bar-coating has also been employed to maximize the transition frequency of P(NDI2OD-T2) FETs.[204] Although there has been significant progress in that regard up to a frequency of 160 Mhz[204,205], other solution-processable semiconductors such as SWCNTs reach values above 100 GHz.[206] In general, the key upside of semiconducting polymers for circuits is their cost-efficient processing options (*e.g.* large-area printability) rather than their potential for high-frequency applications.[6]

Another strategy to improve carrier mobility in p-type devices that was introduced by the Anthopoulos group is the use of binary blends that combine small-molecule and polymer semiconductors.[207] In ternary blends, the addition of dopants was used to further enhance performance, albeit at the expense of limited on/off ratios.[208]

Overall, however, the application of dopants for the improvement of device performance, particularly for n-type transistors,[209–211] has thus far been restricted to very few studies. In general, similar to SWCNT network FETs, n-type polymer FETs suffer from inferior performance compared to p-type transistors and there are far fewer studies on n-type transistors. Besides the presented P(NDI2OD-T2), there have been reports on diketopyrrolopyrrole-,[212] benzodifurandion-,[213] azaisoindigo-[214] and indolonaphthyridine-based[215] polymers used as active materials in n-type transistors. The performance disparity is due to higher injection barriers to commonly used electrode materials, higher susceptibility of electrons to trapping by polar adsorbates and an overall poorer environmental stability of the devices under operational conditions.

The necessary concepts for alleviating these issues by doping are given in a next section; an experimental study that employs this approach is described in Chapter 6.

2.4 Controlling Charge Injection

Contact barriers are a key factor that limit the performance of both SWCNT and polymer FETs. Efficient injection of charge carriers from the metal electrode into the semiconductor is necessary to reduce resistive voltage drops and enable high-performance FETs. This is of particular importance for high-frequency applications that demand transistors with sub-micron channel lengths and accordingly low channel resistances.[151] This section outlines the fundamentals of metal-semiconductor interfaces, how contact resistance affects the performance of FETs as well as means to lower the existing barriers for efficient charge carrier injection. The concept of doping is introduced with a focus on contact doping in n-type FETs. Finally, an overview of existing and applied n-dopants is given and the family of guanidino-functionalized aromatics as new n-dopants in this thesis is presented.

2.4.1 Metal-Semiconductor Interfaces

Upon contact of a metal electrode and a semiconductor, electrons move from the material with the higher Fermi level E_F to the one with the lower E_F until a thermodynamic equilibrium is reached. In Figure 2.11 this alignment of the Fermi levels is illustrated with the metal having the higher work function (WF) than the semiconductor ($\Phi_m > \Phi_{sc}$). The
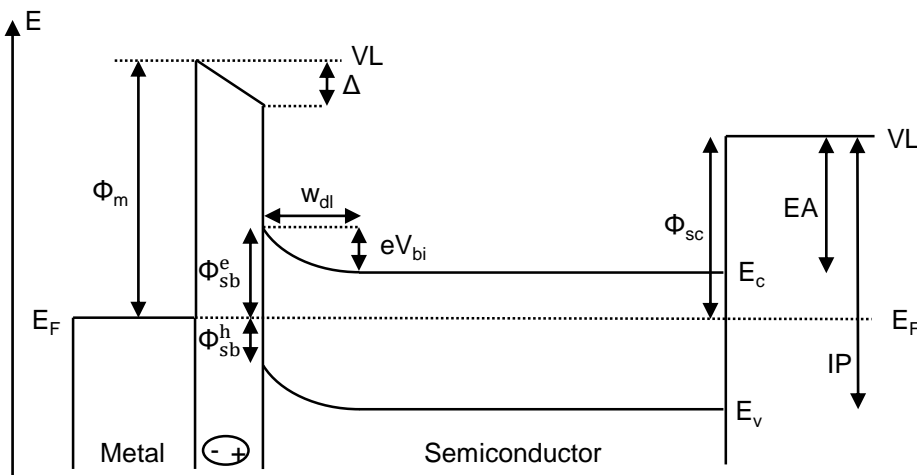
Figure 2.11: Energetic landscape of a metal-semiconductor junction with band bending caused by the alignment of the Fermi levels E_F of both materials. The energies E_v, E_c correspond to valence and conduction band of the semiconductor. In the case of a higher metal than semiconductor work function ($\Phi_m > \Phi_{sc}$), an electron depletion layer with width w_{dl} and built-in potential V_{bi} is formed. The barrier height for the injection of electrons and holes are termed Φ_{sb}^e and Φ_{sb}^h, respectively. These barriers depend on the metal work function as well as the electron affinity EA and ionization potential IP of the semiconductor, respectively, and the interfacial dipole Δ at the metal-semiconductor junction with respect to the vacuum level (VL). Adapted with permission. Copyright 1999 John Wiley and Sons.[216]

formed depletion (or space-charge) layer of width w_{dl} causes a bending of the valence and conduction band energies in the semiconductor, which can be roughly associated with the HOMO and LUMO in an organic material. At the junction of metal and semiconductor, interfacial dipoles Δ can affect the metal WF, leading to a change of interfacial electronic structure.[217] The resulting barriers for the injection of electrons (Φ_{sb}^e) and holes (Φ_{sb}^h) are described by the following expressions:

$$\Phi_{sb}^e = \Phi_m - EA + \Delta \tag{2.14}$$

$$\Phi_{sb}^h = IP - \Phi_m - \Delta \tag{2.15}$$

with EA being the electron affinity and IP the ionization potential of the semiconductor. Low barriers result in a so-called *ohmic* contact whereas high barriers lead to a Schottky contact with undesirably large contact resistance. Injection of charge carriers occurs by surmounting the Schottky barrier *via* thermionic emission or by tunneling through the barrier.[218] While thermionic emission is a temperature-activated process, tunneling is independent of temperature, proportional to the applied electric field, and increases exponentially with decreasing width of the depletion layer ($\propto \exp(-w_{dl})$).[152] The most straightforward strategy to minimize barriers for injection and thus the contact resistance is to match the WF of the metal to the relevant band for charge transport in the semiconductor, *i.e.*, conduction band for electrons and valence band for holes. The WF of metals such as gold (4.8 – 5.4 eV) aligns well with the HOMO of many organic semiconductors while efficient electron injection is best achieved with metals that align with the LUMO of organic semiconductors (typically ≤ 4 eV) such as aluminum or calcium.[149,152] Unfortunately, such low-WF metals suffer from a high sensitivity to even traces of air resulting in unstable device operation in ambient conditions. Further approaches to adjust the WF include the implementation of self-assembled monolayers[219] and contact doping. The latter is described in detail in section 2.4.4.

2.4.2 Contact Resistance

Resistances at both the source (R_s) and the drain (R_d) contacts contribute to the overall contact resistance R_c) in a FET. They originate from the corresponding injection barriers (see previous section). The total resistance R_{tot} of a transistor is the sum of contact and channel resistance R_{ch}:

$$R_{tot} = R_c + R_{ch} = R_s + R_d + R_{ch}. \tag{2.16}$$

While R_c does not depend on L and is inversely proportional to W, the current in a FET and therefore R_{ch} is a direct function of the channel length and width (see Equ. 2.8).[152]

Consequently, FETs with short and narrow channels are more susceptible to drawbacks from high contact resistance. Either contact or channel resistance can be the main bottleneck, depending on the charge carrier mobility of the semiconductor, the height and width of the injection barriers as well as the applied gate voltage.[152] If the total resistance is mainly limited by R_{ch}, *i.e.*, $R_{ch} \gg R_c$, the current-voltage characteristics exhibit a linear increase of the current with increasing drain voltage. In this case, injection of the charge carriers is termed *ohmic* and the contact resistance does not depend on the applied drain voltage. In the other case, *i.e.*, $R_c \gg R_{ch}$, output curves display a characteristic S-shape stemming from a first suppressed, then superlinear increase in current with applied drain voltage and contacts are termed *non-ohmic* (see previous section and 2.3.1). This is associated with an undesired drop in drain bias, which leads to flawed mobility values. High contact resistance may also lead to limitations in the on-current of the transistor.

It has to be noted that direct injection (extraction) of the charge carrier from electrode to semiconductor (and *vice versa*) is only possible in coplanar FETs (*i.e.*, with electrodes and dielectric on the same side of the semiconductor). In the staggered bottom-contact/top-gate architecture (*i.e.*, electrodes and dielectric on opposite sides of the semiconductor) used in this thesis, charges need to additionally move across the semiconductor to reach the charge accumulation layer (see Figure 2.7). This vertical component of the contact resistance decreases with reduced thickness and increased mobility of the semiconductor.[134,220] Furthermore, geometric considerations are taken into account, *i.e.*, in coplanar FETs injection only occurs from the edges of the contact while the entire contact area is available in staggered FETs. The conventional wisdom that FETs in staggered configuration commonly exhibit lower contact resistance than coplanar FETs was recently challenged by Borchert *et al.*[221,222]

A number of methods, each with individual benefits and disadvantages have thus far been demonstrated to determine contact resistance. The most relevant examples include the transmission line method,[223] modeling of current-voltage characteristics (Y-function method),[224] Kelvin probe force microscopy[225] and gated four-point probe (gFPP) method.[226,227] Detailed comparisons can be found in literature.[228] The last-mentioned method has been employed in this study. The measurement principle is briefly explained in the following paragraphs.

The gFPP method allows for the direct extraction of the contact resistance as a function of gate voltage in a single device and separately for source and drain electrode and thus for a more precise extraction of the charge carrier mobility. A specific electrode layout (see Figure 2.12a) that features two voltage sensing probes (V_{p1} and V_{p2}) protruding into the channel at positions L_1 and L_2. These probes enable the measurement of the local potential upon connection to a high-resistance voltmeter during operation of the FET. The
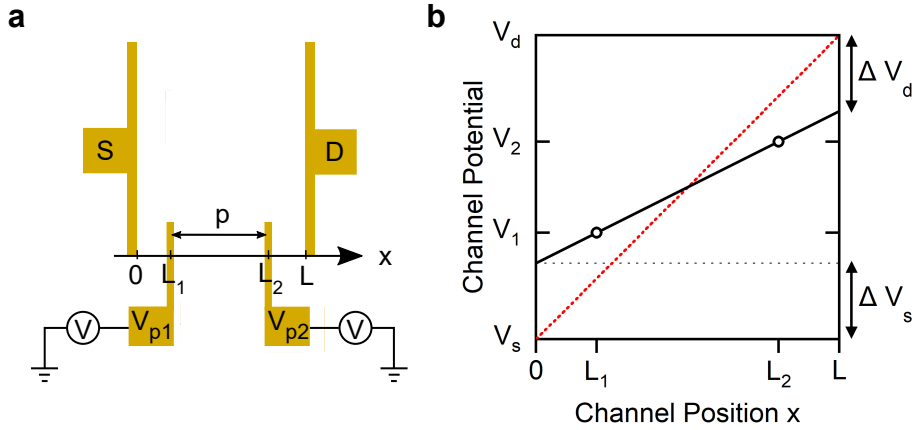
Figure 2.12: (a) Schematic illustration of a FET with gated four-point probe layout: potential inside the channel area can be measured with voltage probes V_{p1} and V_{p2} at positions L_1 and L_2 with probe distance p. (b) The channel potential (black solid line) is extrapolated from the voltages V_1 and V_2 to the remainder of the channel. The differences in voltages to the virtual channel potential at the source and drain electrodes for a transistor without contact resistance (red dashed line) reflect the respective voltage drops ΔV_s and ΔV_d.

GCA (see section 2.3.1) serves as the basis for the extrapolation of the voltages measured by the two probes to positions $x = 0$ and $x = L$. The voltage drops that occur at source (ΔV_s) and drain (ΔV_d) owing to the corresponding injection barriers are extracted as described in Equ. 2.17 and illustrated in Figure 2.12b. Evidently, this method relies on the approximation of a linear channel potential gradient and is only valid for measurements in the linear regime.

$$\Delta V_s = \left[V_1 - \frac{V_2 - V_1}{L_2 - L_1} \cdot L_1 \right] - V_s \text{ and } \Delta V_d = V_d - \left[V_2 + \frac{V_2 - V_1}{L_2 - L_1} \cdot (L - L_2) \right] \quad (2.17)$$

According to Ohm's law, the contact resistances at source and drain electrodes can be obtained using the measured drain current:

$$R_i = \frac{\Delta V_i}{I_d} \text{ with } i = s, d \quad (2.18)$$

The sum of R_s and R_d yields the total contact resistance (see Equ. 2.16) and the contact resistance-corrected charge carrier mobility μ_{corr} in the linear regime can be calculated according to

$$\mu_{corr} = \frac{p}{WC} \frac{\partial I_d / V_{12}}{\partial V_g}, \quad (2.19)$$

with p being the distance between the two voltage probes and V_{12} the voltage difference measured between them. To ensure comparability of different studies regardless of the device geometry, the width-normalized contact resistance $R_c W$ (unit $\Omega\,\text{cm}$) is usually the

reported figure of merit. This contact resistance extraction is crucial to identify the impact of doping at the electrode-semiconductor interface (see following sections).

2.4.3 Fundamentals of Doping

Doping of a semiconductor (inorganic or organic) describes the (controlled) introduction of an impurity (dopant) to a semiconducting host material. Electron donors serve as n-dopants, electron acceptors serve as p-dopants. For inorganic semiconductors such as crystalline silicon, dopant atoms, *e.g.*, boron as p-dopant or arsenic as n-dopant, are directly incorporated into the crystal lattice. This gives rise to additional states in close proximity to the conduction (n-doping) or valence band (p-doping) which results in a shift of the energy bands with respect to the Fermi level. While at very low doping ratios of 10^{-6} – 10^{-3} doping increases the conductivity of the intrinsic semiconductor, higher concentrations (several ‰) of the dopants cause degenerate doping of the semiconductor, which then displays metallic properties.[229]

The report of metallic properties iodine-doped poly(acetylene) in 1977[230] can be considered as the origin of the field of organic electronics. Given that halides or alkali metals readily diffuse through such a polymer matrix, this doped polymer could not be implemented in electronic devices due to insufficient operational stability. Several decades later, larger molecules that are ideally immobile in the semiconductor matrix are under investigation. Their chemical structure should be designed such that charges resulting from electron transfer reactions can be stabilized, *e.g.*, by delocalization to avoid localized electrostatic charge trapping. Strong acceptor molecules such as 2,3,5,6-tetrafluoro-7,7,8,8-tetracyanoquinodimethane (F_4-TCNQ) serve as p-dopants while molecular donors (see section 2.4.5) are used as n-dopants.[11] A simplified model describes the reaction between dopant and host material as an integer charge transfer (see Figure 2.13a). An integer number of electrons is either transferred from the HOMO of the semiconductor host to the LUMO of the p-dopant or from the HOMO of the n-dopant the LUMO of the semiconductor. In some cases, substantial activation barriers may prevent a reaction even if the energetic alignment would allow for a chemical reaction.[231] In other reactions, the formation of a charge-transfer complex is observed upon doping (see Figure 2.13b) with both ionic and covalent contributions to the bond.[232] The larger the energy difference between the two involved frontier orbitals, the more ionic is the character of the bond and the integer charge transfer model describes the adduct more accurately. The smaller the difference in orbital energy, the more covalent are the contributions to the bond as hybrid orbitals are formed and the charge-transfer complex description is more appropriate.[232]

Regardless of the nature of the bond, doping leads to the generation of mobile charge carriers in the semiconductor. While such doping of the bulk of the semiconductor is highly desired for thermoelectric applications,[233] it is often detrimental to the performance
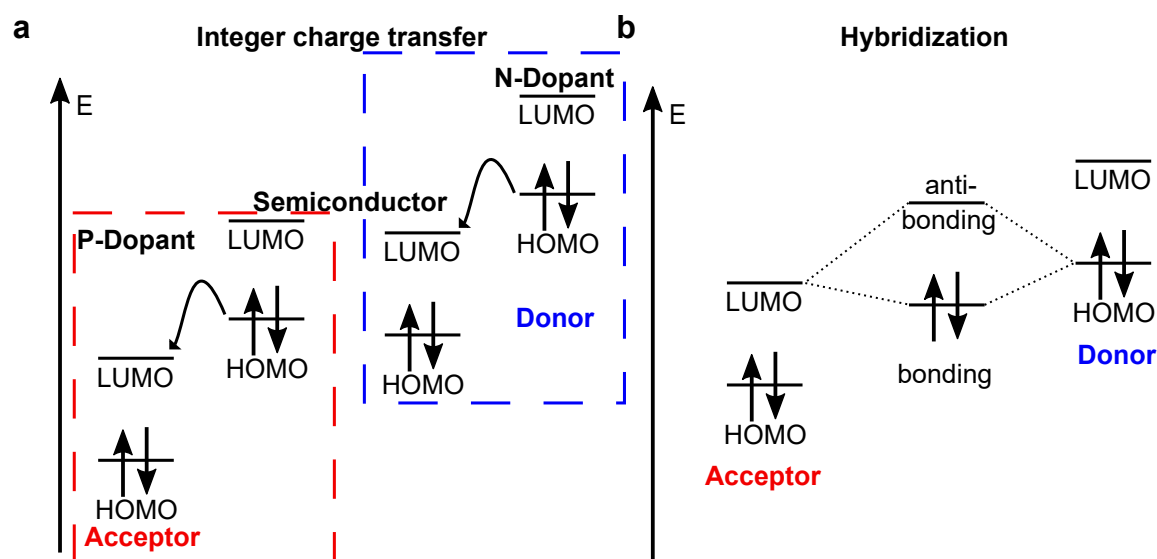
Figure 2.13: Two extreme models of donor-acceptor interaction. (a) Simplified schematic energy level diagram for n-doping (blue) and p-doping (red) of an organic semiconductor in the integer charge transfer model. Activation barriers are omitted for clarity. (b) Hybridization between donor HOMO and acceptor LUMO to form a charge-transfer complex.

of transistors. For a long time, molecular doping of organic semiconductors had thus generally been employed relatively scarcely, mostly in organic photovoltaic, thermoelectric devices and OLEDs, but has received increasing attention for improving the performance of OFETs.[11,12] The next section elucidates the details of these doping approaches specifically designed for FETs.

2.4.4 Channel and Contact Doping

As outlined in the previous section, doping at a suitable concentration leads to the creation of free charges in the semiconductor, which causes an increase in conductivity. For transistors this approach is referred to as channel doping. In some cases, this method has been demonstrated to improve device stability.[234–236] At very low dopant concentrations, channel doping is employed to passivate trap states.[237–239] Depending on the nature of the trap states, this leads to an increase in charge carrier mobility and can enable control of the threshold voltage. However, moderately larger dopant concentrations can lead to large threshold voltage shifts, *i.e.*, the device becomes a depletion mode transistor (in on-state when $V_g = 0$).[12] Additionally, higher dopant concentrations have been demonstrated to interfere with the molecular packing of the semiconductor and negatively affect film morphology.[210] Ultimately, high dopant concentrations can cause degenerate doping, which elevates the off-current level of a transistor, thus lowers current modulation and the achievable on/off current ratio.

In contrast to that, contact doping is predominantly employed to facilitate more efficient

injection of charge carriers and reduce the contact resistance (see section 2.4.2) to improve device performance.[11] As only the contact area is doped, the risk of increased off-currents can be avoided. This doping approach can be used to reduce both the height and the width of the Schottky barrier present at the metal-organic interface. Such a reduction in barrier width was found for an indium tin oxide/zinc phthalocyanine interface upon p-doping with F_4-TCNQ.[240] The thinner barrier enabled tunneling of the charge carriers through the barrier, which resulted in more efficient hole injection into the semiconductor. Olthof *et al.* demonstrated for several electrode materials at a metal-organic interface that a quasi-ohmic contact can be achieved despite a large mismatch of semiconductor and metal WFs.[241]

Another advantage of this doping approach lies in the removal of interfacial trap states present at the contact electrode similar to bulk trap passivation by channel doping. This effect can be even more significant for device performance as the trap density at the contacts has been shown to exceed that in the channel by a factor of 1,000.[242] Such contact trap passivation was demonstrated to result in a substantial decrease in contact resistance[243] and subthreshold swing.[244]

Furthermore, contact doping can be utilized to suppress the injection of the opposite charge carrier in ambipolar transistors by increasing the height of the corresponding Schottky barrier.[245] This offers a particularly large potential for improvement in FETs with narrow-bandgap semiconductors such as SWCNTs and polymers. Here, off-currents especially in the saturation regime can be reduced by many orders of magnitude. Implementation of such devices in complementary circuits leads to much lower power consumption (see section 2.3.1).

As the relative impact of contact resistance on the total resistance increases with decreasing channel length (see section 2.4.2), contact doping is especially relevant for short-channel transistors. In addition to improving the carrier injection, this doping approach has also been employed to reduce short-channel effects such as increased off-currents and poor current saturation.[246]

Note that either channel or contact doping or a combination of both approaches might be desirable depending on intended function and available processing conditions of the involved dopant and semiconductor.

2.4.5 Chemistry of N-Dopants

Due to the much larger number of solution-processed semiconductors suitable for hole transport, p-dopants have been investigated in larger numbers and more detail than n-dopants. In-depth descriptions of p-dopants and their chemistry can be found in literature.[11,12,232] This section only describes the chemical properties of n-dopants with a focus on materials used in FETs, particularly those that have been employed for doping

SWCNTs and semiconducting polymers.

Due to their high-lying HOMOs n-dopants are intrinsically sensitive to oxygen and moisture, imposing strong restrictions on processing conditions. In addition, reaction products of doping often share this disadvantage, which is highly detrimental to stable device operation. Some alternative approaches to achieve solely n-type injection and charge transport in SWCNT FETs lie in the use of low WF metals such as Gd, Y or Sc[247,248] or electrostatic doping *via* HfO$_x$[187,249] or silicon nitride[250] layers. While the performance of the former suffers from the intrinsically poor environmental stability of the metals (similar to that of the n-dopants), electrostatic doping often leads to the creation of additional trap states, *e.g.*, resulting in large current hysteresis.

N-dopants can be categorized into the following groups with certain dopants fitting in more than one compound family. Alkali metals such as sodium have been employed in nanotube transistors but exhibited short operational lifetimes owing to diffusion of the cations through the semiconducting layer.[251] Inorganic salts such as CsF have also been utilized for n-doping P(NDI2OD-T2) FETs.[210] This led to a reduced threshold voltage and improved operational stability due to trap state passivation. A wide range of small-molecule reducing agents with low ionization potentials have been used as n-dopants in OFETs. Figure 2.14 displays selected examples that have been used for doping SWCNTs and/or polymers. Among those are NADH,[252] tetrabutyl ammonium salts[211] and
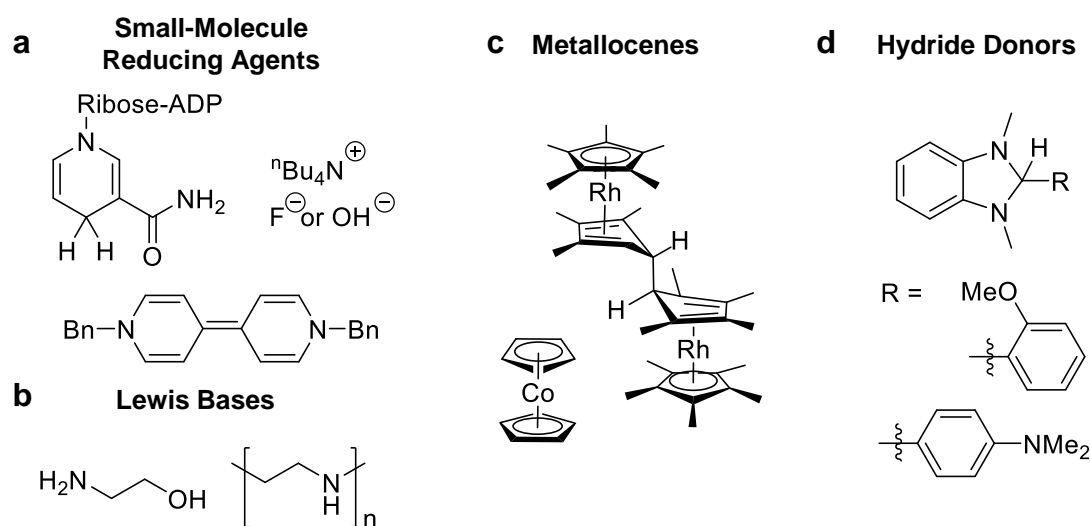
Figure 2.14: Molecular structures of (a) small-molecule reducing agents NADH,[252] tetrabutyl ammonium salts[211] and benzyl viologen[209,253,254] (reduced species), (b) Lewis base dopants ethanolamine[255] and polyethylene imine,[256] (c) metallocene dopants cobaltocene[210] and rhodocene dimer,[257] (d) hydride donors dimethyldihydrobenzimidazoles.[258]

benzyl viologen.[209,253,254] Compounds such as poly(ethylene imine)[256] and ethanolamine[255] function as n-dopants since they provide electron density by virtue of their amine groups acting as Lewis bases. 19-Electron metallocenes such as (decamethyl)cobaltocene have been

employed as dopants in polymer[210] and SWCNT FETs,[259] even though their high reactivity renders them difficult to handle during processing. Another n-dopant family are the dimethyldihydrobenzimidazoles (DMBIs),[258] that serve as hydride donors. Representatives of the latter two can also be dimerized to enhance their air stability, *e.g.*, the rhodocene dimer [Rh(cp*cp)]$_2$ displayed in Figure 2.14c, which was employed as an n-dopant for SWCNT network FETs.[257]

In general, molecular n-doping remains a challenge as the air stability of the dopants – albeit recently somewhat improved by various synthetic approaches – complicates processing, which renders the simultaneous control of all relevant device parameters in FETs particularly difficult.

2.4.6 Guanidino-Functionalized Aromatic Compounds

Guanidino-functionalized aromatic (GFA) compounds are molecules with (multiple) guanidinyl groups attached to the aromatic core, which can further be synthetically modified by additional functionalization (see Figure 2.15a).
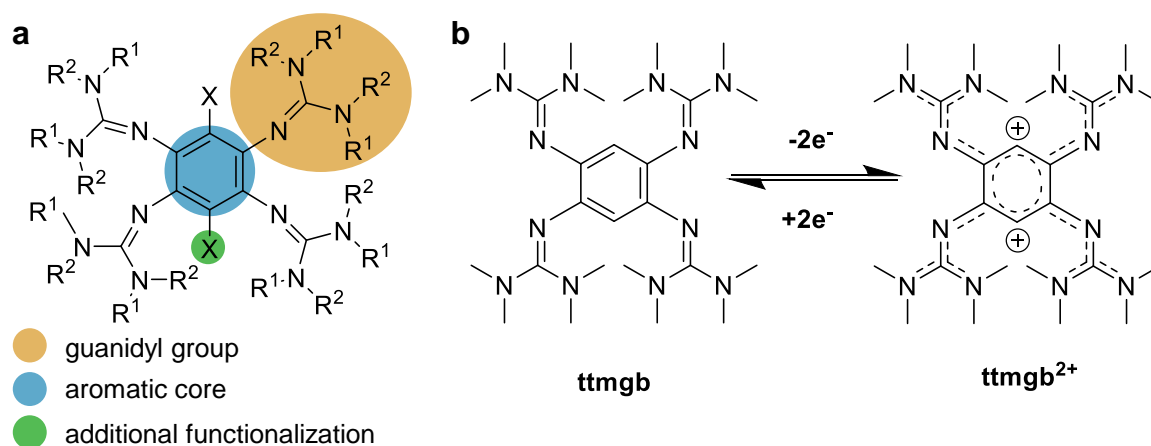
Figure 2.15: (a) General structure of guanidino-functionalized aromatic (GFA) compound comprised of guanidinyl groups (orange; *e.g.*, $R^1 = R^2 = $ Me, -CH$_2$-CH$_2$- or $R^1 = $ H, $R^2 = {}^i$Pr), an aromatic core (blue) and additional substituents (green; X = H, Br, NO$_2$). (b) Reversible two-electron oxidation of 1,2,4,5-tetrakis(tetramethylguanidino)benzene (ttmgb) to form ttmgb^{2+}.

GFAs are powerful organic reducing agents. Their aromatic core serves as an electron reservoir while the guanidyl groups provide an extension to the conjugated π-system and thus stabilize positive charges generated upon oxidation of the GFA.[260] The charges of these stable di- or tetracations, that form during these reactions, are delocalized across aromatic core and guanidinyl groups as exemplified in Figure 2.15b for 1,2,4,5-tetrakis(tetramethylguanidino)benzene (ttmgb).[261] This compound has an oxidation potential of -0.76 V *vs.* Fc/Fc$^+$ in acetonitrile and is thus a somewhat weaker reducing

agent than, *e.g.*, cobaltocene ($<$ -1.3 V *vs.* Fc/Fc$^+$)[262] or DMBI derivatives ($\approx$ -1.9 V *vs.* Fc/Fc$^+$).[263] The two-electron oxidation of most GFA compounds occurs at (almost) identical potentials as measured by cyclic voltammetry.[264] GFA compounds also exhibit a high alkalinity comparable to that of alkali hydroxides.[264] Protonation was identified to occur at the π-bond of the imino-group enabling a much better delocalization of the positive charge in aryl guanidines compared to, *e.g.*, aryl amines.[261] The electronic structure of GFA compounds and thus their reactivity can be readily altered by introducing substituents at the aromatic core or change of the guanidyl groups[265] as well as *via* complexation or protonation.[260] Additionally, exchange of the moieties at the guanidyl groups enables the tuning of solubility in solvents of different polarity.

While the class of GFA compounds was originally introduced as redox-active ligands for transition metal complexes,[266,267] further applications were explored such as their use as redox catalysts,[268] in dehydrogenative coupling reactions, such as for the reduction of thiols to dithiols,[269] as reducing agents in organic synthesis[270] and photochemical reductive carbon-carbon coupling reactions.[271] In addition, their potential as high-charge capacity materials for organic electronics has been proposed.[272] The first molecule of this class of compounds, ttmgb, was synthesized by Peters *et al.* in 2008 and has been developed as a bench mark for GFAs.[260,265,273,274] Due to its reducing strength ttmgb was explored as an n-dopant for both classes of semiconducting materials used in this thesis (see Chapters 5 and 6).

Chapter 3

MATERIALS AND METHODS

This chapter describes the materials, the processing techniques and the characterization methods that were employed in this study.

3.1 Materials

All solvents were purchased from Sigma-Aldrich (unless otherwise specified) and used without further purification.

Single-walled carbon nanotube raw materials were purchased from CHASM Advanced Materials Inc. (CoMoCAT® SWCNTs, diameter range 0.7–1.0 nm, SG65i-L58) and Raymore Industries Inc. (diameter range 0.9–1.5 nm, batch RNB739-220-A329), respectively. Raw materials were dried at 110 °C overnight in ambient air prior to use.

The stabilizing additives used in this thesis are listed in Table 3.1 were used without further purification.

Table 3.1: Stabilizing additives used in this thesis.

Additive	Purity (%)	M (g mol^{-1})
1,10-phenanthroline	99	180.21
4,7-phenanthroline	98	180.21
1,7-phenanthroline	99	180.21
phenanthrene	99.5	178.23
1,10-phenanthroline monohydrate	99	198.25

Their molecular structures are displayed in Figure 3.1.
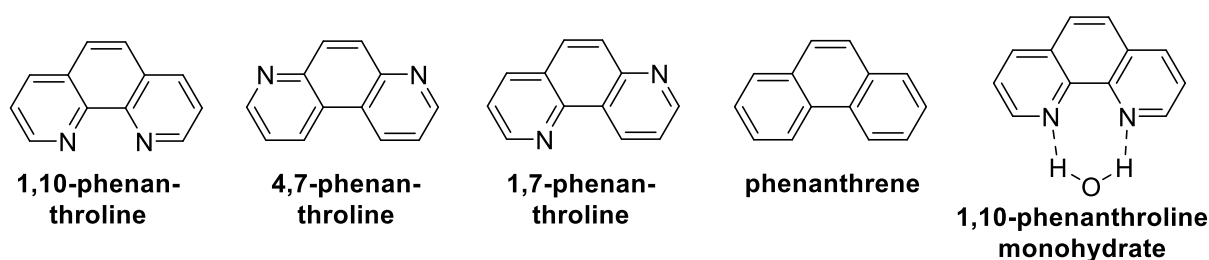
Figure 3.1: Molecular structures of stabilizing additives.

The guanidino-functionalized aromatic compounds ttmgb, ttmgb(PF$_6$)$_2$, ttmg-phen and tdmegb were synthesized and purified in the laboratory of Prof. Dr. Dr. Hans-Jörg Himmel's group as described in literature[273–275] (for IUPAC names, see Table 3.2, for molecular structures, see Figure 3.2). All compounds were stored in dry nitrogen.

hpp was purchased from Sigma-Aldrich and sublimated at 100 °C under vacuum prior to use. Me$_4$G (99 % was purchased from ARCOS and used without further purification (for

molecular structures, see Figure 3.2).

Table 3.2: N-Dopants used in this thesis.

Compound	Abbreviation	M (g mol^{-1})
1,2,4,5-Tetrakis(tetramethylguanidino)benzene	ttmgb	530.77
ttmgb-Bishexafluorophosphate	ttmgb(PF$_6$)$_2$	820.70
2,3,7,8-Tetrakis(tetramethylguanidino)phenazine	ttmg-phen	632.87
1,2,4,5-Tetrakis(*N,N*'-dimethyl-*N,N*'-ethylene-guanidino)benzene	tdmegb	522.71
Hexahydropyrimidopyrimidine	hpp	139.20
Tetramethylguanidine	Me$_4$G	115.18
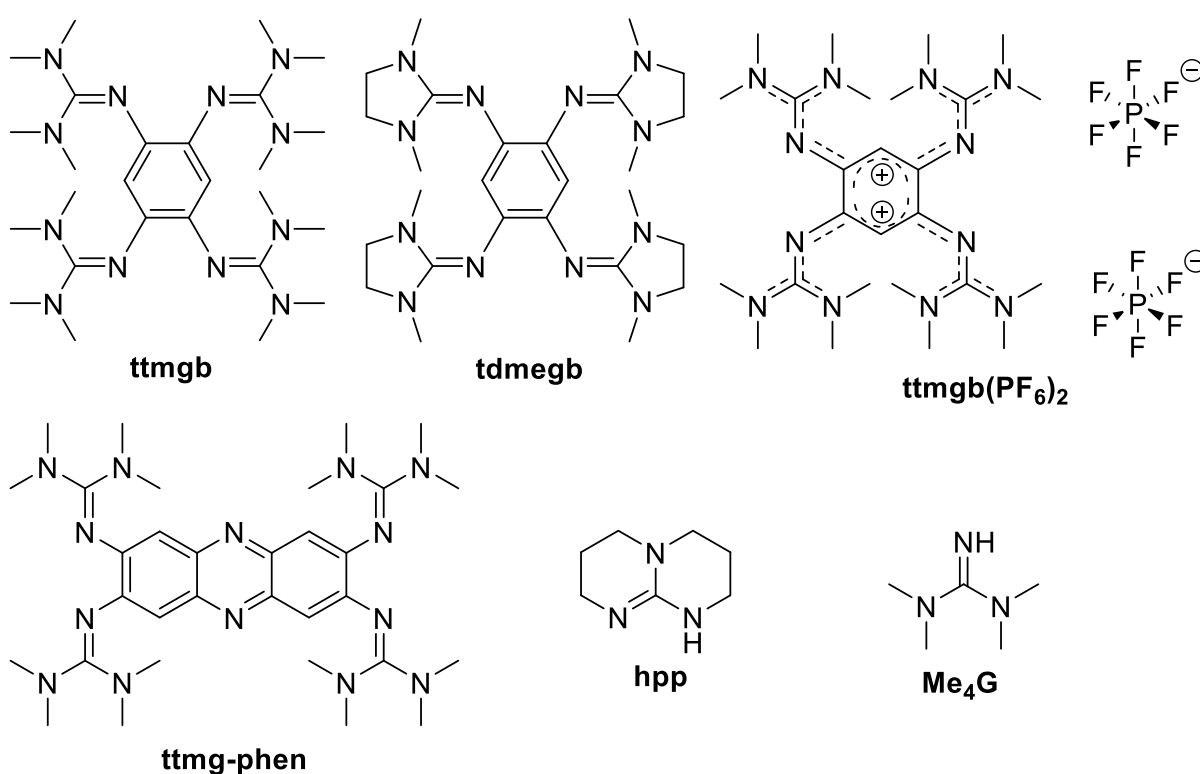
Figure 3.2: Molecular structures of n-dopants.

Molybdenum tris(1-(trifluoroacetyl)-2-(trifluoromethyl)ethane-1,2-dithiolene) (Mo(tfd-COCF$_3$)$_3$, $M = 858.46$ g mol^{-1}) was purchased from Sigma-Aldrich and used without further purification (molecular structure, see Figure 3.3).
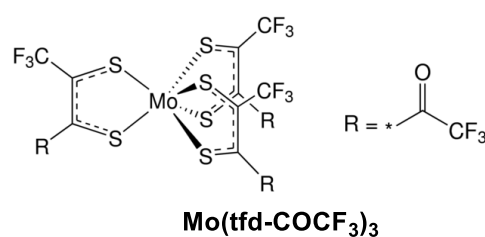
Figure 3.3: Molecular structure of p-dopant (Mo(tfd-COCF$_3$)$_3$).

The polymers PFO-BPy (as wrapping polymer), P(NDI2OD-T2) and DPPT-BT (as semiconductors) and PMMA (as dielectric) were used without further purification. Their IUPAC names as well as their molecular weight and supplier data is given in Table 3.3, their molecular structures are displayed in Figure 3.4.

Table 3.3: Polymers used in this thesis.

Polymer	Supplier	Abbreviation	M_n (kg mol^{-1})	M_w (kg mol^{-1})
Poly[(9,9-dioctylfluorenyl-2,7-diyl)-*alt*-(6,6'-2,2'-bipyridine)]	American Dye Source	PFO-BPy	n/a	34
Poly[*N,N'*-bis(2-octyldodecyl)-naphthalene-1,4,5,8-bis(dicarboximide)-2,6-diyl]-*alt*-5,5'-(2,2'-bithiophene)	Polyera Corp.	P(NDI2OD-T2)	35.3	63.5
Poly[(2,5-bis(2-octyldodecyl)-(5–(benzo[2,1,3]thiadiazole-4,7-diyl)-2,5-diyl)-thiophene-2,5-diyl)–6-(thiophene-2,5-yl)pyrrolo[3,4-*c*]pyrrole-1,4(2*H*,5*H*)-dione)]	FlexInk Ltd.	DPPT-BT	33	87
Poly(methyl methacrylate), syndiotactic	Polymer Source	PMMA	n/a	350
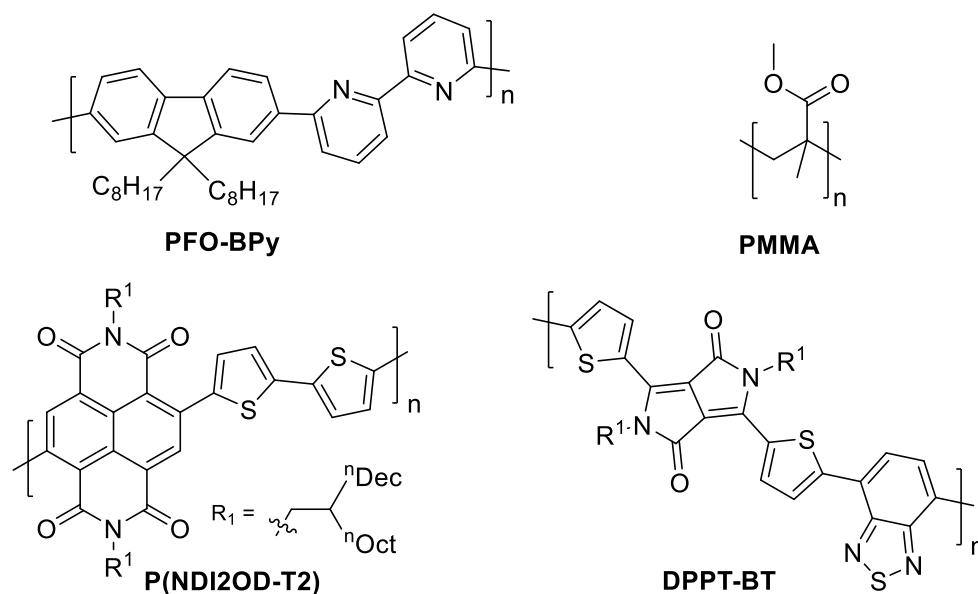
Figure 3.4: Molecular structures of polymers.

3.2 SWCNT Dispersion Preparation

(6,5) SWCNT dispersions were prepared from CoMoCAT® raw material (0.38 g L^{-1}). SWCNTs were selectively dispersed by shear-force mixing in toluene with PFO-BPy. For plasma torch tube dispersions, 1.5 g L^{-1} raw material was dispersed in a PFO-BPy solution in toluene (0.5 g L^{-1}) using bath sonication (Branson 2510) for 55 min at r.t. The dispersions were then subjected to centrifugation at 60,000 g (Beckman Coulter Avanti J26CP centrifuge) for 30 min and the supernatant was collected. This process was repeated at least once. This supernatant was subsequently filtered through a PTFE membrane (Merck Milipore, JGWP, 0.1 µm pore size) which yielded SWCNT filter cakes (approx. 100 µg). Washing with toluene ($T = 80$ °C, three times) removed excess polymer. Next, the filter cake was re-dispersed in toluene (1 mL) using bath sonication for 30 min at r.t. and diluted to the desired concentration.

For the dispersions used in the aggregation experiments, a slightly altered protocol was used as follows: stock solutions were prepared in dry nitrogen atmosphere by dissolving 20 mg additive (phenanthrene, 1,10-phenanthroline, 1,7-phenanthroline, 4,7-phenanthroline or 1,10-phenanthroline monohydrate) in anhydrous toluene, *o*-, *m*-, *p*-xylene or mesitylene (2 mL) and then kept inside a glovebox.

Filter cakes were washed four times with toluene ($T = 80$ °C) to remove as much unbound polymer as possible. Subsequently, they were re-dispersed in the corresponding anhydrous solvent (see above) by bath sonication for 45 min at r.t., diluted to the desired concentration (see sections 3.3.2) and the additive stock solution was added (50 µL per 950 µL dispersion). All dispersions were subjected to bath sonication for 4 min at r.t. immediately

prior to use.

3.3 Device Fabrication

3.3.1 Bottom Electrodes

AF32eco glass substrates (300 µm, SCHOTT AG) were cleaned by bath sonication in acetone and 2-propanol for 10 min, rinsed with de-ionized water and blow-dried. Source-drain electrodes (geometry, see Figure 3.5a and b, Table 3.4) were fabricated on these pre-cleaned glass substrates using standard photolithography (LOR5B, S1813 resists) in combination with e-beam evaporation (HVB-130, Winter Vakuumtechnik GbR) of chromium (2 nm) and gold (30 nm) with subsequent lift-off in *N*-methyl-2-pyrrolidone (NMP). Prior to deposition of the semiconducting layer, the solvent cleaning steps outlined above were performed again. For the deposition methods of the different semiconductors, see below (sections 3.3.2, 3.3.3)

For DPPT-BT FETs with injection layers, source-drain electrodes (for layout and dimensions, see Figure 3.5c, Table 3.4) were fabricated by thermal evaporation (MB-ProVap-3, M. Braun Inertgas-Systeme GmbH) of chromium (2 nm) and gold (30 nm) through shadow masks. Cleaning steps were performed as described above.
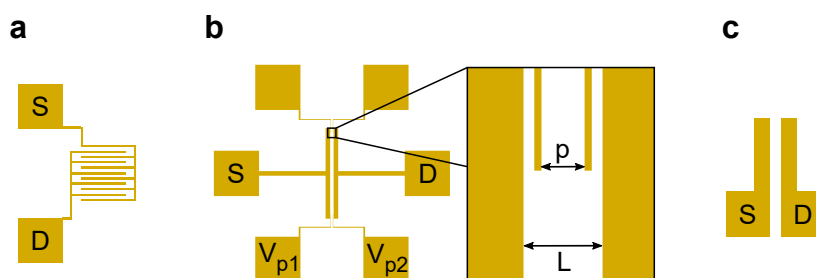
Figure 3.5: Source (S) and drain (D) electrode layouts. (a) Interdigitated electrodes, (b) four-point probe layout (voltage probe (V_{p1}, V_{p2}), probe-to-probe distance $p = 20$ µm, probe width 4 µm, distance to S and D electrode 6 µm) and (c) L-shaped electrodes. Channel lengths and widths are summarized in Table 3.4.

3.3.2 SWCNT Thin Film Preparation

SWCNT dispersions in toluene with concentrations adjusted to the desired network densities (sparse networks: 5.6 µg mL^{-1}, dense networks: 14.4 µg mL^{-1}) were spin-coated at 2000 rpm for 30 s onto the substrates patterned by photolithography (see previous section) and subsequently annealed at 100 °C. This process was conducted three times.

Table 3.4: Channel lengths and widths for different FET geometries.

Electrode layout	L (µm)	W (µm)
Interdigitated	5	10000
Interdigitated	10	10000
Interdigitated	20	10000
Interdigitated	40	5000
Four-point probe	40	1000
L-shaped	42	1500

The re-dispersion for referencing the impact of the stabilizing effect of 1,10-phenanthroline was prepared in *o*-xylene with a concentration of 14.4 µg mL^{-1} to create dense networks. Aged dispersions were subjected to vortexing for 2 seconds immediately before deposition to allow for removal of loose clusters. After spin-washing with tetrahyrofuran and 2-propanol, standard photolithography and oxygen plasma etching were used to pattern the films in order to reduce leakage paths and device cross-talk.

For printed films prepared for ultraviolet photoelectron spectroscopy, an Aerosol Jet 200 printer (Optomec Inc., 200 µm inner diameter nozzle, ultrasonic atomizer, nitrogen carrier gas 15 sccm, sheath gas 30 sccm) was used (SWCNT concentration in toluene 3.6 µg mL^{-1}, 5 vol % terpineol added). Horizontal and vertical lines (line pitch 25 µm) were printed in rectangular shape (3 × 3 mm size). The stage temperature was set to 100°C. Films were then rinsed with tetrahydrofuran and 2-propanol and blow-dried. Next, the substrates were annealed at 300 °C for 30 min in dry nitrogen atmosphere.

3.3.3 Semiconducting Polymer Film Preparation

All processing steps were carried out in dry nitrogen atmosphere. P(NDI2OD-T2) was spin-coated from a solution in toluene (8 g L^{-1}) at 8000 rpm for 60 s and then annealed at 110 °C for 30 min. For the samples with a solution-processed ttmgb top layer (see section 3.3.4), 4,000 rpm for 60 s were chosen as spin-coating parameters to ensure sufficient film coverage after the next processing step while maintaining relevant film properties. Solutions of DPPT-BT in chlorobenzene (8 g L^{-1}) were spin-coated at 1500 rpm for 60 s and then annealed at 200 °C for 30 min.

3.3.4 Processing of Dopants

Dip-Coating

In dry nitrogen atmosphere, substrates with pre-deposited SWCNT networks were dipped into solutions of dopants for 20 min and then annealed as summarized in Table 3.5.

Petry dishes that were carefully cleaned with freshly prepared peroxomonosulfuric acid, subsequently rinsed with de-ionized water and blow-dried to exclude potential contaminants, served as reaction vessel.

Table 3.5: Experimental parameters for dip-coating.

Dopant	Solvent	Concentration (g L^{-1})	Annealing T (°C)	Annealing t (min)
ttmgb	toluene	0.1–10	150	30
Me$_4$G	toluene	undiluted, 25 vol %	80	2
hpp	toluene	2.0, 8.0	80	30
ttmgb(PF$_6$)$_2$	acetonitrile	5.0	100	30
ttmg-phen	acetonitrile	3.0	100	30
(Mo(tfd-COCF$_3$)$_3$)	toluene	2.0	100	30

Spin-Coating

Figure 3.6 provides an overview on the different device architectures and highlights the localization of the dopant. Injection and solution-processed top layers of ttmgb incorporated
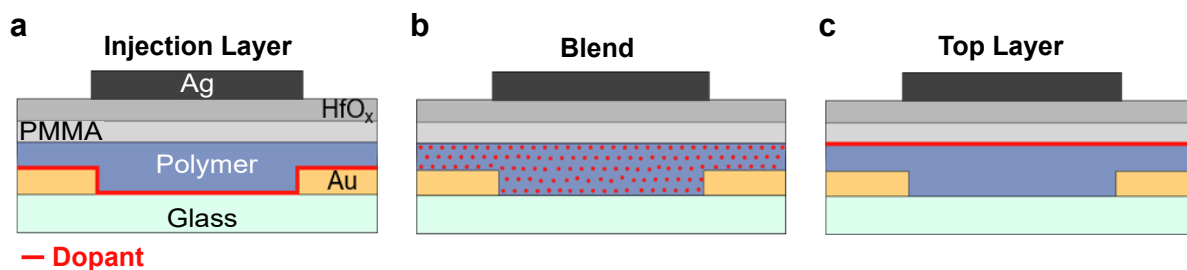
Figure 3.6: Bottom-contact/top-gate field-effect transistors using (a) a dopant (red) injection layer deposited before the semiconducting polymer (purple), (b) a polymer-dopant mixture deposited as a blend and (c) a dopant top layer deposited after the polymer layer.

in polymer FETs were spin-coated from colorless solutions in toluene and then annealed at 110 °C with parameters as described in Table 3.6. Note that pale green solutions indicating small amounts of oxidized ttmgb could not be used and had to be discarded.

For P(NDI2OD-T2)/ttmgb blend layers, freshly prepared solutions of the individual compounds were mixed to yield mass ratios of 0.1, 0.2, 0.3, 0.4, 0.5, 1.0 and 2.0 w% ttmgb. Prior to deposition, the combined solution was stirred at 70 °C for 30 min, cooled to r.t., spin-coated and annealed with parameters identical to the pristine P(NDI2OD-T2) layer (see section 3.3.3).

Table 3.6: Experimental paramenters for spin-coating of ttmgb layers.

Polymer	Architecture	Layer Label in Chapter 6	Spin-Coating Speed (rpm)	ttmgb Concentration $(\mathrm{g\,L^{-1}})$
P(NDI2ODT2)	Injection Layer	Thin	4,000	1.4
P(NDI2ODT2)	Injection Layer	Thick	4,000	2.8
P(NDI2ODT2)	Top Layer	-	1,000	0.5
DPPT-BT	Injection Layer	Thin	4,000	1.4
DPPT-BT	Injection Layer	Medium	4,000	2.8
DPPT-BT	Injection Layer	Thick	4,000	5.6
DPPT-BT	Top Layer	Thin	1,000	1.0
DPPT-BT	Top Layer	Medium	1,000	2.0
DPPT-BT	Top Layer	Thick	1,000	4.0

Evaporation

Vacuum-processed ttmgb layers (thicknesses see Table 3.7) were deposited from aluminum oxide crucibles (M. Braun Inertgas-Systeme GmbH) by thermal evaporation (MB-ProVap-3, M. Braun Inertgas-Systeme GmbH) at a base pressure of approximately $5{\cdot}10^{-7}$ mbar. The temperature of the crucible was adjusted to approximately 75 °C to achieve a rate of $0.5~\mathrm{\AA\,s^{-1}}$ for ttmgb and to 125 °C to achieve a rate of $0.5~\mathrm{\AA\,s^{-1}}$ for tdmegb, respectively, using approximately 10 mg of starting material. Note that evaporation rates are a function of filling level. Special care was taken to mount samples in a way that shading of relevant sample areas from dopant vapor was minimized. Evaporation was performed without rotation of the substrate holder.

Table 3.7: Experimental paramenters for evaporation of dopant layers.

Polymer	Dopant	Architecture	Layer Label in Chapter 6	Layer Thickness (nm)
P(NDI2ODT2)	tdmegb	Injection Layer	Thin	0.8
P(NDI2ODT2)	tdmegb	Injection Layer	Thick	2.0
P(NDI2ODT2)	ttmgb	Top Layer	-	1.1
DPPT-BT	ttmgb	Top Layer	Thin	2.0
DPPT-BT	ttmgb	Top Layer	Thick	4.0

3.3.5 Hybrid Dielectric and Top Gate

After deposition of semiconductor and - if applicable - dopant, spin-coating of 6 $g\,L^{-1}$ PMMA, in *n*-butyl acetate at 4000 rpm for 60 s and atomic layer deposition of HfO_x (Ultratech Savannah S100) using tetrakis(dimethylamino)hafnium (Strem Chemicals Inc.) and water precursors resulted in a hybrid dielectric (layer thicknesses 11 nm PMMA, 61 nm HfO_x). Thermal evaporation (MB-ProVap-3, M. Braun Inertgas-Systeme GmbH) of the gate electrode (silver, 30 nm) finalized the devices.

3.4 Characterization

3.4.1 UV-vis-NIR Absorption Spectroscopy

UV-vis-NIR absorption spectra were recorded under ambient conditions using a Cary 6000i UV-vis-NIR absorption spectrometer using quartz cuvettes with an optical path length of 1 cm. Nanotube Dispersions for aggregation monitoring were diluted to concentrations of approximately 1.0 $\mu g\,mL^{-1}$ and 50 µL of additive stock solution per 950 µL dispersion were added. Aggregation of SWCNT dispersions was monitored by collecting spectra with a cycle time of 20 min for a total of 13 h at r.t. without a temperature controller.

3.4.2 Photoluminescence Spectroscopy

Photoluminescence spectra were recorded by a Fluorolog 3 spectrometer (Horiba Jobin-Yvon GmbH). A liquid nitrogen-cooled InGaAs diode array (800-1600 nm) served as the detector. For the comparison of peak energy of various additives, dispersions were diluted to a (6,5) SWCNT concentration of 0.02 $\mu g\,mL^{-1}$ and to a concentration of 0.5 $\mu g\,mL^{-1}$ for monitoring aggregation. Aggregation was monitored by collecting spectra with a cycle time of 5 min for a total of 180 min in ambient conditions at r.t. using a temperature controller.

3.4.3 Raman Spectroscopy

Raman spectra were collected using a Renishaw InVia Reflex confocal Raman microscope with a ×50 objective ($NA = 0.75$) and a 532 nm Nd:YAG diode laser (2400 lines/mm grating), a 633 nm HeNe laser and a 785 nm diode laser, (both 1200 lines/mm grating). The spectrometer was calibrated to silicon (520.6 cm^{-1}). Samples were prepared by repeated dropcasting of SWCNT dispersions (5 x 10 µL) on aluminum foil with subsequent annealing and rinsing with tetrahydrofuran and toluene. All measurements were recorded as maps using Streamline™ and then averaged (at least 400 spectra).

3.4.4 Ultraviolet Photoelectron Spectroscopy

All ultraviolet photoelectron spectroscopy measurements were performed in the laboratory of Prof. Dr. Yana Vaynzof's group. Chromium (5 nm) and gold (50 nm) were deposited on solvent-cleaned silicon substrates with native oxide (cleaning, see Device Fabrication). Films of ttmgb (toluene, 2.0 g L^{-1}, 800 rpm, 60 s), ttmgb(PF$_6$)$_2$ (acetonitrile, 4.0 g L^{-1}, 800 rpm, 60 s) were spin-coat in dry nitrogen. (6,5) SWCNTs (3.6 µg mL^{-1} in toluene) were deposited using an Aerosol Jet 200 printer (Optomec Inc.) Samples were then transferred to an ultrahigh vacuum chamber (ESCALAB 250Xi) without exposure to air. Measurements were conducted with a Helium I photon line ($h\nu = 21.22$ eV) of a double-differentially pumped Helium discharge lamp (analyzer pass energy of 2 eV).

3.4.5 Kelvin Probe Measurements

All work function (WF) measurements were performed by Dr. Eric Sauter (Prof. Dr. Zharnikov's group) with a Kelvin Probe 2001 system (KP technology Ltd., UK) in ultrahigh vacuum (10^{-8} mbar). Freshly sputtered gold and self-assembled monolayers of 1-hexadecanethiol served as references.

3.4.6 Profilometry

Polymer and hafnium oxide film thicknesses were measured by surface profilometry (DektakXT Stylus Profiler, Bruker Corp.). Polymer films were spin-coated on glass substrates as described (see section 3.3.3) and then scratched several times with a razor blade. Measurements were performed across resulting grooves, thicknesses were averaged from at least five measurements. Hafnium oxide layer thicknesses were determined after lift-off in NMP on photolithographically patterned Si/SiO$_2$ substrates in analogous fashion.

3.4.7 Atomic Force Microscopy

Atomic force microscopy (AFM) images (5×5 µm^2 area, 1024 lines) were recorded under ambient conditions using a Bruker Dimension Icon Atomic Force Microscope and Bruker Scanasyst$^®$ or TESPA-V2 tips (Scanasyst$^®$ or tapping mode in air). The collected AFM images were processed with the open-source software Gwyddion 2.45 (background correction, z-line leveling, line error correction).

3.4.8 Electrical Characterization

Output and Transfer Characteristics

All transfer and output characteristics were recorded in dry nitrogen (unless otherwise indicated) using an Agilent 4155C semiconductor parameter analyzer. Inverters were measured on interconnected p- and n-type transistors with equal channel length and width (see circuit diagram, Figure 2.9). All measurements for assessment of bias stress stability were performed in ambient conditions.

Capacitances

For SWCNT FETs (on-state reached for $0 < V_g \leq 8.0$ V), capacitances were measured with an impedance spectrometer (ModulLab XM MTS System, Solartron Analytical) directly on the transistor in question by having the shorted source-drain electrodes serve as one capacitor plate and the gate electrode serve as the other. For polymer FETs (on-state reached for $V_g \geq 8.0$ V), capacitance measurements were performed using an Agilent E4980 Precision LCR meter using rectangular capacitor plates of area sizes (0.06, 0.03 and 0.015 cm^2). The measurement frequency employed was 1.0 kHz for both measurement methods (unless otherwise specified) and the maximum capacitance was determined in the on-state.

Mobility and Contact Resistance

Field-effect mobilities were calculated according to Equ. 2.10 for the linear regime and 2.11 for the saturation regime (see section 2) using forward sweeps (from off to on). Gated four-point-probe measurements were employed to determine contact resistances and the charge carrier mobility corrected for contact resistance (see Equ. 2.16 – 2.19 in section 2.4.2, for geometry, see Figure 3.5).

Chapter 4

PHENANTHROLINE ADDITIVES FOR ENHANCED STABILITY OF POLYMER-WRAPPED SWCNT DISPERSIONS

This chapter introduces a simple method to slow down aggregation in SWCNT dispersions and reproducibly improve device performance homogeneity in SWCNT network field-effect transistors.

The results described in this chapter were partially published in Schneider *et al. ACS Appl. Nano Mater.* **2020**, *3*, 12314 – 12324.[276] All figures within this chapter were adapted with permission from the American Chemical Society.

4.1 Introduction

Inks of semiconducting SWCNTs (for details on dispersion and purification methods, see section 2.1.3) selected by polymer-wrapping in organic solvents such as toluene have been produced with purity levels sufficient for reproducibly high on/off-current ratios that are mandatory for electronic applications on a large scale.[39,174,176] One of the main roadblocks in their path to commercial success, however, is their high tendency to aggregate in dispersion over time. For a description of the various optical techniques to monitor this behavior, the reader is referred to section 2.1.4. These aggregates of varying size lead to processing problems and device malfunctions, for example, clogged printing nozzles, and inhomogeneities in thin films even to the extent of device failure induced by, *e.g.*, pin holes or hot spots. Electrostatic coupling and charge transport are negatively affected even by the presence of just small SWCNT bundles, which ultimately limits device performance.[42,48] Size and number of nanotube bundles can in fact be managed by elaborate protocols of repeated sonication and centrifugation, however, always at the cost of introducing defects into and shortening the SWCNTs. Post-processing methods such as aggregate removal after deposition can be a valid option but may include additional substrate sonication.[7] Furthermore, inhomogeneities in network density can result in non-uniform effective carrier mobilities and channel resistances in circuits. Whereas it might be possible to control these issues for small-scale device fabrications in the scientific laboratory by exclusively employing freshly prepared dispersions, they are a critical challenge for the large-area processing.

Other commonly used inks, particularly colloid-based ones, for the deposition of, *e.g.*, electrode, dielectric and semiconducting materials are optimized with regard to processability and long-term stability by specific formulations.[277–279] Additives such as small molecules and mixtures of several solvents are frequently employed to fine-tune the morphology of the films for better overall device performance. In principle, an adaptation of this concept to SWCNT inks for large-scale device fabrication with higher reproducibility should be feasible.

Small-diameter (0.757 nm), large-bandgap (1.27 eV) (6,5) SWCNTs dispersed by polymer wrapping with PFO-BPy using shear-force mixing[65] (experimental details, see section 3.2) in toluene were selected as semiconducting material due to their previously demonstrated performance in various optoelectronic devices[29,280] as well as FETs; for the latter that is high charge carrier mobilities and on/off-current ratios.[51,178] Moreover, PFO-BPy also

selectively disperses semiconducting SWCNTs with larger diameters (1.17 – 1.55 nm) frequently used in, *e.g.*, high-mobility FETs,[50,164,281] which enables to test the broader applicability of this concept.

Dispersions with high polymer content benefit from better stability as the polymer increases the dispersion viscosity and slows down diffusion and aggregation. However, fluorene-based wrapping polymers exhibit orders of magnitude lower mobilities than SWCNTs[87,88] and are thus a risk for unwanted detrimental effects on charge transport. Hence, the careful removal of the majority of unbound polymer prior to further processing is considered mandatory for most polymers even though a recent report suggests that this may not be necessary for particular wrapping polymers.[86] These dispersions with low polymer concentrations generally exhibit poor stability with high aggregation tendency. A remedy to somewhat decelerate aggregation in such dispersions can be the use of solvents with higher viscosity.[74,97] Other wrapping polymers can be removed by chemical treatment to yield soluble monomers[85,282,283] or by de-wrapping *via* complex formation with, *e.g.*, ruthenium salts.[89] Yet, none of these approaches for polymer removal have thus far provided a satisfactory solution for the issue of aggregation in large-scale device fabrication. To sum up, there is a strong demand for a facile, inexpensive method with high reliability to increase the stability of SWCNT inks without any detrimental impact on device performance.

In this chapter, the conceptual idea of ink formulation known for other colloids is transferred to dispersions of (6,5) SWCNTs in toluene with low residual wrapping polymer content *via* the application of small-molecule additives, *i.e.*, phenanthrolines. First, the progress in aggregation is monitored using time-dependent UV-vis-NIR absorption spectroscopy. A continuous drop in intensity of the E_{11} transition of the nanotubes over the course of 12 h is established as a key indicator of aggregation. The validity of this parameter is critically reviewed by comparison to the well-known impact of solvent viscosity on dispersion stability. A number of isomers and similar molecules are applied to help elucidate the mechanism of their impact on dispersion stability. Further, photoluminescence spectroscopy is employed to support this discussion and the general applicability of this concept to different nanotube species is tested on SWCNTs with larger diameters. Atomic force microscopy enables an assessment of the impact of the additive on film morphology of dense nanotube networks deposited from inks of increasing age on a larger timescale. Lastly, these films are incorporated into bottom-contact/top-gate FETs. A thorough electrical characterization of these devices is conducted to link the influence of decelerated aggregation in dispersion to changes in morphology and, ultimately, their electrical performance homogeneity.

4.2 Spectroscopic Monitoring of Aggregation

Figure 4.1 provides a general overview of the processing steps involved in this study. Shear-force mixing is a gentle and reproducible method to obtain long SWCNTs (average length ≈ 1.5 µm), which is beneficial for high charge carrier mobilities in nanotube networks.[284,285] For purification, dispersions are then subjected to a centrifugation protocol. The post-centrifugation supernatant rich in PFO-BPy polymer is filtered and the filter residue is washed to remove excess unbound polymer (for experimental details, see section 3.2). Dispersions of (6,5) SWCNTs wrapped by PFO-BPy were prepared by redispersion from filter cakes in toluene or other organic solvents. Employing this process, concentrations of ≈ 15 µg mL^{-1} were obtained, which are necessary for the deposition of dense networks by spin-coating (for experimental details, see 3.3.2). Dispersions with such high SWCNT and relatively low PFO-BPy concentrations (< 30 µg mL^{-1}) are typically prone to display visible signs of aggregation within a few hours of storage time after sonication. It is hence important to keep storage times to a minimum to ensure reproducible device fabrication.
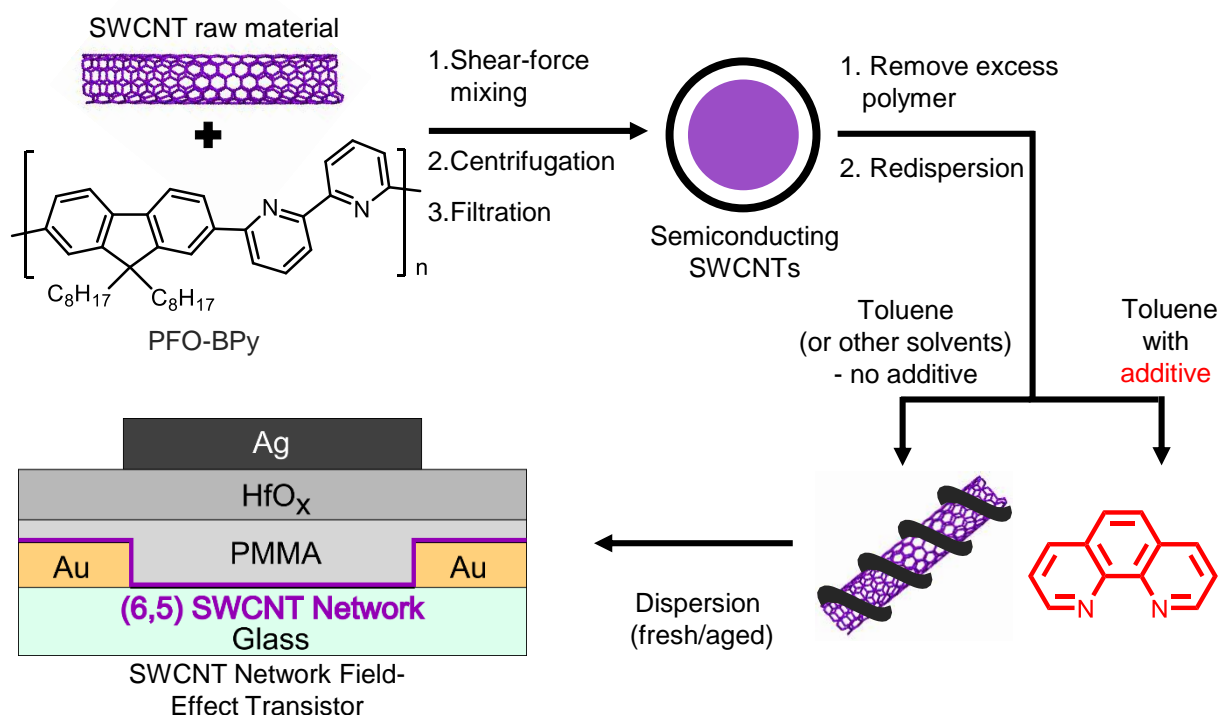
Figure 4.1: Overview of processing steps. Selective dispersion of PFO-BPy-wrapped (6,5) SWCNTs in toluene by shear-force mixing, followed by centrifugation and filtration. Filter cakes are redispersed in toluene (or other solvents) with and without additives (molecular structure: 1,10-phenanthroline). Dispersions are stored for selected amounts of time and then used in the fabrication of bottom-contact/top-gate (6,5) SWCNT network FETs.
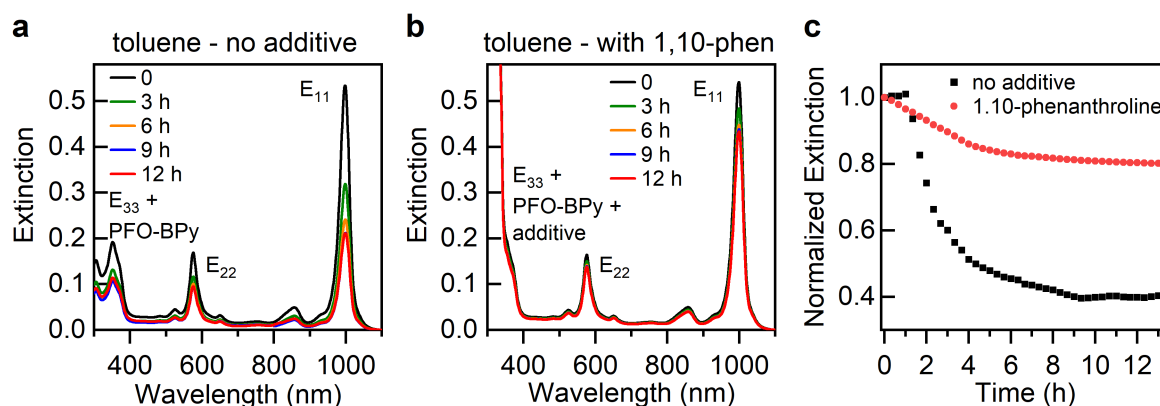
Figure 4.2: Extinction (absorbance and scattering) spectra of (6,5) SWCNT dispersions in toluene (a) without and (b) with additive 1,10-phen measured at different times after ink preparation. (c) Decrease of extinction extracted at the maximum of the E_{11} transition as a function of time after ink preparation; values are normalized to the optical density of the E_{11} at $t = 0$. The decrease in extinction reflects increasing aggregation.

UV-vis-NIR absorption spectroscopy is an effective method to examine aggregation as a function of time in SWCNT dispersions, which was previously shown by Talsma *et al.*: the ink aging can be correlated with decreasing optical density.[97] This observation is demonstrated in Figure 4.2a using a dispersion of (6,5) SWCNTs in toluene with minimized remaining PFO-BPy content. The concentration of the nanotubes is high enough to enable observation of the aggregation process within a reasonable time frame and sufficiently low to ensure linearity of the detector response. During a period of 12 h, the maximum extinction (absorbance and scattering) at the E_{11} transition of the (6,5) SWCNT dispersion decreases continuously. For these repeated collections of absorption spectra without moving the cuvette, the total amount of SWCNTs obviously stays constant. Despite that, the formation of large aggregates results in a noticeable decline in optical density instead of an increasing scattering background, which one might expect. When the cuvette is removed after the experiment, aggregates in the form of a purple cloud of clustered SWCNTs can be perceived visually. The drop in extinction was ascribed to the adsorption of SWCNTs aggregates on the sidewalls of the cuvette, which is most pronounced at the air-liquid interface, and to the sedimentation of larger clusters that moved out of the path of detection.

In contrast to that, upon addition of the *N*-heteropolycycle 1,10-phenanthroline (1,10-phen) to the dispersion before starting the measurement ($c_{1,10\text{-phen}} \approx 0.4 \text{ mg mL}^{-1}$), the decrease in extinction is much weaker (see Figure 4.2b) and there are no visible aggregates (video). The drop in extinction for dispersions without and with 1,10-phen is directly compared in Figure 4.2c. To ensure easy comparability of the values, the data points were normalized to the peak value of the E_{11} optical density at $t = 0$. Figure 4.3a depicts a plot of the extinction normalized to the E_{11} transition for a dispersion without additive. It is

noteworthy that the relative concentration of the PFO-BPy (peak at 355 nm) rises with progressing aggregation time. If one assumes an inhomogeneous coverage of the nanotubes by the wrapping polymer, this would indicate favored aggregation of those SWCNTs with more uncovered surface and hence weaker colloidal stabilization. Interestingly, this effect is also present in the dispersion with 1,10-phen additive (see Figure 4.3b) – although it is much less pronounced and somewhat less clear due to the overlapping strong absorption of the small-molecule additive. Overall, it is apparent that the stability of the dispersion is drastically enhanced by the presence of 1,10-phen.

Next, it was important to establish that the E_{11} extinction decreasing over time as
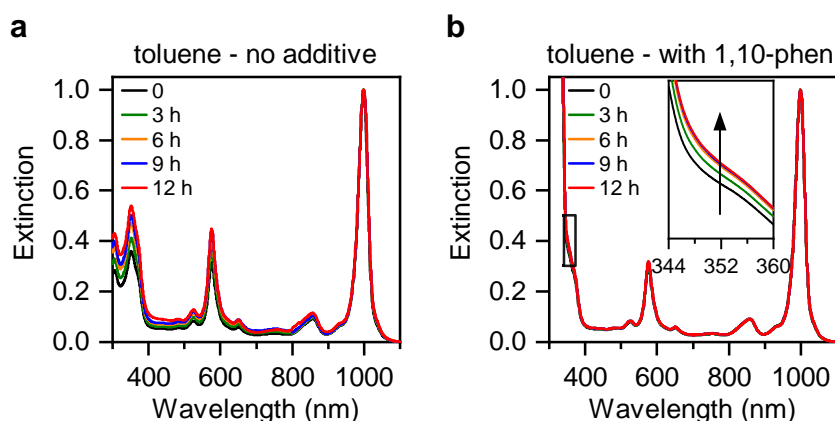
Figure 4.3: Extinction (absorbance and scattering) spectra of (6,5) SWCNT dispersions in toluene (a) without and (b) with additive 1,10-phen measured at different times after ink preparation normalized to the maximum of the E_{11} transition. The inset in (b) displays the relative increase in extinction of the PFO-BPy shoulder with aggregation time. The strongly enhanced signal at shorter wavelengths is attributed to the intense absorption in the UV of the 1,10-phen additive.

determined in the UV-vis-NIR measurements is a valid and reliable metric to quantify the degree of aggregation. For this, SWCNT dispersions in the chemically similar yet compared to toluene higher-viscosity solvents *o*-, *m*-, *p*-xylene and mesitylene were selected. Table 4.1 provides an overview of their viscosities, static dielectric constants and refractive indices. The minor differences in the latter two can be excluded as a source of positive impact on stabilization. Given that the aggregation of SWCNTs is at the least in part a process limited by diffusion, solvents with higher viscosities are expected to slow down aggregation and sedimentation. This is due to the fact that the diffusion constant is reciprocally proportional to the dispersion viscosity.[74,96] As expected, the decrease in maximum extinction at the E_{11} transition with time (see Figure 4.4a) is less pronounced for higher-viscosity solvents.

Table 4.1: Viscosities, static dielectric constants and refractive indices of the employed solvents at 25°C.

Solvent	Viscosity[286] (mPa s)	Dielectric Constant[287] (static)	Refractive Index[288]
toluene	0.556	2.38	1.4944
o-xylene	0.756	2.57	1.5018
m-xylene	0.581	2.35	1.4944
p-xylene	0.611	2.27	1.4929
mesitylene	0.611	2.27	1.4976

The largest impact on stabilization is observed for the solvent with the highest viscosity, *i.e.*, *o*-xylene. The here observed apparent growth in extinction lies within the range of typical experimental error of this method. Note that the not entirely defined dependence of the extinction on the extent of aggregation complicates direct comparisons of different experiments. This effect is most pronounced in the early stages and small discrepancies are not to be misinterpreted. Nonetheless, within the chosen timescales and concentrations, all xylenes and mesitylene result in nanotube dispersions with higher stability compared to those in toluene. Talsma *et al.* made similar observations of such good stabilization for a dispersion of semiconducting SWCNTs dispersed using polydodecylthiophene in *o*-xylene.[97]

To allow for a precise evaluation of peak energy and peak width, the second derivative of the extinction with respect to energy was fitted to the second derivative of a Gaussian according to a method established by Saakov *et al.*[289] The extracted parameters are displayed in Figure 4.4b,c. Most of the small red shift in peak energy that is present for all solvents takes place in the first hours of the experiment. One may speculate that the impact of even loosely clustered nanotubes on their absorption energy is largest in the initial stages of aggregation formation. The red shift caused by the adsorption of the second SWCNT to the first SWCNT is larger than that of the third etc. Unfortunately, there are no apparent trends that could be correlated with solvent properties and ultimately aggregation tendencies. Evidently, there is very little change (tenths of meV) in the peak width of the investigated E_{11} transition of the (6,5) SWCNTs during the 12 h-period of the experiment.

Even though the difference in dispersion stability can indeed be attributed to the variation in viscosity of the employed solvents, the low amounts of a small-molecule additive like phenanthroline ($< 1\,\mathrm{mg\,mL^{-1}}$) to toluene are considered too low to impact the dispersion viscosity[290] - such an increase in viscosity has only been demonstrated for the addition of polymers.[74] Hence, a different mechanism is expected here.
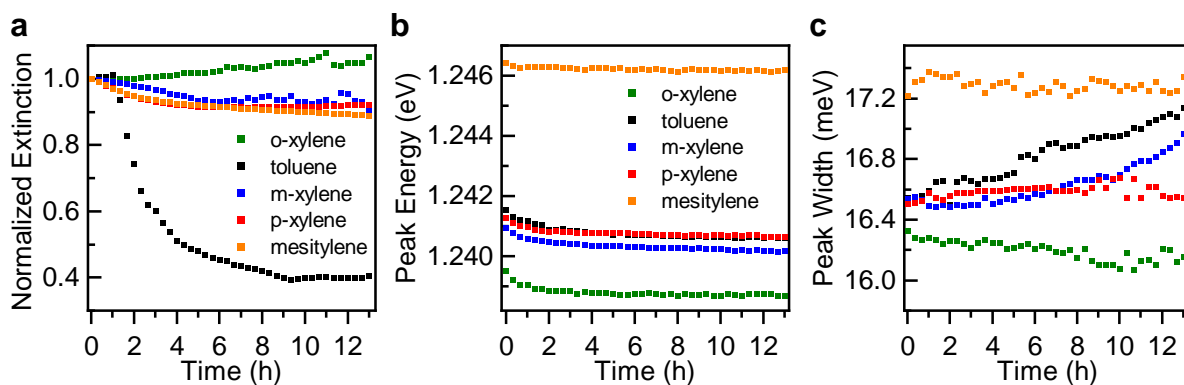
Figure 4.4: (a) Decrease of extinction extracted at the maximum of the E_{11} transition for various solvents as a function of time after ink preparation; values are normalized to the optical density of the E_{11} at $t = 0$. (b) Peak energy and (c) full-width at half maximum of (6,5) SWCNT absorption peak corresponding to the E_{11} transition as a function of time after ink preparation.

It has been documented that polycyclic aromatic hydrocarbons (PAHs), *e.g.*, anthracene, phenanthrene or perylene as well as *N*-heteropolycycles like diazapentacene adsorb onto bare surfaces of SWCNTs. This adsorption process depends on both the structure of the polycyclic aromatic compounds and the curvature of the nanotubes.[291–293] These PAHs have been shown to serve as dispersants for SWCNTs in certain organic solvents, *e.g.*, chloroform, tetrahydrofuran or toluene, albeit with rather smaller SWCNT concentrations than in other dispersions.[294–297] The assumption that some SWCNT surface remains uncovered by PFO-BPy in dispersion with direct exposure to the solvent toluene (as much as 90 percent for SWCNTs wrapped by polyfluorene)[297] appears reasonable. They can hence serve as a potential adsorption site for small-molecule additives such as 1,10-phen facilitated by π-π-interactions. Additionally, thermodynamics favors such adsorption given the much larger concentration of 1,10-phen ($0.4\ \mathrm{mg\,mL^{-1}}$) in comparison to the available surface of the SWCNTs ($\approx 14.5\ \mathrm{\mu g\,mL^{-1}}$). It can be hypothesized that the adsorbed molecules screen attractive van der Waals forces that occur between nanotubes at small distances. In this way, aggregation is potentially inhibited.

The affinity of PAHs to nanotubes depends on their molecular structure as has been demonstrated by previous reports. Tetracene, for example, binds more strongly to the nanotube than phenanthrene.[293] Unfortunately, such comparative studies for the adsorption of *N*-heteropolycycles are unavailable. Therefore, the isosteric nitrogen-free phenanthrene, 1,7- and 4,7-phenanthroline isomers were chosen as further stabilizing additives for (6,5) SWCNT dispersions in toluene while the monohydrate of 1,10-phen served as a reference for a potential effect of the hygroscopy of 1,10-phen. Their normalized extinction as a function of time is depicted in Figure 4.5a; the corresponding molecular structures are shown in Figure 4.5b. All investigated phenanthroline isomers (including the monohydrate)
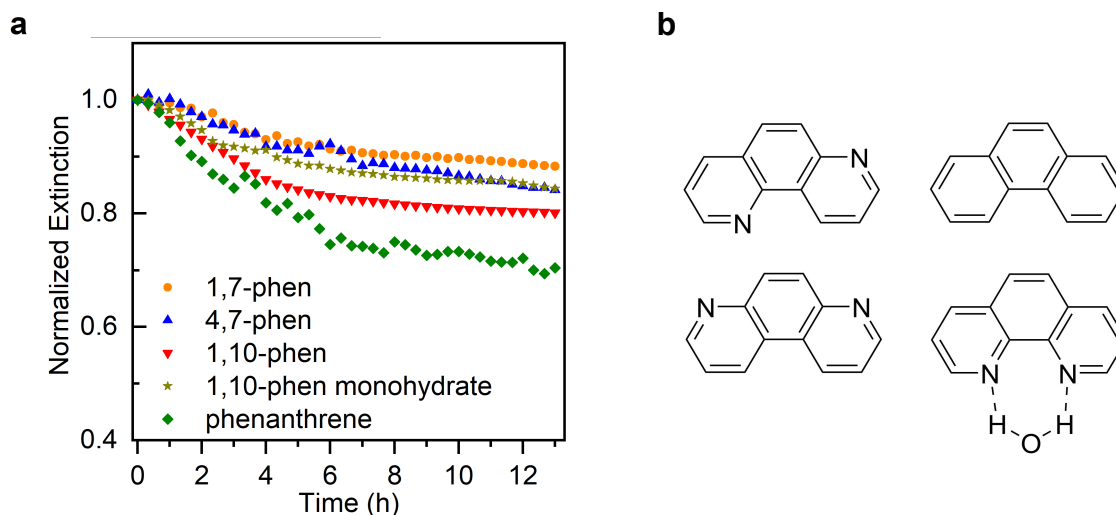
Figure 4.5: (a) Decrease of extinction extracted at the maximum of the E_{11} transition for various additives as a function of time after ink preparation; values are normalized to the optical density of the E_{11} at $t = 0$. (c) In anticlockwise order: molecular structures of 1,7-phenanthroline, 4,7-phenanthroline, 1,10-phen monohydrate and phenanthrene.

displayed similar behavior while the phenanthrene exhibited a more limited impact on dispersion stability. The observed small red shift of E_{11} peak energy in the first few hours of the experiment as well as the general lack of a trend in the peak width is in agreement with the observations made for the different solvents (see Figure 4.6a,b). The overall drop in the E_{11}-to-E_{22} peak intensity ratio (see Figure 4.6c), found for the dispersion with phenanthrene and even more so for the one without additive, can be interpreted as an additional sign for aggregation. It is attributed to the larger impact of the change in dielectric environment on the E_{11} than E_{22} transition.[298,299] In general, dispersion stability seems to benefit from the presence of nitrogen within the aromatic core of these molecules. This is also reflected in a frequently occurring structural motif of efficient dispersants for carbon nanotubes such as flavins and nucleobases.[68,300,301]

Interestingly, the strong stabilizing effect caused by the 1,10-phen monohydrate helps exclude another possible mechanism. It is a well-known, albeit not very carefully recorded behavior of polymer-wrapped SWCNT dispersions in organic solvents, that humidity negatively affects their aggregation behavior. In high-humidity conditions this can lead to problems during processing.[302] One might hypothesize that an additive could act as a water scavenger and stabilize the dispersion. For that matter, 1,10-phen is hygroscopic and could thus desiccate the dispersion solvent. This notion is in conflict with the observations made in the experiments using the non-hygroscopic monohydrate as it displays results similar to the anhydrous analog. Moreover, Karl-Fischer titration experiments yielded no evidence for any water scavenging impact by 1,10-phen. It can hence be excluded that changes in moisture content of the solvent are a significant contributor to the observed
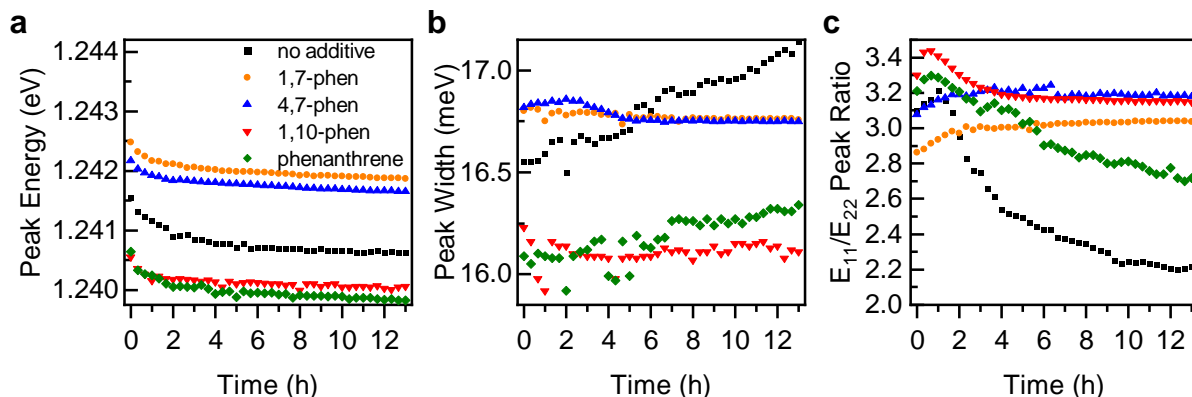
Figure 4.6: (a) Peak energy and (b) full-width at half maximum of (6,5) SWCNT absorption peak corresponding to the E_{11} transition as a function of time after ink preparation. (c) E_{11}/E_{22} absorption peak ratio as a function of time after ink preparation.

stabilizing effect.

Photoluminescence (PL) spectroscopy is another technique that is frequently employed for quality assessment of SWCNT dispersions. Generally, PL exhibits an even higher sensitivity to changes in the immediate nanotube environment compared to absorption. Additionally, nanotubes of varying diameters enable the observation of cross peaks and inter-tube energy transfer in photoluminescence-excitation maps. Alternatively, variance spectroscopy allows for quantitative monitoring of the formation of aggregates and clusters (see section 2.1.4).[106,303] Unfortunately, these methods to observe the formation of aggregates are unsuitable for the polymer-wrapped, monochiral (6,5) SWCNT dispersions investigated here. Instead, PL intensity as well as the wavelength and the width of the emission peaks were monitored as potential metrics for the interaction of nanotubes with the small-molecule additives and their impact on aggregation. Surprisingly, the presence of the additive did not affect the emission, *i.e.*, both the E_{11} peak position and the linewidth remained virtually identical (see Figure 4.7a).

If the stabilizing additive in fact adsorbs onto the surface of the SWCNT, it apparently has little impact on the emission properties of the nanotube. In analogy to the extinction in UV-vis-NIR absorption spectroscopy, the PL intensity of the (6,5) SWCNT dispersion without additive decreased drastically within just 3 h (see Figure 4.7b). In contrast to that, with 1,10-phen additive the PL intensity of the dispersion stayed almost constant (Figure 4.7c). The absence of any PL quenching or trion emission, that might have been caused by the additive, renders doping of the nanotubes unlikely.[161] If optically excited 1,10-phen was present close to the SWCNT, one would anticipate energy transfer. However, PL quenching of 1,10-phen by adding nanotube dispersion could not be measured as both the wrapping polymer PFO-BPy and toluene exhibit emission features at similar wavelengths as 1,10-phen. Unfortunately, demonstrating a potential energy transfer from
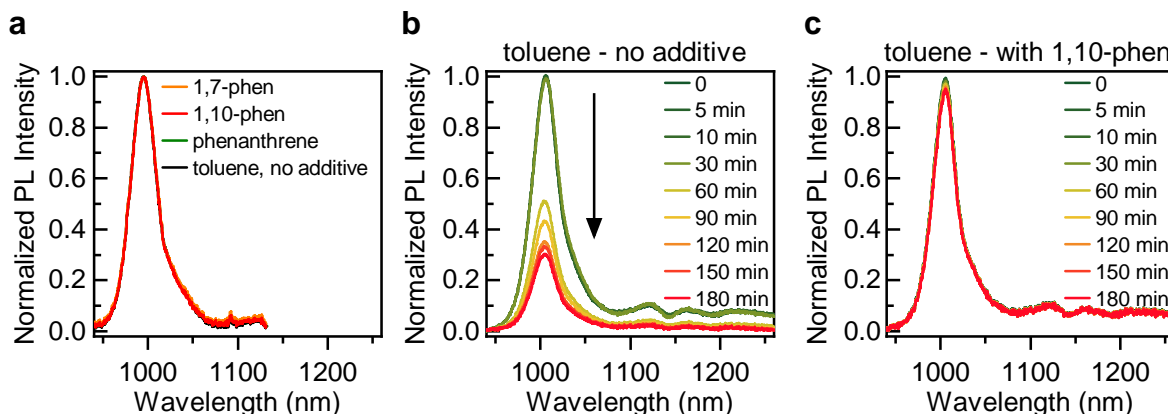
Figure 4.7: (a) PL spectra with baseline correction normalized to the maximum intensity at the E_{11} transition of the (6,5) SWCNT dispersions ($OD(E_{11}) = 0.01$) with and without additives 1,7-phen, 1,10-phen and phenanthrene. (b) PL spectra of (6,5) SWCNT dispersions in toluene (b) without and (c) with additive 1,10-phen measured at different times after ink preparation normalized to the maximum of the E_{11} transition.

the phenanthroline additive to the (6,5) SWCNT is of similar difficulty due to absorption features in the same spectral range of the wrapping polymer and the (6,5) nanotubes, *i.e.*, the E_{33} transition. Consequently, PL spectroscopy is unable to deliver more evidence that the molecular additives adsorb onto the exposed surface of the nanotubes.

With the goal to improve the stability of nanotube dispersions for their use as inks in the fabrication of network FETs, the impact of the 1,10-phen additive on the more commonly used[164,188,304] larger-diameter SWCNTs (1.17 – 1.55 nm) was tested. These tubes are also accessible by polymer wrapping with PFO-BPy and nanotubes from plasma torch synthesis. Dispersions with longer shelf lives of these nanotubes are of major interest for commercial applications as they have been shown to display higher charge carrier mobilities in FETs than the larger-bandgap (6,5) SWCNTs.[50,176] Indeed, the addition of 1,10-phen appears to decelerate the aggregation in dispersions of such large diameter SWCNTs – albeit to a weaker extent compared to the smaller-diameter (6,5) SWCNTs (see Figure 4.8). Unfortunately, most of the PL wavelengths of these plasma torch nanotubes lie outside of the window of detection of commonly available InGaAs detectors. PL spectroscopy could thus not be employed to gain further insight.

As the binding affinity of PAHs is also a function of the relationship between molecular structure and curvature of the nanotubes,[291–293] it can be assumed that another stabilizer might be a better fit for larger-diameter SWCNTs. Yet overall, the concept of small molecular additives appears to be not limited to (6,5) SWCNTs and also easy to apply to the more popular plasma torch nanotubes. With the help of the demonstrated time-dependent UV-vis-NIR absorption experiments, a screening for an additive with optimized stabilizing properties seems to be within immediate reach.
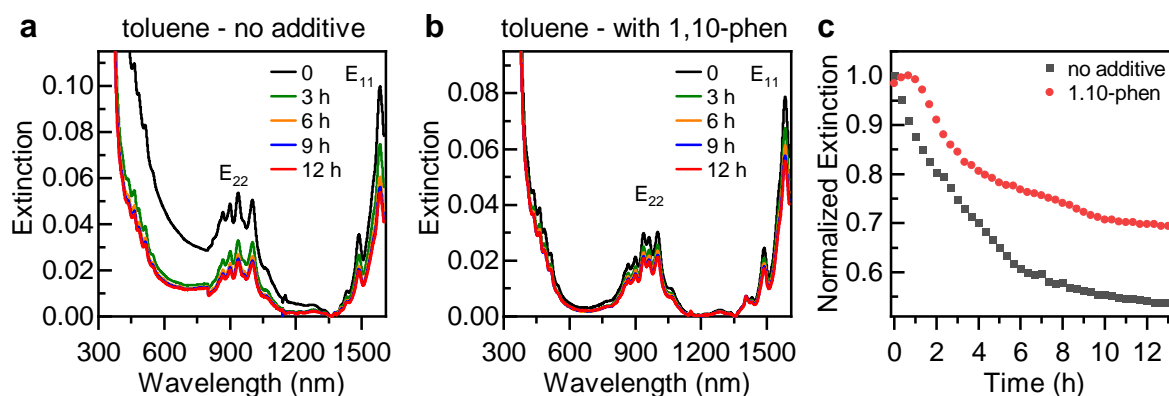
Figure 4.8: Extinction (absorbance and scattering) spectra of large-diameter SWCNT dispersions in toluene (a) without and (b) with additive 1,10-phen measured at different times after ink preparation. (c) Decrease of extinction extracted at the maximum of the E_{11} transition as a function of time after ink preparation; values are normalized to the optical density of the E_{11} at $t = 0$. The decrease in extinction reflects increasing aggregation, more strongly so for the dispersion without additive.

4.3 Thin-Film Morphology

Although spectroscopic insight is generally advantageous for a quick evaluation of the quality of a dispersion, the key factor of interest that governs the final performance in the transistor is the nanotube network morphology. These films are deposited by spin-coating inks at much higher SWCNT concentrations and longer ink aging times become relevant for optimizing the ink formulation. In this study, the low-viscosity, commonly used toluene was selected to demonstrate the stabilizing effect of the additive 1,10-phen. The high-viscosity *o*-xylene was chosen as a supplementary reference as its advantageous impact on dispersion stability and film morphology have been shown in literature and it is more environmentally friendly.[97]

Nanotube networks were spin-coated from (6,5) SWCNT dispersions with relatively high concentrations (approximately 14.5 µg mL^{-1}) and the outlined solvent/additive combinations. Atomic force microscopy (AFM) served as a tool to assess their density and morphology. Conveniently, the use of 1,10-phen does not lead to extra processing steps given that residual additive is rinsed off by good solvents during a routine cleaning step that follows the SWCNT deposition (see section 3.3.2). Note that trace amounts of additive might still be adsorbed on the surface of the nanotubes, which cannot be excluded by AFM analysis.

In this section, two batches of nanotube films produced from extended ink aging times are compared. Batch A features nanotube networks deposited at $t_A = 0$, 1, 24 and 96 h, batch B includes films from inks aged $t_B = 0$, 1 and 7 days. Representative atomic force micrographs from batch A are depicted in Figure 4.9 corresponding to the ink aging times t_A (increasing from left to right). Networks deposited from dispersions in
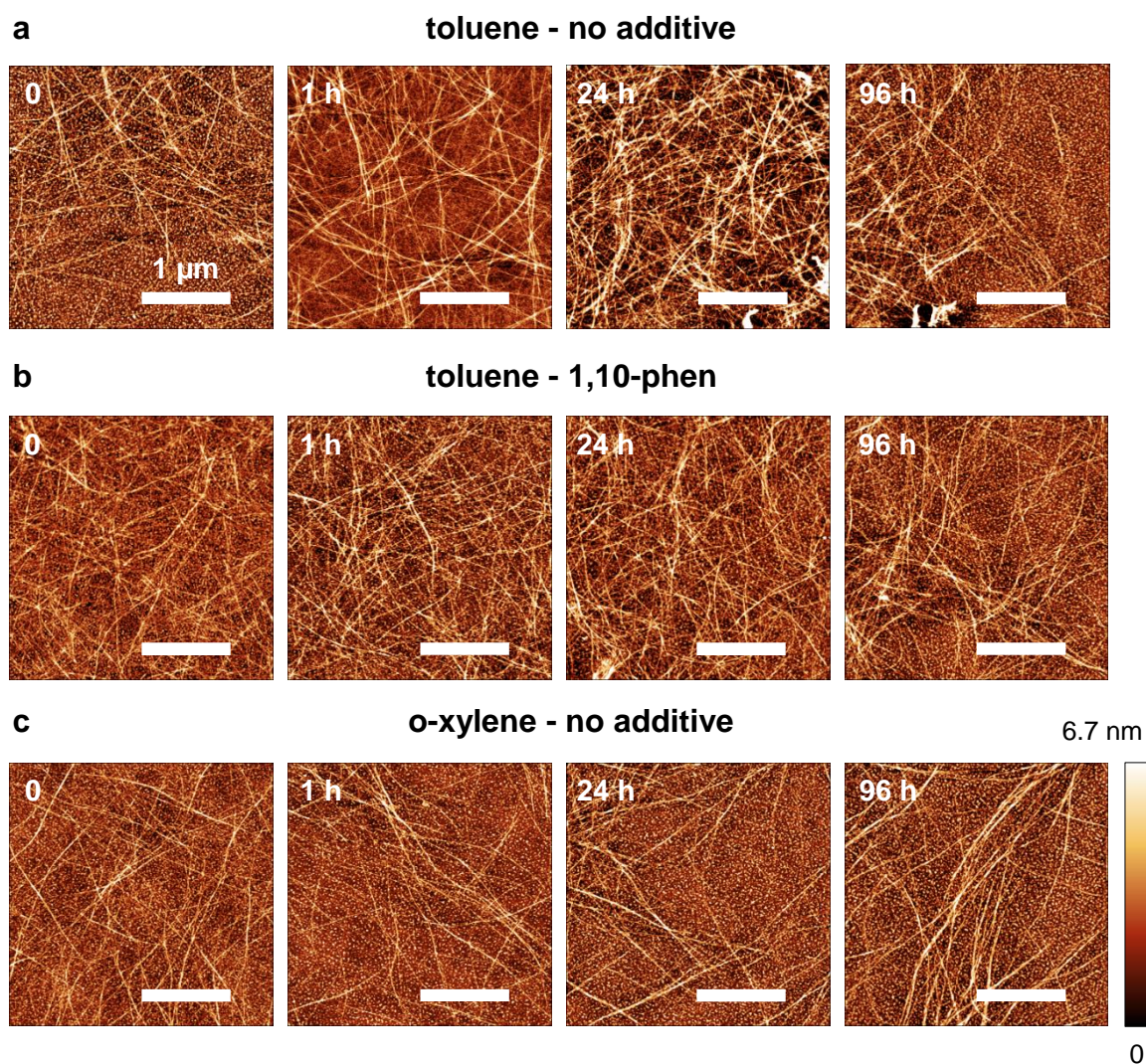
Figure 4.9: AFM images (3.0×3.0 µm², scale bars 1.0 µm) of (6,5) SWCNT networks deposited from inks stored for 0, 1, 24 and 96 h (batch A) with the following solvents: (a) toluene without additive, (b) toluene with 1,10-phen additive and (c) *o*-xylene without additive.

toluene without any additive (see Figure 4.9a) result in dense and relatively homogeneous networks at $t = 0$. After 1 h of ink aging time, some bundles start to appear, their number increases drastically for the network deposited from the one-day-old ink. At an ink age of 96 h, major inhomogeneities in the SWCNT film can be observed with a much higher density of nanotubes on the left side of the micrograph with some bundles and very few tubes on the right (Figure 4.9a, right image). In contrast to that, deposition of networks from the dispersion in toluene with 1,10-phen additive (see Figure 4.9b) not only yields dense and homogeneous nanotube networks for fresh but also aged inks, even though a small number of bundles appears in the network deposited after 96 h of ink aging time. While at $t = 0$ the network spin-coated from the dispersion in *o*-xylene (Figure 4.9c) displays similarly high density and homogeneity as the two toluene-based inks, the number of bundles in the network appears to increase with ink age. After 96 h of ink aging, several thick nanotube bundles are visible. This observation is somewhat surprising given the high stability of the dispersions in *o*-xylene determined by absorption spectroscopy - albeit at much lower SWCNT concentrations and on a shorter timescale.

These general trends are reproduced well in batch B with longer ink aging times. The network produced from a fresh (at $t = 0$) ink in toluene without additive displays a high density and homogeneity (Figure 4.10a) while some inhomogeneities appear after 1 day of ink aging. After 7 days of dispersion storage, a clearly lower mean network density can be observed with some thick bundles present (Figure 4.10a, right image, towards right edge). In stark contrast to that, using the 1,10-phen additive, even after one week of aging time, leads to highly homogeneous and dense SWCNT networks (see Figure 4.10b). The samples produced from *o*-xylene (see Figure 4.10c) in batch B also corroborate the observations from batch A and a general trend similar to the toluene-based ink without additive becomes apparent. The undesirable inhomogeneities in network density, while virtually absent for fresh inks, are clearly visible after one day of ink storage and become even more distinct for longer aging times (here: 1 week).
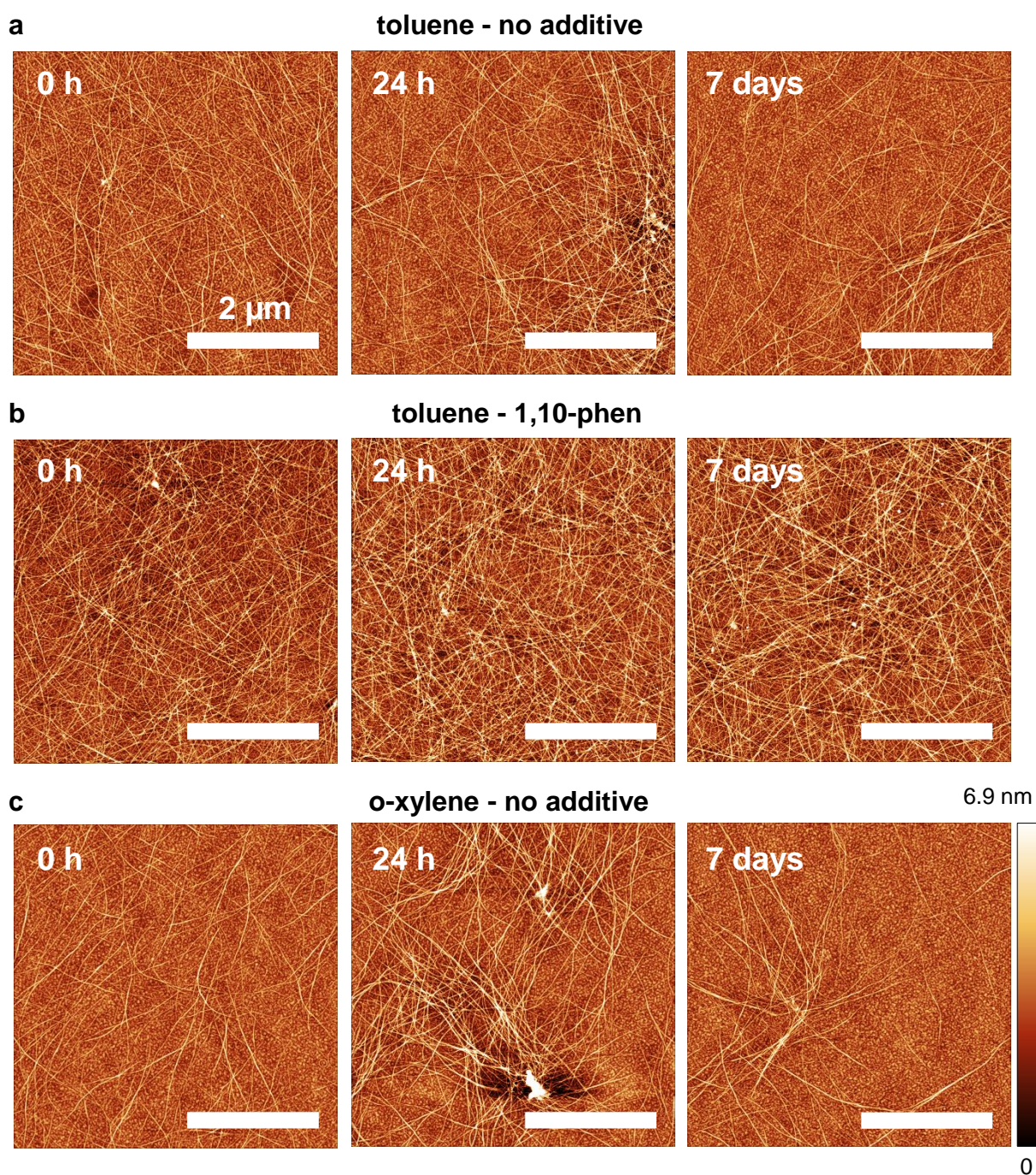
Figure 4.10: AFM images (5.0×5.0 µm^2, scale bars 2.0 µm) of (6,5) SWCNT networks deposited from inks stored for 0, 1, and 7 days (batch B) with the following solvents: (a) toluene without additive, (b) toluene with 1,10-phen additive and (c) *o*-xylene without additive.

4.4 Device Performance

Inhomogeneities such as those in the previous section are known to lead to deterioration of device performance in nanotube FETs,[42,48] transistors fabricated from inks with longer storage times can be anticipated to reflect this negative effect. The (6,5) SWCNT networks (batch A and B) introduced above were hence incorporated into bottom-contact/top-gate FETs (device stack, see Figure 4.1) to conduct an in-depth investigation. The chosen hybrid dielectric of PMMA and HfO_x enables low-voltage, air-stable operation of the transistor while minimizing the number of interfacial trap states by utilizing the benefits of low- and high-k insulators.The output characteristics extracted for all FETs ($L = 40$ µm, $W = 5$ mm, device fabrication, see section 3.3) at $t = 0$ (see Figure 4.11) display good injection with near-ohmic contacts and show decent saturation at high drain voltages for both carriers. Figure 4.12 depicts transfer characteristics of batch A in the linear regime ($V_d = 0.1$ V) for several FETs. These transistors exhibit ambipolar charge transport with well-balanced currents for both carriers. The off-currents are mostly determined by the gate leakage ($\approx 10^{-10}$ A).

Transistors with nanotube networks spin-coated from the fresh, additive-free toluene ink (blue, Figure 4.12a, left) exhibit large on-currents with small device-to-device variation and little hysteresis. After one hour of ink storage, there is hardly any perceivable change in performance (Figure 4.12a, second plot). In contrast to that, using the one-day old dispersion, the on-currents decreased slightly and exhibited a considerably larger device-to-device variation (Figure 4.12a, third plot). After four days of ink aging, on-currents dropped even further while the spread in performance remains approximately constant (Figure 4.12a, right). This overall decline in device performance is in good agreement with the increasing number of bundles and inhomogeneities observed in the nanotube network atomic force micrographs (see Figure 4.9).

Compared to the devices using additive-free dispersions, those made from freshly prepared dispersions in toluene with 1,10-phen additive displayed similar behavior, even with some improvements, *i.e.*, less hysteresis, slightly higher on-currents and less device-to-device variation to the end (red, Figure 4.12b, left). It can be concluded that either the stabilizing additive is removed entirely during the subsequent rinsing step or that potentially remaining 1,10-phen adsorbed onto the SWCNT surface does not impact transport of either charge carrier adversely. Most remarkably, there is hardly any deterioration in performance visible for devices made from inks stored for up to four days (Figure 4.12b, 3 right plots): the constant device-to-device performance spread is an obvious improvement compared to the FETs made from additive-free inks.

Transistors produced with fresh *o*-xylene dispersions (green, Figure 4.12c, left) exhibited on-currents very similar to those fabricated from toluene inks, even though with somewhat
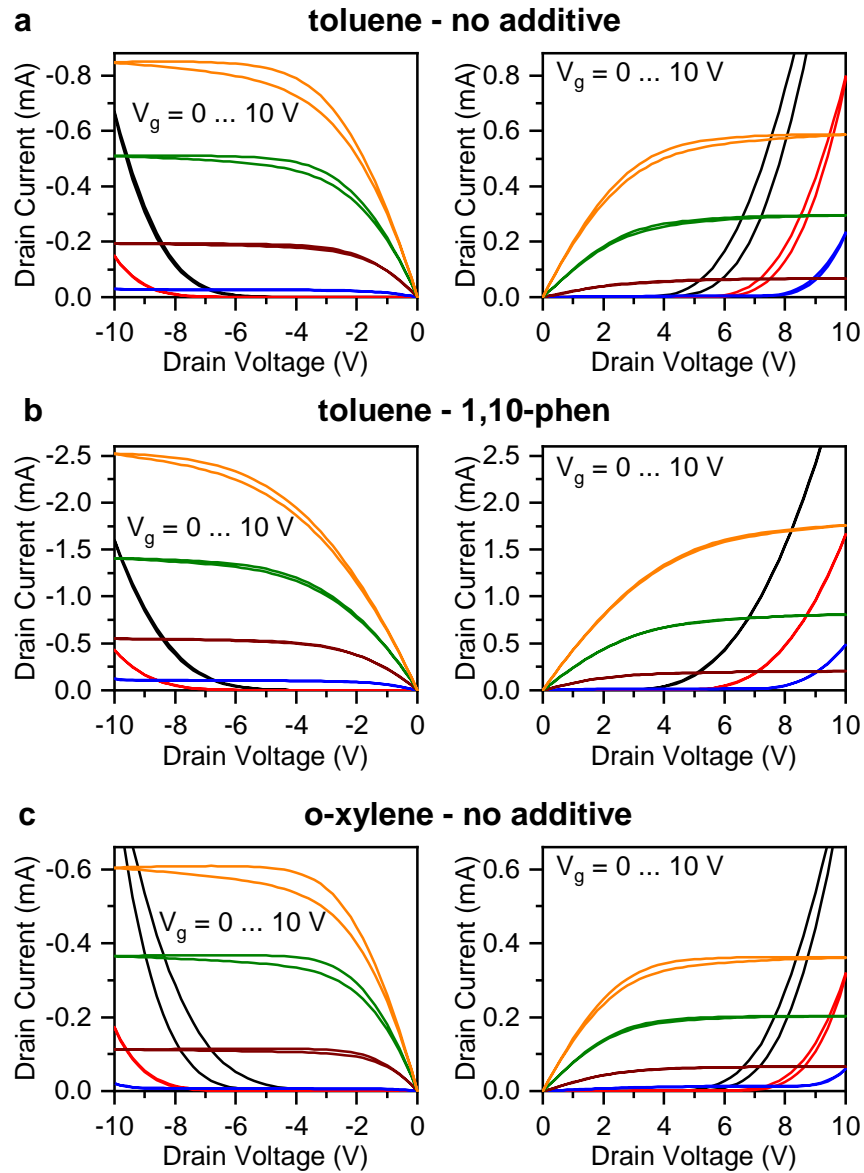
Figure 4.11: Representative output characteristics (holes left, electrons right) of (6,5) SWCNT network FETs ($L = 40$ µm, $W = 5$ mm) prepared with fresh dispersions ($t = 0$) with the following solvents:(a) toluene without additive, (b) toluene with 1,10-phen additive and (c) *o*-xylene without additive.
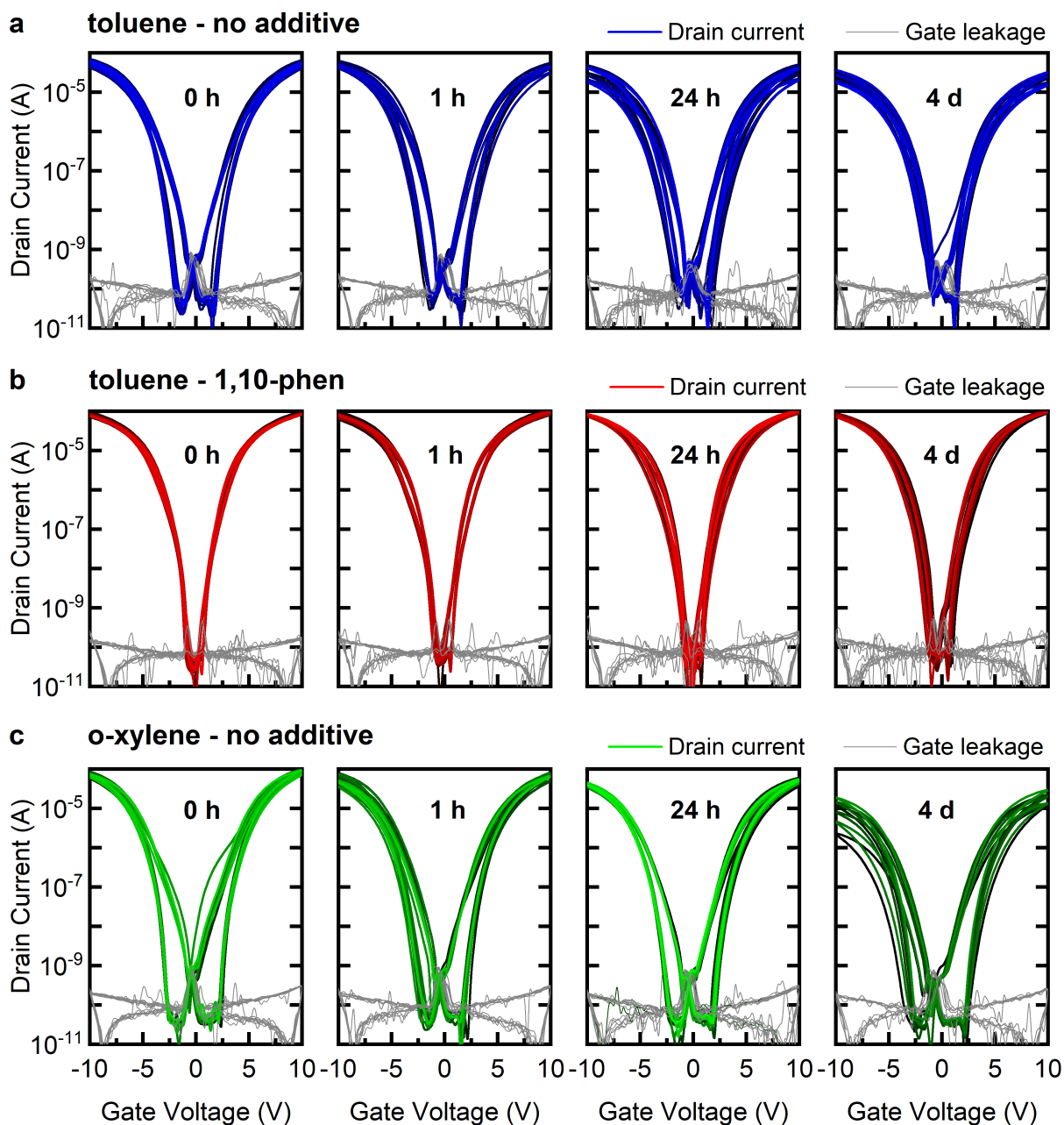
Figure 4.12: Transfer characteristics of (6,5) SWCNT network FETs ($L = 40\,\mu m$, $W = 5\,mm$) measured in the linear regime ($V_d = 0.1$ V). Deposition of the networks was performed from inks stored for 0, 1, 24 and 96 h (batch A) with the following solvents: (a) toluene without additive, (b) toluene with 1,10-phen additive and (c) o-xylene without additive. Drain currents are represented by thick lines; gate leakage currents by thin gray lines.

larger hysteresis. With longer storage time of the dispersions, the on-currents gradually decreased for both holes and electrons while the spread in device performance increased. This is most pronounced at $t = 4$ d. These observations again are in excellent agreement with the corresponding AFM images (see Figure 4.9). The larger hysteresis may be attributed to the smaller nanotube density apparent in these networks. The increased area that remains uncovered by nanotubes enables the adsorption of polar species that serve as potential trap sites.[305]

In order to ensure that these results were reliable and reproducible, a second batch (batch B) of transistors was fabricated incorporating the films described in the previous section. A longer maximum aging time was chosen to explore the limits of stability provided by the phenanthroline additive. The moderately larger current hysteresis compared to batch A as observed in the transfer characteristics for all fresh inks is within the range of typical batch-to-batch variations (see Figure 4.13, first column). The changes that became apparent after one day of ink storage corroborated the behavior observed for batch A, even though the increase of the spread in device performance is somewhat more pronounced for the networks deposited from the toluene dispersion without any additive (see Figure 4.13 a, second column). The trend of decreasing on-currents and increasing device-to-device variation continues for all employed inks (see Figure 4.13, third column) although this effect is most pronounced for the additive-free dispersion in toluene and weakest for the dispersion with 1,10-phen.

In general, this batch reproduces the observations made for batch A with regard to the trends of on-currents and device-to-device variation with ink age for all inks employed (see Figure 4.12). Again, there is an overall good agreement with the atomic force micrographs of the SWCNT networks used in these FETs.

Next, to allow for an in-depth analysis of the transistor performance, charge carrier mobilities were calculated according to Equ. 2.10 (see section 2.3.1). Capacitances were determined by averaging measurements from at least five FETs per substrate (for details, see section 3.4.8) as this parameter not only depends on the dielectric but is also a function of the SWCNT network density.[32,35] The extracted values are depicted in Figure 4.14 for both batches. Note that for batch A $t = 0$ has been adjusted to $t = 0.1$ h to enable a logarithmic display of the timescale. While for batch A the capacitance values measured on the transistors with the films made from the additive-containing toluene ink remained virtually constant with age, capacitances of both inks without stabilizer continuously decreased (see Figure 4.14a). In general, lower capacitances are expected for decreasing surface coverage and thus network density as well as an increasing number of bundles.[32,34] These values are presumably somewhat more representative of the average nanotube network density than the relatively small 3×3 µm^2 (5×5 µm^2) atomic force micrographs. The observations made for batch A are hence in excellent agreement with expectations.
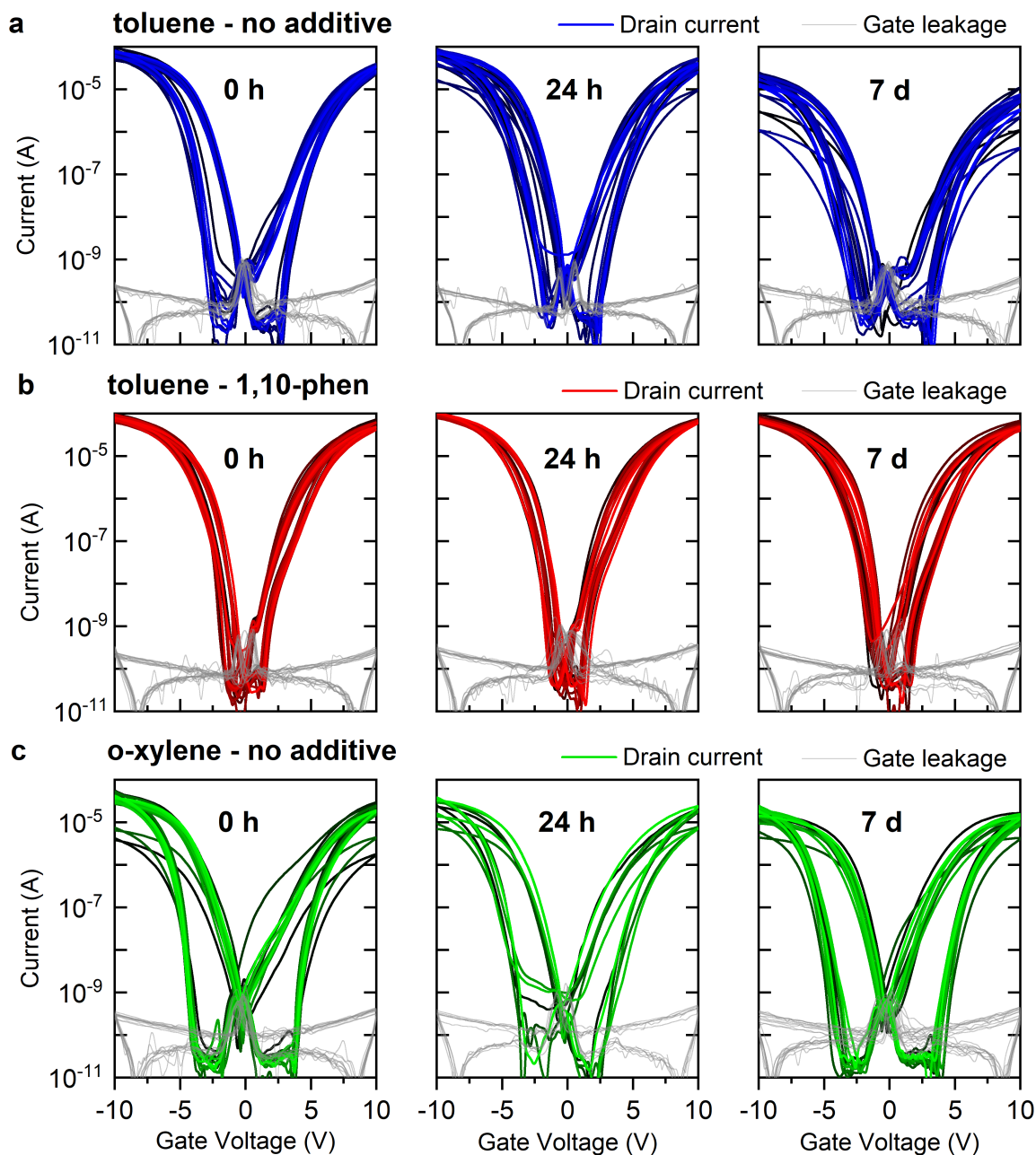
Figure 4.13: Transfer characteristics of (6,5) SWCNT network FETs ($L = 40$ µm, $W = 5$ mm) measured in the linear regime ($V_d = 0.1$ V). Deposition of the networks was performed from inks stored for 0, 1, and 7 days (batch B) with the following solvents: (a) toluene without additive, (b) toluene with 1,10-phen additive and (c) *o*-xylene without additive. Drain currents are represented by thick lines; gate leakage currents by thin gray lines.

For batch B, however, this does not appear to be the case. Here, the capacitance values of the devices produced from both toluene dispersions – with and without additive – remain constant while there is a drop for the transistors made from the *o*-xylene ink (see Figure 4.14b). Given this discrepancy, the incidental correlation should not be over-interpreted.
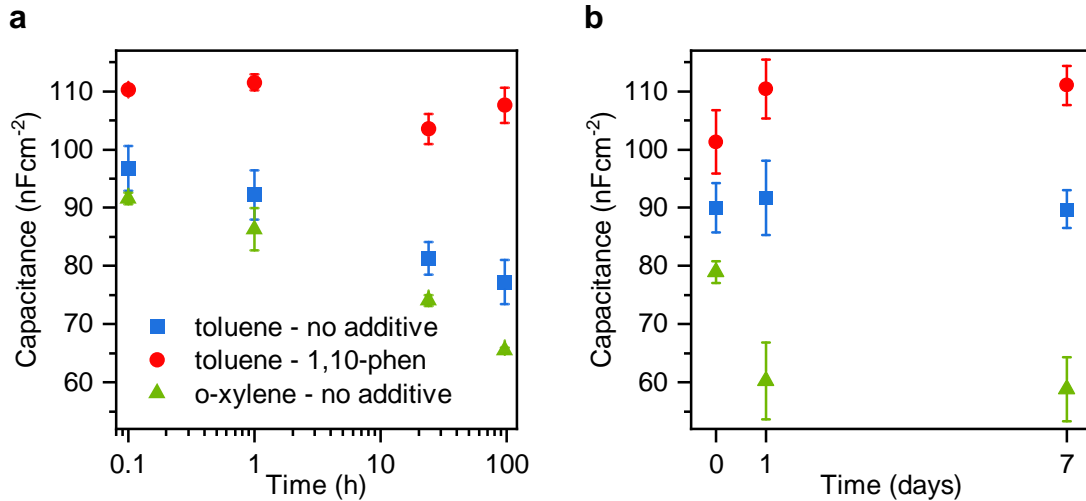
Figure 4.14: Areal capacitances measured directly on at least 5 transistors per sample as a function of ink storage time for (a) batch A and (b) batch B. $t = 0$ is changed to 0.1 h to permit the logarithmic scale on the x-axis. Error bars reflect the standard deviation.

Figure 4.15 displays a representative plot of the mobility for both charge carriers as a function of gate voltage in the linear regime. Values were extracted at the respective
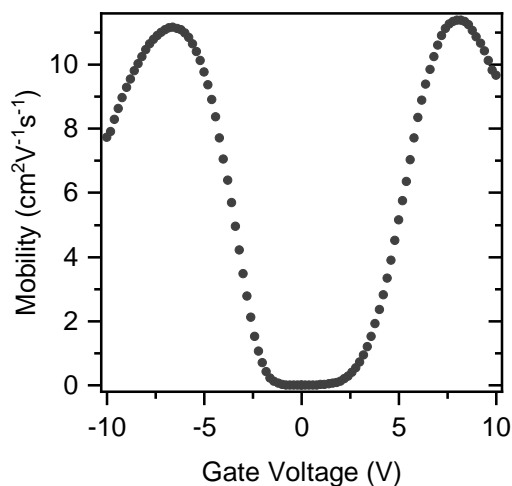
Figure 4.15: Representative charge carrier mobility extracted from FETs ($L = 40$ µm, $W = 5$ mm) for both holes and electrons as a function of gate voltage. Mobilities are obtained at the maximum values. In SWCNTs, they are caused by filling of the first van Hove singularity and are not related to contact resistance.

maxima for each carrier. The occurrence of these maxima is related to the filling of the first van Hove singularity that are characteristic for 1D-semiconductors such as SWCNTs and not related to contact resistance.[28]

The extracted mobilities for both charge carriers for batch A are summarized in the box plot shown in Figure 4.16. In agreement with the observations based on the transfer
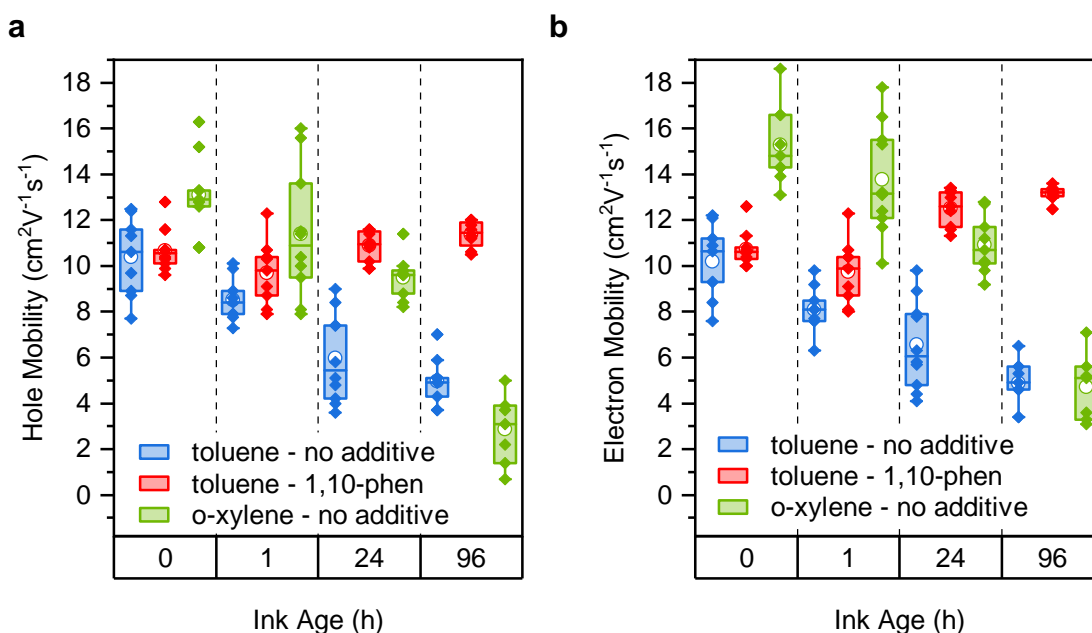
Figure 4.16: Box plots of absolute (a) hole and (b) electron mobilities extracted from (6,5) SWCNT network FETs ($L = 40$ µm, $W = 5$ mm) in the linear regime. Deposition of the networks was performed from inks stored for 0, 1, 24 and 96 h (batch A) with the following solvents: (a) toluene without additive, (b) toluene with 1,10-phen additive and (c) *o*-xylene without additive.

characteristics, devices produced from freshly prepared toluene ink resulted in balanced mobility values for both holes (10.4 $\mathrm{cm^2\,V^{-1}\,s^{-1}}$) and electrons (10.2 $\mathrm{cm^2\,V^{-1}\,s^{-1}}$) without phenanthroline additive. Similarly, those made using the 1,10-phen-containing ink gave values for holes (10.7 $\mathrm{cm^2\,V^{-1}\,s^{-1}}$) and electrons (10.7 $\mathrm{cm^2\,V^{-1}\,s^{-1}}$), respectively. For the transistors based on the *o*-xylene ink at $t = 0$, slightly higher mobilities were obtained: 13.1 $\mathrm{cm^2\,V^{-1}\,s^{-1}}$ (holes) and 15.3 $\mathrm{cm^2\,V^{-1}\,s^{-1}}$ (electrons). Samples prepared from the pristine solvent dispersions (toluene and *o*-xylene, no additive) led to somewhat larger device-to-device variations than for the dispersion with 1,10-phen. While the mobility values (holes and electrons) for both FETs based on additive-free inks continuously decreased with increasing age, the values for the FETs based on the dispersion with phenanthroline remained virtually constant even after four days of ink aging. At the same time, the spread in device performance remained significantly smaller than for the transistors based on the inks without additive. Charge carrier mobilities for batch B are given in Figure 4.17. Again, transistors produced from the fresh toluene-based inks displayed similar charge
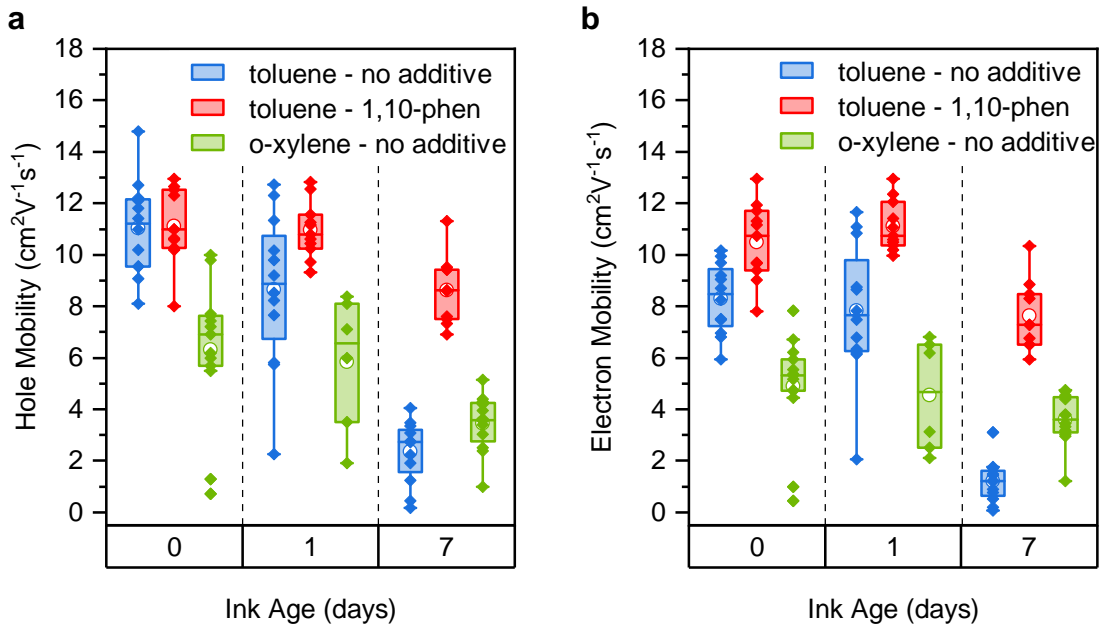
Figure 4.17: Box plots of absolute (a) hole and (b) electron mobilities extracted from (6,5) SWCNT network FETs ($L = 40$ µm, $W = 5$ mm) in the linear regime. Deposition of the networks was performed from inks stored for 0, 1, and 7 days (batch B) with the following solvents: (a) toluene without additive, (b) toluene with 1,10-phen additive and (c) *o*-xylene without additive.

carrier mobilities: 11.0 cm^2 V^{-1} s^{-1} (holes) and 8.3 cm^2 V^{-1} s^{-1} (electrons) for the devices made with the ink without and 11.1 cm^2 V^{-1} s^{-1} (holes) and 10.5 cm^2 V^{-1} s^{-1} (electrons). In analogy to the corresponding transfer characteristics with slightly lower on-currents (see Figure 4.13), the ink based on *o*-xylene displayed somewhat lower mobility values, *i.e.*, 6.3 cm^2 V^{-1} s^{-1} (holes) and 4.9 cm^2 V^{-1} s^{-1} (electrons). Noticeably, for the latter devices, the spread in performance was significantly larger. After one day of ink aging, the performance metrics for the ink with stabilizer remained constant (average value and device-to-device variations), similar to the trends observed for batch A. Concomitantly, there was a drastic increase in performance spread for the corresponding devices produced from additive-free ink in toluene. In contrast to batch A, the *o*-xylene ink-based transistors exhibited only a small drop in mobility with device-to-device variations similar to the toluene-based devices (no additive). After 7 d of ink storage, there was still only a minor decrease in absolute mobility for the samples fabricated from the ink with stabilizer. For the FETs based on inks without additive, however, device performance declined even further, more drastically so for the lower-viscosity toluene-based dispersions.

Figure 4.18 depicts the charge carrier mobility normalized to the fresh ink for both batches. For batch A, there is a clear contrast in the performance trends with ink age between the additive-free samples and those produced with inks containing 1,10-phen. This trend is reproduced in batch B, even though the relative decrease for the *o*-xylene-based transistors

on the longer timescale of one week is more similar to the toluene-based samples using the additive. For the devices produced from the toluene ink without additive, after one week, the decline in average mobility is more than five-fold compared to the corresponding fresh ink devices.
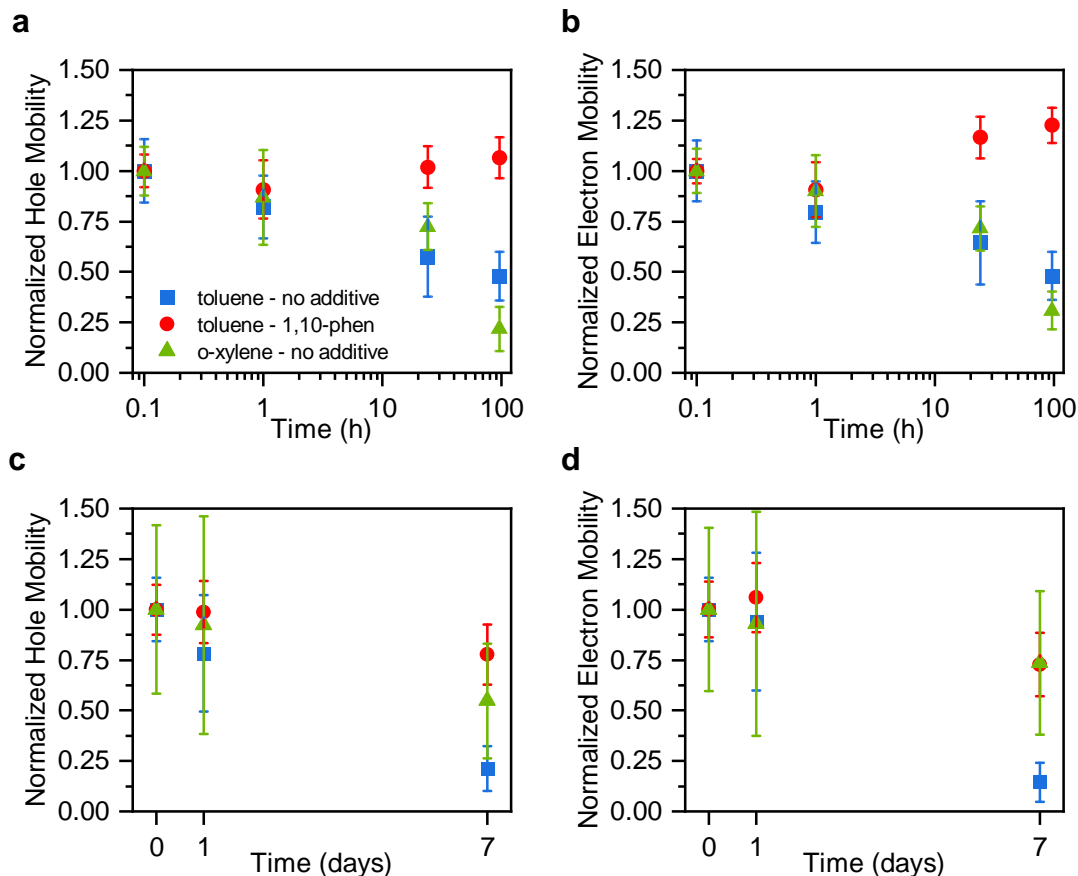
Figure 4.18: Hole (a,c) and electron (b,d) mobilities normalized to the values corresponding to inks deposited at $t = 0$ for batches A (a,b) and B (c,d). Error bars reflect the standard deviation.

In addition to these metrics, reproducible performance over many FETs distributed over large areas is of key importance for large-scale applications in circuits. As demonstrated above, however, inhomogeneities and bundles in the SWCNT network resulting from deposition of (partially) aggregated inks lead to a decline in performance reproducibility. The inhomogeneity parameter is introduced here as a compact metric for the variation in mobility of the transistors investigated in this study. Equ. 4.1 describes the calculation of this parameter.

$$inhomogeneity\ parameter = \sqrt{\left(\frac{\sigma(\mu(t_0))}{\mu(t_0)}\right)^2 + \left(\frac{\sigma(\mu(t_i))}{\mu(t_i)}\right)^2} \tag{4.1}$$

Here, the average carrier mobility for FETs fabricated from ink at $t = 0$ is denoted $\mu(t_0)$, $\mu(t_i)$ the corresponding average carrier mobility for inks aged $t = t_i$ and σ is the respective standard deviation. This parameter describes the relative deviation of the mobility normalized to the respective mobility value for the samples produced with fresh inks. Graphically, it corresponds to the length of the error bar divided by the corresponding average value in Figure 4.18. Large values represent poor device performance homogeneity that would impede operation sufficiently reliable for complex circuits while a perfectly homogeneous sample would have an inhomogeneity parameter of zero. These parameters are depicted in Figure 4.19. For either batch, the mobility homogeneity of the FETs produced from the toluene-based ink with 1,10-phen additive is best at all aging stages. The difference in homogeneity is smallest for the fresh inks and, as a general trend, is largest for inks with the longest shelf-life. Over the maximum ink aging time of one week in batch B, the clearly improved performance homogeneity that is found for the devices based on the ink in toluene with additive is in sharp contrast to the additive-free counterparts. For these, a strong increase with progressing ink age becomes evident.

In summary, the detailed assessment of the FET performance agrees well with the
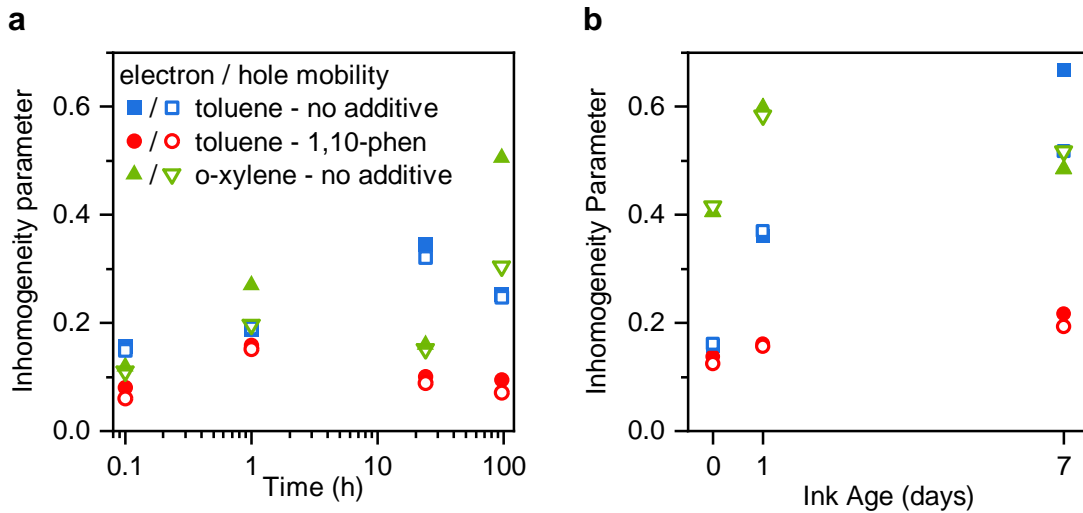
Figure 4.19: Inhomogeneity parameters (see Equ. 4.1) of charge carrier mobilities extracted in the linear regime from (6,5) SWCNT network FETs ($L = 40$ µm, $W = 5$ mm) as a function of ink storage time for (a) batch A and (b) batch B. For batch B, $t = 0$ is changed to 0.1 h to permit the logarithmic scale on the x-axis. Parameters were based on at least 8 devices (batch A) for all ink ages (batch B, at least 10).

morphological data of the nanotube networks as well as the results of the spectroscopic analysis. Introducing the additive 1,10-phenanthroline leads to an improved stability of the (6,5) SWCNT dispersions in toluene, longer shelf-lives and an altogether more homogeneous transistor performance with better reproducibility. These findings are further corroborated by the comparison to the higher-viscosity solvent *o*-xylene, which exhibits inferior homogeneity metrics for aged inks.

4.5 Summary and Conclusions

In this chapter, 1,10-phen was established as a small-molecule stabilizing additive to decelerate aggregate formation in dispersions of (6,5) SWCNTs dispersed by polymer wrapping in organic solvents. The addition of 1,10-phen allows for significantly extended ink shelf-lives (7 d instead of a few hours without additive). The quality of the ink and the process of aggregation can be quantitatively monitored over time by employing ordinary UV-vis-NIR spectroscopy. For that, the continuous decrease in the E_{11} absorption of the nanotubes serves as an indicator. There is a good correlation between the spectroscopically observed stabilization of dispersions with 1,10-phen and, compared to dispersions without additive, the higher uniformity as well as much lower bundle content in nanotube networks deposited by spin-coating of inks with increasing age. This simple tool might constitute an option to screen for additives well-suited for dispersions of other, *e.g.*, larger-diameter nanotubes. The adsorption of the phenanthroline additive onto the bare surface of the nanotube is expected to lead to an increase in shielding of the attractive inter-nanotube van der Waals forces. It is therefore assumed to be the key contributor to prevent aggregation and hence increase dispersion stability.

FETs that were fabricated using the SWCNT dispersions stabilized by the *N*-heteropolycycle additive exhibited substantial improvements in charge carrier mobilities as well as smaller device-to-device variations in comparison to dispersions without additive or using higher-viscosity solvents. This effect increases with progressing ink age.

In conclusion, a more reliable device fabrication with higher reproducibility is facilitated by adding the commercially available, low-cost 1,10-phenanthroline without the need for additional processing steps that could complicate device fabrication. Ink formulations with long-lasting stability constitute a key step forward for increasing the reliability in the processing of nanotube networks, which is mandatory to reach a sufficiently high uniformity for applications on a commercial scale.

Chapter 5

PURELY N-TYPE CHARGE TRANSPORT IN SWCNT NETWORK FIELD-EFFECT TRANSISTORS USING TTMGB

This chapter demonstrates the application of the guanidino-functionalized aromatic compound ttmgb as a powerful n-dopant for exclusively n-type transport in SWCNT network field-effect transistors.

The results described in this chapter were partially published in Schneider *et al. ACS Nano*
2018, *12*, 5859 – 5902.[306] All figures within this chapter were adapted with permission
from the American Chemical Society.

5.1 Introduction

SWCNT networks have become a competitive semiconductor that can be processed from
solution. Their favorable properties such as high chemical stability, mechanical flexibility,
stretchability and excellent charge carrier mobilities enable their use in, *e.g.*, static random
access memory,[254] flexible displays[180] and even microprocessors[7].

One of the remaining key issues is their intrinsic ambipolarity since it inevitably leads
to undesiredly high power dissipation in circuits.[164] A common approach to remedy this
drawback is doping the semiconductor (see section 2.4.4). Whereas p-doping of SWCNTs
can be achieved fairly easily, *e.g.*, by exposure to ambient oxygen, n-doping is significantly
more challenging, particularly with regards to stability and reliability. This issue led to the
combination of p-type SWCNT transistors with n-type transistors based on other materi-
als, for example metal oxides,[307,308] to create complementary circuits, which complicates
processing and inflates cost of fabrication.

Furthermore, efficient n-doping strategies for SWCNTs are also of high interest for efficient
thermoelectric devices.[233,309,310]

The following approaches to enhance n-type transport (as outlined in section 2.4.5) have
been used for SWCNT FETs. Metals with low WFs such as Gd, Y or Sc facilitate
electron injection,[247,248] electrostatic doping by HfO_x[187,249] or silicon nitride[250] as well as
alkali metals[251] all result in n-doping. Chemical doping with polymers or small molecules
containing amine groups, *i.e.*, poly(ethylene imine)[256] and ethanolamine[255] are another
successful strategy. In recent years, a number of reducing agents have been employed, such
as DMBIs,[258] viologen,[253,254] NADH[252] or metallocenes.[257,311]

All of these methods, however, are adversely affected by at least one of the following
disadvantages: costly synthesis and purification of the dopant, undesired shifts in onset
voltage, limited on/off current ratios caused by unwanted degenerate doping and insuffi-
cient stability of the involved compounds and reaction products leading to instable device
operation. Additionally, when hole currents are not completely suppressed, the residual
ambipolarity of the nanotubes heavily restricts potential low-power consumption operating
regimes for circuitry similar to effects caused by degenerate doping (see section 2.4.3 and
2.4.4).

As an approach to tackle these outlined challenges that have thus far limited the use of
n-type nanotube transistors in circuitry, guanidino-functionalized aromatic (GFA) com-
pounds are introduced as a suitable class of n-dopants for carbon nanotube networks

(see section 2.4.6). GFAs are potent reducing agents with high alkalinity that can be synthesized in a facile, cost-effective and scalable manner.[260,261,273,274,312] Upon oxidation stable cations are formed with charges largely delocalized over an ample conjugated π-system. Chemical adaptation of their aromatic core or the guanidino moieties allows for an adjustment of their redox potentials, their solubility and crystallization.[260,312] Additionally, their relatively high air stability renders them more robust for a larger scope of processing techniques compared to the commonly poor air stability exhibited by known n-dopants. In this chapter, the conversion of (6,5) SWCNT networks from ambipolar to solely n-type charge transport behavior is demonstrated using the GFA compound 1,2,4,5-tetrakis(tetramethylguanidino)benzene (ttmgb).[306] Starting with high-quality dispersions prepared by polymer-wrapping in toluene, this conversion is achieved by a simple dip-doping approach of the deposited networks of semiconducting SWCNTs. Detailed electrical characterization of the transformed networks allows for a comprehensive investigation of the performance metrics. Comparison to devices treated with similar but non-redox-active guanidine bases, analysis of the contact resistance in a gated four-point probe structure and an investigation of the energetic alignment of the involved layers using photoelectron spectroscopy help to elucidate the mechanisms involved in this conversion. The application potential of this doping approach is explored by fabrication of complementary inverters and further corroborated by bias stress stability measurements conducted in ambient air.

5.2 Conversion from Ambipolar to N-Type Transport

Dispersions of PFO-BPy-wrapped (6,5) SWCNTs in toluene as introduced in the previous chapter (without the use of phenanthroline stabilizer) served as the starting point to demonstrate the desired transformation from ambipolar to unipolar n-type transport in SWCNT network FETs. The UV-vis-NIR absorption spectrum in Figure 5.1a displays the characteristic features, *i.e.*, sharp E_{11} and E_{22} transitions at 996 nm and 575 nm, respectively, as well as absorption by the wrapping polymer PFO-BPy at 352 nm. Raman spectra (see Figure 5.1b and c, excitation wavelength 532 nm) confirm excellent chiral purity given the sharp RBM peak at 311 cm^{-1} with only minor amounts of possibly (9,1) SWCNTs. The sharp peaks corresponding to G^+, E_2 and G^- modes indicating the absence of any metallic nanotubes and the weak defect-related signal corresponding to the D-mode confirm the high dispersion quality.

These dispersions were used to create sparse networks (linear density 11.5 ± 2.5 µm^{-1}, see representative atomic force micrograph in Figure 5.2a), which were incorporated as the active layer in top-gate/bottom-contact FETs that included a hybrid dielectric of PMMA
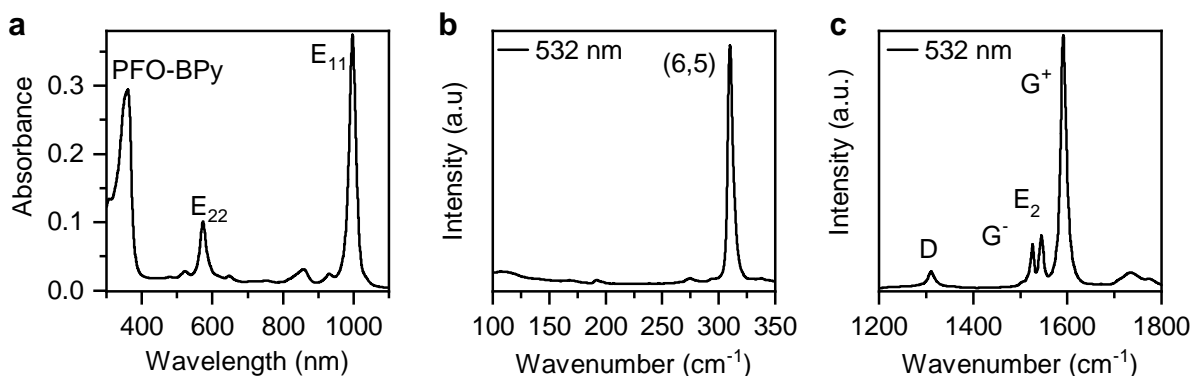
Figure 5.1: (a) UV-vis-NIR absorption spectrum of a diluted (6,5) SWCNT dispersion in toluene. (b-c) Raman spectra measured on (6,5) SWCNT filter cake with an excitation wavelength of 532 nm indicate absence of metallic SWCNTs.

and HfO_x as employed in the previous chapter. Figure 5.2b provides an overview of the device stack.
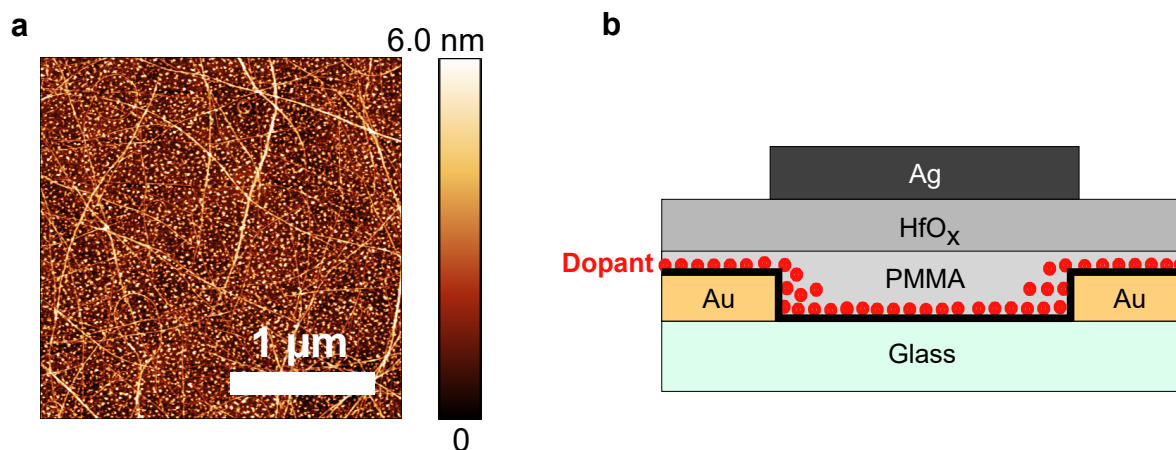
Figure 5.2: (a) Representative atomic force micrograph (2.5×2.5 µm^2) of a sparse (6,5) SWCNT network. (b) Schematic layout of bottom-contact/top-gate device architecture of a (6,5) SWCNT network FET with ttmgb (red).

Processing of the deposited SWCNT networks in dry nitrogen atmosphere ensures intrinsically ambipolar transport behavior, which is, however, detrimental to their use in applications such as circuitry.[164] These FETs can only reach the off-current level at very low source-drain bias because, at high drain voltages, their ambipolarity severely limits their on/off current ratios (see section 2.3.1).

Representative transfer characteristics of a FET ($L = 40$ µm, $W = 5$ mm) with an untreated (6,5) SWCNT network are depicted in Figure 5.3a. As expected, it exhibits quite balanced transport of both holes and electrons. The moderate current hysteresis can be explained by the occurence of shallow trap states, most likely caused by residual

amounts of water adsorbed to the highly polar glass substrate.[8]

The desired transformation to solely electron transport characteristics was achieved by application of the dopant ttmgb (see section 2.4.6) in a dip-coating process. It involved submersing the entire substrate with pre-deposited source and drain electrodes as well as SWCNT networks and subsequent annealing at 150 °C (for a detailed description, see section 3.3.4) prior to the deposition of the hybrid dielectric. The GFA compound ttmgb serves as a highly alkaline, strong reducing agent.[273] Its first oxidation potential measured by cyclic voltammetry -0.76 V *vs.* Fc/Fc$^+$ in acetonitrile implies high reduction strength for the reversible two-electron donor ttmgb (see Figure 2.15b).[265] In addition, the high alkalinity of ttmgb facilitates the removal of trace amounts of water that act as electron traps and are commonly present on polar substrate surfaces, *e.g.*, glass[8,305] (see discussion in section 5.3.2).

A sample treated with ttmgb shows vastly different characteristics (Figure 5.3b). Even at large positive drain (V_d = 4.0 V) and negative gate voltages (V_g = -5.0 V) no hole currents that exceed the gate leakage level can be measured. The onset voltage for electron transport is shifted close to 0 V with a very steep increase of the electron drain current as is evident from a subthreshold swing of only 94 ± 6 mV dec^{-1}. The complete off-state (drain currents similar to gate leakage) at negative gate voltages in combination with the increased electron currents result in increased maximum on/off current ratios of 10^7 for FETs with L = 40 µm and up to $2{\times}10^8$ for FETs with L = 20 µm. Furthermore, there is virtually no current hysteresis in the ttmgb-treated FETs (see discussion in section 5.3.2).
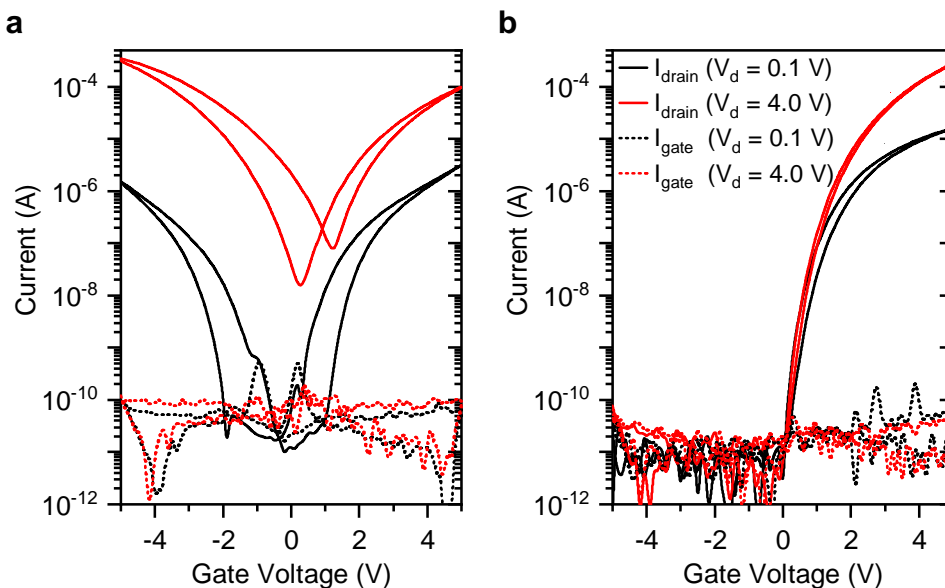
Figure 5.3: Transfer characteristics of (a) untreated and (b) ttmgb-treated, c_{ttmgb} = 2.5 g L^{-1}, (6,5) SWCNT network FETs (L = 40 µm, W = 5 mm) in the linear (V_d = 0.1 V, black) and saturation regime (V_d = 4.0 V, red).

The respective output characteristics for electron accumulation are displayed in Figure 5.4. While the untreated reference sample in Figure 5.4a exhibits good charge carrier injection (indicated by the linear increase of current at low drain voltages), it features the superlinear increase of current at high drain voltages and low gate voltages that is characteristic for ambipolar transport and corresponding hole injection. As can be expected from the transfer characteristics discussed above, this effect is absent for the quasi-ideal unipolar output curves of the ttmgb-treated sample (see Figure 5.4b). In addition, injection of electrons is improved, electron currents reach higher values at all drain and gate voltages compared to the untreated reference and there is no detectable hysteresis while the current still saturates at high drain voltages.
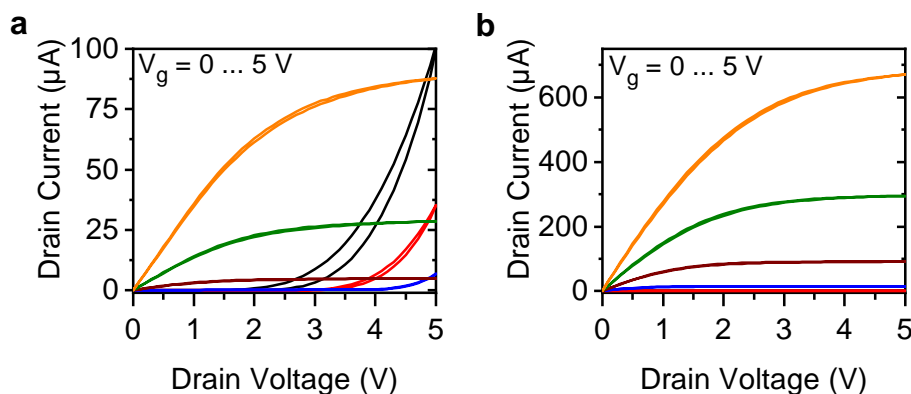
Figure 5.4: Electron output characteristics (forward and reverse sweeps) of (a) untreated and (b) ttmgb-treated, $c_{ttmgb} = 2.5 \text{ g L}^{-1}$, (6,5) SWCNT network FETs ($L = 40$ µm, $W = 5$ mm).

Electron mobilities were extracted according to Equ. 2.10 in the linear and Equ. 2.11 in the saturation regime for forward sweeps (measured from the off- to the on-state). Average values from at least eight devices per substrate are shown in Figure 5.5 for the untreated reference and samples treated with varying concentrations of ttmgb (1.5–2.5 g L^{-1}). The electron mobility for the displayed ttmgb concentration range increases by a factor of 3–5 compared to the untreated reference, resulting in values of approximately 10 ± 2 cm^2 V^{-1} s^{-1}. The similarity of the calculated electron mobilities in linear and saturation regime indicate a decrease of contact resistance (see discussion in the next section). Importantly, the suppression of hole injection is not accompanied by undesired threshold voltage shifts or increased off-current levels (see Figure 5.3b), which would be caused by excess charge carriers provided by degenerate n-doping. These outstanding device parameters exhibited by the (6,5) SWCNT network FETs treated with ttmgb position them within the range of state-of-the-art n-type FETs with metal oxide semiconductors.[1,307,308] They additionally highlight their suitability for applications in active-matrix OLED backplanes as they meet the demanding requirements for high drive currents and current
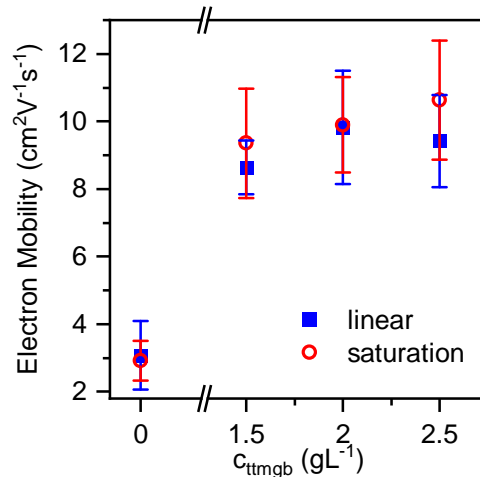
Figure 5.5: Electron mobilities determined from FETs ($L = 40$ µm, $W = 5$ mm) in linear (blue squares) and saturation regime (red circles) for untreated reference and ttmgb-treated samples (three different dopant concentrations). Error bars correspond to standard deviation based on at least 8 devices.

on/off ratios.[313]

As is evident from Figure 5.6, the effect of ttmgb is highly dependent on its concentration in the dipping solution. While concentrations below 1.5 g L^{-1} lead to only partial blocking of hole injection (see Figures 5.6a and b), concentrations above 3.0 g L^{-1} (see Figure 5.6d) lead to onset voltage shifts towards negative gate voltages accompanied by increased off-current levels, very high on-currents and, thus, limited gate modulation. Although this doping regime is detrimental to the performance in FETs, it is highly desired for and may be used in thermoelectric applications of SWCNTs.[233,310]

Given the textbook-like n-type characteristics facilitated by ttmgb-treatment of the (6,5)
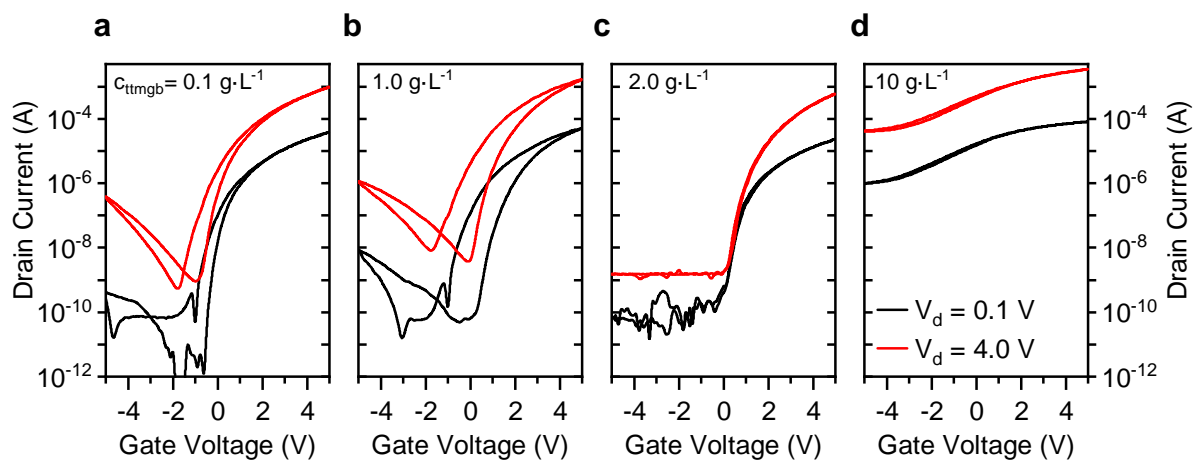
Figure 5.6: Transfer characteristics of (6,5) SWCNT network FETs ($L = 40$ µm, $W = 5$ mm) treated with different concentrations of ttmgb solution in toluene, *i.e.* (a) 0.1, (b) 1.0, (c) 2.0 and (d) 10 g L^{-1}, in the linear ($V_d = 0.1$ V, black) and saturation regime ($V_d = 4.0$ V, red).

SWCNT network FETs, the question of the underlying mechanisms need to be addressed, which appear to be considerably different to established n-doping methods. This analysis is presented in the following section.

5.3 Mechanistic Insights

5.3.1 Comparison of ttmgb to Non-GFA Guanidines

As transistors incorporating a ttmgb layer without nanotubes did not exhibit any charge transport, the improbable hypothesis that ttmgb serves as the semiconductor could be refuted.

This subsection focuses on the direct comparison to treatment of (6,5) SWCNT networks with non-redox-active bases structurally similar to ttmgb, *i.e.*, they contain guanidine units but do not serve as electron donors aside from direct donation of the free electron pair of the amine groups. Electron transfer through the free electron pair located at the nitrogen is attributed to be the primary source of n-doping of SWCNT networks treated with ethanolamine or polyethylenimine.[255,256] The comparison to the highly alkaline but non-redox-active Lewis bases hexahydropyrrimidopyrridine (hpp, Figure 5.7a) and tetramethylguanidine (Me$_4$G, Figure 5.7b) may reveal potential similarities and differences.

As is apparent from both transfer characteristics in Figure 5.7, this treatment results in
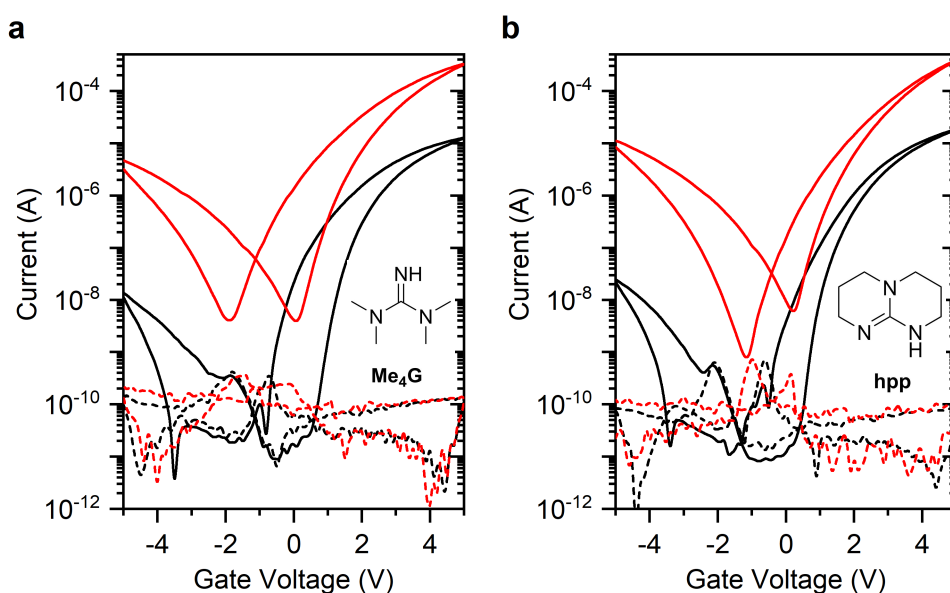
Figure 5.7: Transfer characteristics of (6,5) SWCNT network FET ($L = 40$ µm, $W = 5$ mm) treated with (a) Me$_4$G and (b) hpp in the linear ($V_d = 0.1$ V, black) and saturation regime ($V_d = 4.0$ V, red).

somewhat decreased hole and higher electron currents compared to the reference networks that were not treated with dopant. These changes are remarkably similar for both applied

dopants. For either compound, hysteresis remains relatively large in both linear and saturation regime.

A detailed analysis of the charge carrier mobilities for different concentrations of the tested compounds is given in Figure 5.8. For both non-redox-active bases, electron mobilities exceed the values of the corresponding untreated reference sample although this effect is slightly more pronounced for the hpp-treated samples. The chosen molar concentrations of the non-redox active bases ($M_w(hpp) = 139.2$ g mol^{-1}, $M_w(Me_4G) = 115.8$ g mol^{-1}) are much higher than the devices treated with redox-active ttmgb ($M_w = 530.7$ g mol^{-1}). As ttmgb-treated devices exhibit a strong dependence on dopant concentration, this permits to exclude insufficiently high base concentration as a potential reason for the inferior performance of the transistors treated with non-redox-active bases. In contrast to the fully suppressed hole transport shown by the ttmgb-treated devices, there is only a partial (but still substantial) decrease in hole transport (see hole mobilities, Figure 5.8b), which is also dependent on dopant concentration. Electron threshold voltages (see Figure 5.9a)
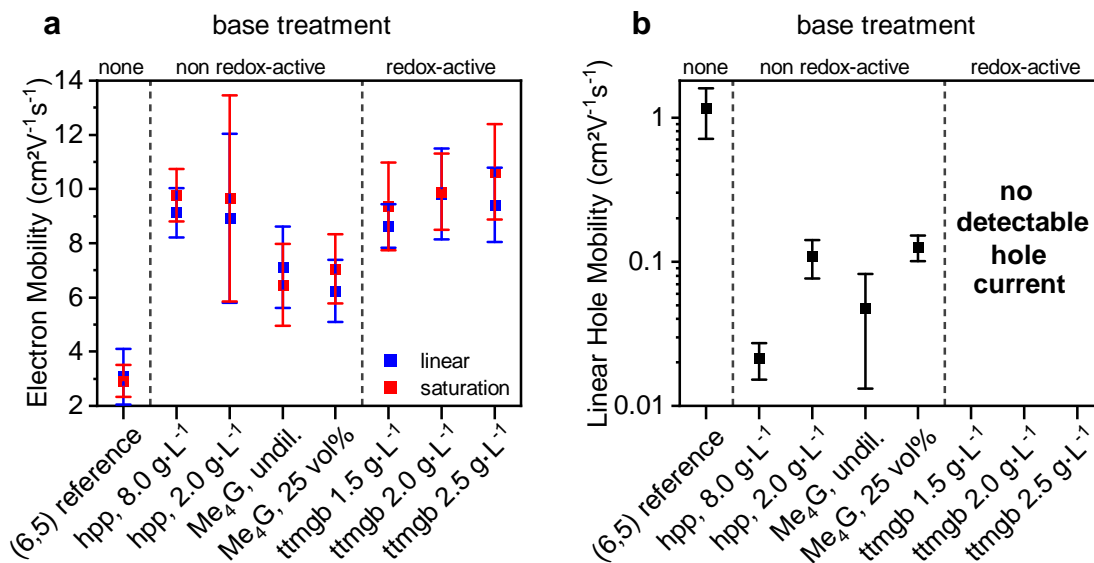
Figure 5.8: (a) Comparison of electron mobilities in the linear (blue squares) and saturation regime (red circles) for untreated (6,5) SWCNT network reference, sample treated with non-redox-active bases (hpp, Me$_4$G) and redox-active ttmgb at varied concentrations. (b) Corresponding hole mobilities in the linear regime. Error bars correspond to standard deviation based on at least 8 devices.

appear to be mostly unaffected by the doping achieved *via* the selected base treatment. In agreement with this, the extracted hole threshold voltages remain at similar values within the margins of error.

It can be concluded that the increase in electron transport might indeed be promoted by treatment with non-redox-active bases similar to results presented in literature.[255,256] Note that weaker GFA reducing agents, such as (2,3,7,8-tetrakis(tetramethylguanidino)phenazine
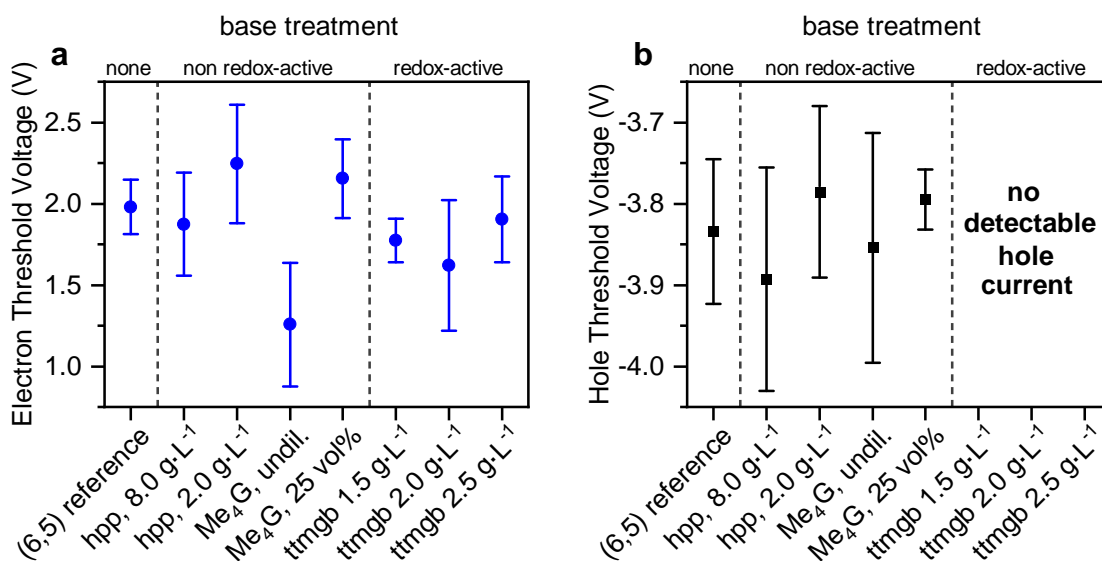
Figure 5.9: Comparison of threshold voltages extracted for (a) electrons in the saturation and (b) holes in the linear regime in untreated (6,5) SWCNT network reference, sample treated with non-redox-active bases (hpp, Me$_4$G) and redox-active ttmgb at varied concentrations. Error bars correspond to standard deviation based on at least 8 devices.

(ttmg-phen, first oxidation potential measured by cyclic voltammetry -0.12 V *vs.* Fc/Fc$^+$),[275] show very similar behavior to the non-redox-active bases and were thus of no further interest for this study. Overall, exclusively by treatment with the strong reducing agent ttmgb, all desired benefits, *i.e.*, solely n-type transport with steep subthreshold swings and without hysteresis, can be achieved successfully. One might speculate that the base-water adduct formed upon the deprotonation of water traces remains an electron trap for both non-redox-active bases while this is not the case for ttmgb, possibly due to better charge delocalization. This is reflected in the much larger hysteresis of the hpp- and Me$_4$G-treated samples.

The absence of a shift in threshold voltage for both charge carriers corroborates the notion that rather than doping in the sense of transfer of excess charge carriers from dopant to the semiconductor, the effects caused by treatment with either redox- and non-redox-active bases might be attributed to contact doping. This is investigated further in subsections 5.3.3 and 5.3.4.

5.3.2 Trap Removal

This subsection focuses on the role of ttmgb as a remover of trap states. The onset voltage close to 0 V, the steep subthreshold swing of 94 ± 6 mV dec^{-1} and the significantly reduced hysteresis compared to the untreated nanotube network transistors hint at a drastically lower trap density in the ttmgb-treated devices. Water and hydroxyl groups are commonly

present on polar surfaces such as SiO_2 or glass, which are hard to remove only by thermal annealing, and have been identified as prime causes for electron traps and current hysteresis in SWCNT FETs.[8,305] It is reasonable to assume that ttmgb would react with both of these moieties. Due to their high alkalinity, GFA compounds such as ttmgb can act as proton sponges[261,314] and readily remove residual water at all relevant interfaces. Additionally, the reducing strength of ttmgb can lead to passivation of remaining electron traps by donation of electrons. One may speculate that the strong delocalization of charges on the resulting reaction product $ttmgb^{2+}$ helps to avoid the new formation of charge-induced traps (for delocalization of charges, see Figure 2.15b).

The suspected decrease in trap density was later investigated in more detail by Gotthardt *et al.*[315] and Statz *et. al.*[316] Trap densities calculated from subthreshold swings[317] were found to decrease by a factor of 7–8 upon treatment with ttmgb compared to the untreated reference SWCNT network transistor for (6,5) SWCNTs and to a lesser extent for large-diameter SWCNTs.[315] To summarize, ttmgb drastically reduces the number of trap states at the involved interfaces, which greatly benefits the transistor performance.

5.3.3 Contact Resistance

In this subsection, the impact of the ttmgb-treatment on contact resistance and charge carrier injection is elucidated.

The (6,5) SWCNTs used within this study have a bandgap of $\sim$1.27 eV, which results in similar injection barriers from gold for both holes and electrons. Ultimately, this leads to an ohmic contact resistance that can be measured, for example, by the gated four-point probe method (see section 2.4.2).

 Figure 5.10 displays the width-normalized contact resistance for electrons as a function of gate voltage. As is expected, the values decrease with increasing gate voltage. The untreated reference sample features a much higher value (3.6×10^4 Ω cm) than the ttmgb-treated (4.0×10^2 Ω cm) (6,5) SWCNT network transistor (values extracted in the on-state ($V_g = 5.0$ V)). This represents a reduction of the contact resistance by two orders of magnitude. It is safe to conclude that this effect is caused by a clearly enhanced electron injection *via* a diminished injection barrier. This is in agreement with expectations for contact doping and hints at a significantly lowered WF of the gold electrodes (see section 5.3.4). Gotthardt *et al.* could successfully reproduce these contact resistance values and show similar effects on electrodes of various metals and, albeit to a lesser extent, for large-diameter nanotubes.[315] At the same time, this change in WF may also partially explain the hampered hole injection. The next section is thus dedicated to shine light on the energetic alignment of electrodes, dopant and semiconductors involved in this study.
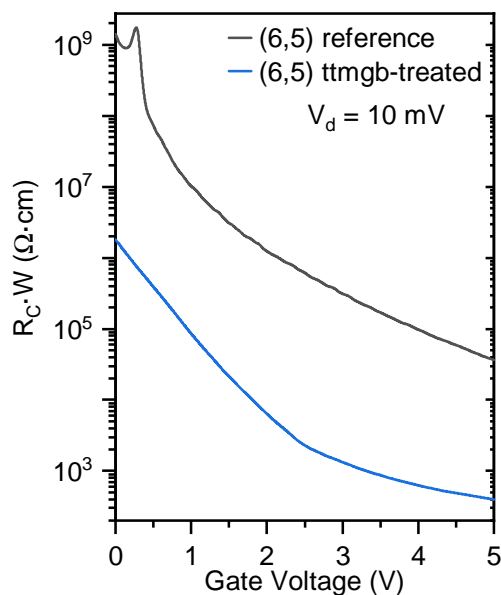
Figure 5.10: Comparision of the gate voltage-dependent, width-normalized electron contact resistance of untreated reference (6,5) SWCNT network (black) and ttmgb-treated (blue) FET extracted using the gated four-point probe method.

5.3.4 Energetic Alignment

The WF of metal electrodes can be determined by ultraviolet photoelectron spectroscopy and Kelvin probe measurements. Here, samples were prepared to determine the energetic alignment of gold, SWCNTs and ttmgb.

The secondary photoemission onset (see Figure 5.11a) served as source for the calculations of the WF of all samples while the HOMO of the materials were extracted from the low binding energy edge of the valence band[318] shown in Figure 5.11b. LUMO energies were calculated from the HOMO and the optical bandgap measured by UV-vis-NIR spectra. The analysis for the solvent-cleaned gold electrodes revealed typical WF values of 4.7 eV. In agreement with the ambipolar device characteristics of the untreated reference nanotube networks, SWCNTs on gold yielded injection barriers of 0.5 eV for holes and 0.7 eV for electrons respectively. Treatment of the gold surface with ttmgb led to a substantial decrease in WF of 1.2 eV to 3.5 eV. Kelvin probe measurements, conducted by Dr. Eric Sauter in the laboratory of Prof. Dr. Zharnikov's group, of analogously prepared samples exhibited a lowering of the WF by 0.6 eV. In a recent study,[315] reductions of the WF by ttmgb treatment on gold, palladium and platinum were all determined to be on the order of 1.0 eV. This reduction in WF can be attributed to an interfacial dipole that points away from the ttmgb molecules located at the metal interface. It is expected to originate from the electron transfer of from ttmgb molecule to the gold substrate in agreement with the expected contact doping.

Surprisingly, the ionization potential of 5.0 eV extracted for ttmgb is a contradiction
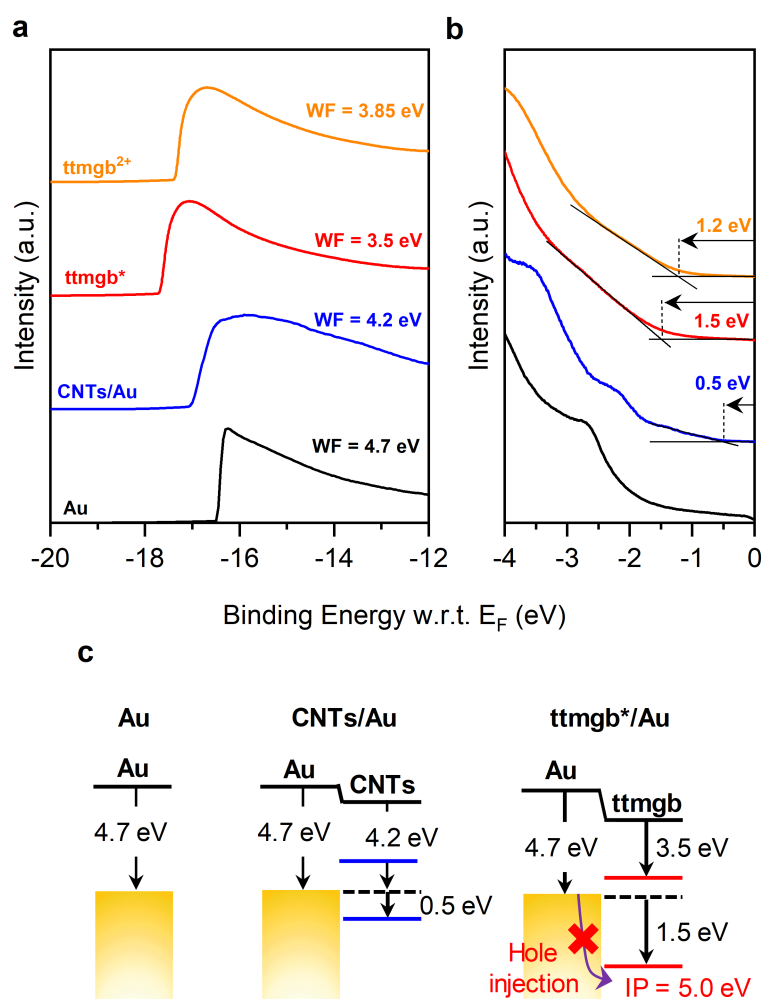
Figure 5.11: (a) Secondary photoemission onset and (b) valence band spectra of gold, CNTs on gold, ttmgb on gold (labeled ttmgb, already oxidized after electron transfer to gold) and ttmgb^{2+} on gold. (c) Summarized energy level diagrams as obtained from UPS measurements. UPS measurements were provided by Prof. Dr. Yana Vaynzof.

to the notion of the dopant acting as a powerful electron donor. The most plausible explanation for this discrepancy to the known donor strength of ttmgb as well as the determined interfacial dipole appears to be that the measured value corresponds to the HOMO-1 of ttmgb, *i.e.*, the HOMO of ttmgb^{2+}. The assumption that the electron transfer to the metal has already occured is in agreement with cyclic voltammograms of ttmgb[265] and is further corroborated by further UPS data on ttmgb-bishexafluorophosphate, a salt that contains the oxidized species ttmgb^{2+}, as it yields a virtually identical ionization potential value of 5.05 eV.

As is highlighted in the corresponding energy level diagrams in Figure 5.11c, these findings also provide insight on the origin of the lack of hole injection and transport in the

corresponding ttmgb-treated transistors. Given the very large difference in energy of 1.5 eV between the gold electrode Fermi level and the HOMO of the oxidized dopant species ttmgb^{2+}, the latter suppresses any injection of holes into the nanotube network, functioning as a hole blocking agent of great efficiency.

Overall, the treatment of gold electrodes with ttmgb not only significantly reduces their WF to facilitate electron injection, which leads to lower contact resistance, the oxidized species ttmgb^{2+} present at the electrode also efficiently blocks hole injection and suppresses hole transport.

5.4 Complementary Inverters

In this section, the application of the described doping *via* ttmgb treatment for the creation of basic circuits based on SWCNT networks is explored. For the most basic complementary circuit, *i.e.*, an inverter, a p- (for transfer characteristics, see Figure 5.12) and an n-type SWCNT were connected according to the circuit diagram displayed in the inset of Figure 5.13a).

The p-type FET based on (6,5) SWCNT networks was fabricated in analogous fash-
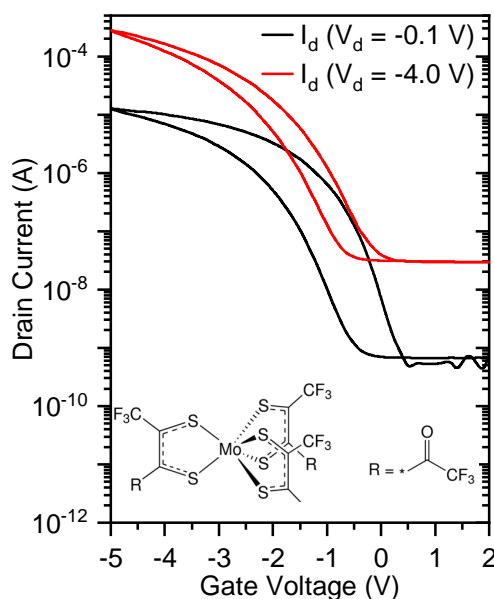
Figure 5.12: Transfer characteristics of a (Mo(tfd-COCF$_3$)$_3$)-treated (6,5) SWCNT network FET ($L = 40$ µm, $W = 5$ mm) displaying p-type behavior in the linear (V_d = -0.1 V, black) and saturation regime (V_d = -4.0 V, red). Inset: molecular structure of Mo(tfd-COCF$_3$)$_3$.

ion to the ttmgb-treated devices by using the dopant Mo(tfd-COCF$_3$)$_3$) (for molecular structure, see inset Figure 5.12)[319]. This sample displays exclusive hole transport ($\mu_{sat} = 3.5$ cm^2 V^{-1} s^{-1}) without any undesired shift in onset voltage. Compared to the analogous n-type transistor, on-currents are smaller, the off-current is elevated by more

than one order of magnitude and there is also moderate current hysteresis.

Figure 5.13a depicts inverter characteristics with full rail-to-rail operation with maximum gains of 52 (Figure 5.13b) for three different supply voltages (V_{DD}). The maximum power consumption during switching for a supply voltage of 1.0 V (gain = 18) is just 45 nW, which is an excellent value compared to previous reports.[186] Note, however, that this value was obtained without optimizing the p-type transistor as this just served as a proof-of-concept. Given the elevated off-current level even at low drain voltages in the simple transistor, one can assume a significant potential for performance improvements.
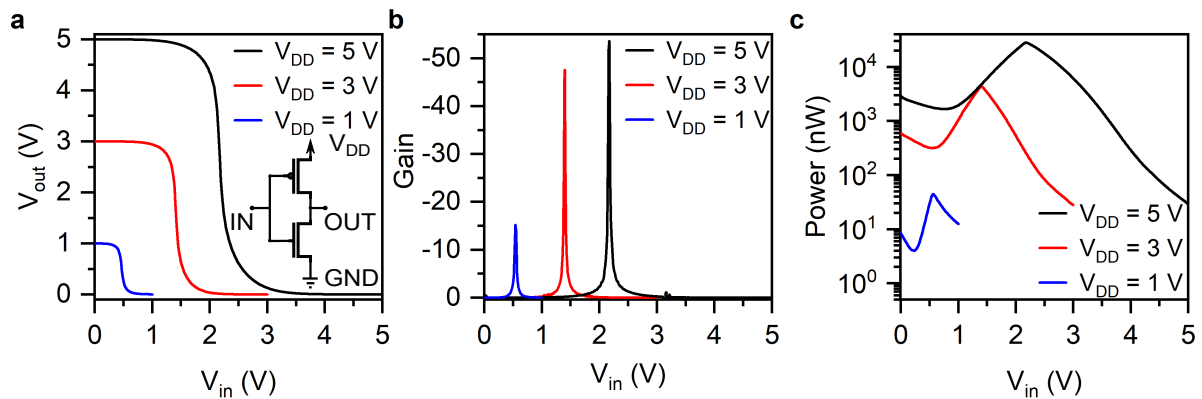
Figure 5.13: (a) Single-sweep voltage transfer characteristics of a complementary inverter based on n-type (ttmgb-treated) and p-type ((Mo(tfd-COCF$_3$)$_3$)-treated) SWCNT network FET transistors ($L = 40$ µm, $W = 5$ mm). Inset: Circuit diagram for inverter. (b) Gains corresponding to (a) and (c) power dissipation corresponding to (a,b) at varied supply voltages (V_{DD}).

It may thus be concluded that the here employed wet chemical p- and n-doping of SWCNT networks serves as a suitable method for the fabrication of low-power complementary circuits.

5.5 Environmental Stability

As has been highlighted in section 2.4.5 and the introduction to this chapter, one major challenge for carbon-based n-type FETs is their environmental stability. As has been shown before,[320] the hybrid dielectric of PMMA and HfO$_x$ layers incorporated into the bottom-contact/top-gate device stack serves as a good self-encapsulant.

In order to test the environmental stability for operation conditions, ttmgb-treated FETs were subjected to continuous bias stress ($V_d = 1.0$ V, $V_g = 4.0$ V) for ten hours in ambient air. Transfer characteristics for measurements in the saturation regime collected immediately before and after bias stress are shown in Figure 5.14a. There is virtually no
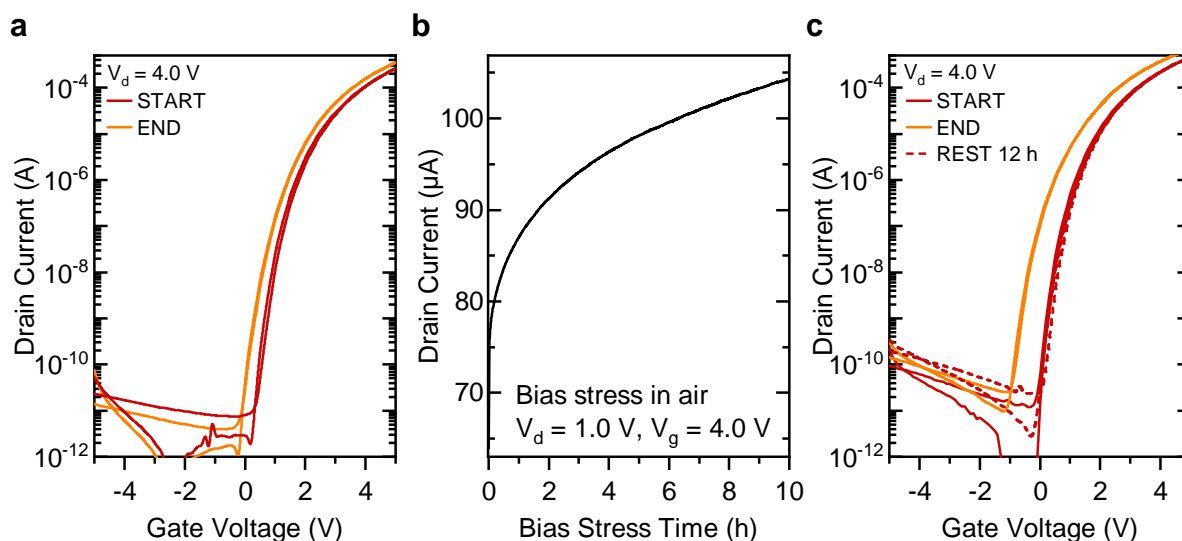
Figure 5.14: (a) Transfer characteristics of ttmgb-treated, $c_{ttmgb} = 2.5\,\mathrm{g\,L^{-1}}$, (6,5) SWCNT network FET ($L = 40\,\mu m$, $W = 5\,mm$) in the saturation regime ($V_d = 4.0$ V) before (red) and after (orange) operation under continuous bias stress in ambient air. (b) On-state drain current as a function of time during continuous operation (10 h) under bias stress ($V_d = 1.0$ V, $V_g = 4.0$ V). (c) Transfer characteristics as described in (a) of sample with largest shift in onset voltage. Measurement after a resting period (12 h, no bias) in air demonstrates full reversibility of onset voltage shift.

difference between the two curves except for a small shift in onset voltage by ~ 0.4 V that results in a gradual increase of the on-current over time (factor ~ 1.6, see Figure 5.14b). Interestingly, this shift is reversible when the sample is rested in air without bias stress even in the case of the largest on-voltage shift detected (approximately 1.0 V) among all samples tested (see Figure 5.14c).

This outstanding stability under bias stress conditions for the nanotube network FETs treated with ttmgb excludes any unwanted dopant degradation or migration. It thus underlines the applicability of the introduced n-type SWCNT network transistors for longterm device operation in practice and applications in circuitry.

5.6 Summary and Conclusions

To sum up, in this chapter the guanidino-functionalized aromatic compound ttmgb was established as a suitable contact dopant to convert intrinsically ambipolar SWCNT network FETs to unipolar n-type transistors with excellent performance metrics. The ttmgb-treated devices feature high electron mobility, outstanding on/off current ratios, remarkably steep subthreshold slopes while hole injection and transport are entirely suppressed. The injection barrier for electrons is significantly reduced by contact doping of the gold electrodes upon electron donation by ttmgb while the newly formed $ttmgb^{2+}$ serves as an efficient

hole blocking agent. A comparison to chemically similar non-redox-active bases reveal that only with the particular combination of redox chemistry and high alkalinity of ttmgb, the density of electron traps within the channel area is drastically lowered, which results in current-voltage characteristics free of hysteresis even in ambient air. Note that ttmgb does not significantly increase the maximum carrier mobility in the SWCNT network but the reduced contact resistance drastically decreases the carrier density (correponding to a lower gate voltage) at which this maximum is reached.[315]

Complementary inverters fabricated from p- and n-doped SWCNT network FETs exhibit full rail-to-rail operation with high gains and small power dissipation, which highlights the application potential of the demonstrated method. This is furthermore underlined by the excellent device stability under bias stress conditions in ambient air.

A comparison with known stronger dopants with lower redox potentials such as decamethylcobaltocene[321] or DMBI derivatives[258] reveal undesired threshold voltage shifts or limited current modulation caused by unwanted introduction of excess charge carriers while electrostatic doping approaches usually result in devices with large current hysteresis[187] due to additional trap states. While certain desired aspects of n-doping have been successfully achieved in literature, a purely n-type SWCNT network FET with high electron mobility, excellent switching behavior, low electron trap densities, no hysteresis and high operational stability had thus far not been realized. The excellent performance metrics of the ttmgb-doped FETs render them a competition to state-of-the-art n-type FETs based on solution-processable metal oxides.[1,307,308]

This investigation already sparked further fundamental research with regards to compatibility to other electrode metals, large-diameter SWCNTs and was used to draft guidelines for doping of SWCNT networks for electric and thermoelectric devices.[315,316] One of the questions that remain to be answered is the potential applicability of GFA compounds to other materials such as semiconducting polymers.

Chapter 6

IMPROVED ELECTRON INJECTION AND TRANSPORT IN SEMICONDUCTING POLYMERS USING GFA DOPANTS

This chapter explores the application of guanidino-functionalized aromatic (GFA) dopants for performance improvements in polymer field-effect transistors.

The results described in this chapter were partially published in the article Schneider *et al.*
J. Mater. Chem. C **2021**, *9*, 7485-7493.[322] All figures within this chapter were adapted
from this reference with permission from the Royal Society of Chemistry.

6.1 Introduction

Due to their mechanical flexibility, their solution processability and the sheer limitless
options in chemical design, semiconducting polymers have received considerable attention
for their use in OFETs. Application of OFETs in flexible displays, sensors, wearables and
organic circuitry have been successfully demonstrated.[204,323–325] However, some crucial
limitations have yet to be overcome. Similar to the FETs based on SWCNT networks,
a particularly important one is the realization of purely n-type polymer FETs with high
electron mobilities, low contact resistance while maintaining stable operation. Although
there has been significant progress in the past two decades, n-type OFETs still lag behind
the p-type counterparts.[117] As outlined in the previous chapter, for efficient, low-power
complementary circuits, both transistor types are mandatory and should, in ideal cir-
cumstances, feature well-balanced charge carrier mobilities as well as high on/off current
ratios. Concomitantly, suppression of the opposite carrier injection and transport to avoid
ambipolarity is key to minimize power consumption.[124]

While the application of high WF metals (such as gold) is beneficial for stable device
operation compared to low WF metals (such as calcium), it hampers efficient electron
injection and thus increases contact resistance. High contact resistance results in unwanted
large voltage drops[152,228] at the contacts and severely restricts the maximum switching
frequency of a transistor.[151,221,326]

In general, the use of molecular dopants is an established strategy to lead to sig-
nificant performance improvements for both p- and n-type transistors (see also sec-
tion 2.4.5).[11,12,327] Specifically, they can improve charge carrier injection by contact
doping,[236,237,328–331] modify the threshold voltage,[235–237,329,330] lower the trap state density
inside the channel[236–238] and suppress ambipolarity by limiting injection of the opposite
carrier (see section 2.4.4).[236,245,306]

The most widely used of these methods is contact doping which enables a reduction of the
injection barrier for charges and thus leads to lower contact resistance.[152,328,329,331] In this
case, tunneling of the charge carriers is facilitated by reducing the height of the Schottky
barrier as well as its width (see corresponding background sections 2.4.1 to 2.4.4). In
contrast to this, bulk or channel doping, commonly achieved by mixing dopant and semi-
conductor, aims to improve the threshold voltage control, reduce the number of trap states
and enhance operational stability of the devices.[234,235,332] Another established method,
called transfer or remote doping, includes the targeted diffusion of dopant molecules into

or through the semiconductor which has been shown to be beneficial for retaining the morphology of the semiconductor in some cases.[236,333,334]

Unlike in the field of thermoelectrics,[233] doping for OFETs is not meant to permanently enhance the number of mobile charge carriers (see section 2.4.4,).[11,12] The large conductivity of the active layer resulting from degenerate doping would be accompanied by an enhanced off-current level, limited carrier concentration modulation and thus poor on/off-current ratios. To avoid this, dopant redox potentials, their concentration and localization in the device warrant a careful optimization.

Compared to the substantial progress that has been made for p-type FETs, efficient n-doping has proven to be a major challenge due to the inherent high sensitivity to oxygen and moisture of the strongly reducing n-dopants. This is an issue both during processing and for operational device stability (see sections 2.3.4 and 2.4.5).[9,12] Of the n-dopants commonly used in OFETs (see section 2.4.5), examples that have been employed in polymer FETs include tetrabutylammonium salts,[211] benzyl viologen[209] and cobaltocene.[210] So far, n-dopants that enable accurate control over all important parameters and, at the same time, do not suffer from at least one of the outlined drawbacks, have remained elusive.

In chapter 5, the GFA compound ttmgb was presented as an efficient contact dopant in SWCNT network FETs. This reducing agent lowers the WF of different metals by approximately 1 eV[315] while improving electron injection and reducing contact resistance. Furthermore, the oxidized compound ($ttmgb^{2+}$), which forms at the electrode surface, was identified as an efficient blocker of hole injection and transport. Additionally, the highly alkaline ttmgb is able to passivate electron traps commonly caused by water adsorbates present in the device.

In this chapter, the influence of the GFA dopants ttmgb and 1,2,4,5-tetrakis(*N,N'*-dimethyl-*N,N'*-ethylene-guanidino)benzene (tdmegb) on the two semiconducting polymers P(NDI2OD-T2) and DPPT-BT in bottom-contact/top-gate FETs is investigated.[322] These two n-dopants feature similar redox potentials but vary drastically with regard to their solubility in organic solvents. Here, their impact on device performance is thoroughly examined depending on the chosen dopant processing, *i.e.*, localization of the dopant. Contact resistance measurements using a gFPP electrode structure help clarify the role of the change in injection behavior upon doping. Lastly, the application potential of this doping approach is explored by bias stress stability measurements conducted in ambient air.

6.2 P(NDI2OD-T2) Field-Effect Transistors

Similar to the architecture using SWCNT networks presented in the previous chapter, bottom-contact/top-gate FETs were fabricated with the predominantly electron transport-

ing yet still slightly ambipolar P(NDI2OD-T2) as semiconductor (molecular structure, see Figure 6.1).
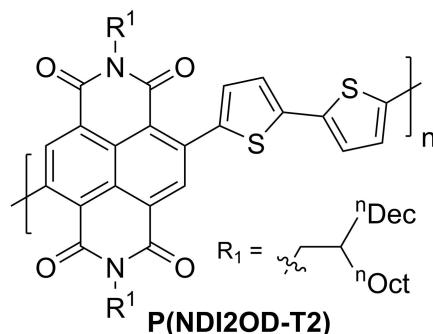
Figure 6.1: Molecular structure of semiconducting polymer P(NDI2OD-T2).

As shown in Chapters 4 and 5, the hybrid dielectric of PMMA and HfO_x helps to minimize the trap density at the interface to the semiconductor and facilitates low-voltage, air-stable operation. Three different options to implement the use of the two GFA dopants ttmgb and tdmegb, *i.e.*, deposition as injection, bulk and top layer, are explored (see Figure 3.6). Brief descriptions of the deposition process are given in the corresponding subsections. For a detailed description of the experimental procedure, the reader is referred to section 3.3.4. The chosen n-dopants ttmgb and tdmegb (molecular structures in Figure 6.2) were deposited by physical vapor deposition in vacuum (both dopants) and by spin-coating (ttmgb).
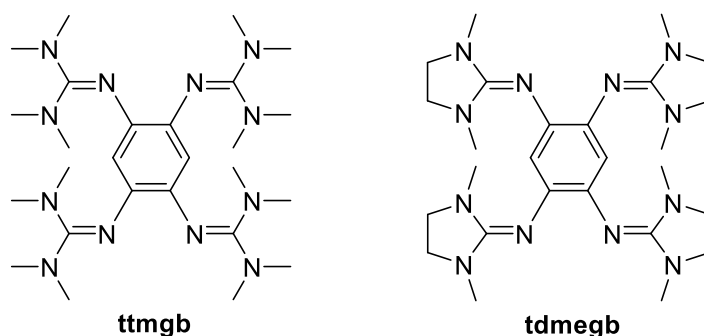
Figure 6.2: Molecular structures of ttmgb and tdmegb.

These two GFA compounds are two-electron donors with similar redox potentials (ttmgb: -0.76 V, tdmegb: -0.79 V vs. Fc/Fc^+, respectively), share a high alkalinity and are able to passivate water-induced trap states. Their solubility behavior, however, differs noticeably. While ttmgb is soluble in a number of organic solvents including the unpolar toluene (solvent used for P(NDI2OD-T2)), tdmegb is only soluble in very polar solvents such as NMP and hardly soluble in toluene, which allows for additional orthogonal processing

options.

Figure 6.3 provides a comprehensive overview over the obtained morphology of representative P(NDI2OD-T2) films treated with all processing methods explored in this study. As expected, the films feature the ribbon-like structures characteristic for P(NDI2OD-T2),[126] which appear mostly unaffected by the dopant molecules, regardless of the processing technique. The only exception to this rule are the samples with spin-coated ttmgb top layers, which is discussed in the corresponding section 6.2.3.
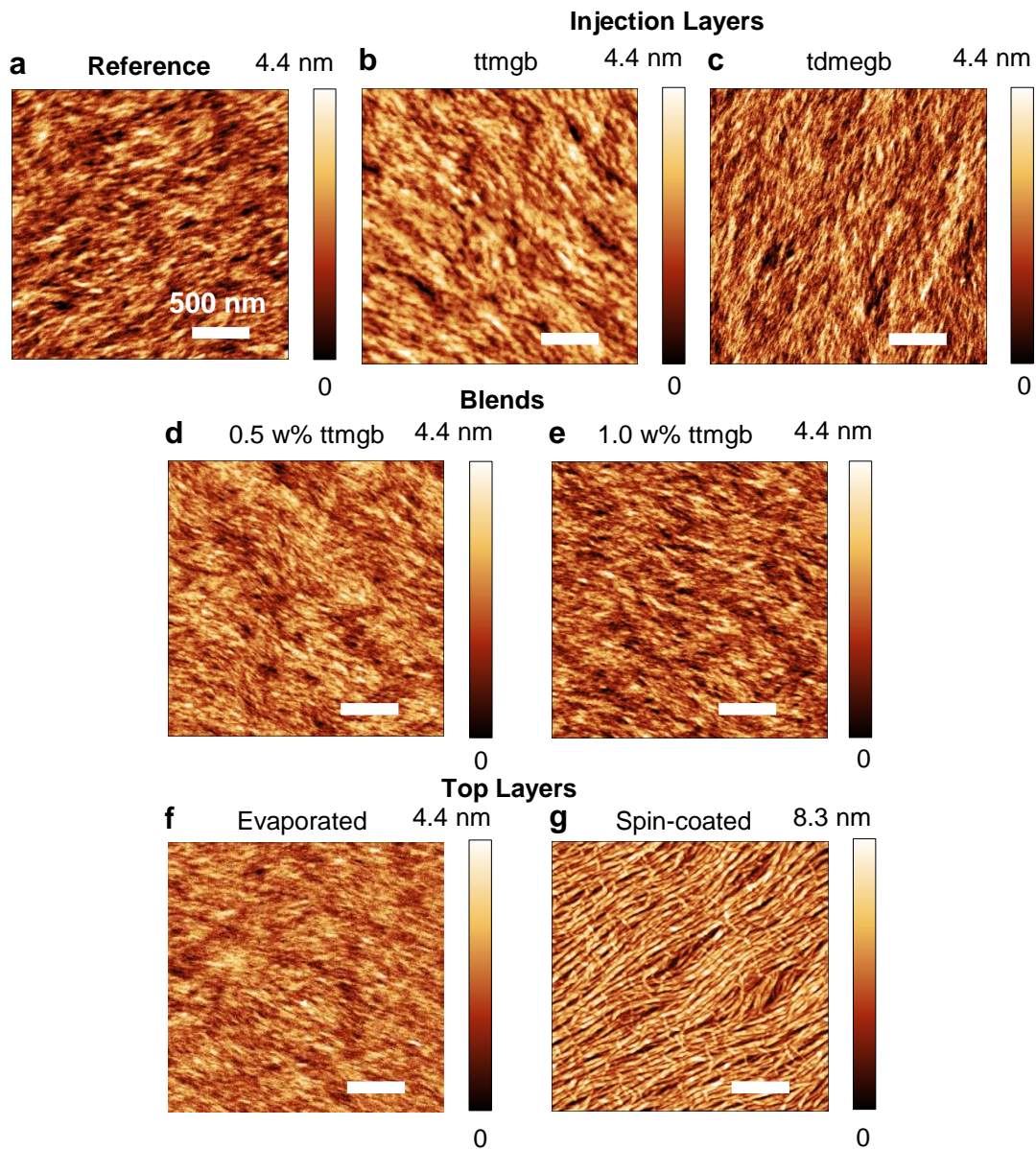
Figure 6.3: AFM images ($2.5{\times}2.5\ \mu m^2$, scale bars 500 nm) of P(NDI2OD-T2) films. (a) Untreated reference sample, P(NDI2OD-T2) films spin-coated on top of (b) ttmgb and (c) tdmegb injection layers. P(NDI2OD-T2)/ttmgb blend layers with (d) 0.5 w% and (e) 1.0 w% ttmgb. P(NDI2OD-T2) films with (f) evaporated and (g) spin-coated ttmgb top layers.

6.2.1 Injection Layers

As displayed in Figure 3.6a, the GFA dopants were deposited on top of the electrodes as injection layers prior to spin-coating the P(NDI2OD-T2) film. Layers of ttmgb were spin-coated from toluene solution while tdmegb was deposited by vapor-processing in high vacuum (experimental details, see section 3.3.4). Figure 6.4 depicts the output characteristics of FETs with ttmgb (see Figure 6.4b,c) and tdmegb (see Figure 6.4e,f) injection layers compared to those of the respective untreated reference sample. The films with thin ttmgb layer reveal a distinctly enhanced electron injection (note the difference in scaling of the y-axis) as illustrated by the corresponding insets (identical y-axis scaling). While, at low drain voltages, the drain currents increase is steeper and more linear, current saturation at high drain voltages remains. For the thicker ttmgb injection layer, a similar behavior is observed.

For the tdmegb injection layers, the injection improvement is even more pronounced for
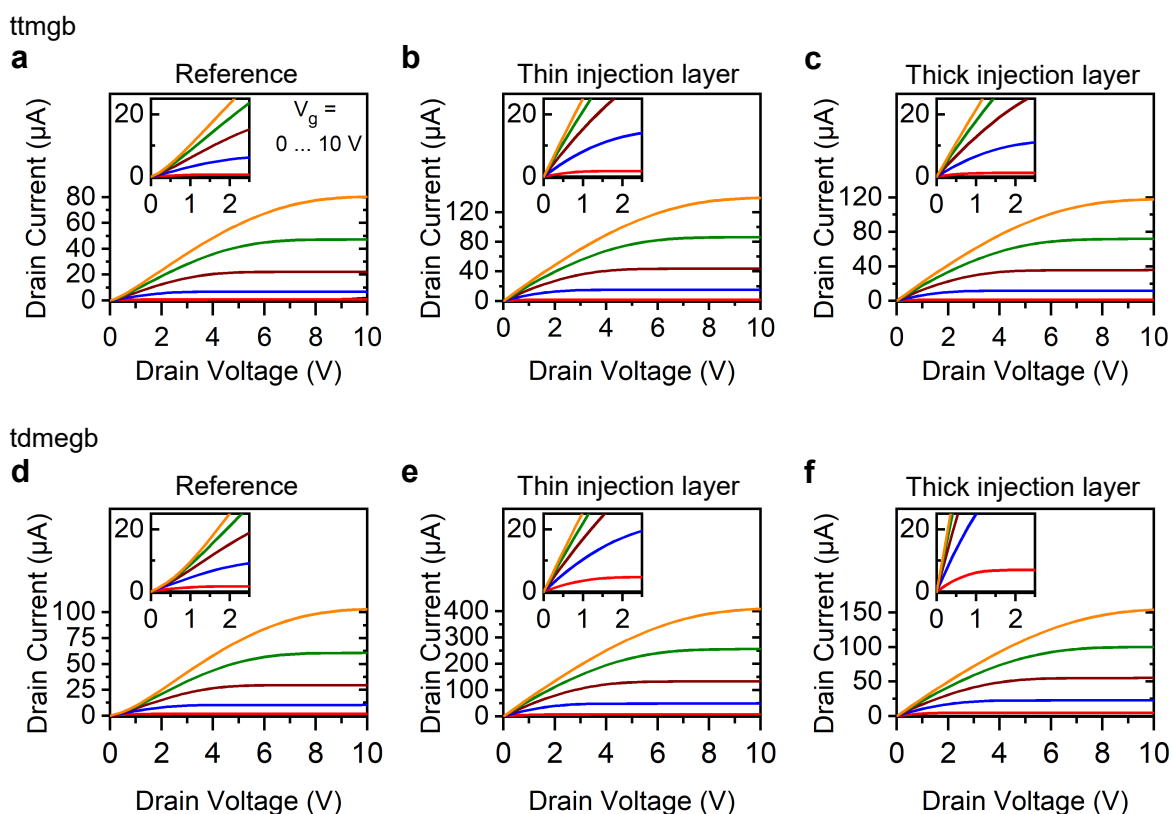
Figure 6.4: Output characteristics (forward and reverse sweeps for positive gate and drain voltages, electron transport) of P(NDI2OD-T2) FETs ($L = 40$ µm, $W = 5$ mm) with $V_g = 0 - 10$ V (steps of 2.0 V) for (a) untreated reference, a sample treated with (b) a thin and (c) a thick injection layer of ttmgb. (d-f) Corresponding data sets for tdmegb injection layers. Insets display zoom-ins on the linear regime (low drain voltage region) to highlight injection properties.

the thin layer in comparison to the corresponding ttmgb layer. The insets demonstrate a

larger increase of the current in the low drain voltage regime. Interestingly, the saturation current remains lower for the thick tdmegb injection layer sample.

In agreement with the increased on-currents observed above, transfer characteristics of
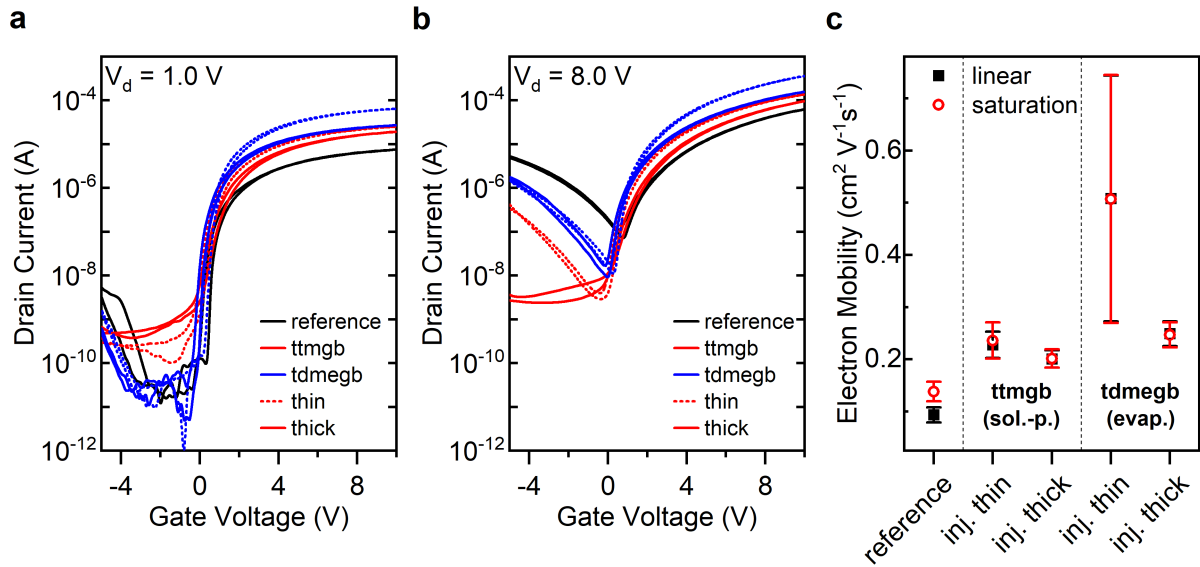
Figure 6.5: Transfer characteristics of P(NDI2OD-T2) FETs ($L = 40$ µm, $W = 5$ mm) with dopant injection layers measured in (a) the linear and (b) the saturation regime. Data correspond to an untreated reference (black) and devices with solution-processed ttmgb (red) as well as evaporated tdmegb thin (dotted lines) and thick layers (solid lines). (c) Electron mobilities corresponding to (a,b) in linear (black squares) and saturation regime (red circles). Error bars denote standard deviation based on at least 8 measured devices.

the samples with injection layers generally exhibit higher electron currents compared to the untreated P(NDI2OD-T2) reference samples in the linear (Figure 6.5a) and saturation regime (Figure 6.5b). While this applies to both dopants, hole currents are more efficiently suppressed by ttmgb as is evidenced by the much lower hole currents at negative gate voltages in the saturation regime. The limited influence of tdmegb on hole injection can most likely be attributed to the poor electrode surface coverage by this dopant as uncovered electrode surface permits injection of positive charge carriers. The impact of ttmgb on hole injection grows with increasing ttmgb film thickness.

The extracted electron mobilities of the reference samples in both transport regimes lie within the usual range of spin-coated, commercially obtainable P(NDI2OD-T2).[130,335] Upon ttmgb treatment, mobility values increase to $0.18 - 0.32$ cm^2 V^{-1} s^{-1}. Crucially, hysteresis remains quite small and onset voltages stay close to 0 V. In contrast to that, treatment with tdmegb leads to a more drastic enhancement of the electron mobilities for the thin injection layer. Unfortunately, this is accompanied by a large increase of the device-to-device variation, which can be attributed to the lack of uniformity in surface

coverage of the gold electrodes even on one substrate. A variety of surface treatments to remedy the non-uniformity of the dopant film, including UV/ozone, polar seeding layers and oxygen plasma treatment, did not lead to the desired improvement in morphology. Altogether, even at incomplete coverage of the injecting gold electrode, treatment with both dopants resulted in the desired drastic enhancement of electron injection from gold into the semiconducting P(NDI2OD-T2). Contrary to that, suppression of the hole current occurred only at higher surface coverage of the electrodes and only efficiently so with ttmgb. Evidently, as demonstrated in previous studies on carbon nanotube network transistors[306,315,316] this effect can be attributed to contact doping as well as a reduction of the gold WF as determined by Kelvin probe experiments[306,315] (see discussion in section 5.3.4). It can be assumed that the presence of the respective GFA compound at this interface has little effect on charge transport given that transport inside the transistor channel takes place at the other interface of the polymer layer (interface to the dielectric). The lack of a shift in onset voltage and the absence of a noticeably increased off-current level, either of which would indicate doping of the semiconductor, are in agreement with this conclusion. The impact of this doping approach on contact resistance and its influence on the electron mobility will be further reviewed in section 6.3.

6.2.2 Blends

An alternative approach to doping semiconducting polymers is to blend a solution of the dopant with the P(NDI2OD-T2) ink prior to deposition. Ideally, this leads to a neutralization of trap states in the bulk of the polymer film.[332,336] Predicated on the absence of phase separation during processing, this may also improve the uniformity of the doping profile. P(NDI2OD-T2) features a characteristic ribbon-like morphology which is not altered by small amounts of hetero-additives.[200] Consequently, direct molecular doping could be a feasible approach. Solutions of the GFA dopant ttmgb and P(NDI2OD-T2) in toluene were intermixed prior to spin-coating (details, see section 3.3.4). The spin-coated films did indeed not display any significant differences to the reference sample (see Figure 6.3d,e). Then, the impact of ttmgb concentration on charge injection and transport was examined. Even at very low concentrations of ttmgb (0.1 w%), electron injection improved drastically. This effect is illustrated in Figure 6.6. Similar to the observations for the injection layers, there is a significantly steeper increase of the drain current in the low drain voltage regime in comparison to the untreated reference sample. Interestingly, this effect does not scale with dopant concentration as evident from the output characteristics of a sample with 2.0 w% ttmgb (see Figure 6.6c).

As shown in Figure 6.7, electron on-currents increase for concentrations up to 0.5 w% (linear regime, see Figure 6.7a) and decrease again for concentrations of 1 w% and 2 w%.
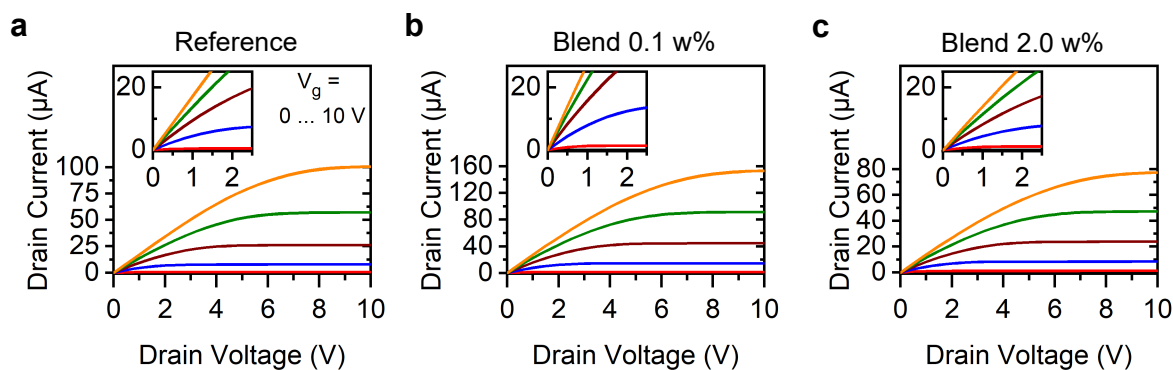
Figure 6.6: Electron output characteristics (forward and reverse sweeps) of P(NDI2OD-T2) FETs ($L = 40$ μm, $W = 5$ mm) obtained from $V_g = 0 - 10$ V with steps of 2.0 V for (a) untreated reference, a blend layer with (b) 0.1 w% and (c) 2.0 w% ttmgb. Insets display zoom-ins on the linear regime (low drain voltage region) to highlight injection properties.

Yet, the latter still exceed the corresponding values of the untreated P(NDI2OD-T2) reference. The increase in off-currents unmodulated by the gate voltage observed for concentrations starting from 0.5 w% implies an unwanted transfer of electrons from ttmgb to P(NDI2OD-T2). Noticeably, the ionization potential of the dopant depends on its dielectric environment (3.7 – 4.2 eV).[260] Hence, it is conceivable that electrons may transfer to P(NDI2OD-T2) (LUMO of -4.0 eV).[337] The minor shift in onset voltage (-0.7 V) and the significantly decreased subthreshold slope observed for the sample with the highest ttmgb concentration (2.0 w%) in comparison with the untreated reference corroborate this hypothesis.[330] Contrary to the injection layers, it is reasonable to deduce a potential direct impact on charge transport caused by the presence of ttmgb at the semiconductor-dielectric interface. In the saturation regime, on-currents display a trend identical to the linear regime as is shown in Figure 6.7b. In contrast to that, the suppression of hole current at negative gate voltages increases with ttmgb concentration. This is in agreement with the above mentioned notion that the suppression of the hole current becomes more efficient with increasing surface coverage of the injecting electrode by the dopant.

Electron mobilities were extracted for all dopant concentrations investigated. They are displayed in Figure 6.7c as relative mobilities referenced to the untreated P(NDI2OD-T2) sample. The highest relative mobility is obtained for the sample with a concentration of 0.4 w% (respective absolute values are in the range of 0.20 – 0.33 cm^2 V^{-1} s^{-1}). For larger concentrations, however, the mobility increase is not as strong. The increase in the saturation mobilities is less pronounced compared to the linear mobilities; most likely due to the smaller impact of contact resistance on the saturation currents. Despite the absence of any significant differences in film morphology (see Figure 6.3d,e), the lower performance improvements for higher ttmgb concentrations may be attributed to a disturbance of the stacking of the P(NDI2OD-T2) polymer backbone.
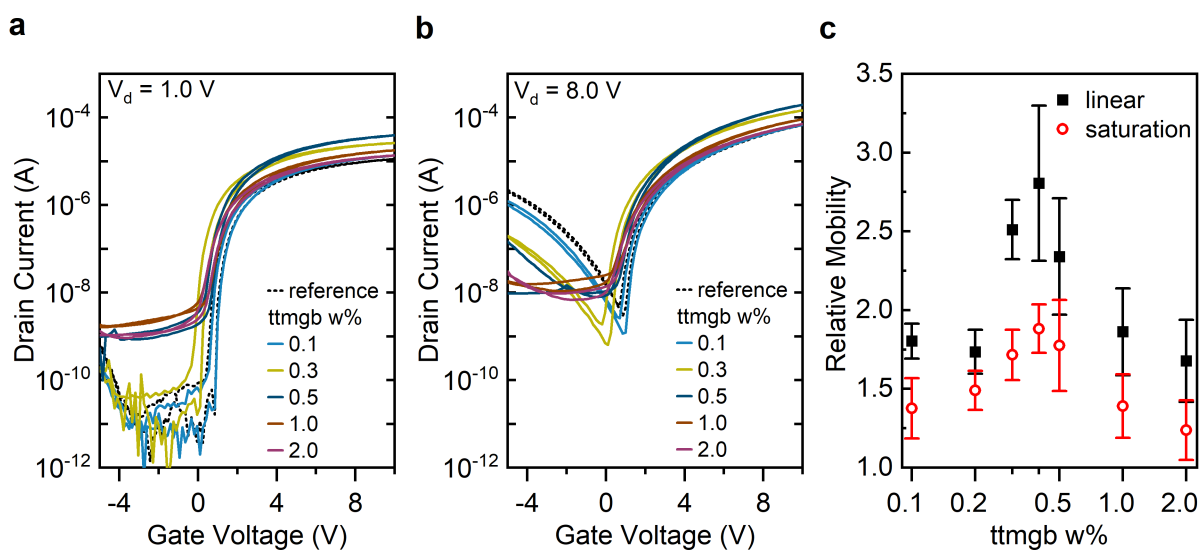
Figure 6.7: Transfer characteristics of P(NDI2OD-T2)/ttmgb blend FETs ($L = 40$ µm, $W = 5$ mm) measured in (a) the linear and (b) the saturation regime corresponding to an untreated reference sample and blends with concentrations of ttmgb in the range of 0.1 – 2.0 w%. (c) Relative electron mobilities of the P(NDI2OD-T2)/ttmgb blends in comparison to the untreated reference sample extracted for linear (black squares) and saturation regime (red circles). Note: log-scale for ttmgb concentration. Error bars denote standard deviation based on at least 8 measured devices.

Overall, the P(NDI2OD-T2)/ttmgb blend layers at optimized concentrations indeed result in the desired improvements of device performance. Unfortunately, the sought low off-current levels are not reached. The causes are probably incomplete blocking of hole injection and transport at low dopant loading and undesired electron transfer from ttmgb to P(NDI2OD-T2) at high dopant concentrations.

6.2.3 Top Layers

The deposition of a dopant (solution- or vapor-processed) on top of the semiconductor with subsequent diffusion into the semiconducting layer is another option to achieve doping. For the selected device architecture, *i.e.*, bottom-contact/top-gate, this results in a positioning of the dopant at the semiconductor-dielectric interface – the location of charge accumulation. It might hence affect the charge transport within the transistor channel. An impact on charge injection, however, appears less likely. Deposition of ttmgb on top of the P(NDI2OD-T2) layer was conducted either by vapor processing in high vacuum or by spin-coating a solution in toluene. Due to the high solubility of P(NDI2OD-T2) in all possible solvents for ttmgb, intermixing and thus partly dissolving the pre-deposited polymer layer are likely detrimental effects. It would likely lead to severely diminished polymer film thicknesses and disruption of the polymer film morphology.

The output characteristics of devices prepared as described in section 3.3.4 are depicted in

Figure 6.8. They reveal that the evaporated ttmgb top layer results in enhanced electron injection with high similarity to the doping approaches outlined above – albeit to a lesser extent. Interestingly, this applies mostly to the low drain voltage regime.

The respective transfer characteristics in the linear (Figure 6.9a) and saturation regime
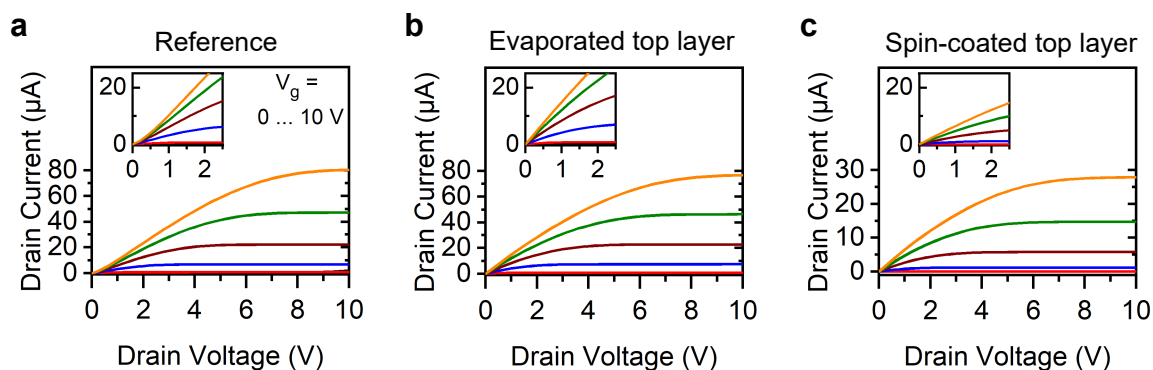
Figure 6.8: Electron output characteristics (forward and reverse sweeps) of P(NDI2OD-T2) FETs ($L = 40$ µm, $W = 5$ mm) obtained from $V_g = 0 - 10$ V with steps of 2.0 V for (a) untreated reference, a sample treated with (b) an evaporated and (c) a spin-coated top layer of ttmgb. Insets display zoom-ins on the linear regime (low drain voltage region) to highlight injection properties.

(Figure 6.9b) support this observation. Contrary to expectations, this indicates presence of the dopant at the electrode-semiconductor interface. Diffusion of ttmgb across the P(NDI2OD-T2) film to the gold electrodes – potentially facilitated by the solvent *n*-butyl acetate during deposition of the PMMA dielectric layer – might be a possible explanation. Concomitantly, the off-current level increases in the linear regime. Unfortunately, in the saturation regime hole injection is only partially suppressed. While the linear electron mobility is enhanced, the corresponding values in the saturation regime lie within the range of the untreated reference sample (see Figure 6.9c). Again, this larger impact on the linear regime hints at a potential decrease in contact resistance (see discussion in section 6.3).

The spin-coated ttmgb layer on top of P(NDI2OD-T2) led to rather different observations. Despite careful attention to optimizing the fabrication conditions, these transistors still featured somewhat smaller electron on-currents in comparison to the untreated reference (see Figure 6.9b, c). Furthermore, it is noteworthy that they exhibit a flatter subthreshold slope hinting at an increase in trap state density.[220,330] This reduced performance might be explained by the diminished semiconductor film thickness. Indeed, the morphology of the P(NDI2OD-T2) exhibits drastic changes as demonstrated by AFM analysis (see Figure 6.3g). The layer thickness decreased to 7 nm (corresponding reference 30 nm) while the roughness increased significantly. Various optimization experiments were carried out (*e.g.*, spin-coating parameter screening, change of ttmgb solvent) but remained unsuccessful. Doping of the semiconductor appears unlikely given the lack of shift in onset voltage. One
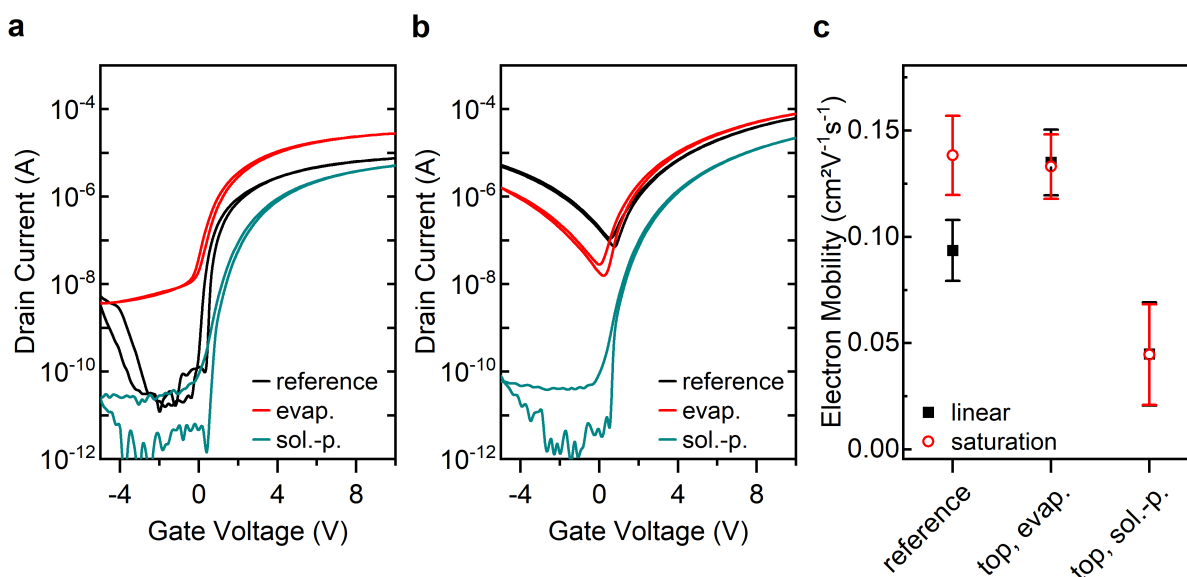
Figure 6.9: Transfer characteristics of P(NDI2OD-T2) FETs ($L = 40$ μm, $W = 5$ mm) with dopant top layers measured in (a) the linear and (b) the saturation regime. Data correspond to an untreated reference sample (black), devices with evaporated (red) and solution-processed ttmgb (blue) top layers. (c) Electron mobilities corresponding to (a,b) in linear (black squares) and saturation regime (red circles). Error bars denote standard deviation based on at least 10 measured devices.

can assume that partial dissolution of P(NDI2OD-T2) during the spin-coating of ttmgb leads to this degradation which is also reflected in the lower electron mobility (see Figure 6.9c).

In summary, depositing ttmgb on top of P(NDI2OD-T2) resulted in only very moderate performance improvements for the vapor-processed ttmgb sample. While, somewhat surprisingly, hole blocking was most efficient in the spin-coated ttmgb top layer (among all processing options including injection and blend layers), it also led to a detrimental reduction of the semiconductor film thickness and, ultimately, lower electron currents compared to untreated reference transistors.

6.3 Contact Resistance

Determination of the contact resistance enables an in-depth analysis of the effect of the used GFA dopants on electron injection in P(NDI2OD-T2) transistors. A gFPP device layout (background, see section 2.4.2, dimensions and layout, see section 3.3.1) served as the basis for the extraction of the gate voltage-dependent, width-normalized contact resistance and electron mobilities in the linear regime corrected for contact resistance. For this, a method established by Pesavento *et al.* was employed.[226,227]

While the unpatterned P(NDI2OD-T2) films (patterning of the semiconducting layer was not performed) can potentially lead to an overestimation of contact resistance,[227] an overall comparison of the obtained values is still reasonable as the layout applied for all samples was the same and the precision in alignment of gate electrode and channel area was high. The width-normalized contact resistance values are displayed in Figure 6.10 as as function of gate voltage.
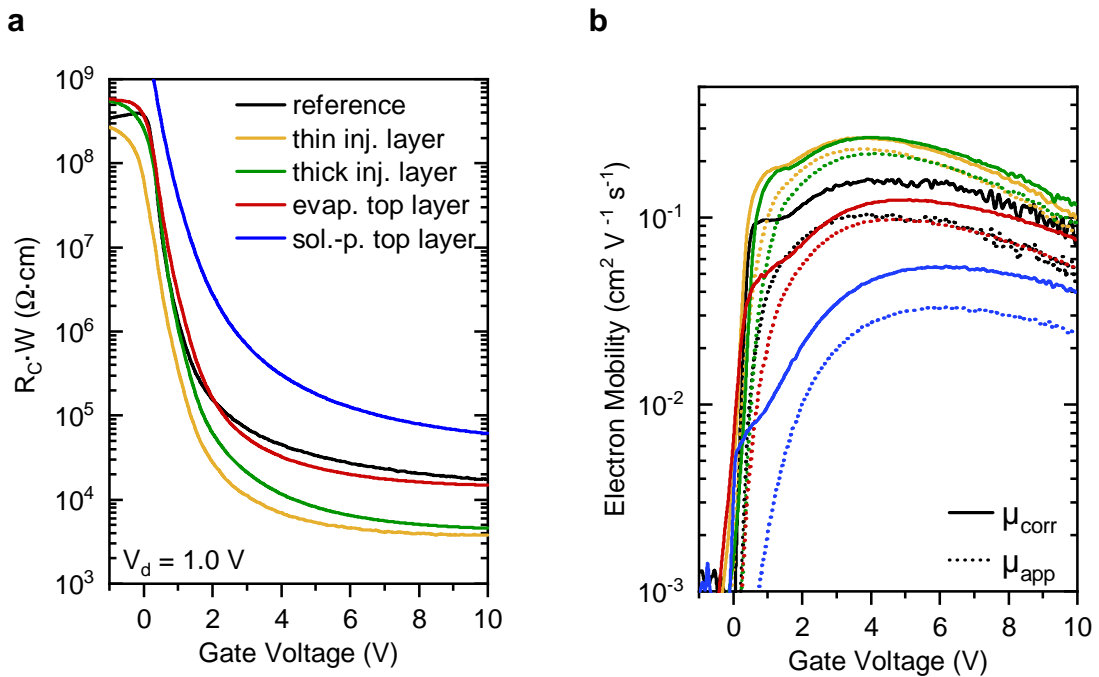
Figure 6.10: (a) Width-normalized contact resistances of P(NDI2OD-T2) FETs ($L = 40$ µm, $W = 1$ mm) as a function of gate voltage. Data was extracted using the gFPP method in the linear regime for an untreated reference device and samples with dopant ttmgb deposited before (thin, thick injection layer) or after the semiconducting polymer (evaporated or solution-processed top layer). (b) Gate voltage-dependent apparent (μ_{app}, dotted lines) and contact resistance-corrected (μ_{corr}, solid lines) electron mobilities for devices corresponding to (a).

All contact resistance values lie within the range of values previously reported for top-gated P(NDI2OD-T2) FETs[338] and, in agreement with expectations, drop with increasing gate voltage. In general, injection layers of ttmgb resulted in a distinct drop of the contact resistance by roughly one order of magnitude in comparison to the untreated reference transistors. In contrast to that, the evaporated ttmgb top layer produced only a very modest decrease in contact resistance, which is in agreement with the only moderate performance improvements (see section 6.2.3) evident from output and transfer characteristics. Even more so, the spin-coated ttmgb top layer led to an increased contact resistance. This can most likely be attributed to the reduced P(NDI2OD-T2) film thickness resulting from the

dissolution of the polymer in the dopant solvent. A lower injection efficiency might be caused by imperfect coverage of the electrodes in accordance with previous findings.[220] The apparent (not corrected for contact resistance) and the contact resistance-corrected electron mobilities extracted in the linear regime for the various doping techniques exhibit only minor differences, particularly for high gate voltages. This indicates a limited impact of the dopant on charge transport across the channel corroborating the classification of the used doping scheme as contact doping.

6.4 Environmental Stability

The environmental stability of OFETs has been identified as a key factor in literature, particularly with regard to application and commercialization.[201,339] This relates to the chemical stability of both materials and the operational stability of the device, for example dopant diffusion. Although ttmgb is sufficiently stable to permit handling in air for brief amounts of time, all relevant device fabrication steps were conducted in dry nitrogen atmosphere. As has been shown in Chapter 5, the PMMA/HfO$_x$ hybrid dielectric can serve as a self-encapsulant for the FETs.
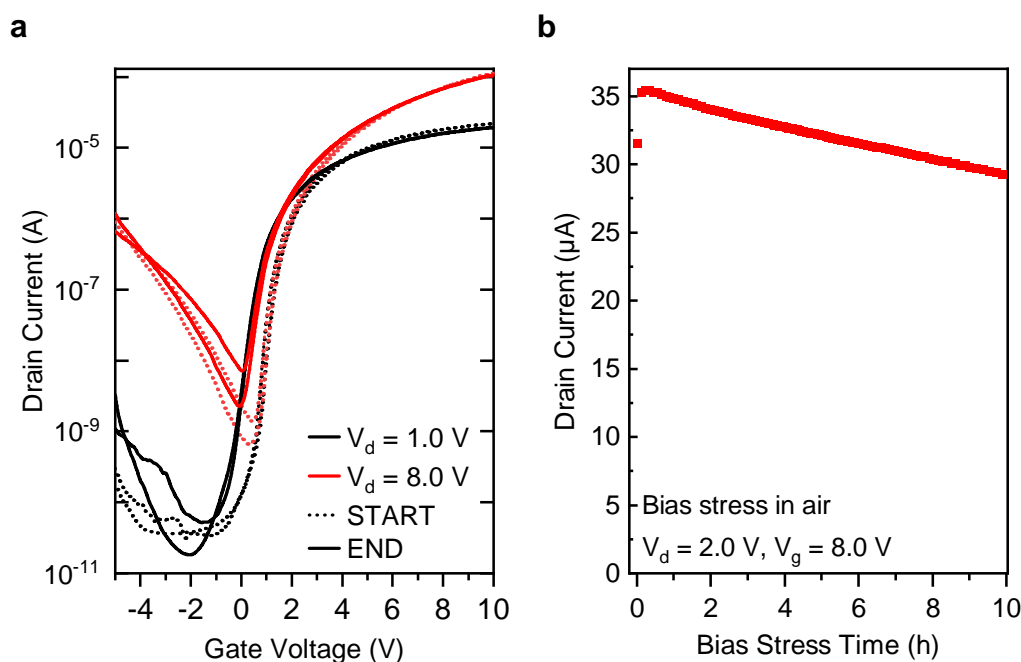
Figure 6.11: (a) Transfer characteristics of a P(NDI2OD-T2) FET ($L = 40$ µm, $W = 1$ mm) with a thin ttmgb injection layer measured in ambient air prior to (dotted lines) and after (solid lines) subjecting the device to continuous bias stress for 10 h ($V_d = 2.0$ V, $V_g = 8.0$ V). Black lines correspond to measurements in the linear regime, red lines to the saturation regime. (b) Drain current in the on-state during operation under continuous bias stress.

In order to put the stability of P(NDI2OD-T2) transistors with ttmgb injection layers to the test, they were measured in ambient atmosphere under continuous bias stress (V_d = 2.0 V, V_g = 8.0 V) for 10 h. Figure 6.11a displays transfer curves collected directly prior to and after the bias stress period in both linear and saturation regime. A direct comparison of these characteristics reveals outstanding stability, almost without any changes in hysteresis as well as in on- and off-currents. There is only a minor shift in onset voltage (approximately -0.7 V). As demonstrated in Figure 6.11, the on-current remains at over 90 % of its initial value after 10 h of continuous stress. These observations exclude any undesired diffusion or degradation of ttmgb under bias stress conditions. These data emphasize the suitability of ttmgb for use as a contact dopant in polymer FET applications.

6.5 DPPT-BT Field-Effect Transistors

To fully explore the potential of GFA dopants for application with other polymeric semiconductors in addition to the established P(NDI2OD-T2), an investigation of DPPT-BT, a narrow bandgap polymer with a diketopyrrolopyrrole acceptor unit, was conducted (molecular structure, see Figure 6.12).[212] DPPT-BT exhibits ambipolar transport but with higher
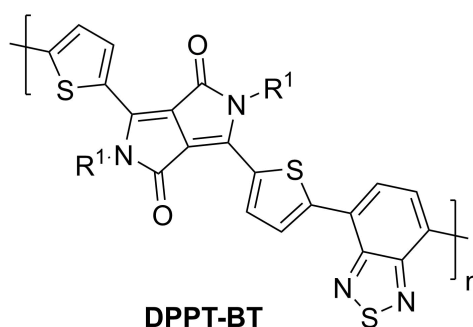
Figure 6.12: Molecular structure of semiconducting polymer DPPT-BT.

electron than hole mobility – normally approx. one order of magnitude difference.[122,340] Brief descriptions of the dopant processing conditions are outlined in the subsections while the corresponding experimental details are given in sections 3.3.3 and 3.3.4. As a general observation, DPPT-BT film morphology remained largely unaffected. This is illustrated in the AFM images in Figure 6.13 by ttmgb – regardless of the chosen dopant deposition method.
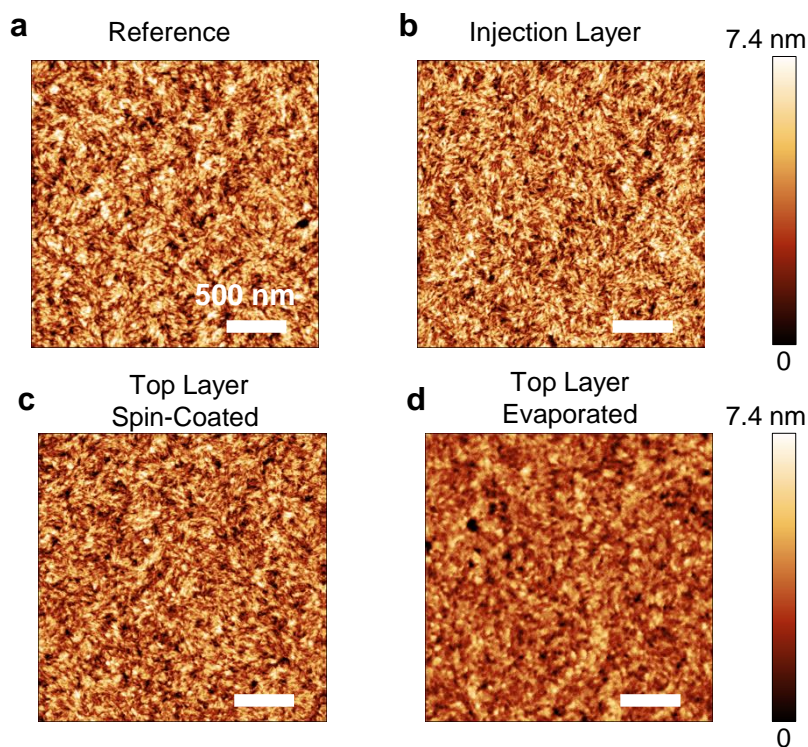
Figure 6.13: AFM images (2.5×2.5 µm^2, scale bars 500 nm) of DPPT-BT films. (a) Untreated reference sample, (b) DPPT-BT film with ttmgb injection layer, (c) spin-coated and (d) evaporated ttmgb top layers.

6.5.1 Injection Layers

Given the successful application of GFA dopants as injection layers for P(NDI2OD-T2), this approach served as the starting point for DPPT-BT. However, the solvent of choice for DPPT-BT, chlorobenzene, results in partial dissolution of the pre-deposited ttmgb layer. This ttmgb film degradation is reflected in only modest performance improvements in general. Firstly, note that the overall lower currents in comparison with the P(NDI2OD-T2) samples are due to an altered electrode layout (experimental details see section 3.3.1). The untreated reference displays non-ohmic electron injection (see Figure 6.14a) as evident from the characteristic S-shape in the output curve at low drain voltages. While the injection of electrons is enhanced, even for a thick ttmgb injection layer there is only a moderate increase in electron on-current (see Figure 6.14b,c). These observations are corroborated by the transfer characteristics in the linear (Figure 6.15a) and saturation regime (Figure 6.15b). The apparently lower effect of the ttmgb treatment in the saturation regime is in agreement with ttmgb acting as a contact dopant. The lack of suppression of hole injection and transport, particularly at high drain voltages can also be attributed to the poor coverage of the bottom electrodes by ttmgb stemming from the partial removal of the dopant layer during processing.
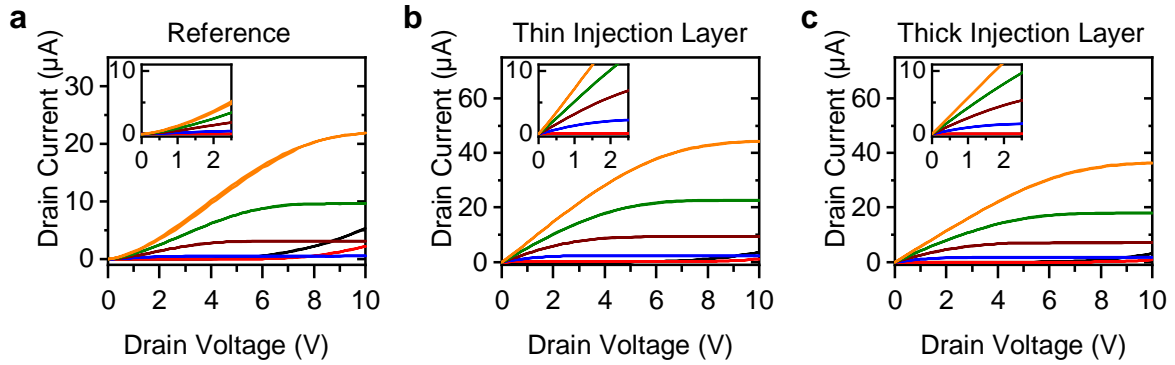
Figure 6.14: Electron output characteristics (forward and reverse sweeps) of DPPT-BT FETs ($L = 42$ µm, $W = 1.5$ mm) obtained from $V_g = 0 - 10$ V with steps of 2.0 V for (a) untreated reference, a sample treated with (b) a thin and (c) a thick injection layer of ttmgb. Insets display zoom-ins on the linear regime (low drain voltage region) to highlight injection properties.
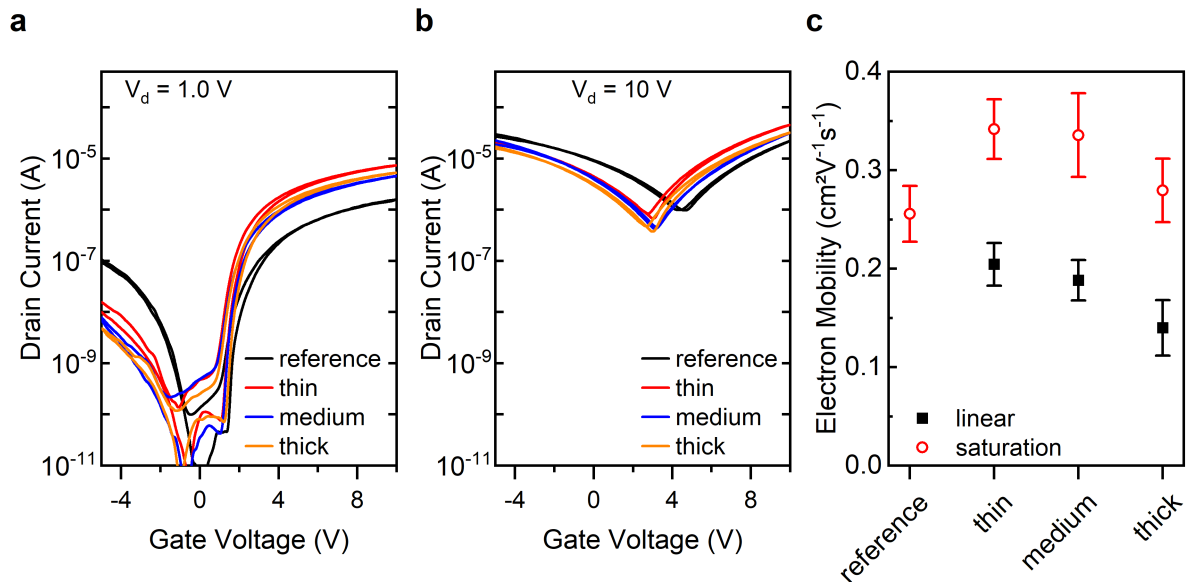
Figure 6.15: Transfer characteristics of DPPT-BT FETs ($L = 40$ µm, $W = 5$ mm) with ttmgb injection layers measured in (a) the linear and (b) the saturation regime. Data correspond to an untreated reference sample (black), devices with solution-processed thin (red), medium (blue) and thick (organge) ttmgb injection layers. (c) Electron mobilities corresponding to (a,b) in linear (black squares) and saturation regime (red circles). Error bars denote standard deviation based on at least 8 measured devices.

Electron mobilities (see Figure 6.15) were determined to be within the range of reported literature values.[122,212] Due to the large non-ohmic contact resistance at low drain voltages the corresponding values in the linear regime could not be extracted. Lastly, the slight decrease in electron mobility with higher dopant film thickness (1 – 4 nm, see section 3.3.4) makes further experiments with increased dopant film thickness obsolete. One may speculate that the intermixing of ttmgb with DPPT-BT interferes with the stacking of

the polymer and thus negatively affects charge transport.

In conclusion, ttmgb injection layers lead to only limited improvements in DPPT-BT FETs.

6.5.2 Top Layers

Given the very low solubility of DPPT-BT in toluene, the solvent for ttmgb, the dopant was also applied on top of DPPT-BT using both thermal evaporation and spin-coating as deposition techniques. As illustrated above (Figure 6.13c,d), there was no significant impact by the dopant on polymer morphology or thickness (30 nm) for either deposition method.

The output characteristics (Figure 6.16) reveal that the dopant top layer does indeed improve the poor injection behavior (S-shape of electron current at low drain voltages) of the untreated reference to a linear increase for the same voltage regime while saturation at high drain voltages remains. This enhancement is accomplished with both deposition techniques, although only the vapor processing of the dopant leads to a strong increase in on-currents.
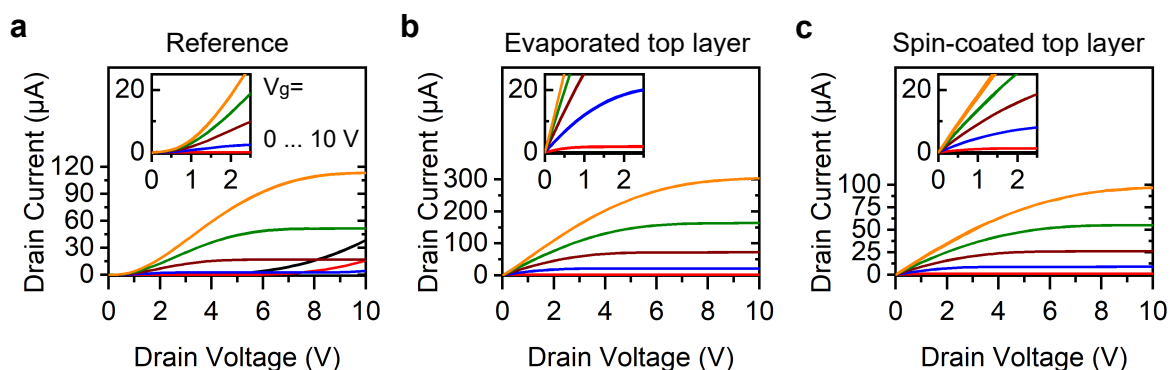
Figure 6.16: Electron output characteristics (forward and reverse sweeps) of DPPT-BT FETs ($L = 40$ µm, $W = 5$ mm) obtained from $V_g = 0 - 10$ V with steps of 2.0 V for (a) untreated reference, a sample treated with (b) an evaporated and (c) a spin-coated top layer of ttmgb. Insets display zoom-ins on the linear regime (low drain voltage region) to highlight injection properties.

The transfer characteristics (Figure 6.17a, b) indicate a significant decrease of hole injection and transport for both dopant deposition methods, however, to a larger extent for the solution-processed sample. As expected, the degree of hole blocking increases with dopant layer thickness (see Figure 6.17b).

The on-currents peak at slightly higher values compared to the untreated reference, which can be attributed to a small shift in onset voltage (approximately -0.4 V). As depicted in Figure 6.17c, the electron mobilities mostly stayed within the range of $0.3 - 0.5$ cm^2 V^{-1} s^{-1}
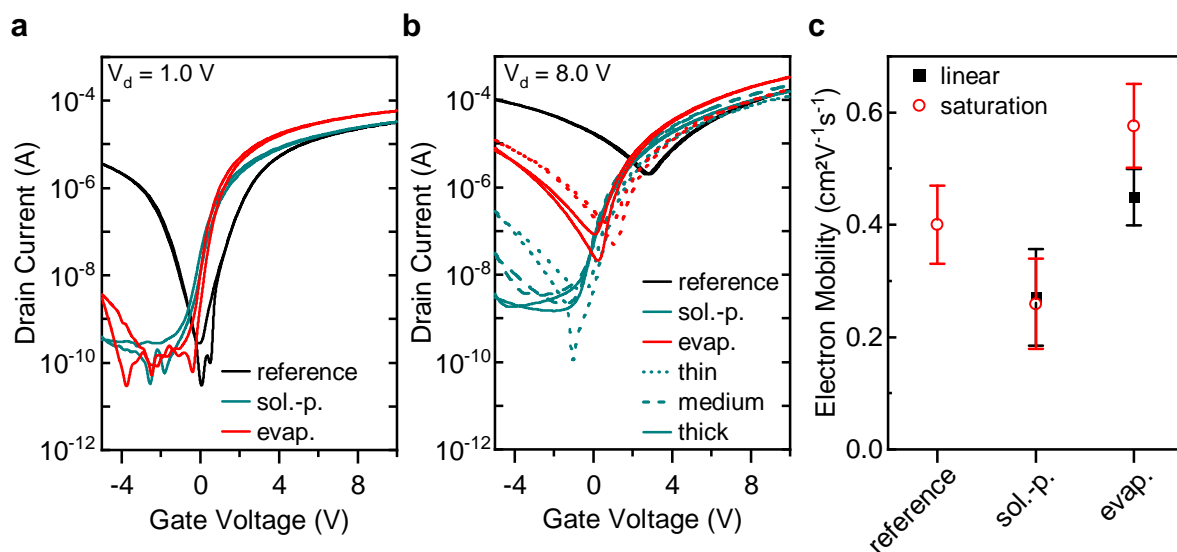
Figure 6.17: Transfer characteristics of DPPT-BT FETs ($L = 40$ µm, $W = 5$ mm) with ttmgb top layers measured in (a) the linear and (b) the saturation regime. Data correspond to an untreated reference sample (black), devices with solution-processed (blue) and evaporated (red) ttmgb top layers. (c) Electron mobilities corresponding to thick ttmgb layers (a,b) in linear (black squares) and saturation regime (red circles). Error bars denote standard deviation based on at least 10 measured devices.

comparable to values reported in literature.[122,340]

Similar to the discussion for the P(NDI2OD-T2) FETs, it is reasonable to assume that ttmgb might diffuse through the polymer film. This is in agreement with the enhanced electron injection and suppression of hole injection even though the dopant was deposited on top of the polymer – on the opposite side of the interface to the gold electrodes. Such diffusion could lead to the observed effects, *i.e.*, contact doping at the injecting electrodes and potentially a reduction of the bulk resistance of the DPPT-BT film above the contacts and hence a decrease of the overall contact resistance in such staggered FETs.[220] It is not yet clear if degenerate doping of DPPT-BT by ttmgb is indeed a possible pathway. The DPPT-BT LUMO lies marginally higher (-3.8 eV)[340] than the value of P(NDI2OD-T2). Concomitantly, DPPT-BT supplies an environment with higher polarity resulting in a diminished ionization potential of the dopant.[260]

A reliable extraction of the electron mobility in the linear regime was not possible given the non-linear increase of electron current at low drain voltages. Whereas the spin-coating of ttmgb resulted in a moderate decrease in mobility in the saturation regime compared to the reference sample without dopant, the thick ttmgb layer deposited by evaporation produced an increase of electron mobility with peak values exceeding 0.6 $cm^2\,V^{-1}\,s^{-1}$.
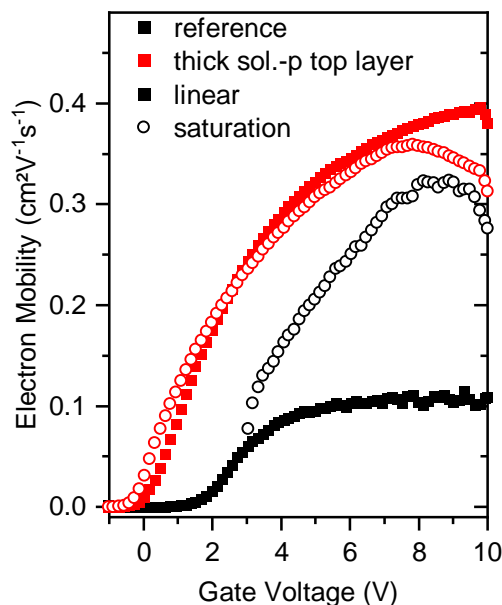
Figure 6.18: Electron mobilities as a function of gate voltage determined for DPPT-BT FETs ($L = 40\,\mu m$, $W = 5\,mm$) corresponding to untreated reference (black) and a device with a thick solution-processed ttmgb top layer (red). Filled squares correspond to measurements in the linear regime, empty circles to the saturation regime.

Figure 6.18 displays the electron mobility in both transport regimes as a function of gate voltage.

In conclusion, the GFA compound ttmgb can indeed be employed (top layer architecture) to change the commonly ambipolar behavior of DPPT-BT FETs to solely n-type transistors with significant improvements in electron injection. In contrast to P(NDI2OD-T2), for which the solution-processed dopant top layer led to undesired effects, most importantly a decrease in electron mobility, the deposition of ttmgb on top of the polymer resulted in the best performance of DPPT-BT FETs. While the best performance for P(NDI2OD-T2) was achieved with injection layers, this processing approach did not result in significant improvements for DPPT-BT. This highlights that the incorporation of the dopant into a device not only depends on the energetic alignment of dopant and semiconductor but also on a parameters that include, *e.g*, solubility, processing technique, morphology of either component. Careful optimization for either material combination is thus mandatory.

6.6 Summary and Conclusions

In this chapter, the impact of the GFA compounds ttmgb and tdmegb as n-dopants in polymer FETs on charge injection and transport has been investigated. As a new addition

to the previously demonstrated use in FETs with single-walled carbon nanotube networks as active material,[306,315,316] these dopants lead to more efficient electron injection and transport in the semiconducting polymers P(NDI2OD-T2) and DPPT-BT. Significant improvements in electron injection as well as blocking of hole injection and transport was achieved upon treatment with these two dopants.

Depending on the doping method (injection, blend or top layer), processing conditions were carefully optimized. In the best cases, they yielded solely n-type FETs with significantly decreased contact resistance and improved electron mobilities compared to the undoped reference transistors. At the same time, by focussing on contact rather than channel doping, high on/off current ratios were accomplished, hysteresis remained low and undesired onset voltage shifts were prevented. Measurements in air under continuous bias stress revealed excellent device stability. These findings underline the versatility of GFA compounds as dopants in organic field-effect transistors. They illustrate the significance of investigating various feasible processing options for both molecular dopants and the semiconducting polymer in a device rather than an exclusive focus on the redox potential of the compounds involved.

Chapter 7

CONCLUSION AND OUTLOOK

This chapter recapitulates on the findings of this thesis and discusses potential future research for n-doping of carbon-based semiconductors.

Prior to the start of this thesis SWCNTs had already undergone a long development from a laboratory curiosity to a candidate for numerous electronics applications with realistic commercial potential. Dispersions of semiconducting SWCNTs had finally reached purity levels sufficient to overcome the previously assumed inevitable trade-off between high charge carrier mobilities and high on/off current ratios. Concomitantly, SWCNT ink production was successfully scaled up for solution-processed devices. However, significant challenges remained that included inhomogeneity in device performance caused by the tendency of the nanotubes to form aggregates as well as the overall inferior device performance of n-type transistors compared to their p-type counterparts. The poor stability of n-type semiconductors led to inferior device stability. In addition, high barriers for electron injection with high contact resistances hinder efficient charge injection and result in lower on-currents. These limitations must be overcome to harness the full potential of SWCNT network FETs in large-scale circuit applications. The latter limitation of inferior n-type transistor performance is also highly relevant for other solution-processable semiconductors such as semiconducting polymers. This thesis provides approaches that represent a substantial step forward to overcome these issues.

The small-molecule additive 1,10-phen was introduced as a stabilizer for dispersions of (6,5) SWCNTs prepared by polymer wrapping in organic solvents. Time-dependent UV-vis-NIR spectroscopy served as a simple yet effective tool to monitor the aggregation process and assess SWCNT ink quality. The decrease in the E_{11} absorption intensity over time was established as a reliable metric to quantify the progress of aggregation. SWCNT networks deposited from inks with and without 1,10-phen stabilizer resulted in a good agreement between the spectroscopic assessment and the observed film homogeneity. With advancing ink age (up to one week), the number of aggregates and nanotube bundles increased. This successful correlation facilitates screening for other additives suitable for, *e.g.*, SWCNTs with larger diameters or adaptations of the processing conditions such as a different solvent or wrapping polymer. Due to the high nephrotoxicity of 1,10-phen scaling up the dispersion volume for large-area processing may require a more environmentally compatible additive with similar stabilization properties.

The nanotube networks deposited from inks with and without stabilizer were incorporated as active material into FETs. The comparison of the inks with 1,10-phen to those without additive as well as dispersions with higher-viscosity solvents revealed a significant decrease of device-to-device variation for samples prepared with the 1,10-phen stabilized SWCNT dispersions. This trend became more pronounced with increasing ink age. The presented ink formulation approach is cost-efficient and does not require any additional processing steps. It thus constitutes a substantial step forward toward more reliable device fabrication, which is mandatory to realize the desired transition of SWCNTs from the scientific

laboratory to commercialization.

Preliminary tests with phenanthroline additives in dispersions with larger-diameter SWC-NTs displayed a similar albeit somewhat weaker stabilization effect. These nanotubes are preferred for maximum performance in FETs as they exhibit higher charge carrier mobilities and have been used to demonstrate applications such as a nanotube computer, large-scale integrated circuits or microprocessors.[7,188,304]

In addition to the improvements for more reliable device fabrication, the demonstrated method might be of wide-spread interest for working with SWCNT dispersions. The current conventional strategy of breaking up aggregates, *i.e.*, repeated sonication, has its limitations as extended sonication periods inevitably entail damage to the nanotubes. In a recent project, 1,10-phen was demonstrated to stabilize SWCNT dispersions in a very polar environment (solution of 1,3,5-trichlorobenzene in chloroform) to enable deposition of aligned SWCNT networks by zone-casting.[341] Given that aggregation strongly affects electronic as well as optical properties, dispersions with long-lasting stability also extend the time frame of spectroscopic experiments, which are otherwise limited due to perturbations caused by aggregation. For example, transient absorption measurements require high SWCNT concentrations and often long measurement times.[342]

The GFA compound ttmgb was introduced to address the prevailing limitations of carbon-based n-type transistors. The strongly reducing ttmgb served as a contact dopant for the conversion of (6,5) SWCNT network transistors from ambipolar to unipolar n-type charge transport behavior. An electron transfer from ttmgb to the gold electrodes leads to a substantial decrease of the gold WF, thus improves electron injection by lowering the injection barrier with reduced contact resistance. The oxidized ttmgb^{2+}, that forms at the electrode-semiconductor interface, serves as an efficient hole blocking agent. The ttmgb treatment hence leads to high apparent electron mobility, excellent switching behavior with high on/off current ratios and low subthreshold swings. At the same time, hole injection and transport are fully suppressed.

The noteworthy absence of hysteresis even in ambient conditions in the I-V-characteristics of these devices can be attributed to trap passivation caused by ttmgb. Polar adsorbates such as water, that act as electron traps, are neutralized by virtue of the high alkalinity of ttmgb. In a subsequent study,[315] trap densities in such networks were found to decrease approximately seven- to eight-fold upon treatment with ttmgb.

The proof-of-concept complementary inverters using p- and n-doped nanotube network transistors display rail-to-rail operation with high gains and low power consumption. Importantly, the good stability of the devices during bias stress operation in air highlights the application potential of doping with ttmgb.

The applicability of doping with ttmgb to large-diameter SWCNTs as well as high WF

electrode metals further underline the versatility of this dopant.[315] (6,5) SWCNT networks treated with ttmgb also served as a trap-free reference in temperature-dependent, gated Seebeck measurements. This helped to establish fundamental guidelines for the optimization of charge and thermoelectric transport in SWCNT networks.[316] Further studies on fundamental properties that need networks free of electron traps might become feasible, such as investigations on the trion formation in SWCNT network FETs.

An important limitation of the presented ttmgb doping approach lies in the processing of the dopant. The employed dip-coating process leads to inhomogeneities in the film as crystallites of different size form during the annealing process. This inevitably leads to device-to-device variations that are not an issue for laboratory-scale investigations but would likely be an obstacle relying on near-unity device yield in large-area processing.

More defined layers and homogeneous layers could in principle be achieved by evaporation of the dopant in high vacuum but the unfavorable film formation properties and high solubility of ttmgb in most solvents impose strong restrictions on the processing options. A possible strategy to overcome this limitation is the synthetic modification of the dopant.[261] Different side chains in GFAs can be used to alter their solubility to allow for orthogonal processing. Ideally, simultaneous optimization of the crystallization properties could result in more homogeneous films and lower device-to-device performance variation in large arrays of FETs.

Another synthetic approach could be changes to the aromatic core of the GFA for n-dopants with altered donor strength.[272] While weaker dopants might be beneficial for larger-diameter SWCNTs with a smaller bandgap, stronger dopants could be employed to reach the degenerate doping regime necessary for thermoelectric applications. As indicated by the transfer characteristics for (6,5) SWCNT devices doped with very large concentrations of ttmgb, this introduction of excess carriers using GFAs is possible in principle.

Given that purely n-type transport in nanotube network transistors was successfully realized with GFAs, the approach was adapted for semiconducting polymers. Due to the different properties of semiconducting polymers compared to SWCNT networks, *e.g.*, the much lower porosity, the processing of the dopants had to be adapted. Dopants ttmgb and tdmegb with similar redox but different solubility behavior were used in several device architectures (as injection, blend and top layer). Facilitated by a careful optimization of the processing of these dopants, the performance in transistors based on the predominantly n-type yet slightly ambipolar polymers P(NDI2OD-T2) and DPPT-BT was improved. The dopants lead to an improved electron injection and suppression of hole injection.

In the best cases, FETs exhibited purely n-type charge transport behavior, substantially lower contact resistance and higher electron mobilities in comparison to the untreated

reference transistors. With an emphasis on contact doping instead of channel doping, high on/off current ratios were achieved while maintaining low hysteresis and preventing undesired shifts in onset voltage. Similar to the SWCNT network FETs, the doped transistors exhibited robust stability under bias stress in ambient conditions.

However, the unfavorable film formation properties of both employed GFA dopants imposed some limitations on the achieved performance improvements in semiconducting polymer FETs. The lowest contact resistance, highest electron mobilities and best hole blocking properties were all achieved in different device architectures for the P(NDI2OD-T2) transistors. The outlined synthetic approaches might provide a possibility to overcome this limitation to facilitate even better performance in polymer FETs doped by GFAs.

Nevertheless, the successful transfer of the GFA-doping approach to another solution-processable semiconductor highlights the versatility of this newly presented class of dopants. In general, the findings in this study underline the importance of considering dopant and semiconductor processing compatibility rather than a selection of dopants based exclusively on the alignment of energy levels.

Overall, n-type FETs that simultaneously exhibit high electron mobility, fully suppressed hole transport, excellent switching behavior, no hysteresis and good environmental stability were successfully demonstrated using SWCNT networks, which renders them a competition to state-of-the-art n-type FETs based on metal oxides. The limitations of the stronger literature-known dopants such as metallocenes[321] or DMBI derviatives,[258] that commonly lead to inferior switching behavior, hysteresis or undesired threshold voltage shifts, were overcome. For polymer FETs, however, despite significant performance improvements upon GFA treatment, not all desired features were realized in the same device configuration as GFA compound with more suitable processability remains to be developed.

High device reproducibility, reduced contact resistance and stable operation are important for high-performance devices. Improved ink stability and the new n-dopants introduced in this thesis represent a step forward in the development of solution-processed FETs with aforementioned properties.

BIBLIOGRAPHY

(1) Petti, L.; Münzenrieder, N.; Vogt, C.; Faber, H.; Büthe, L.; Cantarella, G.; Bottacchi, F.; Anthopoulos, T. D.; Tröster, G. *Appl. Phys. Rev.* **2016**, *3*, 21303.

(2) Goetz, K. P.; Li, Z.; Ward, J. W.; Bougher, C.; Rivnay, J.; Smith, J.; Conrad, B. R.; Parkin, S. R.; Anthopoulos, T. D.; Salleo, A.; Anthony, J. E.; Jurchescu, O. D. *Adv. Mater.* **2011**, *23*, 3698–3703.

(3) Schwartz, G.; Tee, B. C.-K.; Mei, J.; Appleton, A. L.; Kim, D. H.; Wang, H.; Bao, Z. *Nat. Commun.* **2013**, *4*, 1859.

(4) Lau, P. H.; Takei, K.; Wang, C.; Ju, Y.; Kim, J.; Yu, Z.; Takahashi, T.; Cho, G.; Javey, A. *Nano Lett.* **2013**, *13*, 3864–3869.

(5) Lefebvre, J.; Ding, J.; Li, Z.; Finnie, P.; Lopinski, G.; Malenfant, P. R. *Acc. Chem. Res.* **2017**, *50*, 2479–2486.

(6) Zaumseil, J. *Adv. Electron. Mater.* **2019**, *5*, 1800514.

(7) Hills, G.; Lau, C.; Wright, A.; Fuller, S.; Bishop, M. D.; Srimani, T.; Kanhaiya, P.; Ho, R.; Amer, A.; Stein, Y.; Murphy, D.; Arvind; Chandrakasan, A.; Shulaker, M. M. *Nature* **2019**, *572*, 595–602.

(8) Aguirre, C. M.; Levesque, P. L.; Paillet, M.; Lapointe, F.; St-Antoine, B. C.; Desjardins, P.; Martel, R. *Adv. Mater.* **2009**, *21*, 3087–3091.

(9) Tietze, M. L.; Rose, B. D.; Schwarze, M.; Fischer, A.; Runge, S.; Blochwitz-Nimoth, J.; Lüssem, B.; Leo, K.; Brédas, J. L. *Adv. Funct. Mater.* **2016**, *26*, 3730–3737.

(10) Lüssem, B; Riede, M; Leo, K *Phys. Status Solidi A* **2013**, *210*, 9–43.

(11) Lüssem, B.; Keum, C. M.; Kasemann, D.; Naab, B.; Bao, Z.; Leo, K. *Chem. Rev.* **2016**, *116*, 13714–13751.

(12) Xu, Y.; Sun, H.; Liu, A.; Zhu, H. H.; Li, W.; Lin, Y. F.; Noh, Y. Y. *Adv. Mater.* **2018**, *30*, 1801830.

(13) Kroto, H. W.; Heath, J. R.; O'Brien, S. C.; Curl, R. F.; Smalley, R. E. *Nature* **1985**, *318*, 162–163.

(14) Iijima, S. *Nature* **1991**, *354*, 56–58.

(15) Novoselov, K. S.; Geim, A. K.; Morozov, S. V.; Jiang, D; Zhang, Y; Dubonos, S. V.; Grigorieva, I. V.; Firsov, A. A. *Science* **2004**, *306*, 666–669.

(16) Wong, H.-S. P.; Akinwande, D., *Carbon nanotube and graphene device physics*; Cambridge University Press, Cambridge: 2011.

(17) Saito, R.; Fujita, M.; Dresselhaus, G.; Dresselhaus, M. S. *Appl. Phys. Lett.* **1992**, *60*, 2204–2206.

(18) Charlier, J. C.; Blase, X.; Roche, S. *Rev. Mod. Phys.* **2007**, *79*, 677–732.

(19) Saito, R; Dresselhaus, G; Dresselhaus, M. S. *Phys. Rev. B* **2000**, *61*, 2981–2990.

(20) Lefebvre, J; Fraser, J. M.; Finnie, P; Homma, Y. *Phys. Rev. B* **2004**, *69*, 75403.

(21) Kataura, H.; Kumazawa, Y; Maniwa, Y; Umezu, I; Suzuki, S; Ohtsuka, Y.; Achiba, Y *Synth. Met.* **1999**, *103*, 2555–2558.

(22) Weisman, R. B.; Bachilo, S. M. *Nano Lett.* **2003**, *3*, 1235–1238.

(23) Dresselhaus, M. S.; Dresselhaus, G; Jorio, A; Souza Filho, A. G.; Saito, R *Carbon* **2002**, *40*, 2043–2061.

(24) Rao, A. M.; Richter, E; Bandow, S.; Chase, B.; Eklund, P. C.; Williams, K. A.; Fang, S; Subbaswamy, K. R.; Menon, M; Thess, A; Smalley, R. E.; Dresselhaus, G; Dresselhaus, M. S. *Science* **1997**, *275*, 187–191.

(25) Grimm, S.; Schießl, S. P.; Zakharko, Y.; Rother, M.; Brohmann, M.; Zaumseil, J. *Carbon* **2017**, *118*, 261–267.

(26) He, X.; Gao, W.; Xie, L.; Li, B.; Zhang, Q.; Lei, S.; Robinson, J. M.; Hároz, E. H.; Doorn, S. K.; Wang, W.; Vajtai, R.; Ajayan, P. M.; Wade Adams, W.; Hauge, R. H.; Kono, J. *Nat. Nanotechnol.* **2016**, *11*, 633–638.

(27) Perebeinos, V.; Tersoff, J; Avouris, P. *Phys. Rev. Lett.* **2005**, *94*, 86802.

(28) Zhou, X.; Park, J.-Y.; Huang, S.; Liu, J.; McEuen, P. P. *Phys. Rev. Lett.* **2005**, *95*, 146805.

(29) Graf, A.; Held, M.; Zakharko, Y.; Tropf, L.; Gather, M. C.; Zaumseil, J. *Nat. Mater.* **2017**, *16*, 911.

(30) Zaumseil, J. *Adv. Funct. Mater.* **2020**, *30*, 1905269.

(31) Ilani, S.; Donev, L. A. K.; Kindermann, M.; McEuen, P. L. *Nat. Phys.* **2006**, *2*, 687–691.

(32) Zaumseil, J. *Semicond. Sci. Technol.* **2015**, *30*, 74001.

(33) Schießl, S. P.; Gannott, F.; Etschel, S. H.; Schweiger, M.; Grünler, S.; Halik, M.; Zaumseil, J. *Adv. Mater. Interfaces* **2016**, 1600215.

(34) Cao, Q.; Xia, M.; Kocabas, C.; Shim, M.; Rogers, J. A.; Rotkin, S. V. *Appl. Phys. Lett.* **2007**, *90*, 23516.

(35) Schießl, S. P.; Rother, M.; Lüttgens, J.; Zaumseil, J. *Appl. Phys. Lett.* **2017**, *111*, 193301.

(36) Kumar, S; Pimparkar, N; Murthy, J. Y.; Alam, M. A. *Appl. Phys. Lett.* **2006**, *88*, 123505.

(37) Snow, E. S.; Campbell, P. M.; Ancona, M. G.; Novak, J. P. *Appl. Phys. Lett.* **2005**, *86*, 33105.

(38) Rouhi, N.; Jain, D.; Burke, P. J. *ACS Nano* **2011**, *5*, 8471–8487.

(39) Derenskyi, V.; Gomulya, W.; Gao, J.; Bisri, S. Z.; Pasini, M.; Loo, Y.-L.; Loi, M. A. *Appl. Phys. Lett.* **2018**, *112*, 72106.

(40) Gaviria Rojas, W. A.; Hersam, M. C. *Adv. Mater.* **2020**, *32*, 1905654.

(41) Znidarsic, A.; Kaskela, A.; Laiho, P.; Gaberscek, M.; Ohno, Y.; Nasibulin, A. G.; Kauppinen, E. I.; Hassanien, A. *J. Phys. Chem. C* **2013**, *117*, 13324–13330.

(42) Nirmalraj, P. N.; Lyons, P. E.; De, S.; Coleman, J. N.; Boland, J. J. *Nano Lett.* **2009**, *9*, 3890–3895.

(43) Fuhrer, M. S.; Lim, A. K. L.; Shih, L; Varadarajan, U; Zettl, A; McEuen, P. L. *Phys. E (Amsterdam, Neth.)* **2000**, *6*, 868–871.

(44) Topinka, M. A.; Rowell, M. W.; Goldhaber-Gordon, D.; McGehee, M. D.; Hecht, D. S.; Gruner, G. *Nano Lett.* **2009**, *9*, 1866–1871.

(45) Kim, D. H.; Shin, H.-J.; Lee, H. S.; Lee, J.; Lee, B.-L.; Lee, W. H.; Lee, J.-H.; Cho, K.; Kim, W.-J.; Lee, S. Y.; Choi, J.-Y.; Kim, J. M. *ACS Nano* **2012**, *6*, 662–670.

(46) Norton-Baker, B.; Ihly, R.; Gould, I. E.; Avery, A. D.; Owczarczyk, Z. R.; Ferguson, A. J.; Blackburn, J. L. *ACS Energy Lett.* **2016**, *1*, 1212–1220.

(47) Ravi, S.; Kaiser, A. B.; Bumby, C. W. *Phys. Status Solidi B* **2013**, *250*, 1463–1467.

(48) Barman, S. N.; LeMieux, M. C.; Baek, J.; Rivera, R.; Bao, Z. *ACS Appl. Mater. Interfaces* **2010**, *2*, 2672–2678.

(49) Schießl, S. P.; de Vries, X.; Rother, M.; Massé, A.; Brohmann, M.; Bobbert, P. A.; Zaumseil, J. *Phys. Rev. Mater.* **2017**, *1*, 46003.

(50) Brohmann, M.; Rother, M.; Schießl, S. P.; Preis, E.; Allard, S.; Scherf, U.; Zaumseil, J. *J. Phys. Chem. C* **2018**, *122*, 19886–19896.

(51) Brohmann, M.; Berger, F. J.; Matthiesen, M.; Schießl, S. P.; Schneider, S.; Zaumseil, J. *ACS Nano* **2019**, *13*, 7323–7332.

(52) Itkis, M. E.; Pekker, A.; Tian, X.; Bekyarova, E.; Haddon, R. C. *Acc. Chem. Res.* **2015**, *48*, 2270–2279.

(53) Sheng, P. *Phys. Rev. B* **1980**, *21*, 2180.

(54) Yimer, Y. Y.; Bobbert, P. A.; Coehoorn, R *J. Phys.: Condens. Matter* **2008**, *20*, 335204.

(55) Massé, A.; Friederich, P.; Symalla, F.; Liu, F.; Nitsche, R.; Coehoorn, R.; Wenzel, W.; Bobbert, P. A. *Phys. Rev. B* **2016**, *93*, 195209.

(56) Guo, T.; Nikolaev, P.; Thess, A.; Colbert, D. T.; Smalley, R. E. *Chem. Phys. Lett.* **1995**, *243*, 49–54.

(57) Journet, C; Maser, W. K.; Bernier, P; Loiseau, A; De La Chapelle, M. L.; Lefrant, d. l. S.; Deniard, P; Lee, R; Fischer, J. E. *Nature* **1997**, *388*, 756–758.

(58) Ando, Y.; Zhao, X.; Hirahara, K.; Suenaga, K.; Bandow, S.; Iijima, S. *Chem. Phys. Lett.* **2000**, *323*, 580–585.

(59) Kim, K. S.; Kingston, C. T.; Ruth, D.; Barnes, M.; Simard, B. *Chem. Eng. J.* **2014**, *250*, 331–341.

(60) Lolli, G.; Zhang, L.; Balzano, L.; Sakulchaicharoen, N.; Tan, Y.; Resasco, D. E. *J. Phys. Chem. B* **2006**, *110*, 2108–2115.

(61) Jung, Y. J.; Wei, B.; Vajtai, R.; Ajayan, P. M.; Homma, Y.; Prabhakaran, K.; Ogino, T. *Nano Lett.* **2003**, *3*, 561–564.

(62) Liu, J.; Hersam, M. C. *MRS Bull.* **2010**, *35*, 315–321.

(63) Liu, B.; Wu, F.; Gui, H.; Zheng, M.; Zhou, C. *ACS Nano* **2017**, *11*, 31–53.

(64) Hennrich, F.; Krupke, R.; Arnold, K.; Rojas Stütz, J. A.; Lebedkin, S.; Koch, T.; Schimmel, T.; Kappes, M. M. *J. Phys. Chem. B* **2007**, *111*, 1932–1937.

(65) Graf, A.; Zakharko, Y.; Schießl, S. P.; Backes, C.; Pfohl, M.; Flavel, B. S.; Zaumseil, J. *Carbon* **2016**, *105*, 593–599.

(66) Coleman, J. N. *Adv. Funct. Mater.* **2009**, *19*, 3680–3695.

(67) McDonald, T. J.; Engtrakul, C.; Jones, M.; Rumbles, G.; Heben, M. J. *J. Phys. Chem. B* **2006**, *110*, 25339–25346.

(68) Tu, X.; Manohar, S.; Jagota, A.; Zheng, M. *Nature* **2009**, *460*, 250–253.

(69) Liu, H.; Nishide, D.; Tanaka, T.; Kataura, H. *Nat. Commun.* **2011**, *2*, 309.

(70) Krupke, R.; Hennrich, F.; von Löhneysen, H.; Kappes, M. M. *Science* **2003**, *301*, 344–347.

(71) Fagan, J. A.; Khripin, C. Y.; Silvera Batista, C. A.; Simpson, J. R.; Hároz, E. H.; Hight Walker, A. R.; Zheng, M. *Adv. Mater.* **2014**, *26*, 2800–2804.

(72) Li, H.; Gordeev, G.; Garrity, O.; Peyyety, N. A.; Selvasundaram, P. B.; Dehm, S.; Krupke, R.; Cambré, S.; Wenseleers, W.; Reich, S.; Zheng, M.; Fagan, J. A.; Flavel, B. S. *ACS Nano* **2020**, *14*, 948–963.

(73) Nish, A.; Hwang, J.-Y.; Doig, J.; Nicholas, R. J. *Nat. Nanotechnol.* **2007**, *2*, 640–646.

(74) Jakubka, F.; Schießl, S. P.; Martin, S.; Englert, J. M.; Hauke, F.; Hirsch, A.; Zaumseil, J. *ACS Macro Lett.* **2012**, *1*, 815–819.

(75) Gomulya, W.; Costanzo, G. D.; De Carvalho, E. J. F.; Bisri, S. Z.; Derenskyi, V.; Fritsch, M.; Froehlich, N.; Allard, S.; Gordiichuk, P.; Herrmann, A.; Marrink, S. J.; Dos Santos, M. C.; Scherf, U.; Loi, M. A. *Adv. Mater.* **2013**, *25*, 2948–2956.

(76) Ozawa, H.; Fujigaya, T.; Niidome, Y.; Hotta, N.; Fujiki, M.; Nakashima, N. *J. Am. Chem. Soc.* **2011**, *133*, 2651–2657.

(77) Hwang, J.-Y.; Nish, A.; Doig, J.; Douven, S.; Chen, C.-W.; Chen, L.-C.; Nicholas, R. J. *J. Am. Chem. Soc.* **2008**, *130*, 3543–3553.

(78) Lemasson, F. A.; Strunk, T.; Gerstel, P.; Hennrich, F.; Lebedkin, S.; Barner-Kowollik, C.; Wenzel, W.; Kappes, M. M.; Mayor, M. *J. Am. Chem. Soc.* **2010**, *133*, 652–655.

(79) Lee, H. W.; Yoon, Y.; Park, S.; Oh, J. H.; Hong, S.; Liyanage, L. S.; Wang, H.; Morishita, S.; Patil, N.; Park, Y. J.; Park, J. J.; Spakowitz, A.; Galli, G.; Gygi, F.; Wong, P. H.; Tok, J. B.; Kim, J. M.; Bao, Z. *Nat. Commun.* **2011**, *2*, 541.

(80) Samanta, S. K.; Fritsch, M.; Scherf, U.; Gomulya, W.; Bisri, S. Z.; Loi, M. A. *Acc. Chem. Res.* **2014**, *47*, 2446–2456.

(81) Gao, J.; Loi, M. A.; De Carvalho, E. J. F.; Dos Santos, M. C. *ACS Nano* **2011**, *5*, 3993–3999.

(82) Deria, P.; Von Bargen, C. D.; Olivier, J.-H.; Kumbhar, A. S.; Saven, J. G.; Therien, M. J. *J. Am. Chem. Soc.* **2013**, *135*, 16220–16234.

(83) Gomulya, W.; Rios, J. M. S.; Derenskyi, V.; Bisri, S. Z.; Jung, S.; Fritsch, M.; Allard, S.; Scherf, U.; Dos Santos, M. C.; Loi, M. A. *Carbon* **2015**, *84*, 66–73.

(84) Ding, J.; Li, Z.; Lefebvre, J.; Du, X.; Malenfant, P. R. *J. Phys. Chem. C* **2016**, *120*, 21946–21954.

(85) Li, Z.; Ding, J.; Guo, C.; Lefebvre, J.; Malenfant, P. R. L. *Adv. Funct. Mater.* **2018**, *28*, 1705568.

(86) Mirka, B.; Rice, N. A.; Williams, P.; Tousignant, M. N.; Boileau, N. T.; Bodnaryk, W. J.; Fong, D.; Adronov, A.; Lessard, B. H. *ACS Nano* **2021**, *15*, 8252–8266.

(87) Redecker, M; Bradley, D. D. C.; Inbasekaran, M; Woo, E. P. *Appl. Phys. Lett.* **1998**, *73*, 1565–1567.

(88) Bird, M. J.; Reid, O. G.; Cook, A. R.; Asaoka, S.; Shibano, Y.; Imahori, H.; Rumbles, G.; Miller, J. R. *J. Phys. Chem. C* **2014**, *118*, 6100–6109.

(89) Joo, Y.; Brady, G. J.; Kanimozhi, C.; Ko, J.; Shea, M. J.; Strand, M. T.; Arnold, M. S.; Gopalan, P. *ACS Appl. Mater. Interfaces* **2017**, *9*, 28859–28867.

(90) Israelachvili, J. *Acc. Chem. Res.* **1987**, *20*, 415–421.

(91) Dörfler, H.-D., *Grenzflächen und kolloid-disperse Systeme: Physik und Chemie*; Springer Verlag Berlin, Heidelberg: 2002.

(92) Hiemenz, P. C.; Rajagopalan, R., *Principles of Colloid and Surface Chemistry, revised and expanded*; CRC Press, Boca Raton: 2016.

(93) Bouchard, D.; Zhang, W.; Powell, T.; Rattanaudompol, U. *Environ. Sci. Technol.* **2012**, *46*, 4458–4465.

(94) Ju, L.; Zhang, W.; Wang, X.; Hu, J.; Zhang, Y. *Colloids Surfaces, A Physicochem. Eng. Asp.* **2012**, *409*, 159–166.

(95) Broersma, S. *J. Chem. Phys.* **1960**, *32*, 1632–1635.

(96) Tsyboulski, D. A.; Bachilo, S. M.; Kolomeisky, A. B.; Weisman, R. B. *ACS Nano* **2008**, *2*, 1770–1776.

(97) Talsma, W.; Sengrian, A. A.; Salazar-Rios, J. M.; Duim, H.; Abdu-Aguye, M.; Jung, S.; Allard, S.; Scherf, U.; Loi, M. A. *Adv. Electron. Mater.* **2019**, *5*, 1900288.

(98) Chen, Q.; Saltiel, C.; Manickavasagam, S.; Schadler, L. S.; Siegel, R. W.; Yang, H. *J. Colloid Interface Sci.* **2004**, *280*, 91–97.

(99) Wang, J.; Blau, W. J. *J. Phys. Chem. C* **2008**, *112*, 2298–2303.

(100) Khan, I. A.; Aich, N.; Afrooz, A. R. M. N.; Flora, J. R. V.; Schierz, P. A.; Ferguson, P. L.; Sabo-Attwood, T.; Saleh, N. B. *Chemosphere* **2013**, *93*, 1997–2003.

(101) Silvera Batista, C. A.; Zheng, M.; Khripin, C. Y.; Tu, X.; Fagan, J. A. *Langmuir* **2014**, *30*, 4895–4904.

(102) Koh, B.; Cheng, W. *Langmuir* **2014**, *30*, 10899–10909.

(103) Heller, D. A.; Barone, P. W.; Swanson, J. P.; Mayrhofer, R. M.; Strano, M. S. *J. Phys. Chem. B* **2004**, *108*, 6905–6909.

(104) O'Connell, M. J.; Bachilo, S. M.; Huffman, C. B.; Moore, V. C.; Strano, M. S.; Haroz, E. H.; Rialon, K. L.; Boul, P. J.; Noon, W. H.; Kittrell, C.; Ma, J.; Hauge, R. H.; Weisman, R. B.; Smalley, R. E. *Science* **2002**, *297*, 593–596.

(105) Sanchez, S. R.; Bachilo, S. M.; Kadria-Vili, Y.; Lin, C. W.; Weisman, R. B. *Nano Lett.* **2016**, *16*, 6903–6909.

(106) Sanchez, S. R.; Bachilo, S. M.; Weisman, R. B. *J. Phys. Chem. C* **2018**, *122*, 26251–26259.

(107) Rossi, G; Chance, R. R.; Silbey, R *J. Chem. Phys.* **1989**, *90*, 7594–7601.

(108) Köhler, A.; Dos Santos, D. A.; Beljonne, D.; Shuai, Z; Brédas, J.-L.; Holmes, A. B.; Kraus, A.; Müllen, K.; Friend, R. H. *Nature* **1998**, *392*, 903–906.

(109) Scholes, G. D.; Rumbles, G. *Nat. Mater.* **2006**, 683–696.

(110) Kang, B.; Kim, R.; Lee, S. B.; Kwon, S.-K.; Kim, Y.-H.; Cho, K. *J. Am. Chem. Soc.* **2016**, *138*, 3679–3686.

(111) Cleave, V.; Yahioglu, G.; Barny, P. L.; Friend, R. H.; Tessler, N. *Adv. Mater.* **1999**, *11*, 285–288.

(112) Yim, K.-H.; Zheng, Z.; Liang, Z.; Friend, R. H.; Huck, W. T. S.; Kim, J.-S. *Adv. Funct. Mater.* **2008**, *18*, 1012–1019.

(113) Coakley, K. M.; McGehee, M. D. *Chem. Mater.* **2004**, *16*, 4533–4542.

(114) Dhanabalan, A.; van Duren, J. K. J.; van Hal, P. A.; van Dongen, J. L. J.; Janssen, R. A. J. *Adv. Funct. Mater.* **2001**, *11*, 255–262.

(115) Baran, D.; Balan, A.; Celebi, S.; Meana Esteban, B.; Neugebauer, H.; Sariciftci, N. S.; Toppare, L. *Chem. Mater.* **2010**, *22*, 2978–2987.

(116) Beaujuge, P. M.; Reynolds, J. R. *Chem. Rev.* **2010**, *110*, 268–320.

(117) Paterson, A. F.; Singh, S.; Fallon, K. J.; Hodsden, T.; Han, Y.; Schroeder, B. C.; Bronstein, H.; Heeney, M.; McCulloch, I.; Anthopoulos, T. D. *Adv. Mater.* **2018**, *30*, 1801079.

(118) Nielsen, C. B.; Turbiez, M.; McCulloch, I. *Adv. Mater.* **2013**, *25*, 1859–1880.

(119) Sirringhaus, H.; Brown, P. J.; Friend, R. H.; Nielsen, M. M.; Bechgaard, K.; Langeveld-Voss, B. M. W.; Spiering, A. J. H.; Janssen, R. A. J.; Meijer, E. W.; Herwig, P; de Leeuw, D. M. *Nature* **1999**, *401*, 685–688.

(120) McCulloch, I.; Heeney, M.; Bailey, C.; Genevicius, K.; MacDonald, I.; Shkunov, M.; Sparrowe, D.; Tierney, S.; Wagner, R.; Zhang, W.; Chabinyc, M. L.; Joseph Kline, R.; McGehee, M. D.; Toney, M. F. *Nat. Mater.* **2006**, *5*, 328–333.

(121)   Deen, M. J.; Kazemeini, M. H.; Haddara, Y. M.; Yu, J.; Vamvounis, G.; Holdcroft, S.; Woods, W. *IEEE Trans. Electron Devices* **2004**, *51*, 1892–1901.

(122)   Held, M.; Zakharko, Y.; Wang, M.; Jakubka, F.; Gannott, F.; Rumer, J. W.; Ashraf, R. S.; McCulloch, I.; Zaumseil, J. *Org. Electron.* **2016**, *32*, 220–227.

(123)   Xiao, M.; Kang, B.; Lee, S. B.; Perdigão, L. M.; Luci, A.; Warr, D. A.; Senanayak, S. P.; Nikolka, M.; Statz, M.; Wu, Y.; Sadhanala, A.; Schott, S.; Carey, R.; Wang, Q.; Lee, M.; Kim, C.; Onwubiko, A.; Jellett, C.; Liao, H.; Yue, W.; Cho, K.; Costantini, G.; McCulloch, I.; Sirringhaus, H. *Adv. Mater.* **2020**, *32*, 2000063.

(124)   Baeg, K.-J.; Caironi, M.; Noh, Y.-Y. *Adv. Mater.* **2013**, *25*, 4210–4244.

(125)   Samitsu, S.; Shimomura, T.; Heike, S.; Hashizume, T.; Ito, K. *Macromolecules* **2008**, *41*, 8000–8010.

(126)   Steyrleuthner, R.; Schubert, M.; Howard, I.; Klaumünzer, B.; Schilling, K.; Chen, Z.; Saalfrank, P.; Laquai, F.; Facchetti, A.; Neher, D. *J. Am. Chem. Soc.* **2012**, *134*, 18303–18317.

(127)   Chang, J.-F.; Sun, B.; Breiby, D. W.; Nielsen, M. M.; Sölling, T. I.; Giles, M.; McCulloch, I.; Sirringhaus, H. *Chem. Mater.* **2004**, *16*, 4772–4776.

(128)   Bucella, S. G.; Luzio, A.; Gann, E.; Thomsen, L.; McNeill, C. R.; Pace, G.; Perinot, A.; Chen, Z.; Facchetti, A.; Caironi, M. *Nat. Commun.* **2015**, *6*, 8394.

(129)   Noriega, R.; Salleo, A. In *Organic Electronics II: More Materials and Applications*; John Wiley & Sons, Weinheim: 2012; Chapter 3, pp 67–104.

(130)   Tremel, K.; Fischer, F. S.; Kayunkid, N.; Pietro, R. D.; Tkachov, R.; Kiriy, A.; Neher, D.; Ludwigs, S.; Brinkmann, M. *Adv. Energy Mater.* **2014**, *4*, 1–13.

(131)   Matsidik, R.; Komber, H.; Luzio, A.; Caironi, M.; Sommer, M. *J. Am. Chem. Soc.* **2015**, *137*, 6705–6711.

(132)   Noriega, R.; Rivnay, J.; Vandewal, K.; Koch, F. P.; Stingelin, N.; Smith, P.; Toney, M. F.; Salleo, A. *Nat. Mater.* **2013**, *12*, 1038–1044.

(133)   Vissenberg, M.; Matters, M. *Phys. Rev. B* **1998**, *57*, 12964.

(134)   Caironi, M.; Bird, M.; Fazzi, D.; Chen, Z.; Di Pietro, R.; Newman, C.; Facchetti, A.; Sirringhaus, H. *Adv. Funct. Mater.* **2011**, *21*, 3371–3381.

(135)   Liu, T.; Troisi, A. *Adv. Funct. Mater.* **2014**, *24*, 925–933.

(136)   Venkateshvaran, D.; Nikolka, M.; Sadhanala, A.; Lemaur, V.; Zelazny, M.; Kepa, M.; Hurhangee, M.; Kronemeijer, A. J.; Pecunia, V.; Nasrallah, I.; Romanov, I.; Broch, K.; McCulloch, I.; Emin, D.; Olivier, Y.; Cornil, J.; Beljonne, D.; Sirringhaus, H. *Nature* **2014**, *515*, 384–388.

(137) Kronemeijer, A. J.; Pecunia, V.; Venkateshvaran, D.; Nikolka, M.; Sadhanala, A.; Moriarty, J.; Szumilo, M.; Sirringhaus, H. *Adv. Mater.* **2014**, *26*, 728–733.

(138) Chen, Z.; Lee, M. J.; Shahid Ashraf, R.; Gu, Y.; Albert-Seifried, S.; Meedom Nielsen, M.; Schroeder, B.; Anthopoulos, T. D.; Heeney, M.; McCulloch, I.; Sirringhaus, H. *Adv. Mater.* **2012**, *24*, 647–652.

(139) Fazzi, D.; Caironi, M.; Castiglioni, C. *J. Am. Chem. Soc.* **2011**, *133*, 19056–19059.

(140) Wetzelaer, G. J. A. H.; Kuik, M.; Olivier, Y.; Lemaur, V.; Cornil, J.; Fabiano, S.; Loi, M. A.; Blom, P. W. M. *Phys. Rev. B - Condens. Matter Mater. Phys.* **2012**, *86*, 165203.

(141) Khim, D.; Luzio, A.; Bonacchini, G. E.; Pace, G.; Lee, M. J.; Noh, Y. Y.; Caironi, M. *Adv. Mater.* **2018**, *30*, 1705463.

(142) Luzio, A.; Criante, L.; D'Innocenzo, V.; Caironi, M. *Sci. Rep.* **2013**, *3*, 1–6.

(143) Higgins, S. G.; Muir, B. V. O.; Dell'Erba, G.; Perinot, A.; Caironi, M.; Campbell, A. J. *Adv. Electron. Mater.* **2016**, *2*, 1500272.

(144) Li, M.; Mangalore, D. K.; Zhao, J.; Carpenter, J. H.; Yan, H.; Ade, H.; Yan, H.; Müllen, K.; Blom, P. W. M.; Pisula, W.; de Leeuw, D. M.; Asadi, K. *Nat. Commun.* **2018**, *9*, 451.

(145) Scherf, U. *J. Mater. Chem.* **1999**, *9*, 1853–1864.

(146) Lamport, Z. A.; Haneef, H. F.; Anand, S.; Waldrip, M.; Jurchescu, O. D. *J. Appl. Phys.* **2018**, *124*, 071101.

(147) Schmechel, R.; Ahles, M.; von Seggern, H. *J. Appl. Phys.* **2005**, *98*, 84511.

(148) Chua, L.-L.; Ho, P. K. H.; Sirringhaus, H.; Friend, R. H. *Appl. Phys. Lett.* **2004**, *84*, 3400–3402.

(149) Zaumseil, J; Sirringhaus, H *Chem. Rev.* **2007**, *107*, 1296–1323.

(150) Sze, S. M.; Ng, K. K., *Physics of Semiconductor Devices.* John Wiley & Sons, Hoboken: 2006.

(151) Klauk, H. *Adv. Electron. Mater.* **2018**, *4*, 1700474.

(152) Waldrip, M.; Jurchescu, O. D.; Gundlach, D. J.; Bittle, E. G. *Adv. Funct. Mater.* **2019**, 1904576.

(153) Zschieschang, U.; Holzmann, T.; Kuhn, A.; Aghamohammadi, M.; Lotsch, B. V.; Klauk, H. *J. Appl. Phys.* **2015**, *117*, 104509.

(154) Cong, S.; Cao, Y.; Fang, X.; Wang, Y.; Liu, Q.; Gui, H.; Shen, C.; Cao, X.; Kim, E. S.; Zhou, C. *ACS Nano* **2016**, *10*, 10068–10074.

(155) Crone, B; Dodabalapur, A; Lin, Y.-Y.; Filas, R. W.; Bao, Z; LaDuca, A; Sarpeshkar, R; Katz, H. E.; Li, W. *Nature* **2000**, *403*, 521–523.

(156) Rost, C.; Karg, S.; Riess, W.; Loi, M. A.; Murgia, M.; Muccini, M. *Appl. Phys. Lett.* **2004**, *85*, 1613–1615.

(157) Zaumseil, J.; Donley, C. L.; Kim, J.-S.; Friend, R. H.; Sirringhaus, H. *Adv. Mater.* **2006**, *18*, 2708–2712.

(158) Martel, R; Derycke, V; Lavoie, C; Appenzeller, J; Chan, K. K.; Tersoff, J; Avouris, P. *Phys. Rev. Lett.* **2001**, *87*, 256805.

(159) Rother, M.; Schießl, S. P.; Zakharko, Y.; Gannott, F.; Zaumseil, J. *ACS Appl. Mater. Interfaces* **2016**, *8*, 5571–5579.

(160) Avouris, P.; Freitag, M.; Perebeinos, V. *Nat. Photonics* **2008**, *2*, 341–350.

(161) Jakubka, F.; Backes, C.; Gannott, F.; Mundloch, U.; Hauke, F.; Hirsch, A.; Zaumseil, J. *ACS Nano* **2013**, *7*, 7428–7435.

(162) Lefebvre, J.; Ding, J.; Li, Z.; Cheng, F.; Du, N.; Malenfant, P. R. L. *Appl. Phys. Lett.* **2015**, *107*, 243301.

(163) Martel, R.; Schmidt, T; Shea, H. R.; Hertel, T; Avouris, P. *Appl. Phys. Lett.* **1998**, *73*, 2447–2449.

(164) Schießl, S. P.; Fro, N.; Held, M.; Gannott, F.; Schweiger, M.; Forster, M.; Scherf, U.; Zaumseil, J. *ACS Appl. Mater. Interfaces* **2015**, *7*, 682–689.

(165) Close, G. F.; Yasuda, S.; Paul, B.; Fujita, S.; Wong, H.-S. P. *Nano Lett.* **2008**, *8*, 706–709.

(166) Sun, D.-M.; Timmermans, M. Y.; Tian, Y.; Nasibulin, A. G.; Kauppinen, E. I.; Kishimoto, S.; Mizutani, T.; Ohno, Y. *Nat. Nanotechnol.* **2011**, *6*, 156–161.

(167) Zhao, C.; Zhong, D.; Han, J.; Liu, L.; Zhang, Z.; Peng, L.-M. *Adv. Funct. Mater.* **2019**, *29*, 1808574.

(168) Qiu, C.; Zhang, Z.; Xiao, M.; Yang, Y.; Zhong, D.; Peng, L.-M. *Science* **2017**, *355*, 271–276.

(169) Zhang, Y.; Chang, A.; Cao, J.; Wang, Q.; Kim, W.; Li, Y.; Morris, N.; Yenilmez, E.; Kong, J.; Dai, H. *Appl. Phys. Lett.* **2001**, *79*, 3155–3157.

(170) Kang, S. J.; Kocabas, C.; Ozel, T.; Shim, M.; Pimparkar, N.; Alam, M. A.; Rotkin, S. V.; Rogers, J. A. *Nat. Nanotechnol.* **2007**, *2*, 230–236.

(171) Liu, B.; Liu, J.; Li, H.-B.; Bhola, R.; Jackson, E. A.; Scott, L. T.; Page, A.; Irle, S.; Morokuma, K.; Zhou, C. *Nano Lett.* **2015**, *15*, 586–595.

(172) Zhang, G.; Qi, P.; Wang, X.; Lu, Y.; Li, X.; Tu, R.; Bangsaruntip, S.; Mann, D.; Zhang, L.; Dai, H. *Science* **2006**, *314*, 974–977.

(173) Joo, Y.; Brady, G. J.; Arnold, M. S.; Gopalan, P. *Langmuir* **2014**, *30*, 3460–3466.

(174) Liu, L.; Han, J.; Xu, L.; Zhou, J.; Zhao, C.; Ding, S.; Shi, H.; Xiao, M.; Ding, L.; Ma, Z.; Jin, C.; Zhang, Z.; Peng, L.-M. *Science* **2020**, *368*, 850–856.

(175) Ding, J.; Li, Z.; Lefebvre, J.; Cheng, F.; Dubey, G.; Zou, S.; Finnie, P.; Hrdina, A.; Scoles, L.; Lopinski, G. P.; Kingston, C. T.; Simard, B.; Malenfant, P. R. L. *Nanoscale* **2014**, *6*, 2328–2339.

(176) Brady, G. J.; Way, A. J.; Safron, N. S.; Evensen, H. T.; Gopalan, P.; Arnold, M. S. *Sci. Adv.* **2016**, *2*, e1601240.

(177) Chen, B.; Zhang, P.; Ding, L.; Han, J.; Qiu, S.; Li, Q.; Zhang, Z.; Peng, L.-M. *Nano Lett.* **2016**, *16*, 5120–5128.

(178) Rother, M.; Brohmann, M.; Yang, S.; Grimm, S. B.; Schießl, S. P.; Graf, A.; Zaumseil, J. *Adv. Electron. Mater.* **2017**, *3*, 1700080.

(179) Kim, B.; Geier, M. L.; Hersam, M. C.; Dodabalapur, A. *ACS Appl. Mater. Interfaces* **2015**, *7*, 27654–27660.

(180) Sun, J.; Sapkota, A.; Park, H.; Wesley, P.; Jung, Y.; Maskey, B. B.; Kim, Y.; Majima, Y.; Ding, J.; Ouyang, J.; Guo, C.; Lefebvre, J.; Li, Z.; Malenfant, P. R. L.; Javey, A.; Cho, G. *Adv. Electron. Mater.* **2020**, *6*, 1901431.

(181) Liang, Y.; Xia, J.; Liang, X. *Sci. Bull.* **2016**, *61*, 794–800.

(182) Malhofer, A.; Rother, M.; Zakharko, Y.; Graf, A.; Schießl, S. P.; Zaumseil, J. *Org. Electron.* **2017**, *45*, 151–158.

(183) Cao, Y.; Brady, G. J.; Gui, H.; Rutherglen, C.; Arnold, M. S.; Zhou, C. *ACS Nano* **2016**, *10*, 6782–6790.

(184) Liu, L.; Ding, L.; Zhong, D.; Han, J.; Wang, S.; Meng, Q.; Qiu, C.; Zhang, X.; Peng, L.-M.; Zhang, Z. *ACS Nano* **2019**, *13*, 2526–2535.

(185) Zhang, H.; Xiang, L.; Yang, Y.; Xiao, M.; Han, J.; Ding, L.; Zhang, Z.; Hu, Y.; Peng, L.-M. *ACS Nano* **2018**, *12*, 2773–2779.

(186) Geier, M. L.; Prabhumirashi, P. L.; McMorrow, J. J.; Xu, W.; Seo, J.-W. T.; Everaerts, K.; Kim, C. H.; Marks, T. J.; Hersam, M. C. *Nano Lett.* **2013**, *13*, 4810–4814.

(187) Lau, C.; Srimani, T.; Bishop, M. D.; Hills, G.; Shulaker, M. M. *ACS Nano* **2018**, *12*, 10924–10931.

(188) Shulaker, M. M.; Hills, G.; Patil, N.; Wei, H.; Chen, H.-Y.; Wong, H.-S. P.; Mitra, S. *Nature* **2013**, *501*, 526–530.

(189) Dodabalapur, A. *Mater. Today* **2006**, *9*, 24–30.

(190) Choi, H. H.; Cho, K.; Frisbie, C. D.; Sirringhaus, H.; Podzorov, V. *Nat. Mater.* **2017**, *17*, 2–7.

(191) Bittle, E. G.; Basham, J. I.; Jackson, T. N.; Jurchescu, O. D.; Gundlach, D. J. *Nat. Commun.* **2016**, *7*, 1–7.

(192) McCulloch, I.; Salleo, A.; Chabinyc, M. *Science* **2016**, *352*, 1521–1522.

(193) Kline, R. J.; DeLongchamp, D. M.; Fischer, D. A.; Lin, E. K.; Richter, L. J.; Chabinyc, M. L.; Toney, M. F.; Heeney, M.; McCulloch, I. *Macromolecules* **2007**, *40*, 7960–7965.

(194) Fei, Z.; Pattanasattayavong, P.; Han, Y.; Schroeder, B. C.; Yan, F.; Kline, R. J.; Anthopoulos, T. D.; Heeney, M. *J. Am. Chem. Soc.* **2014**, *136*, 15154–15157.

(195) Zhang, X.; Bronstein, H.; Kronemeijer, A. J.; Smith, J.; Kim, Y.; Kline, R. J.; Richter, L. J.; Anthopoulos, T. D.; Sirringhaus, H.; Song, K.; Heeney, M.; Zhang, W.; McCulloch, I.; DeLongchamp, D. M. *Nat. Commun.* **2013**, *4*, 2238.

(196) Fei, Z.; Han, Y.; Gann, E.; Hodsden, T.; Chesman, A. S. R.; McNeill, C. R.; Anthopoulos, T. D.; Heeney, M. *J. Am. Chem. Soc.* **2017**, *139*, 8552–8561.

(197) Kim, R.; Amegadze, P. S. K.; Kang, I.; Yun, H.-J.; Noh, Y.-Y.; Kwon, S.-K.; Kim, Y.-H. *Adv. Funct. Mater.* **2013**, *23*, 5719–5727.

(198) Crossland, E. J. W.; Rahimi, K.; Reiter, G.; Steiner, U.; Ludwigs, S. *Adv. Funct. Mater.* **2011**, *21*, 518–524.

(199) Trefz, D.; Gross, Y. M.; Dingler, C.; Tkachov, R.; Hamidi-Sakr, A.; Kiriy, A.; McNeill, C. R.; Brinkmann, M.; Ludwigs, S. *Macromolecules* **2018**, *52*, 43–54.

(200) Wang, S.; Fabiano, S.; Himmelberger, S.; Puzinas, S.; Crispin, X.; Salleo, A.; Berggren, M. *Proc. Natl. Acad. Sci.* **2015**, *112*, 10599–10604.

(201) Nikolka, M.; Nasrallah, I.; Rose, B.; Ravva, M. K.; Broch, K.; Sadhanala, A.; Harkin, D.; Charmet, J.; Hurhangee, M.; Brown, A.; Illig, S.; Too, P.; Jongman, J.; McCulloch, I.; Bredas, J. L.; Sirringhaus, H. *Nat. Mater.* **2017**, *16*, 356–362.

(202) Xue, X.; Chandler, G.; Zhang, X.; Kline, R. J.; Fei, Z.; Heeney, M.; Diemer, P. J.; Jurchescu, O. D.; Oconnor, B. T. *ACS Appl. Mater. Interfaces* **2015**, *7*, 26726–26734.

(203) Brinkmann, M.; Wittmann, J.-C. *Adv. Mater.* **2006**, *18*, 860–863.

(204) Perinot, A.; Caironi, M. *Adv. Sci.* **2019**, *6*, 1801566.

(205) Perinot, A.; Giorgio, M.; Mattoli, V.; Natali, D.; Caironi, M. *Adv. Sci.* **2021**, *8*, 2001098.

(206) Zhong, D.; Shi, H.; Ding, L.; Zhao, C.; Liu, J.; Zhou, J.; Zhang, Z.; Peng, L.-M. *ACS Appl. Mater. Interfaces* **2019**, *11*, 42496–42503.

(207) Smith, J.; Zhang, W.; Sougrat, R.; Zhao, K.; Li, R.; Cha, D.; Amassian, A.; Heeney, M.; McCulloch, I.; Anthopoulos, T. D. *Adv. Mater.* **2012**, *24*, 2441–2446.

(208) Panidi, J.; Paterson, A. F.; Khim, D.; Fei, Z.; Han, Y.; Tsetseris, L.; Vourlias, G.; Patsalas, P. A.; Heeney, M.; Anthopoulos, T. D. *Adv. Sci.* **2018**, *5*, 1700290.

(209) Huseynova, G.; Shrestha, N. K.; Xu, Y.; Shin, E.-Y.; Park, W.-T.; Ji, D. *Org. Electron.* **2018**, *62*, 572–580.

(210) Liu, C.; Jang, J.; Xu, Y.; Kim, H. J.; Khim, D.; Park, W. T.; Noh, Y. Y.; Kim, J. J. *Adv. Funct. Mater.* **2015**, *25*, 758–767.

(211) Kim, J.; Khim, D.; Baeg, K.-J.; Park, W.-T.; Lee, S.-H. *Adv. Funct. Mater.* **2016**, *26*, 7886–7894.

(212) Sonar, P.; Singh, S. P.; Li, Y.; Soh, M. S.; Dodabalapur, A. *Adv. Mater.* **2010**, *22*, 5409–5413.

(213) Dou, J.-H.; Zheng, Y.-Q.; Lei, T.; Zhang, S.-D.; Wang, Z.; Zhang, W.-B.; Wang, J.-Y.; Pei, J. *Adv. Funct. Mater.* **2014**, *24*, 6270–6278.

(214) Yue, W.; Nikolka, M.; Xiao, M.; Sadhanala, A.; Nielsen, C. B.; White, A. J. P.; Chen, H.-Y.; Onwubiko, A.; Sirringhaus, H.; McCulloch, I. *J. Mater. Chem. C* **2016**, *4*, 9704–9710.

(215) Fallon, K. J.; Wijeyasinghe, N.; Manley, E. F.; Dimitrov, S. D.; Yousaf, S. A.; Ashraf, R. S.; Duffy, W.; Guilbert, A. A. Y.; Freeman, D. M. E.; Al-Hashimi, M.; Nelson, J.; Durrant, J. R.; Chen, L. X.; McCulloch, I.; Marks, T. J.; Clarke, T. M.; Anthopoulos, T.; Bronstein, H. *Chem. Mater.* **2016**, *28*, 8366–8378.

(216) Ishii, H.; Sugiyama, K.; Ito, E.; Seki, K. *Adv. Mater.* **1999**, *11*, 605–625.

(217) Osikowicz, W.; de Jong, M. P.; Braun, S.; Tengstedt, C.; Fahlman, M.; Salaneck, W. R. *Appl. Phys. Lett.* **2006**, *88*, 193504.

(218) Lu, C.; An, L.; Fu, Q.; Liu, J.; Zhang, H.; Murduck, J. *Appl. Phys. Lett.* **2006**, *88*, 133501.

(219) Heimel, G.; Romaner, L.; Zojer, E.; Bredas, J.-L. *Acc. Chem. Res.* **2008**, *41*, 721–729.

(220) Richards, T. J.; Sirringhaus, H. *J. Appl. Phys.* **2007**, *102*, 094510.

(221) Borchert, J. W.; Peng, B.; Letzkus, F.; Burghartz, J. N.; Chan, P. K.; Zojer, K.; Ludwigs, S.; Klauk, H. *Nat. Commun.* **2019**, *10*, 1119.

(222) Borchert, J. W.; Zschieschang, U.; Letzkus, F.; Giorgio, M.; Weitz, R. T.; Caironi, M.; Burghartz, J. N.; Ludwigs, S.; Klauk, H. *Sci. Adv.* **2020**, *6*, eaaz5156.

(223) Gundlach, D. J.; Zhou, L; Nichols, J. A.; Jackson, T. N.; Necliudov, P. V.; Shur, M. S. *J. Appl. Phys.* **2006**, *100*, 24509.

(224) Xu, Y.; Minari, T.; Tsukagoshi, K.; Chroboczek, J. A.; Ghibaudo, G. *J. Appl. Phys.* **2010**, *107*, 114507.

(225) Bürgi, L; Sirringhaus, H; Friend, R. H. *Appl. Phys. Lett.* **2002**, *80*, 2913–2915.

(226) Pesavento, P. V.; Chesterfield, R. J.; Newman, C. R.; Frisbie, C. D. *J. Appl. Phys.* **2004**, *96*, 7312–7324.

(227) Pesavento, P. V.; Puntambekar, K. P.; Frisbie, C. D.; McKeen, J. C.; Ruden, P. P. *J. Appl. Phys.* **2006**, *99*, 094504.

(228) Natali, D.; Caironi, M. *Adv. Mater.* **2012**, *24*, 1357–1387.

(229) Salzmann, I.; Heimel, G. *J. Electron Spectrosc. Relat. Phenom.* **2015**, *204*, 208–222.

(230) Shirakawa, H.; Louis, E. J.; MacDiarmid, A. G.; Chiang, C. K.; Heeger, A. J. *J. Chem. Soc. Chem. Commun.* **1977**, 578–580.

(231) Tietze, M. L.; Burtone, L.; Riede, M.; Lüssem, B.; Leo, K. *Phys. Rev. B* **2012**, *86*, 35320.

(232) Jacobs, I. E.; Moulé, A. J. *Adv. Mater.* **2017**, *29*, 1703063.

(233) Kroon, R.; Mengistie, D. A.; Kiefer, D.; Hynynen, J.; Ryan, J. D.; Yu, L.; Müller, C. *Chem. Soc. Rev.* **2016**, *45*, 6147–6164.

(234) Wei, P.; Oh, J. H.; Dong, G.; Bao, Z. *J. Am. Chem. Soc.* **2010**, *132*, 8852–8853.

(235) Hein, M. P.; Zakhidov, A. A.; Lüssem, B.; Jankowski, J.; Tietze, M. L.; Riede, M. K.; Leo, K. *Appl. Phys. Lett.* **2014**, *104*, 013507.

(236) Khim, D.; Baeg, K. J.; Caironi, M.; Liu, C.; Xu, Y.; Kim, D. Y.; Noh, Y. Y. *Adv. Funct. Mater.* **2014**, *24*, 6252–6261.

(237) Olthof, S.; Singh, S.; Mohapatra, S. K.; Barlow, S.; Marder, S. R.; Kippelen, B.; Kahn, A. *Appl. Phys. Lett.* **2012**, *101*, 253303.

(238) Tietze, M. L.; Pahner, P.; Schmidt, K.; Leo, K.; Lüssem, B. *Adv. Funct. Mater.* **2015**, *25*, 2701–2707.

(239) Olthof, S.; Mehraeen, S.; Mohapatra, S. K.; Barlow, S.; Coropceanu, V.; Brédas, J.-L.; Marder, S. R.; Kahn, A. *Phys. Rev. Lett.* **2012**, *109*, 176601.

(240) Blochwitz, J.; Fritz, T.; Pfeiffer, M.; Leo, K.; Alloway, D. M.; Lee, P. A.; Armstrong, N. R. *Org. Electron.* **2001**, *2*, 97–104.

(241) Olthof, S.; Tress, W.; Meerheim, R.; Lüssem, B.; Leo, K. *J. Appl. Phys.* **2009**, *106*, 103711.

(242) Xu, Y.; Minari, T.; Tsukagoshi, K.; Chroboczek, J.; Balestra, F.; Ghibaudo, G. *Solid. State. Electron.* **2011**, *61*, 106–110.

(243) Minari, T.; Darmawan, P.; Liu, C.; Li, Y.; Xu, Y.; Tsukagoshi, K. *Appl. Phys. Lett.* **2012**, *100*, 59.

(244) Kano, M.; Minari, T.; Tsukagoshi, K. *Appl. Phys. Lett.* **2009**, *94*, 101.

(245) Xu, Y.; Sun, H.; Shin, E. Y.; Lin, Y. F.; Li, W.; Noh, Y. Y. *Adv. Mater.* **2016**, *28*, 8531–8537.

(246) Wang, J. Z.; Zheng, Z. H.; Sirringhaus, H *Appl. Phys. Lett.* **2006**, *89*, 83513.

(247) Ding, L.; Wang, S.; Zhang, Z.; Zeng, Q.; Wang, Z.; Pei, T.; Yang, L.; Liang, X.; Shen, J.; Chen, Q.; Cui, R.; Li, Y.; Peng, L.-M. *Nano Lett.* **2009**, *9*, 4209–4214.

(248) Yang, Y.; Ding, L.; Han, J.; Zhang, Z.; Peng, L.-M. *ACS Nano* **2017**, *11*, 4124–4132.

(249) Zhang, J.; Wang, C.; Fu, Y.; Che, Y.; Zhou, C. *ACS Nano* **2011**, *5*, 3284–3292.

(250) Ha, T.-J.; Chen, K.; Chuang, S.; Yu, K. M.; Kiriya, D.; Javey, A. *Nano Lett.* **2015**, *15*, 392–397.

(251) Derycke, V; Martel, R; Appenzeller, J; Avouris, P. *Appl. Phys. Lett.* **2002**, *80*, 2773–2775.

(252) Kang, B. R.; Yu, W. J.; Kim, K. K.; Park, H. K.; Kim, S. M.; Park, Y.; Kim, G.; Shin, H.; Kim, U. J.; Lee, E. *Adv. Funct. Mater.* **2009**, *19*, 2553–2559.

(253) Lee, S. Y.; Lee, S. W.; Kim, S. M.; Yu, W. J.; Jo, Y. W.; Lee, Y. H. *ACS Nano* **2011**, *5*, 2369–2375.

(254) Geier, M. L.; McMorrow, J. J.; Xu, W.; Zhu, J.; Kim, C. H.; Marks, T. J.; Hersam, M. C. *Nat. Nanotechnol.* **2015**, *10*, 944–948.

(255) Xu, Q.; Zhao, J.; Pecunia, V.; Xu, W.; Zhou, C.; Dou, J.; Gu, W.; Lin, J.; Mo, L.; Zhao, Y.; Cui, Z. *ACS Appl. Mater. Interfaces* **2017**, *9*, 12750–12758.

(256) Shim, M.; Javey, A.; Shi Kam, N. W.; Dai, H. *J. Am. Chem. Soc.* **2001**, *123*, 11512–11513.

(257) Geier, M. L.; Moudgil, K.; Barlow, S.; Marder, S. R.; Hersam, M. C. *Nano Lett.* **2016**, *16*, 4329–4334.

(258) Wang, H.; Wei, P.; Li, Y.; Han, J.; Lee, H. R.; Naab, B. D.; Liu, N.; Wang, C.; Adijanto, E.; Tee, B. C.-K. *Proc. Natl. Acad. Sci. U. S. A.* **2014**, *111*, 4776–4781.

(259) Xu, J.-L.; Dai, R.-X.; Xin, Y.; Sun, Y.-L.; Li, X.; Yu, Y.-X.; Xiang, L.; Xie, D.; Wang, S.-D.; Ren, T.-L. *Sci. Rep.* **2017**, *7*, 1–10.

(260) Eberle, B.; Hübner, O.; Ziesak, A.; Kaifer, E.; Himmel, H.-J. **2015**, 8578–8590.

(261) Himmel, H.-J. *Synlett* **2018**, *29*, 1957–1977.

(262) Connelly, N. G.; Geiger, W. E. *Chem. Rev.* **1996**, *96*, 877–910.

(263) Zhu, X.-Q.; Zhang, M.-T.; Yu, A.; Wang, C.-H.; Cheng, J.-P. *J. Am. Chem. Soc.* **2008**, *130*, 2501–2516.

(264) Himmel, H.-J. *Zeitschrift fuer Anorg. und Allg. Chemie* **2013**, *639*, 1940–1952.

(265) Peters, A.; Herrmann, H.; Magg, M.; Kaifer, E.; Himmel, H.-J. *Eur. J. Inorg. Chem.* **2012**, *2*, 1620–1631.

(266) Eberle, B.; Damjanović, M.; Enders, M.; Leingang, S.; Pfisterer, J.; Krämer, C.; Hübner, O.; Kaifer, E.; Himmel, H.-J. *Inorg. Chem.* **2016**, *55*, 1683–1696.

(267) Wiesner, S.; Wagner, A.; Kaifer, E.; Himmel, H.-J. *Chem. Eur. J.* **2016**, *22*, 10438–10445.

(268) Wild, U.; Schön, F.; Himmel, H.-J. *Angew. Chem. Int. Ed.* **2017**, *56*, 16410–16413.

(269) Wild, U.; Federle, S.; Wagner, A.; Kaifer, E.; Himmel, H.-J. *Chem. Eur. J.* **2016**, *22*, 11971–11976.

(270) Herrmann, H.; Ziesak, A.; Wild, U.; Leingang, S.; Schrempp, D.; Wagner, N.; Beck, J.; Kaifer, E.; Wadepohl, H.; Himmel, H.-J. *ChemPhysChem* **2014**, *15*, 351–365.

(271) Stang, S; Kaifer, E; Himmel, H.-J. *Chem. Eur. J.* **2014**, *20*, 5288–5297.

(272) Eberle, B.; Kaifer, E.; Himmel, H.-J. *Angew. Chemie* **2017**, *129*, 3408–3412.

(273) Peters, A.; Kaifer, E.; Himmel, H.-J. *Eur. J. Org. Chem.* **2008**, *2008*, 5907–5914.

(274) Emeljanenko, D.; Peters, A.; Vitske, V.; Kaifer, E.; Himmel, H.-J. *Eur. J. Inorg. Chem.* **2010**, 4783–4789.

(275) Bindewald, E.; Lorenz, R.; Hübner, O.; Brox, D.; Herten, D. P.; Kaifer, E.; Himmel, H.-J. *Dalt. Trans.* **2015**, *44*, 3467–3485.

(276) Schneider, S.; Lefebvre, J.; Diercks, N. J.; Berger, F. J.; Lapointe, F.; Schleicher, J.; Malenfant, P. R.; Zaumseil, J. *ACS Appl. Nano Mater.* **2020**, *3*, 12314–12324.

(277) Reiser, B.; González-García, L.; Kanelidis, I.; Maurer, J. H. M.; Kraus, T. *Chem. Sci.* **2016**, *7*, 4190–4196.

(278) Puthussery, J.; Seefeld, S.; Berry, N.; Gibbs, M.; Law, M. *J. Am. Chem. Soc.* **2011**, *133*, 716–719.

(279) Lewis, J. A. *Curr. Opin. Solid State Mater. Sci.* **2002**, *6*, 245–250.

(280) Berger, F. J.; Higgins, T. M.; Rother, M.; Graf, A.; Zakharko, Y.; Allard, S.; Matthiesen, M.; Gotthardt, J. M.; Scherf, U.; Zaumseil, J. *ACS Appl. Mater. Interfaces* **2018**, *10*, 11135–11142.

(281) Mistry, K. S.; Larsen, B. A.; Blackburn, J. L.; Renewable, N.; States, U. *ACS Nano* **2013**, *7*, 2231–2239.

(282) Toshimitsu, F.; Nakashima, N. *Nat. Commun.* **2014**, *5*, 5041.

(283) Pochorovski, I.; Wang, H.; Feldblyum, J. I.; Zhang, X.; Antaris, A. L. *J. Am. Chem. Soc.* **2015**, *137*, 4328–4331.

(284) Kang, S. J.; Kocabas, C.; Ozel, T.; Shim, M.; Pimparkar, N.; Alam, M. A.; Rotkin, S. V.; Rogers, J. A. *Nat. Nanotechnol.* **2007**, *2*, 230–236.

(285) Kuwahara, Y.; Nihey, F.; Ohmori, S.; Saito, T. *Carbon* **2015**, *91*, 370–377.

(286) Al-Kandary, J. A.; Al-Jimaz, A. S.; Abdul-Latif, A. H. M. *J. Chem. Eng. Data* **2006**, *51*, 2074–2082.

(287) Maryott, A. A.; Smith, E. R., *Table of dielectric constants of pure liquids*; US Government Printing Office, Washington D. C.: 1951.

(288) Al-Kandary, J. A.; Al-Jimaz, A. S.; Abdul-Latif, A.-H. M. *J. Chem. Thermodyn.* **2006**, *38*, 1351–1361.

(289) Saakov, V. S.; Drapkin, V. Z.; Krivchenko, A. I.; Rozengart, E. V.; Bogachev, Y. V.; Knyazev, M. N., *Derivative spectrophotometry and electron spin resonance (ESR) spectroscopy for ecological and biological questions*; Springer Science & Business Media, Heidelberg: 2012.

(290) Feng, S.; Ma, D.; Qiu, Y.; Duan, L. *Rsc Adv.* **2018**, *8*, 4153–4161.

(291) Gotovac, S.; Honda, H.; Hattori, Y.; Takahashi, K.; Kanoh, H.; Kaneko, K. *Nano Lett.* **2007**, *7*, 583–587.

(292) Debnath, S.; Cheng, Q.; Hedderman, T. G.; Byrne, H. J. *J. Phys. Chem. C* **2010**, *114*, 8167–8175.

(293) Yoo, J.; Ozawa, H.; Fujigaya, T.; Nakashima, N. *Nanoscale* **2011**, *3*, 2517–2522.

(294) Hedderman, T. G.; Keogh, S. M.; Chambers, G.; Byrne, H. J. *J. Phys. Chem. B* **2006**, *110*, 3895–3901.

(295) Debnath, S.; Cheng, Q.; Hedderman, T. G.; Byrne, H. J. *Carbon* **2010**, *48*, 1489–1497.

(296) Mateo-Alonso, A.; Ehli, C.; Chen, K. H.; Guldi, D. M.; Prato, M. *J. Phys. Chem. A* **2007**, *111*, 12669–12673.

(297) Shea, M. J.; Mehlenbacher, R. D.; Zanni, M. T.; Arnold, M. S. *J. Phys. Chem. Lett.* **2014**, *5*, 3742–3749.

(298) Miyauchi, Y. *J. Mater. Chem. C* **2013**, *1*, 6499–6521.

(299) Amori, A. R.; Hou, Z.; Krauss, T. D. *Annu. Rev. Phys. Chem.* **2018**, *69*, 81–99.

(300) Sharifi, R.; Samaraweera, M.; Gascon, J. A.; Papadimitrakopoulos, F. *J. Am. Chem. Soc.* **2014**, *136*, 7452–7463.

(301) Zheng, M.; Jagota, A.; Semke, E. D.; Diner, B. A.; McLean, R. S.; Lustig, S. R.; Richardson, R. E.; Tassi, N. G. *Nat. Mater.* **2003**, *2*, 338–342.

(302) Sun, Z.; O'Connor, I.; Bergin, S. D.; Coleman, J. N. *J. Phys. Chem. C* **2009**, *113*, 1260–1266.

(303) Zheng, Y.; Sanchez, S. R.; Bachilo, S. M.; Weisman, R. B. *J. Phys. Chem. C* **2018**, *122*, 4681–4690.

(304) Shulaker, M. M.; Hills, G.; Park, R. S.; Howe, R. T.; Saraswat, K.; Wong, H. S.; Mitra, S. *Nature* **2017**, *547*, 74–78.

(305) Kim, W.; Javey, A.; Vermesh, O.; Wang, Q.; Li, Y.; Dai, H. *Nano Lett.* **2003**, *3*, 193–198.

(306) Schneider, S.; Brohmann, M.; Lorenz, R.; Hofstetter, Y. J.; Rother, M.; Sauter, E.; Zharnikov, M.; Vaynzof, Y.; Himmel, H.-J.; Zaumseil, J. *ACS Nano* **2018**, *12*, 5895–5902.

(307) Chen, H.; Cao, Y.; Zhang, J.; Zhou, C. *Nat. Commun.* **2014**, *5*, 4097.

(308) Kim, B.; Jang, S.; Geier, M. L.; Prabhumirashi, P. L.; Hersam, M. C.; Dodabalapur, A. *Nano Lett.* **2014**, *14*, 3683–3687.

(309) Brownlie, L.; Shapter, J. *Carbon* **2018**, *126*, 257–270.

(310) Blackburn, J. L.; Ferguson, A. J.; Cho, C.; Grunlan, J. C. *Adv. Mater.* **2018**, *30*, 1704386.

(311) Fukumaru, T.; Fujigaya, T.; Nakashima, N. *Sci. Rep.* **2015**, *5*, 7951.

(312) Himmel, H.-J. In *Guanidines as Reagents and Catalysts II*; Springer International Publishing, Basel: 2015; Chapter 4, pp 165–203.

(313) Nathan, A., Striakhilev, D., Chaji, R., Shtiani, S., Lee, C.-H., Sazonov, A., Robertson, J., Milne, W. *Mater. Res. Soc. Symp. Proc.* **2006**, *910*, 0910–A16–01–L09–01.

(314) Vitske, V.; König, C.; Hübner, O.; Kaifer, E.; Himmel, H.-J. *Eur. J. Inorg. Chem.* **2010**, 115–126.

(315) Gotthardt, J. M.; Schneider, S.; Brohmann, M.; Leingang, S.; Sauter, E.; Zharnikov, M.; Himmel, H.-J.; Zaumseil, J. *ACS Appl. Electron. Mater.* **2021**, *3*, 804–812.

(316) Statz, M.; Schneider, S.; Berger, F. J.; Lai, L.; Wood, W. A.; Abdi-Jalebi, M.; Leingang, S.; Himmel, H.-J.; Zaumseil, J.; Sirringhaus, H. *ACS Nano* **2020**, *14*, 15552–15565.

(317) Kalb, W. L.; Haas, S.; Krellner, C.; Mathis, T.; Batlogg, B. *Phys. Rev. B - Condens. Matter Mater. Phys.* **2010**, *81*, 1–13.

(318) Kahn, A.; Koch, N.; Gao, W. *J. Polym. Sci. Part B Polym. Phys.* **2003**, *41*, 2529–2548.

(319) Paniagua, S. A.; Baltazar, J.; Sojoudi, H.; Mohapatra, S. K.; Zhang, S.; Henderson, C. L.; Graham, S.; Barlow, S.; Marder, S. R. *Mater. Horiz.* **2014**, *1*, 111–115.

(320) Held, M.; Schießl, S. P.; Miehler, D.; Gannott, F.; Zaumseil, J. *Appl. Phys. Lett.* **2015**, *107*, 083301.

(321) Xu, J. L.; Dai, R. X.; Xin, Y.; Sun, Y. L.; Li, X.; Yu, Y. X.; Xiang, L.; Xie, D.; Wang, S. D.; Ren, T. L. *Sci. Rep.* **2017**, *7*, 1–10.

(322) Schneider, S.; Gotthardt, J. M.; Steuer, L.; Leingang, S.; Zaumseil, J. *J. Mater. Chem. C* **2021**, *9*, 7485–7493.

(323) Kweon, O. Y.; Lee, M. Y.; Park, T.; Jang, H.; Jeong, A.; Um, M. K.; Oh, J. H. *J. Mater. Chem. C* **2019**, *7*, 1525–1531.

(324) Sirringhaus, H. *Adv. Mater.* **2014**, *26*, 1319–1335.

(325) Takeda, Y.; Hayasaka, K.; Shiwaku, R.; Yokosawa, K.; Shiba, T.; Mamada, M.; Kumaki, D.; Fukuda, K.; Tokito, S. *Sci. Rep.* **2016**, *6*, 1–9.

(326) Zschieschang, U.; Borchert, J. W.; Giorgio, M.; Caironi, M.; Letzkus, F.; Burghartz, J. N.; Waizmann, U.; Weis, J.; Ludwigs, S.; Klauk, H. *Adv. Funct. Mater.* **2019**, *30*, 1903812.

(327) Quinn, J. T.; Zhu, J.; Li, X.; Wang, J.; Li, Y. *J. Mater. Chem. C* **2017**, *5*, 8654–8681.

(328) Minari, T.; Darmawan, P.; Liu, C.; Li, Y.; Xu, Y.; Tsukagoshi, K. *Appl. Phys. Lett.* **2012**, *100*, 093303.

(329) Singh, S.; Mohapatra, S. K.; Sharma, A.; Fuentes-Hernandez, C.; Barlow, S.; Marder, S. R.; Kippelen, B. *Appl. Phys. Lett.* **2013**, *102*, 2–6.

(330) Liu, S.; DeWeerd, N. J.; Reeves, B. J.; San, L. K.; Dahal, D.; Radha Krishnan, R. K.; Strauss, S. H.; Boltalina, O. V.; Lüssem, B. *Adv. Electron. Mater.* **2019**, *5*, 1900109.

(331) Kim, Y.; Broch, K.; Lee, W.; Ahn, H.; Lee, J.; Yoo, D.; Kim, J.; Chung, S.; Sirringhaus, H.; Kang, K.; Lee, T. *Adv. Funct. Mater.* **2020**, *30*.

(332) Paterson, A. F.; Treat, N. D.; Zhang, W.; Fei, Z.; Wyatt-Moon, G.; Faber, H.; Vourlias, G.; Patsalas, P. A.; Solomeshch, O.; Tessler, N.; Heeney, M.; Anthopoulos, T. D. *Adv. Mater.* **2016**, *28*, 7791–7798.

(333) Kang, K.; Watanabe, S.; Broch, K.; Sepe, A.; Brown, A.; Nasrallah, I.; Nikolka, M.; Fei, Z.; Heeney, M.; Matsumoto, D.; Marumoto, K.; Tanaka, H.; Kuroda, S.-I.; Sirringhaus, H. *Nat. Mater.* **2016**, *15*, 896–902.

(334) Patel, S. N.; Glaudell, A. M.; Kiefer, D.; Chabinyc, M. L. *ACS Macro Lett.* **2016**, *5*, 268–272.

(335) Statz, M.; Venkateshvaran, D.; Jiao, X.; Schott, S.; McNeill, C. R.; Emin, D.; Sirringhaus, H.; Di Pietro, R. *Commun. Phys.* **2018**, *1*, 16.

(336) Scaccabarozzi, A. D.; Scuratti, F.; Barker, A. J.; Basu, A.; Paterson, A. F.; Fei, Z.; Solomeshch, O.; Petrozza, A.; Tessler, N.; Heeney, M.; Anthopoulos, T. D.; Caironi, M. *Adv. Electron. Mater.* **2020**, *6*, 2000539.

(337) Yan, H.; Chen, Z.; Zheng, Y.; Newman, C.; Quinn, J. R.; Dötz, F.; Kastler, M.; Facchetti, A. *Nature* **2009**, *457*, 679–686.

(338) Caironi, M.; Newman, C.; Moore, J. R.; Natali, D.; Yan, H.; Facchetti, A.; Sirringhaus, H. *Appl. Phys. Lett.* **2010**, *96*, 94–97.

(339) Bobbert, P. A.; Sharma, A.; Mathijssen, S. G.; Kemerink, M.; De Leeuw, D. M. *Adv. Mater.* **2012**, *24*, 1146–1158.

(340) Kronemeijer, A. J.; Gili, E.; Shahid, M.; Rivnay, J.; Salleo, A.; Heeney, M.; Sirringhaus, H. *Adv. Mater.* **2012**, *24*, 1558–1565.

(341) Mager, H. Synthesis of Horizontally Aligned Semiconducting Single-Walled Carbon Nanotube Networks via Zone-Casting, Master Thesis, Ruprecht-Karls Universität Heidelberg, 2020.

(342) Megerle, U.; Pugliesi, I.; Schriever, C.; Sailer, C. F.; Riedle, E. *Appl. Phys. B* **2009**, *96*, 215–231.

EIDESSTATTLICHE VERSICHERUNG

Eidesstattliche Versicherung gemäß §8 der Promotionsordnung der Naturwissenschaftlich-Mathematischen Gesamtfakultät der Universität Heidelberg

Bei der eingereichten Dissertation zum Thema

Processing and N-Doping of Polymer and Carbon Nanotube Field-Effect Transistors

handelt es sich um meine eigenständig erbrachte Leistung.

Ich habe nur die angegebenen Quellen benutzt und mich keiner unzulässigen Hilfe Dritter bedient. Insbesondere habe ich wörtlich oder sinngemäß aus anderen Werken übernommene Inhalte als solche kenntlich gemacht.

Diese Arbeit oder Teile davon habe ich bislang nicht an einer Hochschule des In- oder Auslands als Bestandteil einer Prüfungs- oder Qualifikationsleistung vorgelegt.

Die Richtigkeit der vorstehenden Erklärungen bestätige ich.

Die Bedeutung der eidesstattlichen Versicherung und die strafrechtlichen Folgen einer unrichtigen oder unvollständigen eidesstattlichen Versicherung sind mir bekannt.

Ich versichere an Eides statt, dass ich nach bestem Wissen die reine Wahrheit erklärt und nichts verschwiegen habe.

Heidelberg, 23.09.2021   ....

                                                                        Severin Schneider